

**MODELLING THE SOUND
INSULATION OF CORRUGATED ROOF
STRUCTURES: AN EXTENDED
TRANSFER MATRIX APPROACH**

PhD Thesis

Acoustics Research Centre, University of Salford
Salford, UK

Author: James Massaglia
Supervisor: Prof. Andy Moorhouse

*Submitted in partial fulfilment of the requirements of the
degree of Doctor of Philosophy*

May, 2017

TABLE OF CONTENTS

II.	List of Figures	vii
III.	List of Tables	xix
IV.	Acknowledgements	xx
V.	Abstract	xxiii
VI.	Abbreviations and Symbols	xxiv
1	Introduction	1
1.1	Background	1
1.2	Aim.....	3
1.3	Approach	4
1.4	Layout of the thesis	5
2	Dual Leaf Roof Systems	6
2.1	Profiled metal sheets	6
2.2	Infill and cavity layers.....	9
2.3	Structural frame: spacer kits and point-to-point connections.....	9
2.4	Roof system specifications.....	12
2.5	Dual leaf partitions	17
2.6	Conclusions	18
3	Literature Review	20
3.1	Overview of modelling techniques	20

3.2	Dual leaf structures.....	22
3.3	Point connected structures.....	23
3.4	Profiled plates.....	24
3.5	The Transfer Matrix Method.....	26
3.6	Porous material models	27
4	Building blocks.....	29
4.1	The Transfer Matrix Method.....	29
4.1.1	Introduction.....	29
4.1.2	Wavenumber domain	29
4.1.3	System geometry.....	31
4.1.4	Fluid layers.....	32
4.1.5	Elastic solids	33
4.1.6	Porous layers.....	35
4.1.7	Thin plates.....	36
4.1.8	Interface matrices.....	36
4.1.9	Termination conditions	37
4.1.10	Impedance, Transmission, Reflection and Absorption coefficients	38
4.1.11	Finite size corrections	40
4.1.12	Excitation mechanism.....	44
4.1.13	Conclusions.....	44
4.2	Porous material modelling	44

4.2.1	Introduction.....	44
4.2.2	Measurement method.....	45
4.2.3	Equivalent fluids	46
4.2.4	Simple approaches	46
4.2.5	Poroelastic behaviour.....	47
4.2.6	Determining porous material properties	50
4.2.7	Conclusions.....	55
4.3	Plates	55
4.3.1	Thin plate theory	56
4.3.2	Orthotropic plate model	58
4.3.3	Conclusions.....	61
4.4	Ribbed plate: periodic model	62
4.4.1	Floquet periodicity and pressure fields	62
4.4.2	Geometry and definitions.....	65
4.4.3	The forced plate equation.....	67
4.4.4	Beam forces	68
4.4.5	Transmission and Reflection coefficients.....	70
4.4.6	Conclusions for ribbed plates.....	73
4.5	Conclusions	73
5	Point-connected plate models	75
5.1	Point connected plates	75

5.1.1	Introduction.....	75
5.1.2	System description	76
5.1.3	Pressure in the fluid spaces	77
5.1.4	Plate equations of motion.....	81
5.1.5	Rod forces	84
5.1.6	Profiled panels	87
5.1.7	Considerations on applicability and limitations.....	88
5.1.8	Conclusions.....	89
5.2	Point connected plates with intermediate beams.....	89
5.2.1	Beam equations.....	90
5.2.2	Forced plate equations	95
5.2.3	Rod forces	96
5.2.4	Beam compressional stiffness.....	98
5.2.5	Considerations on applicability and limitations.....	99
5.2.6	Conclusions.....	99
5.3	Model outputs and combination with the TMM	99
5.3.1	Combination with the TMM via effective properties	101
5.3.2	Combining plates	104
5.3.3	Programming.....	108
5.3.4	Convergence and truncation	109
5.4	Conclusions	114

6	Results: profiled plates	117
6.1	Ribbed panels	117
6.1.1	Ribbed panels as equivalent orthotropic plates.....	118
6.1.2	Profile resonances	130
6.1.3	Ribbed plates compared to standing seam corrugations	134
6.1.4	Periodically ribbed plate as a TMM layer.....	137
6.2	Trapezoidal profile panels: differences between FEM model and orthotropic plate formulation	138
6.3	Corrugated metal sheets: comparisons with measured data.....	142
6.4	Conclusions	149
7	Results: dual leaf structures	150
7.1	Single and dual leaf structures without structural connections	150
7.1.1	Structures with flat panels.....	150
7.1.2	Interfacing layers: bonded versus unbonded solids and poroelastic materials	157
7.1.3	Factory-made composites	159
7.1.4	Conclusions.....	163
7.2	Point connected plates: validation and surveys.....	163
7.2.1	FEM validation	164
7.2.2	Halters and brackets: comparison of compressional stiffness	166
7.2.3	Halter and bracket connectors in roof systems	170
7.2.4	Effect of connector stiffness and spacing on dual leaf structures	172

7.2.5	Effect of top hat purlins	174
7.2.6	Conclusions.....	180
7.3	Corrugated roof structures: comparisons with laboratory measurements	181
7.3.1	Rooflights.....	181
7.3.2	Roof structures with soft fibrous infill.....	185
7.3.3	Roof structure with high density infill and top-hat purlins.....	193
7.3.4	Roof structures with high density boards, multiple panels	196
7.3.5	Roof structures with damping sheets (“acoustic matting”).....	202
7.3.6	Conclusions for full systems	205
7.4	Conclusions for laboratory measurement comparisons	206
8	Conclusions	209
9	References	215
	Appendix A: Rain noise.....	221
	Appendix B: Plates interconnected by rods	227

II. LIST OF FIGURES

Figure 1: Sound insulation measurement setup for ISO 10140-2.....	2
Figure 2: Trapezoidal profile diagram	7
Figure 3: Bar and bracket spacer kit; MCRMA (2013).....	10
Figure 4: Halter spacer kit, with standing seam top sheet	11
Figure 5: Halter spacer kit with top-hat purlin.....	11
Figure 6: Combined halter and bar and bracket spacer kit	12
Figure 7: MCRMA Roof System Specification 1; MCRMA (2013).....	13
Figure 8: MCRMA Roof System Specification 2; MCRMA (2013).....	13
Figure 9: MCRMA Roof System Specification 3; MCRMA (2013).....	14
Figure 10: MCRMA Roof System Specification 4; MCRMA (2013).....	15
Figure 11: MCRMA Roof System Specification 5; MCRMA (2013).....	16
Figure 12: Rooflight cross-section; MCRMA (2013).....	16
Figure 13: Factory-made composite cross-section; MCRMA (2013)	17
Figure 14: Dimensions and wavenumber vector k , showing Cartesian coordinates x, y, z and spherical coordinates ϕ and θ	30
Figure 15: A layered system with n layers in the Transfer Matrix framework.....	31
Figure 16: Angle of incidence correction factor (Gauss) with two different values of β , compared to field incidence, and a ray tracing model of sound energy at the walls of a reverberation room (H. Kang et al. 2000).....	40

Figure 17: Double glazing 1/3 octave band transmission loss; laboratory measurement versus TMM with no corrections (∞), Gaussian incidence ($\beta = 1$ and 2), and field incidence with a limiting angle of 78 degrees.....	41
Figure 18: Gaussian incidence (H. Kang et al. 2000) versus radiation efficiency correction (Villot et al. 2001).....	42
Figure 19: Diagram of an iterative method used to determine Young's modulus and flow resistivity of fibrous materials. RMSE = root mean square error.	52
Figure 20: Real and imaginary parts of normalised surface impedance of high density mineral wool (140 kg/m^3); comparison of impedance tube measurement (dashed lines) with transfer matrix model using Delany-Bazley equivalent fluid formulation (solid lines)	53
Figure 21: Real and imaginary parts of normalised surface impedance of high density mineral wool (140 kg/m^3); comparison of impedance tube measurement (dashed lines) with transfer matrix model using a poroelastic layer (solid lines)	53
Figure 22: Relationship between density and Young's Modulus of mineral wool samples, with a fitted curve	55
Figure 23: Relationship between density and flow resistivity of mineral wool samples, showing an exponentially fitted curve to the measured data, and the Bies-Hansen empirical formula (Equation (4.39))	55
Figure 24: Incident wave orientation with respect to panel corrugations; the wave fronts on the surface of the plate are shown in red.....	59
Figure 25: Trapezoidal plate geometry	60
Figure 26: Ribbed plate dimensions; hw is the total depth, aR the rib width, aa the pitch, and h the plate thickness.....	61

Figure 27: Periodically beam-stiffened plate geometry, showing incident, reflected and transmitted pressure wave vectors	65
Figure 28: Double plate model diagram	76
Figure 29: TMM modelled transmission loss of corrugated dual leaf structure with different panel orientations	88
Figure 30: Point connected plates with intermediate beams.....	89
Figure 31: Refractive index obtained with the reverse method, for a single poroelastic layer (top left), two poroelastic layers of different properties (top right) and three layers, with an air gap between two poroelastic layers (bottom)	103
Figure 32: Diagram of roof structure with high density board	105
Figure 33: Two plates in contact, showing global neutral axis.....	107
Figure 34: Sound reduction index modelling tool main window	108
Figure 35: Flow diagram of calculation program	109
Figure 36: Sum across frequencies of difference between consecutive τ values with increasing number of θ, ϕ pairs	111
Figure 37: Number of θ, ϕ pairs required for convergence for each frequency bin ($Var\tau < 0.1\text{dB}$)	112
Figure 38: Transmission loss of dual leaf corrugated roof structure with connections spaced at 1m and 0.4 m, showing error margins in red	113
Figure 39: Change in TL summed over 120 frequency bins with increasing m and n truncation number N for dual leaf wall with mineral wool infill and point connections.....	114
Figure 40: Ribbed plate geometry in Comsol	119

Figure 41: Relative difference in FEM modelled TL of panel A between 5 and 8 elements per wavelength at 2 kHz.....	120
Figure 42: Transmission loss of panel A for incident angle $\theta = \pi/4$ and two wave orientations, $\phi = 0^\circ$ (top) and $\phi = 90^\circ$ (bottom), showing FEM, analytical and equivalent orthotropic results	121
Figure 43: TL of panel A calculated with ribbed plate analytical model (top) compared to an equivalent orthotropic plate (bottom), showing all angles of incidence, with a wave oriented in the stiffest dimension	122
Figure 44: Comparison of diffuse field transmission loss of panel A for analytical ribbed plate model and equivalent orthotropic plate.....	123
Figure 45: Transmission loss of panel B for incident angle $\theta = \pi/4$ and two wave orientations, $\phi = 0^\circ$ (top) and $\phi = 90^\circ$ (bottom), showing analytical and equivalent orthotropic results	124
Figure 46: TL of panel B calculated with ribbed plate analytical model (top) compared to an equivalent orthotropic plate (bottom), showing all angles of incidence, with a wave oriented in the stiffest dimension	125
Figure 47: Comparison of diffuse transmission loss of panel B for analytical ribbed plate model and equivalent orthotropic plate.....	125
Figure 48: Transmission loss of panel C for incident angle $\theta = \pi/4$ and two wave orientations, $\phi = 0^\circ$ (top) and $\phi = 90^\circ$ (bottom), showing analytical and equivalent orthotropic results	126

Figure 49: TL of panel C calculated with ribbed plate analytical model (top) compared to an equivalent orthotropic plate (bottom), showing all angles of incidence, with a wave oriented in the stiffest dimension	127
Figure 50: Diffuse transmission loss of panel C, analytical ribbed plate model versus equivalent orthotropic plate	127
Figure 51: Transmission loss of panel D for incident angle $\theta = \pi/4$ and two wave orientations, $\phi = 0^\circ$ (top) and $\phi = 90^\circ$ (bottom), showing analytical and equivalent orthotropic results	128
Figure 52: TL of panel D calculated with ribbed plate analytical model (top) compared to an equivalent orthotropic plate (bottom), showing all angles of incidence, with a wave oriented in the stiffest dimension	129
Figure 53: Diffuse field transmission loss of panel D for analytical ribbed plate model and equivalent orthotropic plate, full resolution (top) and averaged in third octave frequency bands (bottom)	129
Figure 54: Transmission loss through periodically ribbed plate, with period of 400mm. Top graph shows incident wave across ribs, bottom graph incident wave along ribs	131
Figure 55: Normal incidence transmission loss of ribbed plate showing mode frequencies.	133
Figure 56: Transmission loss of analytical ribbed plate model for a range of trace wavenumbers, plotted with the wavenumber in air k_0 , the bending wavenumber of the plate k_B and the wavenumber multiples $k_B n$	134
Figure 57: Comsol model of top hat corrugated aluminium plate with incident wave at $\theta = \pi/4$ and $f = 1.2$ kHz, showing in-plane motion	135

Figure 58: Comsol model of beam stiffened aluminium plate with incident wave at $\theta = \pi/4$ and $f = 1.2$ kHz, showing bending of plate and beam 135

Figure 59: Transmission loss of beam stiffened **aluminium** panel and top-hat corrugated panel of 1 mm thickness and 20 mm depth for incident angle $\theta = \pi/4$ 136

Figure 60: Transmission loss of beam stiffened **steel** panel and top-hat corrugated panel of 1 mm thickness and 20 mm depth for incident angle $\theta = \pi/4$ 136

Figure 61: Transmission loss through a single trapezoidal corrugated sheet of varying depth, incidence $\theta = \pi/4$ and wave direction along corrugations (stiffest dimension)..... 139

Figure 62: Transmission loss through a single 2 mm thick corrugated sheet of varying depth, normal incidence wave 140

Figure 63: Transmission loss through a single 4 mm thick corrugated sheet (100 mm pitch) – Panel 1 – of varying depth and wave direction (along and across corrugations); comparison with equivalent orthotropic (‘analytical’) model 141

Figure 64: Transmission loss through a single 2 mm thick corrugated sheet (150 mm pitch) – Panel 2 – of varying depth and wave direction (along and across corrugations); comparison with equivalent orthotropic (‘analytical’) model 142

Figure 65: Measured diffuse sound transmission loss of 0.7mm gauge corrugated steel sheets of varying depth (47mm deep sheet is 0.6 mm gauge) compared to a TMM prediction for a 0.7mm thick flat steel panel (‘Flat’) 144

Figure 66: Measured vs predicted transmission loss of KZ400 400 mm pitch 146

Figure 67: Measured vs predicted transmission loss of SS600 600 mm pitch 146

Figure 68: Measured vs predicted transmission loss of CF750 250 mm pitch 147

Figure 69: Measured vs predicted transmission loss of SS1200 400 mm pitch 147

Figure 70: Measured vs predicted transmission loss of KL200 203 mm pitch (INSUL database)	148
Figure 71: Measured vs predicted transmission loss of NG1997 190 mm (Ng & Zheng 1998)	148
Figure 72: 4 mm single glazing, comparison of measured TL with elastic solid layer model, with corrections for incident field and spatial windowing.....	152
Figure 73: 10 mm laminated single glazing, comparison of measured TL with elastic solid layer model, with corrections for incident field and spatial windowing, and adjusted loss factor η	153
Figure 74: 6-12-6mm double glazing, comparison of measured TL with TMM results, with and without corrections for incident field and spatial windowing.....	154
Figure 75: Cross section from Stani et al.: plasterboard partition with 12.5mm sheets and empty 115mm cavity, with double 50mm aluminium C-shaped studs separated by 15mm .	155
Figure 76: Plasterboard partition with 12.5mm sheets and empty 100mm cavity: laboratory measured versus modelled with incidence window and spatial window (Data from Stani et al.)	156
Figure 77: Plasterboard partition with 12.5mm sheets and 100mm cavity filled with mineral wool with air flow resistivity of $5.4 \text{ kPa}\cdot\text{s}\cdot\text{m}^{-2}$: laboratory measured versus modelled with incidence window and spatial window (Data from Stani et al.)	156
Figure 78: Sandwich plate consisting of mineral wool placed between two steel plates. Predicted transmission loss with and without 1mm air gaps between the plates and the mineral wool.	158

Figure 79: 6mm and 4mm glass panels modelled using the TMM, as single panels, and together, both bonded and unbonded	159
Figure 80: Factory made composite diagram. Corrugated composite panel, two steel sheets with polyisocyanurate (PIR) core	160
Figure 81: Diffuse TL of corrugated composite panel with polyisocyanurate (PIR) core and 100mm depth: comparison of measurements to TMM model with varying Young's modulus E of the core (E=5e6 nominal static value, E=2e7 empirical estimate) (y axis gridlines are in 10dB increments).....	161
Figure 82: Diffuse TL of corrugated composite panel with polyisocyanurate (PIR) core and 40mm depth; comparison of measurement to TMM model (Young's Modulus E estimated). (y axis gridlines are in 5dB increments)	162
Figure 83: Dual leaf system with connecting rods, unit cell geometry produced in COMSOL	164
Figure 84: Comparison of analytical and FEM calculated transmission loss through the infinite periodic double plate structure with point connections at 100mm by 100mm for an incident plane wave at $\theta = \pi/4$, with rod Young's modulus varying from 10^6 to 10^9	166
Figure 85: Comsol geometry of halter (left) and bracket (right)	167
Figure 86: Prescribed displacement areas on bracket (left) and halter (right).....	168
Figure 87: Comparison of FEM calculated stiffness matrix values k_{ij} between 1.6mm steel bracket (dashed line) and 3-5mm aluminium halter (solid line); free rotation	169
Figure 88: Comparison of FEM calculated stiffness matrix values k_{ij} between 1.6mm steel bracket (dashed line) and 3-5mm aluminium halter (solid line); constrained rotation.....	170

Figure 89: Modelled dual leaf corrugated roof structure with bracket and halter connectors (stiffness derived from FEM), compared to the same structure with no connectors; showing bracket with constrained and free rotation.....	171
Figure 90: Transmission loss of modelled dual leaf structure with point connections of varying x/y spacing shown in mm	173
Figure 91: Diffuse field transmission loss of dual leaf roof structure with connectors of varying stiffness.....	174
Figure 92: Halter connectors onto top hat beam, or purlin. MCRMA (2013).....	175
Figure 93: Geometry of point connected plates with connections onto rectangular section (left) and “top hat” section (right) beams, produced in Comsol.....	175
Figure 94: TL of point connected plates with intermediate rectangular section beams modelled in Comsol and analytically, varying the Young’s modulus of the beam. The compressional stiffness of the beam was modelled as a stiffness value in series with that of the rod.	176
Figure 95: TL of point connected plates with intermediate beams modelled in Comsol; result of changing beam section from rectangular to top hat.....	177
Figure 96: 100mm aluminium halter mounted on 1.25mm steel top-hat purlin, Comsol geometry	178
Figure 97: Axial stiffness matrix k_{ij} for a halter (solid line) and a halter + top-hat purlin (dashed line).....	179
Figure 98: Modelled dual leaf corrugated roof structure with halter and halters on top-hat beam section (stiffness derived from FEM), compared to the same structure with no connectors	180

Figure 99: Rooflight diagram showing steel fixings..... 182

Figure 100: Comparison of TMM modelled rooflight TL with measured diffuse field transmission loss (y axis gridlines are in 10dB steps) 182

Figure 101: Predicted transmission loss of rooflight system with (bottom) and without (top) point connections at 500mm x and y spacing; wave travelling along corrugations 184

Figure 102: Diffuse field predicted transmission loss of rooflight with and without point connections at 500mm x and y spacing (y axis gridlines are in 10dB steps)..... 185

Figure 103: Diagram of simple dual leaf roof structure (L3057) with halter connectors (item 3); MCRMA (2013) 186

Figure 104: Transmission loss of typical commercial corrugated roof system with soft fibrous infill and halters at 1400mm by 400mm spacing; measured (dashed) versus periodic point-connected model (solid) (y axis gridlines are in 10dB steps) 187

Figure 105: Corrugated metal roof with bracket connectors (cavity infill not shown); MCRMA (2013)..... 188

Figure 106: Diffuse transmission loss of corrugated metal roof R02 with bracket connectors against TMM model with and without rigid point connections (y axis gridlines are in 10dB steps) 190

Figure 107: Diffuse transmission loss of corrugated metal roof R04 with bracket connectors against TMM model with and without FEM-derived bracket connector stiffness (y axis gridlines are in 10dB steps)..... 191

Figure 108: Diffuse transmission loss of corrugated metal roof R07 against TMM model with and without point connections (y axis gridlines are in 10dB steps) 192

Figure 109: Corrugated metal roof (R08) with 140mm cavity and bracket connectors against TMM model with and without point connections (y axis gridlines are in 20dB steps).....	193
Figure 110: Roof structure L-2297 with halters and two layers of high density infill (180kg/m ²), MCRMA (2013)	194
Figure 111: Comparison of measured and modelled TL of roof structure L2297 (y axis gridlines are in 10dB steps).....	196
Figure 112: Diagram of roof structure ‘BG’ with halter connections, mineral wool infill, and high density cementitious board, MCRMA (2013)	198
Figure 113: Measured and modelled diffuse transmission loss of ‘BG’ roof structure with high density board (y axis gridlines are in 20dB steps).....	199
Figure 114: Measured and modelled diffuse transmission loss of ‘BG’ roof structure with high density board; low frequency results (y axis gridlines are in 5dB steps)	200
Figure 115: Roof structure diagram; 1: 0.9mm profiled aluminium sheet 2: halter connectors 3&5: 180 kg/m ² mineral wool 4: 15mm plasterboard 6: top hat beam 7: vapour control film 8: profiled steel decking, MCRMA (2013).....	200
Figure 116: Comparison between TMM modelled and measured transmission loss of roof structure L2510, showing both fully bonded and decoupled TM models (y axis gridlines are in 10dB steps)	202
Figure 117: Comparison between TMM modelled and measured diffuse transmission loss of roof structure L2510, showing the effect of adjusted rod compressional stiffness values (y axis gridlines are in 20dB steps)	202

Figure 118: Measured diffuse field transmission loss of roof structure with and without a 10 kg/m ² damping membrane. Mass per unit area without membrane: 14 kg/m ² ; with membrane: 23.8 kg/m ² (y axis gridlines are in 10dB steps)	204
Figure 119: TMM modelled structure with and without a 5mm rubber membrane. (y axis gridlines are in 20dB steps).....	204
Figure 120: Modelled structure with periodic point connections with and without a 5mm rubber membrane (stiffness of point connections estimated from measurements) comparison with measurement results (y axis gridlines are in 10dB steps)	205
Figure 121: Paraboloidal rain drop force in the time domain	222
Figure 122: Rain drop force $F(\omega)$ in the frequency domain	223
Figure 123: Incident sound power of simulated standard rainfall	223
Figure 124: TMM modelled sound intensity of 4/16/4mm double glazing, compared to measurement (Guigou-Carter & Villot 2003).....	225

III. LIST OF TABLES

Table 1: Common corrugated metal panels found in roof structures; MCRMA (2013)	8
Table 2: Values of the four by four elastic solid transfer matrix a_{ij}	34
Table 3: Properties, formulas and values used in the Biot-Allard model of a porous material with an incompressible frame (Allard & Atalla 2009)	49
Table 4: Approximation of properties for fibrous materials	50
Table 5: Dimensions of modelled ribbed panels A and B	119
Table 6: Values of kL for the first ten modes of a free-free beam obtained numerically.....	132
Table 7: List of modelled corrugated panels with dimensions and material properties	138
Table 8: Types of corrugated panels, showing approximate trapezoidal dimensions	144
Table 9: Features of corrugated roof structures with low density mineral wool	188

IV. ACKNOWLEDGEMENTS

This work was funded by the Metal Cladding and Roof Manufacturers Association, and partly by the Salford University acoustic laboratories. A great many thanks to the MCRMA members who had the patience to sit through my tedious presentations and provided me with more data than I could handle.

I owe a debt of gratitude to my supervisor, Andy, for his unwavering support in the face of my equally unwavering pessimism. Not only has he given me the opportunity of carrying out this research in the first place, he has also helped and encouraged me every step of the way, not to mention all the jazz jams. Many thanks also to my co-supervisor Andy Elliott, especially for producing the initial literature review that set the direction of this work.

A special thanks goes to Dmitry, without whom I would probably not have much to show for. He produced a beautifully written derivation, and helped me understand many of the principles involved, free of charge. He has also not charged me a penny for his friendship, from which I have benefited immensely, in terms of the number of jokes in poor taste that I get to hear.

Thanks also to the Salford University laboratory staff for allowing me to abuse the equipment with impunity, and teaching me along the way. I must also mention Henric, the studio technician, for all the music, cigarette breaks and for his infinite wisdom.

Of course, the acoustics research squad deserve all the praise they can get. Thanks especially to Ahmed for all the peanuts, to Greg and, of course, Nigel for the many fruitful discussions, mostly about how to format text in LaTeX (I eventually gave up). A great many pints at the

Crescent were had with the team, as brief but welcome diversions from the sound insulation of roof structures.

I am also grateful to all my friends and fellow board gamers who kept my spirits up throughout.

During the many stressful moments, Kate was a great support to me. She was often more stressed than me, and had more valid reasons to be, so it certainly put things into perspective.

I must also thank my family, as they've been behind me every step of the way. They still believe in me, despite the overwhelming evidence that suggests I don't deserve it.

“All that is necessary for the triumph of evil is that good men do nothing.”

Attributed to Edmund Burke

V. ABSTRACT

Over the course of this work, the transfer matrix method (TMM) was implemented and studied for its potential in predicting the sound insulation characteristics of corrugated dual leaf roof structures. A model of periodically connected plates, using Fourier expansions, was derived independently and extended in this work to include the stiffness of connectors and orthotropic plates, and intermediate beams in the framework of the structure. The same principles were applied in deriving the transmission loss through periodically stiffened plates, as a proxy for corrugated panels. At the same time, corrugated plates were modelled as equivalent orthotropic panels, a process which is compatible with the TMM without particular modifications. Infill materials were modelled using simple fluid representations and more complex poroelastic behaviour. The point-connected plate models were combined with the TMM to enable multiple layers of infill materials between the two plates, by using an effective fluid approach. The stiffness of typical roof connectors was obtained with numerical simulations, and used in predicting transmission loss. Corrections were introduced to simulate diffuse laboratory conditions and enable meaningful comparisons to available data. The limitations of a simple orthotropic plate model compared to laboratory measurements and the ribbed plate model were identified. A number of measurements of dual leaf partitions and full roof systems were compared to the TMM and point-connected plate models, finding typically good agreement at low to mid-frequency, and a strong dependence of high frequency transmission loss on connector stiffness.

VI. ABBREVIATIONS AND SYMBOLS

TL	Transmission Loss
TMM	Transfer Matrix Method
MCRMA	Metal Cladding and Roof Manufacturers Association
x, y, z	Cartesian coordinates
v	Velocity
w	Displacement
p	Pressure
σ	Stress
T	Transmitted wave complex amplitude
R	Reflected wave complex amplitude
τ	Transmission loss
c	Speed of sound
ρ	Density

k	Wavenumber
k_x, k_y, k_z	Cartesian components of wavenumber vector
k_t	Trace wavenumber, $k_t = \sqrt{k_x^2 + k_y^2}$
c_0	Speed of sound in air
ρ_0	Density of air
k_0	Wavenumber in air
η	Loss factor
E	Young's Modulus
ν	Poisson's ratio
I	Area moment of inertia
B	Bending stiffness
m'	Mass per unit area
ω	Angular frequency
θ	Angle of incidence
ϕ	Angle of orientation

$\delta_x, \delta_y, \delta_z$ Differential operators in Cartesian coordinates

∇^2 Laplace operator, $\nabla^2 = \delta_x^2 + \delta_y^2 + \delta_z^2$

1 INTRODUCTION

1.1 BACKGROUND

The sound insulation properties of materials and structures are important in many areas of acoustics. In automotive engineering, sound insulation is a sought after parameter in the design of car bodies, mufflers and other details in determining the transmission of engine noise and other sources into and out of the vehicle. In building acoustics, an understanding of sound insulation is vital in many areas, for instance: the reduction of noise from ventilation ducts, in minimising privacy and disturbance issues, in reducing noise in classrooms, lecture theatres and other critical spaces, as well as preventing noise outbreak from industrial buildings. Several modelling techniques and measurement methods, some of which will be outlined here, have been developed over time to predict the acoustic features of such systems. The main focus of this work is in characterising the acoustic performance of roof structures with corrugated metal sheets, and dual leaf structures with multiple layers more generally.

Laboratory measurements of sound insulation of building elements are carried out according to BS EN ISO 10140-2, in a test environment consisting of two reverberant rooms, the source and receiving rooms, either side of the element under test, as illustrated in Figure 1. The frequency range of most sound insulation measurements is between 50 Hz and 5 kHz, which will be the range considered over the course of this work. The rooms are specially designed to meet requirements of ISO 3741 which intend to maximise the diffusivity of the field, having very little acoustic absorption, large volumes, non-parallel walls and diffusers installed. The rooms are also well isolated from each other, ensuring that flanking transmission (transmission of sound via paths other than through the element under test) is minimal. The calculations employed to obtain the 1/3 octave band sound transmission loss, or

Sound Reduction Index (SRI), are based on the assumption of a perfectly diffuse field, and are limited to the high frequency region, above the Schroeder frequency of the reverberant chambers.

Field measurements are carried out on buildings according to BS EN ISO 140-2. In this case too, sound insulation values are determined with the assumption of a perfectly diffuse field in both rooms, though the strict design criteria for reverberant chambers are not met. A major challenge in the prediction of reverberant sound transmission is accounting for all factors that influence and determine the measurement results, including: structure size, mounting and edge conditions, screws and fixings, coupling between layers (e.g. fully bonded versus partially bonded materials), seal imperfections, test room dimensions and diffusivity of the sound field.

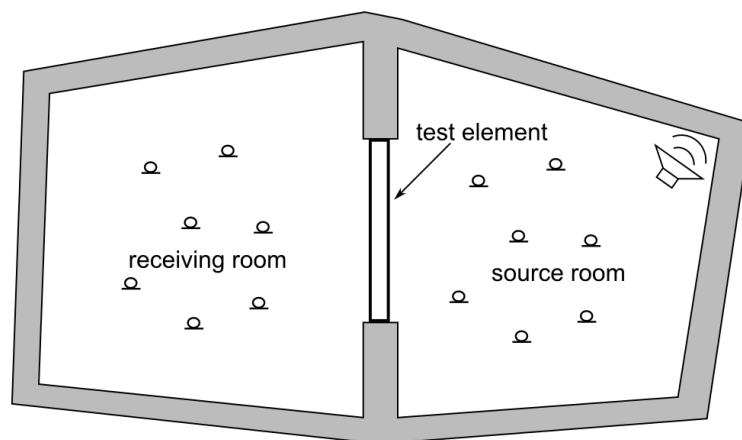


Figure 1: Sound insulation measurement setup for ISO 10140-2

Another obstacle to our understanding, which will not be explored in this work, is the observed difference between in situ and laboratory measurements. While the determination of in situ characteristics is fundamental to any application, in laboratory conditions it is easier to control the variables involved. Having said that, a large variability between measurements of nominally identical structures has been observed across laboratories following the same

procedures (Fausti et al. 1999). This has been attributed to the factors listed above, including – importantly – those unrelated to the structure that is being evaluated for its sound transmission characteristics.

This work will be focussing on the prediction of sound insulation of roof constructions with corrugated metal sheets, as part of a research project for the benefit of the Metal Cladding and Roof Manufacturers Association. Members of the association have been using the product of work carried out by Lam and Windle (1993) to predict the sound insulation of common roof structures over the last few decades. However, over this timespan, roof constructions have increased in depth and complexity, along with greater requirements for thermal and acoustic performance. Generally these are dual leaf structures, which have corrugated metal sheets on either side and are connected periodically by point-to-point connectors, often including beams in the framework. The profiled metal sheets have particular sound transmission characteristics related to their profiles which need to be accounted for. In such constructions, multiple layers of mineral or glass wool infill are often used, including high density materials, as well as additional rigid boards and membranes. The main challenge of the work will be to account for structure-borne transmission as well as the behaviour of profiled plates and multiple layers of infill, so the focus will be on the structures themselves as opposed to the influences of the test environment.

1.2 AIM

The aim of the project is to develop an approach to modelling sound transmission through multi-layered structures with corrugated and profiled sheets and structural connectors, with particular focus on roof systems. Different methods of modelling corrugated and profiled sheets are compared in the process. The effect of the test environment must be accounted for

to some degree in order to compare the models with available laboratory measurements. At the same time the aim is constrained by the requirement to produce a useable software tool to aid in the design of such structures.

1.3 APPROACH

A purely analytical approach to modelling is not feasible for complex multi-layered structures with structural connections. Throughout this thesis and in many of the referenced works, classically derived expressions for even geometrically simple point connected or framed structures can quickly become intractable. Useful design parameters in these cases are hard to obtain, making analytical approaches, in a practical sense, indistinguishable from numerical approaches if not for their relative computational efficiency. Modal approaches to finite structures become more cumbersome with each additional panel or layer; these approaches require accurate knowledge of the edge conditions of each subsystem.

Accounting for multiple layers of infill materials will necessarily require including an approach which can handle multilayer systems. The transfer matrix method (TMM) was chosen for its unrivalled capability in modelling arbitrary arrangements of layers. The TMM is used in combination with analytical models of panels with periodic framework (point-to-point connections and beams) by reducing multiple layers of materials to an effective single layer, making the analytical expressions much easier to derive. The averaging in 1/3 octave bands, which is commonplace in building acoustic measurements and standards, reduces the amount of detail in the transmission loss curve, making the TMM feasible despite its assumption of laterally infinite layers resulting in no modal behaviour. Methods also exist to artificially “finitise” an infinite structure and approximate laboratory conditions (Villot et al. 2001; H. Kang et al. 2000). Alongside the transfer matrix model, finite element analysis will

be carried out in Comsol 4.3, for validation purposes and to derive the relevant mechanical properties of structural connections.

The main novel areas of this research include: the implementation of corrugated and profiled plates within the transfer matrix framework, and its comparison against laboratory measurements of sound insulation; the combination of transfer matrix method with classical models of structural connections; a model of double plate systems with point-to-point connections onto beams.

1.4 LAYOUT OF THE THESIS

This thesis is structured in the following way. Chapter 2 contains details of common roof structures according to MCRMA specifications. Chapter 3 contains a review of the literature on sound transmission through dual leaf structures and all aspects relevant to this work. Chapter 4 lays out the theory and modelling approach to individual components in a dual leaf structure or general multilayer system of different material types, including different approaches to modelling corrugated panels. Chapter 5 outlines derivations of two analytical models to account for sound transmission in double plate systems with point-to-point connections, and details of their combination with the Transfer Matrix Method. Chapters 6 and 7 are presentations of results and comparisons between measurement, FEM analysis and the modelling techniques presented in Chapters 4 and 5. Chapter 8 contains a summary of the findings.

2 DUAL LEAF ROOF SYSTEMS

This chapter will provide details of the dual leaf roof structures under examination, based on information provided by the Metal Cladding and Roof Manufacturers Association. The elements here described will provide the focus for the modelling frameworks proposed in this thesis.

The components of each roof include metal sheets, infill materials, structural framework and connectors. The possible configurations of roof systems include simple cladded roofs with a single layer of insulation, rooflights with no cavity infill, factory-made composites with an expanding foam core, and more complex structures with multiple connectors, internal beams, and high density boards.

2.1 PROFILED METAL SHEETS

The roof structures examined consist, at a minimum, of two profiled panels separated by a spacer kit to provide structure. The two sheets are referred to as the ‘top sheet’ and the ‘liner’ or ‘decking’ (depending on the profile) at the bottom. A list of common profiles was compiled by the MCRMA (see Table 1 for a list of profiles with depictions).

Panel thicknesses range from 0.5 to 1.5 mm, and are made of steel, aluminium or glass-reinforced plastics (in the case of rooflights). The most common types of profiles are trapezoidal for the liner, and ‘standing seam’ for the top sheet. Often sheets have additional smaller ridges to further increase stiffness. Profile depths for most sheets are between 20 and 60 mm, except for decking, which can reach depths of up to 210 mm. Profiled sheets can also be perforated, to expose the absorptive cavity infill and reduce reverberation in a building.

Trapezoidal profiles are described by their pitch, crown, valley and depth, as shown in Figure 2. Standing seam profiles are common top sheets; their profile is not trapezoidal, as they have ribs that protrude in the normal direction to the panel with depths of 50-75 mm; the tips of the ribs have a circular roll, which allows joining each section together.

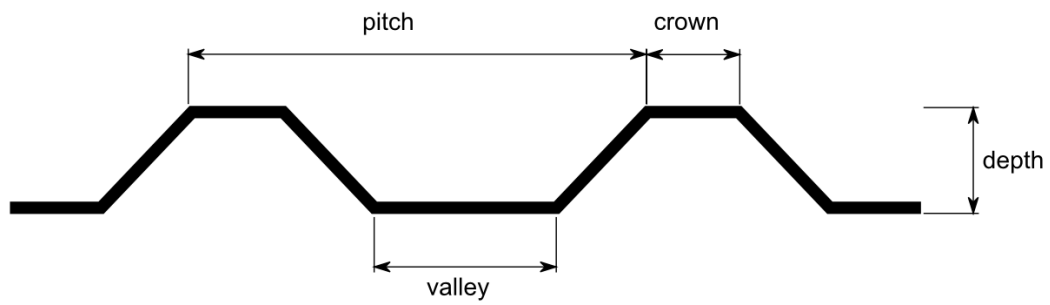


Figure 2: Trapezoidal profile diagram

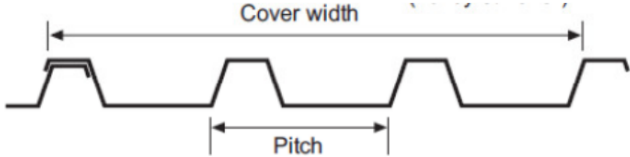
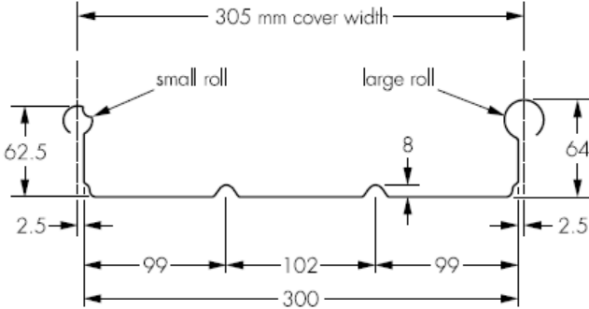
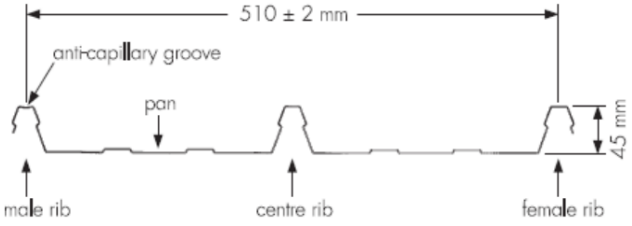
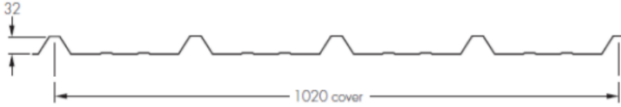
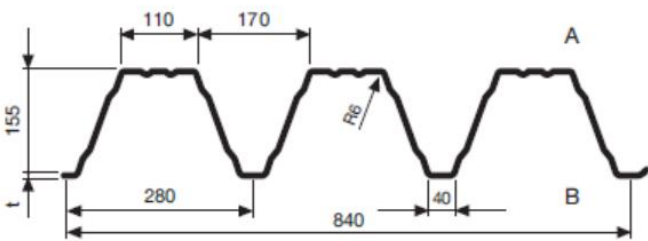
Cladding type	Schematic
Top sheet: trapezoidal 24-50mm depth	 <p>A schematic diagram of a trapezoidal top sheet. It shows a series of trapezoidal ribs. A horizontal dimension line at the top indicates the 'Cover width' spanning two full ribs. A horizontal dimension line below the ribs indicates the 'Pitch', which is the distance between the centers of two adjacent ribs.</p>
Top sheet: 'standing seam' 45-60mm depth	 <p>A schematic diagram of a standing seam top sheet. The total width is labeled as '305 mm cover width'. The diagram shows two types of rolls: a 'small roll' and a 'large roll'. Dimensions include: 62.5 mm for the height of the small roll, 2.5 mm for the thickness of the sheet, 99 mm for the distance from the edge to the center of the small roll, 102 mm for the distance between the centers of two small rolls, 99 mm for the distance from the center of a small roll to the center of a large roll, 8 mm for the height of the large roll, 64 mm for the height of the large roll, and 2.5 mm for the thickness of the sheet. The total length of the sheet shown is 300 mm.</p>
Top sheet: secret fix 45-60mm depth	 <p>A schematic diagram of a secret fix top sheet. The total width is labeled as '510 ± 2 mm'. The diagram shows a 'male rib' on the left, a 'pan' in the center, and a 'female rib' on the right. An 'anti-capillary groove' is shown between the male and female ribs. The height of the female rib is labeled as '45 mm'.</p>
Liner sheet (bottom): trapezoidal 19-37mm depth	 <p>A schematic diagram of a trapezoidal liner sheet. The depth of the sheet is labeled as '32'. The total width is labeled as '1020 cover'.</p>
Decking sheet 32-210mm depth	 <p>A schematic diagram of a decking sheet. The depth of the sheet is labeled as '155'. The thickness of the sheet is labeled as 't'. The diagram shows a series of trapezoidal ribs. Dimensions include: 110 mm for the top width of a rib, 170 mm for the distance between the centers of two ribs, 280 mm for the distance from the center of one rib to the center of the next, 840 mm for the total width of the sheet, and 40 mm for the distance from the center of a rib to the edge. Labels 'A' and 'B' are placed at the top and bottom right of the sheet respectively.</p>

Table 1: Common corrugated metal panels found in roof structures; MCRMA (2013)

2.2 INFILL AND CAVITY LAYERS

Materials used as cavity infill in roof systems are usually mineral fibres, either glassfibre or rockfibre. The insulation is also often specially cut to fill the trapezoidal lags in the profiled metal sheets. They have a range of densities from 10 to 200 kg/m³; low density quilts are most common, between 10 and 50 kg/m³, while ‘high performance’ systems tend to have higher density materials, above 50 kg/m³. Quilts can be modelled to reasonable accuracy with a simple equivalent fluid, as waves through the solid portion contribute less to the overall transmission. Higher density materials are generally stiffer, and come in rigid slabs, adding mass to the system but also potentially affecting the vibration of panels in the system in more complex ways, through transmission of shear and compressional waves in the solid portion.

Other possible layers in the space between the two profiled metal sheets are flat high density boards, of thicknesses between 8 and 20mm. Cement particle boards have a typical density of 1250 kg/m³, and plasterboard a density of 850 kg/m³. Additionally, high density mats are often added to further increase the mass of the system.

2.3 STRUCTURAL FRAME: SPACER KITS AND POINT-TO-POINT CONNECTIONS

The roof structures under examination have spacer kits which serve as structural support, and separate the top sheet and liner/decking to form the cavity space. These kits contain point-to-point connectors that come in two types: brackets and halters.

Brackets are L-shaped connectors, typically made of galvanised steel, between 1 and 2mm thick and come in a variety of designs, typically with ridges along its length. They are commonly mounted in a ‘bar and bracket’ spacer kit, as shown in Figure 3. In mounting, the

top of the bracket is inserted into the ‘bar’, a U-shaped metal stud, and the bottom of the bracket is screwed directly to the bottom metal sheet, while the bar is screwed to the top sheet.

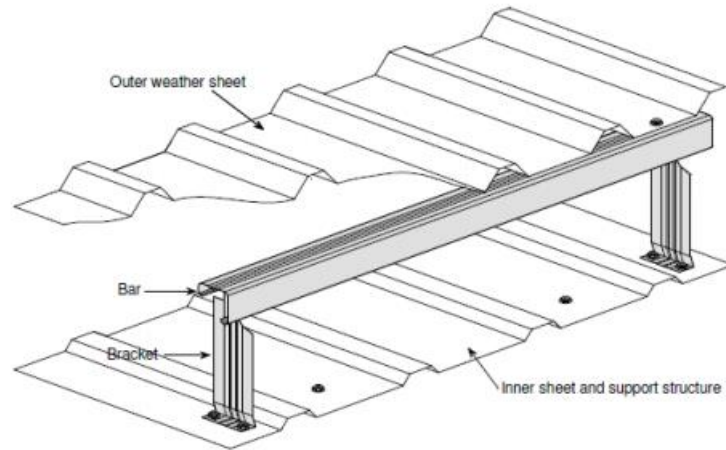


Figure 3: Bar and bracket spacer kit; MCRMA (2013)

Halters are T-shaped connectors, used in systems when the top sheets have a ‘standing seam’ profile. Their top portion is inserted in the ridges of the top sheet as shown in Figure 4, and they are commonly screwed directly to the liner/decking. They are most commonly made of aluminium, however steel or plastic are also used. The maximum height of this spacer kit is 200mm. In roofs of greater depth, the halters are connected to top hat beams (purlins), as shown in Figure 5. Both types of point-to-point connectors can be found in the same roof structure to further increase depth; this is shown in in Figure 6.

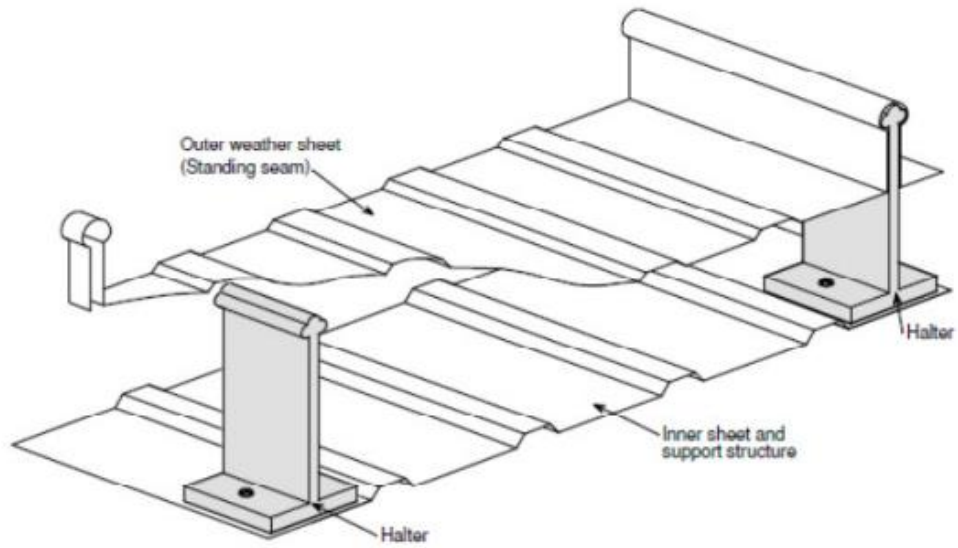


Figure 4: Halter spacer kit, with standing seam top sheet

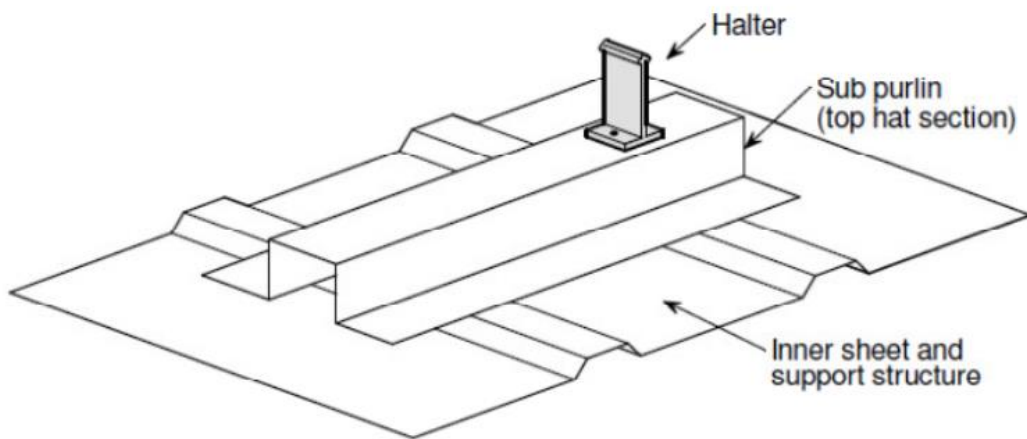


Figure 5: Halter spacer kit with top-hat purlin

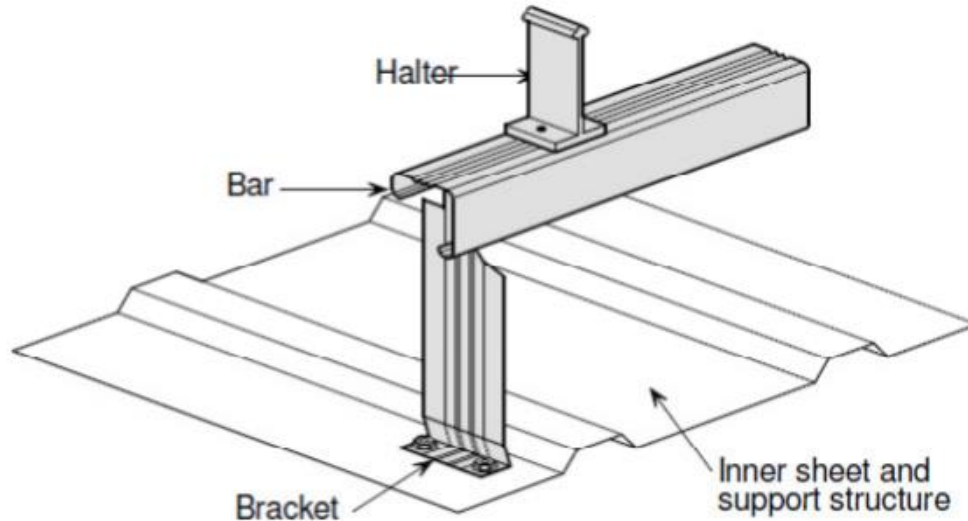


Figure 6: Combined halter and bar and bracket spacer kit

2.4 ROOF SYSTEM SPECIFICATIONS

One of the most common dual leaf roof systems is shown in Figure 7 (MCRMA Roof System Specification 1). It consists of two corrugated metal panels (a ‘top sheet’ and a ‘liner’ at the bottom in the same orientation), with a spacer kit (halters in this case), and a single layer of mineral wool. The rafter spacing is typically between 1m and 2.4m. The large beams at the base are the rafters of the building on which the roof is installed. All systems are mounted onto rafters, however this is typically not the case for laboratory tests of sound insulation; since the aim is to predict laboratory performance, rafters are not considered for acoustic modelling.

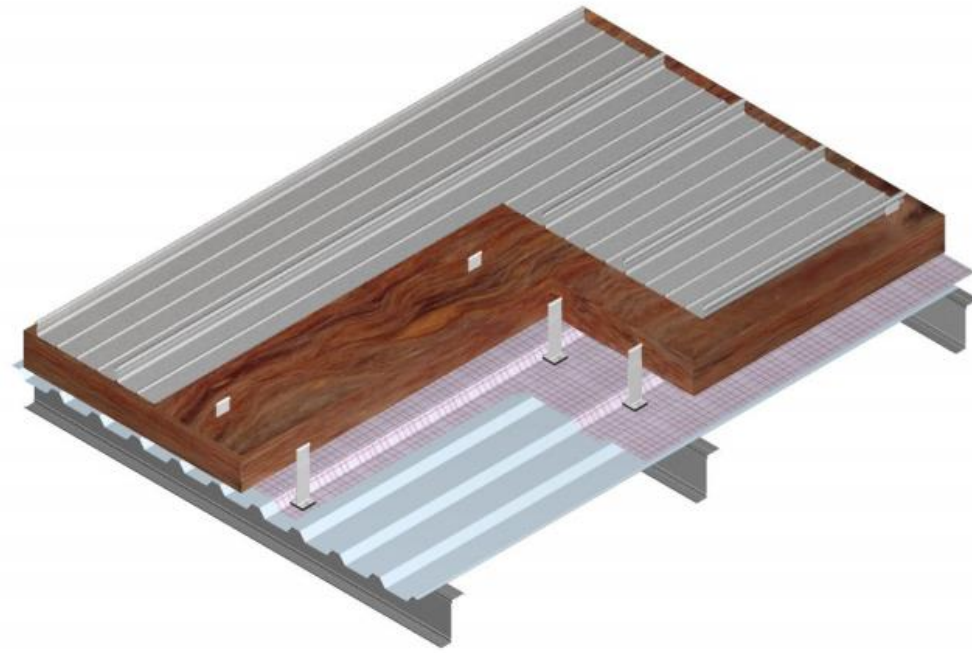


Figure 7: MCRMA Roof System Specification 1; MCRMA (2013)

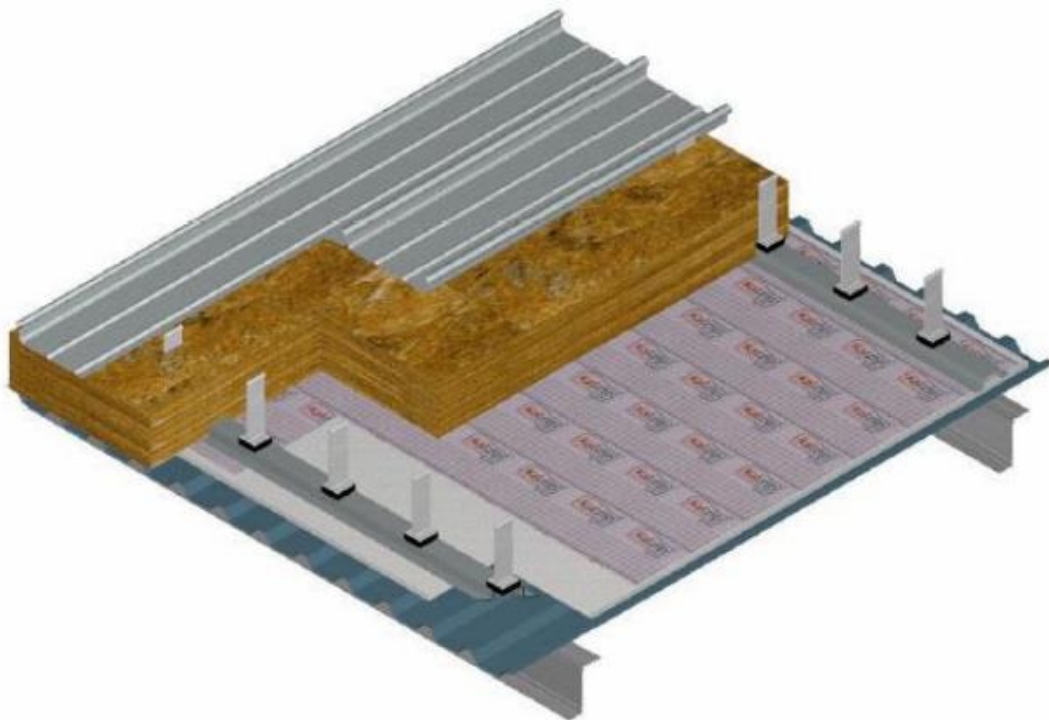


Figure 8: MCRMA Roof System Specification 2; MCRMA (2013)

The roof system shown in Figure 8 has an additional high density board between the liner and spacer (halves with top-hat purlins), and multiple layers of infill. When multiple layers are used, they tend to differ in density and can be combinations of soft quilts and hard slabs. Figure 9 shows a roof system specification which is the same as Spec. 2, but with perforated decking.

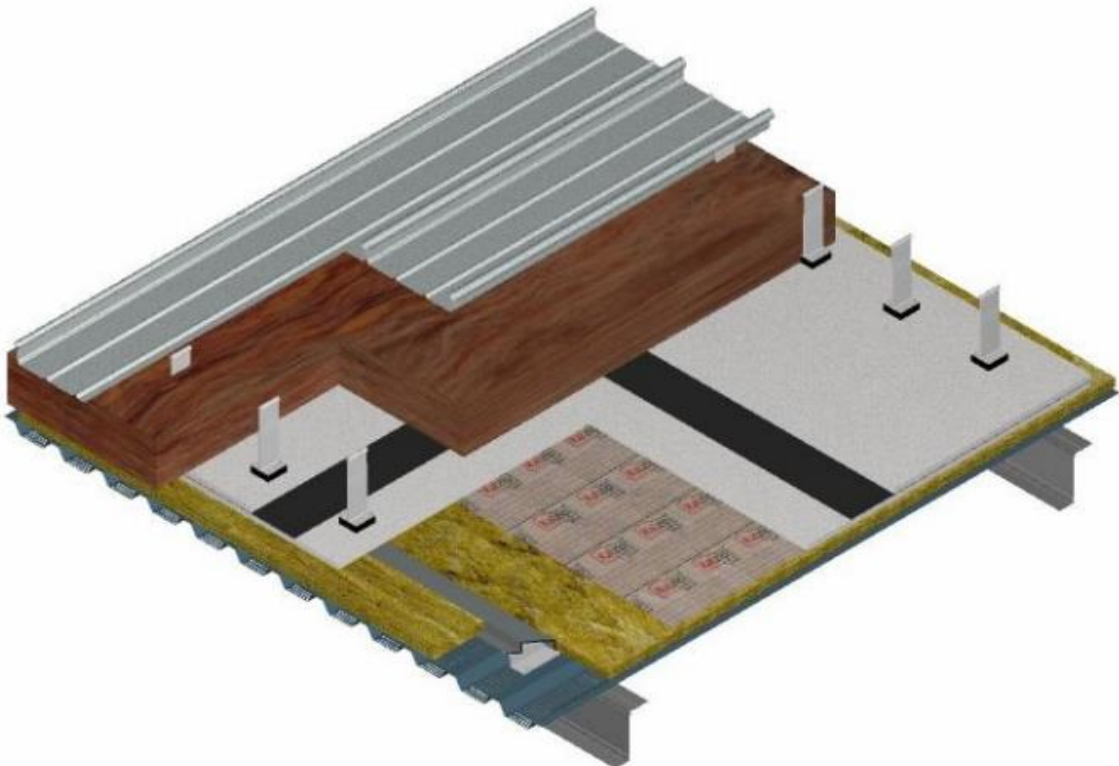


Figure 9: MCRMA Roof System Specification 3; MCRMA (2013)

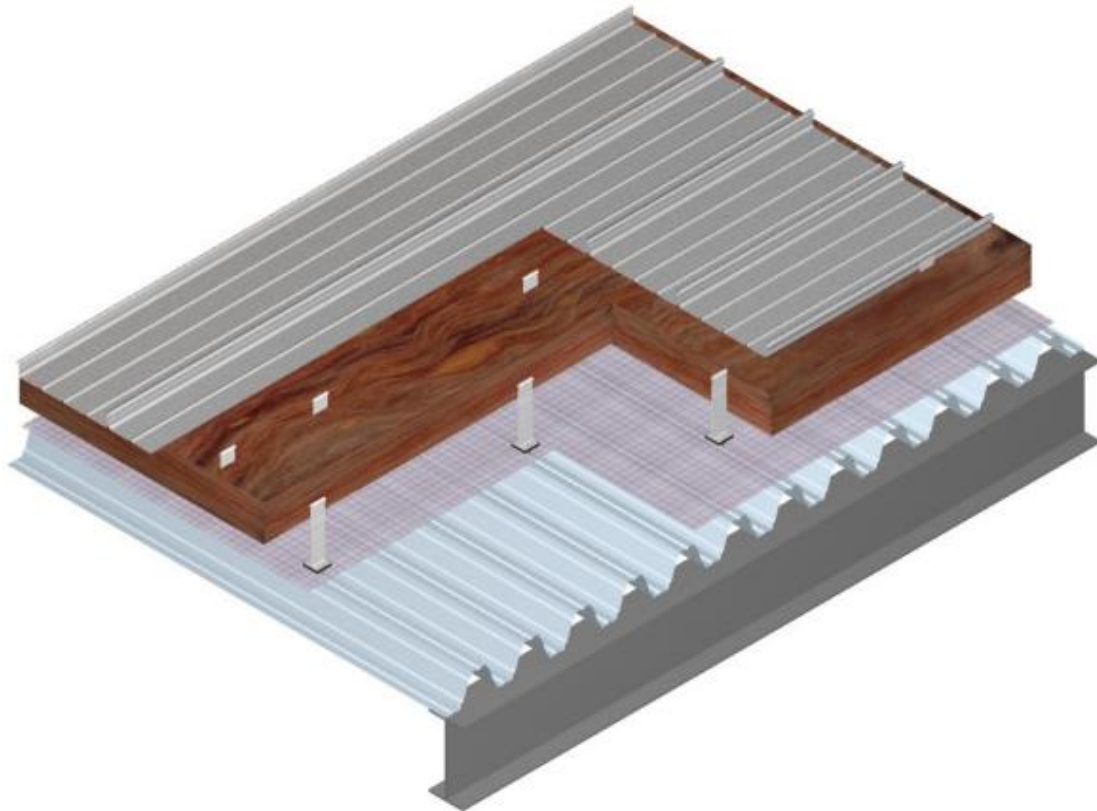


Figure 10: MCRMA Roof System Specification 4; MCRMA (2013)

Spec. 4 roofs, as shown in Figure 10, are similar to Type 1, but have a decking sheet instead of a liner, at a 90 degree orientation from the top sheet.

Spec. 5 roofs are as Spec. 4, but with multiple layers of infill and/or high density boards. The spacer kit in the example in Figure 11 is mounted directly on a mineral wool slab as opposed to a metal sheet.

In all of the above roofs, 5-10mm sheets of rubber are often introduced to increase the overall mass and improve acoustic performance. These can be single layers, or multiple layers sandwiched between high density boards.

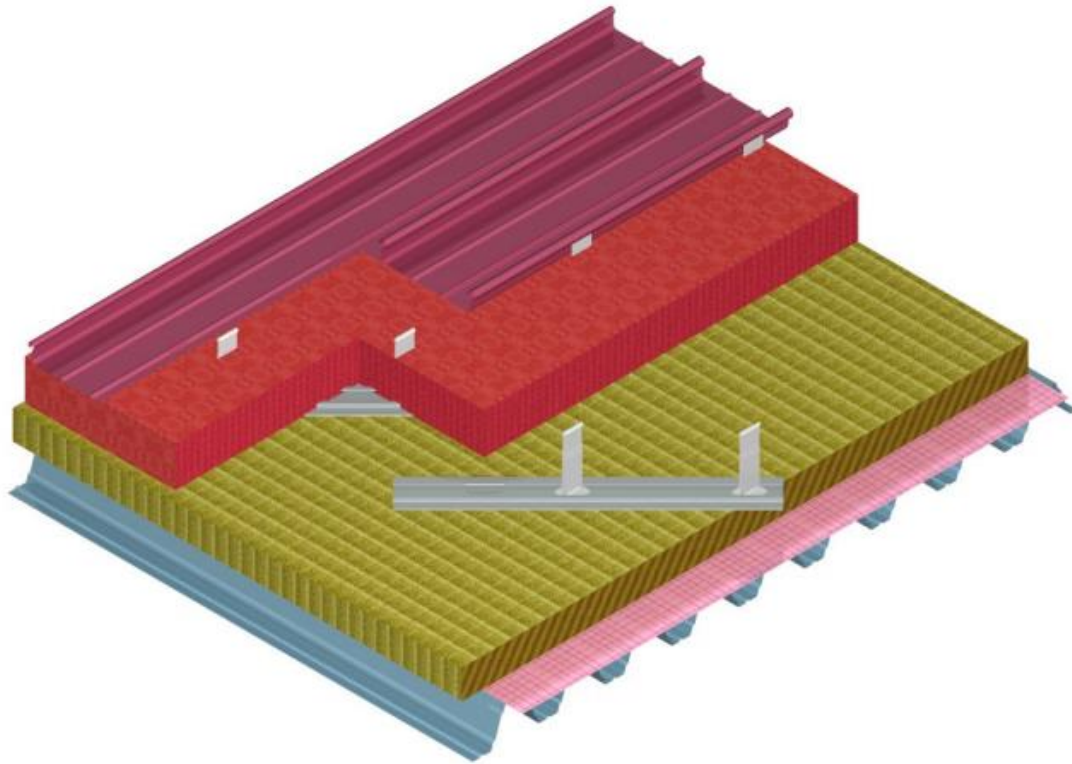


Figure 11: MCRMA Roof System Specification 5; MCRMA (2013)

Rooflights are perhaps the simplest structures, where all sheets are made of glass-reinforced plastic (GRP), of mass per unit area between 2 and 5 kg/m², with no absorptive layers in the cavity, except for a thin, clear membrane that has little impact on the transmission of sound. Liner sheets can be flat as well as corrugated. The top and liner sheets are secured with bolt fasteners.

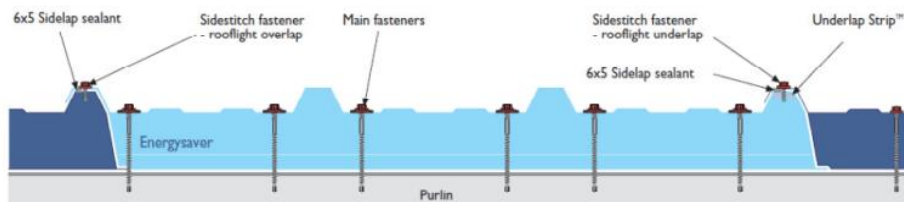


Figure 12: Rooflight cross-section; MCRMA (2013)

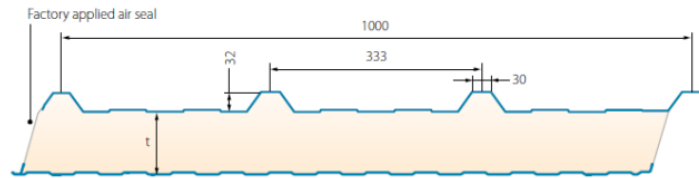


Figure 13: Factory-made composite cross-section; MCRMA (2013)

Composites, shown in Figure 13, are roof structures with polyurethane (or similar) filler (the core) injected between two profiled metal sheets. They typically have profiled steel or aluminium sheets of smaller thickness than other systems, around 0.5mm, and smaller depth, especially for the liner.

2.5 DUAL LEAF PARTITIONS

Although the main focus of this thesis is the modelling of profiled metal constructions, there is value in studying simpler constructions as an intermediate step so as to reveal more clearly the influence of certain features. Double glazing and light weight plasterboard partitions are common and widely studied constructions, for which laboratory measured transmission loss data is available.

Double glazing partitions consist of two glass layers separated by an empty cavity, filled with either air, a gas, or a vacuum for higher insulation. Any framework is typically confined to the outer edges of the structure, so that the geometry for the bulk of the partition is simple. The absence of cavity infill and framework make double glazing partitions an ideal candidate starting point before attempting to model more complex dual leaf structures.

Drywall partitions consist of, at a minimum, two plasterboard sheets (of thicknesses of around 10-15mm) separated by a cavity and connected by framework. In the majority of cases, and especially for high performance acoustic partitions, the cavity is filled with one or more sheets of fibrous insulation, like mineral wool or glass wool. The framework in the bulk of the partition typically consists of rectangular sections formed by studs, made of either timber or aluminium, with vertical studs at, commonly, 600-900mm spacing, and screwed to the panels at regular intervals. As such, the studs can be said to be in rigid contact with the plasterboard panels at the location of the screws. In most cases, plasterboard partitions have flat panels and low density mineral wool infill which make them more amenable to modelling.

2.6 CONCLUSIONS

In this chapter, all the common components of roof structures were described, with details provided by the MCRMA, as well as key details of plasterboard and glazing partitions.

The roof systems under study are composed of two corrugated panels with various profile types, most commonly with a trapezoidal or ribbed shape. They contain cavity infill that ranges from soft quilt to hard, high density slabs of mineral or glass wool. Many roof structures examined have multiple layers of infill material. High density boards, cement and plasterboard, are also used in high performance roof constructions, as well as rubber matting. Spacer kits are structural elements which connect the top and bottom metal sheets. Two types of point-to-point connectors are commonly used, halters and brackets, which have different geometries and installation details. Halters are used with standing seam panels, which are ribbed panels of high depth, and are at times mounted on top of top-hat purlins (beams with a

top-hat profile). Brackets are commonly mounted as part of a ‘bar and bracket’ system, with their top portion inserted into a steel stud (the ‘bar’).

In summary, the elements present in roof structures (and other dual leaf structures) which will need to be addressed to produce a complete modelling framework, are:

- Profiled metal panels, with trapezoidal or ribbed geometry
- Mineral wool and glass wool infill
- Multiple, layered materials
- High density boards
- Rubber/damping mats
- Point-to-point connectors – T-shaped ‘halters’ and L-shaped ‘brackets’ – in spacer kits which can include intermediate beams

Most of these features will need to be addressed in order to produce a complete model of their behaviour, so in the following chapter, the relevant literature is surveyed to determine a suitable approach.

3 LITERATURE REVIEW

In this chapter, the literature relating to the modelling of multilayer and dual leaf roof structures is reviewed, including existing approaches to corrugated and profiled metal sheets, fibrous infill and point-to-point connections.

3.1 OVERVIEW OF MODELLING TECHNIQUES

A survey of the existing literature revealed many techniques, and their relative benefits and drawbacks, for evaluating acoustic transmission through various common building elements. The models fall broadly within two categories: deterministic (analytical or numerical) and statistical. These are suited for different purposes, depending on whether one aims to reproduce the entire sound insulation measurement environment, a realistic finite structure in isolation, or an idealised and simplified equivalent.

Deterministic approaches include analytical and numerical models. These vary in their assumptions, depending on how many features they include, whether they are investigating finite or infinite geometries, or resonant and non-resonant transmission. Analytical models are useful design tools which give the most direct access to relationships between geometry, material properties and transmission loss and other acoustic parameters.. Often their computational cost is low compared to other approaches. In practice, for anything other than simple geometries and systems, they often involve many variables, infinite summations, and operations that can only be evaluated numerically. This makes it difficult to derive useful relationships between the parts of a system other than by carrying out a parametric survey. The Transfer Matrix Method (TMM) is one such framework, outlined in Section 3.5. The TMM models an arrangement of layers via ‘transfer matrices’, which represent the relationship between field variables either side of a single layer. The Finite Element Method

(FEM) is a powerful tool, in which all aspects of a system are modelled deterministically by subdivision of the entire domain into smaller elements. Its application to building acoustics, and in particular in the determination of sound insulation, has been limited to low frequency, especially when simulating the test rooms as well as the structure (Maluski & Gibbs 2000), as the computational cost increases with frequency and size of the geometry, due to the required increase in resolution. Attempts to improve computational efficiency in this domain have been carried out, among others by Brunskog and Davidsson (2004) who combined FEM with wave-based methods of determining the room response in acoustic transmission rooms to reduce the number of elements. FEM is also a popular choice for numerical validation of models, as it allows complete control over the variables and assumptions involved. Numerical methods like these can give accurate answers and allow freedom to determine all inputs at the cost of decreased computational efficiency and lack of access to the direct relationships between inputs and outputs; they act effectively as black boxes.

Statistical models, such as Statistical Energy Analysis (SEA), are based on statistical assumptions about the nature of the systems involved and the energy transmission mechanisms. SEA features extensively in Hopkins (Hopkins 2007) and Craik and Smith (2000), and has shown to be a reliable modelling tool. It is particularly suited to problems with a large number of interacting elements which are not amenable to analytical solutions or simulations. SEA can be used as a design tool to identify the influence of different paths to total sound transmission. This method can work very well in cases where the modal density is high, so that contributions from different sources and paths can be said to add incoherently. Deterministic approaches, tend to be less reliable at higher frequencies as their accuracy is undermined by the effect of small variations in parameters, and uncertainties related to the determination of material properties and edge conditions of a real structure.

3.2 DUAL LEAF STRUCTURES

Of particular importance to the aims of this thesis is the ability to predict sound insulation for dual leaf constructions and therefore in this section the development of relevant theories is reviewed. Early theoretical work on sound transmission through dual leaf structures was carried out by London (1950). Assuming layers of infinite extent, London modelled the normal incidence transmission loss through parallel plates in bending separated by a cavity, finding it was not sufficient to predict performance measured in a reverberant transmission suite. To overcome some of the limitations of the infinite model, modal analysis was introduced that accounts for modes resulting from finite panel and room sizes with various termination conditions. Classical modal models of sound transmission problems were formulated to calculate transmission of reverberant sound through single plates and dual leaf structures of finite size (Sewell 1970). This approach yielded insights into the mechanisms of sound transmission, with regards to the simple cases considered. Modal density increases with frequency; each sub-system introduces an additional modal expansion, leading the computational cost to increase with frequency and number of panels.

In contrast to more detailed models, Sharp devised a prediction scheme (Sharp 1978) which is simple to implement and, as such, well known and applied in acoustic engineering. It is based on theory for infinite plates, and splits the frequency range of single and dual leaf structures into distinct regions that determine the slope per octave of reverberant transmission loss. It identifies, for single plates, the *mass region* at low frequency with 6dB per octave increase, a *critical (or coincidence) frequency* where transmission loss dips more or less sharply depending on internal panel damping, and the region above this frequency where it increases again. Each region is described by a single equation that describes diffuse field sound transmission loss. For dual leaf structures, the combined behaviour results in the mass-

air-mass resonance due to the air cavity between the two panels acting as a lumped spring at low frequency, and greater slope between the m-s-m resonance and the critical frequencies of both panels. With Sharp's formulation, the diffuse transmission loss of a double wall can be obtained approximately by knowing the transmission loss of each individual panel. This approach can be used in the design stage, but is limited to single and dual leaf walls with one layer of absorption.

3.3 POINT CONNECTED STRUCTURES

Structural connections in dual leaf systems (studwork, framework, connectors, and fasteners) are very common, being essential for installation, mounting and support of wall and roof systems. A number of existing models assume that transmission through studwork and through the bulk of the structure are separate paths, so that the energy transmission through each portion can be obtained independently. This assumption is reasonable in cases where modal density is high. There are plenty of examples of this approach in Cremer et al. (2005) and Vigran (2008). A model of this kind for point and line connections was developed and adapted to the Transfer Matrix Method (TMM) framework (described in the next section) by Vigran (2010), which accounts for periodicity effects of the framework, though, crucially, not for the interaction between the structure-borne and airborne paths. Many analytical models for infinite double plate structures with periodic framework have been developed. The approaches listed here make use of Fourier transforms of the equations of motion for plates in bending. Geometrically periodic components are introduced by way of Dirac comb functions, which are evaluated using the Poisson summation formula to represent them as harmonic series; this approach enables solutions to be found more easily. Lin and Garrelick (1977) modelled plates connected by spaced ribs, which is typical of lightweight partitions. Brunskog (2005), further, accounted for the finite cavities which are created by

structural ribs. A similar approach was taken by Xin and Lu (2011), in modelling double plate structures with a square grid of beams connecting both plates. Roof structures tend to have point-to-point connections, as has been shown in the previous chapter, so the work of Takahashi (1983) is particularly relevant, as it describes a model of point-excited double plates connected periodically by thin rods, which includes the rotational and compressional stiffness of the structural connectors. Takahashi found significant influence of connectors on transmission, with decreased stiffness being associated mostly but not always with lower transmission. Obtaining useful design parameters from the derived mathematical expressions is often not possible, even for geometrically simple structures, given the density of modes related to the periodic framework is often very high for common stud and connector spacings.

3.4 PROFILED PLATES

A key feature of the cladding constructions to be modelled is that the inner and outer leaf consist invariably of profiled metal panels. Any computational solution will need to account for such profiling and the relevant literature is therefore reviewed in this section. The motion of solid plates is often approached through ‘thin plate’ solutions, i.e. solutions to the bending wave equation (Cremer et al. 2005), which assumes the thickness of the plates is significantly smaller than the bending wavelength. When plates in a multilayer configuration are in contact with other solids, it is necessary to account for shear and longitudinal waves in each medium to characterise their combined behaviour. This can be achieved by treating the layer as a linear elastic solid (Folds & Loggins 1977), an approach that will also be implemented in the course of this work. The most popular, and simplest, method of modelling corrugated or ribbed panels is by constructing an equivalent flat, orthotropic thin plate in bending. This approach is described by Cremer (Cremer et al. 2005), with derivations of the bending stiffness formulas for sinusoidal and periodically ribbed plates. The bending stiffness of

trapezoidal profile plates can be found in Bies and Hansen (1996), and it can be derived more generally for any geometry by calculating the area moment of inertia of the plate section. There are some examples in the literature of applications of this theory. Often there are large differences between the measured performance of profiled plates and equivalent orthotropic plates when predicting performance of single panels, e.g. in (Ng & Zheng 1998). Lam and Windle (1993) identified profile related resonances that changed with profile dimensions, that were independent of edge conditions. They were able to reproduce the location of resonances by finite element analysis of the plate vibration, concluding that the dips in transmission loss observed in diffuse field measurements were predominantly due to these vibrational modes.

Fully periodic analytical approaches have been mostly limited to ribbed structures, as the motion of periodically spaced beams on plates is more tractable than taking into account a trapezoidal geometry, which can be more easily modelled with FEM. Early classically derived models of transmission of sound through infinite, periodically stiffened plates were formulated by Mace (1980), for point as well as airborne excitation, using Fourier transforms of the governing equations. As for the already mentioned models of periodic double plate structures, periodic elements are accounted for using Poisson summation to represent spatial Dirac comb functions as sums of complex exponentials. A similar route was taken by Maxit (2009) for beam stiffened plates with the inclusion of beam rotations, and Sakagami and Gen (1999) for the reflection of sound from ribbed panels with a back cavity. Maxit, among others, concludes that the behaviour at low frequency, where the bending wavelength is greater than the rib spacing, can be approximated by an equivalent flat orthotropic plate. There are, however, several limitations to comparing infinite, perfectly periodic models to real panels, some of which outlined by Mayr and Gibbs (2011) in their analysis of experimental results of ribbed floor constructions, showing that strong periodicity effects predicted by an exactly periodic model are rarely seen in practice. A review of the relevant

literature by Brunskog (Brunskog & Hammer 2000) suggested nearly-periodic models as an avenue to reduce this discrepancy, which was followed by the development of a method, applied to periodically ribbed panels, to account for small deviations from a perfectly periodic system, by introducing a randomly distributed phase disturbance in each space-harmonic (Brunskog 2004).

3.5 THE TRANSFER MATRIX METHOD

Multiple layers of infill are often present in roof structures. A suitable framework that can account for this is the transfer matrix method (TMM). The TMM is a wave-based method of obtaining the transmission, reflection or absorption of plane waves impinging on arbitrarily layered, laterally infinite systems, and can be found in a variety of applications. A detailed description of the method applied to acoustic fields can be found in Brouard et al. (1995) and Lauriks et al. (1992). A number of different media can be modelled, including poroelastic layers, and anisotropic materials. Allard and Atalla (2009) present a good overview of the method in its application to the calculation of sound insulation and absorption, including extensions and corrections to increase its predictive power. The TMM is flexible and has been used to characterise dual leaf wall systems, sandwich structures and other building acoustics. Layers in a TMM modelled system are assumed to be of infinite lateral extent, so on its own it cannot account for modal behaviour in the lateral dimensions, as well as structural connections, profiled panels and, in general, discontinuities along more than one dimension. The TMM can be combined with other modelling techniques to overcome its shortfalls. Dijckmans and Vermeir (2013) combined a wave-based model of laboratory rooms (with rectangular geometry) with the Transfer Matrix approach for structures with multiple layers including dual leaf walls, as well as a modal approach for plates; this model replicated as closely as possible the sound insulation measurement, with point sources placed in the

source room to simulate a loudspeaker excitation. Low frequency behaviour in particular was captured very accurately, as well as the effect of panel edge conditions.

In the classical TMM method, the structures modelled extend to infinity in the plane. Short of modelling the measurement rooms as in this case, an important development was the introduction of finite size and diffuse field corrections. Often in the prediction of acoustic properties of single leaf walls in a diffuse field, the angle of incidence of waves onto the medium is artificially limited to around 80 degrees, on the assumption that grazing incidence waves are less likely. Two papers have explored this further, and introduced more refined correction factors. Villot et al. (2001) developed a spatial windowing correction by considering the radiation efficiency of a finite, rectangular structure. Kang et al. (2000), via ray tracing models, have determined the distribution of incident energy with angle at the walls of different sized rooms, determining an angle dependent weighting with a similar effect on transmission loss as with spatial windowing. These corrections have rendered the TMM useful in assessing non-resonant transmission of even small systems, particularly when results are averaged in fractional octave bands, as with most sound insulation measurements, though they are artificial in that they only affect the incident and transmitted fields as opposed to the vibration of the structure itself.

3.6 POROUS MATERIAL MODELS

Porous materials such as mineral fibres and open-celled foams are omnipresent as cavity infill in wall and roof system, for their acoustic as well as thermal isolation properties. A building acoustics model would not be complete without the inclusion of such materials, with theoretical or empirical models of their acoustic behaviour.

The simplest approaches tend to assume a rigid, fixed frame, so that they only need to deal with the transmission in the fluid portion of the material. A classical approach, the Rayleigh model, assumes that materials are a series of parallel fluid-filled cylinders surrounded by a rigid frame. Solving the Navier-Stokes equation, which includes viscous effects, leads to relationships between acoustical properties, flow resistance, density and speed of sound in the medium. Delany and Bazley discovered empirical relationships between flow resistivity and the acoustical properties of a range of fibrous materials (Delany & Bazley 1970). Their formulas are still widely used today in a range of applications. Their approach was later refined by separating the low and high frequency ranges (Miki 1990). Attenborough also developed a four-parameter analytical model for rigid-framed porous materials (Attenborough 1983). The contexts in which these equivalent fluid models can be applied range from room acoustics to the attenuation of duct insulation. This type of theory is often limited to materials of low density and stiffness, and which are not mounted or bonded to solid panels, as they lack the necessary stress components. Any of these methods may be used within the modelling frameworks presented in this work to characterise the behaviour of porous materials in the cavity of a dual leaf wall.

Biot (1956) developed a complete theory for porous material acoustics, to model both fluid and solid stages of a porous material (its *poroelastic* behaviour) and the interaction between these stages. A number of assumptions which apply to fibrous materials allow for a simplification of the requirements for properties, which could be sufficient to provide reasonable accuracy in the prediction of full, built-up systems with mineral or glass wool infill. These principles are summarised in Allard and Atalla (2009).

It has been seen that many of the elements identified in the introduction are important in the modelling of profiled panel constructions and have been studied in various contexts.

However, these elements have not previously been brought together. In the following chapter the key building blocks of the model will be described in more detail, before being combined into an overall modelling framework in the later chapters.

4 BUILDING BLOCKS

This chapter describes the individual building blocks required to model a full partition, roof system or multi-layer structure. Key equations and derivations are shown where necessary, so that the reader is able to reproduce the results.

4.1 THE TRANSFER MATRIX METHOD

4.1.1 Introduction

This section describes the transfer matrix method (TMM), including a well-established approach to modelling layered systems with different material types, using interface matrices to relate fluids, porous and poroelastic materials, viscoelastic solids, and thin plates or membranes. A comprehensive paper on the method was written by Brouard et al. (1995) – similar notation is used in this section.

4.1.2 Wavenumber domain

Figure 14 shows the surface of the modelled system in grey, in relation to spatial coordinates. A plane wave's direction is represented by the wavenumber vector k , which has a fixed magnitude at each frequency, dependent on the medium, and is described over the course of this report in terms of the spherical coordinates, θ and ϕ . θ is known as the angle of incidence, where $\theta = 0$ represents normal incidence, and $\theta = \frac{\pi}{2}$ rads represents grazing

incidence. ϕ is the angle of polarisation, which describes the orientation of the wave in the xy plane.

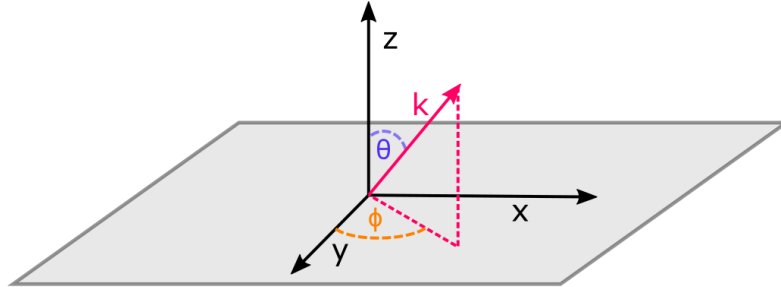


Figure 14: Dimensions and wavenumber vector \vec{k} , showing Cartesian coordinates x, y, z and spherical coordinates ϕ and θ

The components of the wavenumber vector are:

$$k_x = k \sin \theta \cos \phi \quad (4.1)$$

$$k_y = k \sin \theta \sin \phi \quad (4.2)$$

$$k_z = k \cos \theta \quad (4.3)$$

The relationship between these components satisfies the Helmholtz equation for a given periodic pressure distribution p :

$$(\nabla^2 + k^2)p = 0 \quad (4.4)$$

The wavenumber in the medium k is given by the sum of the squares of each component:

$$k^2 = k_x^2 + k_y^2 + k_z^2 \quad (4.5)$$

4.1.3 System geometry

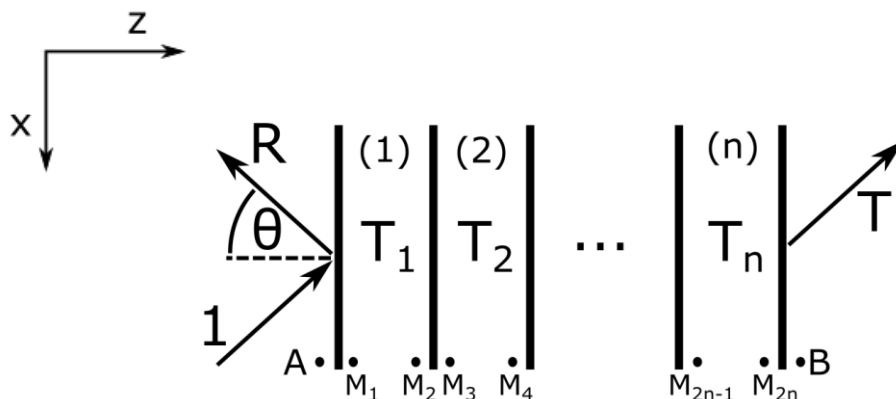


Figure 15: A layered system with n layers in the Transfer Matrix framework

The transfer matrix method is a wave-based model in which matrices are used to represent transformations within a component of a system. In this thesis, a variant of the TMM is used that applies to modelling transmission of acoustic waves through systems of many laterally-infinite layers.

Consider the geometry shown in Figure 15, which is a system of n layers, which may be different media, surrounded by semi-infinite fluid spaces either side. The TMM representation is two dimensional, as it considers the plane of the incoming wave, along z (through the layers) and x (along the layers). The surrounding fluid is air, with density $\rho_0 = 1.213 \text{ kg/m}^3$ and speed of sound $c_0 = 343 \text{ m/s}$. An incident plane wave p_i of amplitude equal to 1 is impinging on the leftmost layer, and takes the form:

$$p_i = e^{i(k_{x_0}x + k_{z_0}z)} e^{-i\omega t} \quad (4.6)$$

with wavenumber $k_0^2 = k_{x_0}^2 + k_{z_0}^2$, where $k_0 = \frac{\omega}{c_0}$. A plane wave is reflected, and one transmitted from the rightmost layer. The trace wavenumber k_t is the same for all layers, being forced by the incident wave $k_t^2 = k_{x_0}^2$, so that only the z components of wavenumber

vary between layers. A transfer matrix T is a matrix of size N by N which relates field variables at one side of a layer (point M_1 for layer 1) to the field variables at the other side (point M_2 for layer 1), where N is the number of field variables in the medium.

$$V(M_1) = T_1 \times V(M_2)$$

Where $V(M_1)$ and $V(M_2)$ are field variable vectors that define the medium (for a fluid, these are pressure and velocity) at, respectively, points M_1 and M_2 . In this framework, more layers can be added by simply multiplying their transfer matrices together, provided that the matrices are of compatible dimensions:

$$V(A) = T_1 \times T_2 \times \dots \times T_n \times V(B)$$

where $T_1, T_2 \dots$ are the transfer matrices for each layer, and n is the total number of layers in the system.

4.1.4 Fluid layers

In a fluid, the field variables are pressure and velocity, so the vector V^f (superscript f denoting a fluid) becomes:

$$V^f = \begin{bmatrix} p \\ v_z \end{bmatrix}$$

where p is pressure and v_z is velocity in the z direction. The transfer matrix for a fluid layer is a 2 by 2 matrix T^f :

$$T^f = \begin{bmatrix} \cos k_z d & j \frac{\omega \rho}{k_z} \sin k_z d \\ j \frac{k_z}{\omega \rho} \sin k_z d & \cos k_z d \end{bmatrix} \quad (4.7)$$

where ρ is the fluid density, and d is the layer thickness in the z direction, and k_z is the z component of the wavenumber, given by:

$$k_z = \sqrt{k^2 - k_{x_0}^2} \quad (4.8)$$

4.1.5 Elastic solids

In a viscoelastic solid layer there are four field variables in total: longitudinal and shear stress together with their associated velocities. The field variable vector for a solid, V^s , is then:

$$V^s = [v_x \quad v_z \quad \sigma_{zz} \quad \sigma_{xz}]^T \quad (4.9)$$

v_z and v_x are the z and x components of velocity, σ_{zz} and σ_{xz} are, respectively, the longitudinal and shear components of stress. There are then two wave types in the solid medium, which are characterised by a longitudinal wavenumber k and a shear wavenumber κ ; these are found by knowing the longitudinal and shear wavespeed in the material: $k = \frac{\omega}{c_l}$ and $\kappa = \frac{\omega}{c_s}$. The z component of these wavenumbers are obtained by applying the usual relations that satisfy the Helmholtz equation:

$$k_z = \sqrt{k^2 - k_t^2} \quad (4.10)$$

$$\kappa_z = \sqrt{\kappa^2 - k_t^2} \quad (4.11)$$

The viscoelastic solid transfer matrix size is a four by four, relating longitudinal and shear stress and velocity either side of the layer. The elements a_{ij} of the transfer matrix are given by Folds and Loggins (1977), and are shown in Table 2.

$a_{11} = G \cos P + (1 - G) \cos Q$	$a_{31} = -HG(1 - G)(\cos P - \cos Q)$
$a_{12} = i \left[\frac{(1 - G) \sin P}{E} \right] - iFG \sin Q$	$a_{32} = -iH \left\{ \frac{[(1 - G)^2 \sin P]}{E} + FG^2 \sin Q \right\}$
$a_{13} = -\left(\frac{1}{H}\right) (\cos P - \cos Q)$	$a_{33} = a_{22}$
$a_{14} = -\left(\frac{i}{H}\right) \left[\left(\frac{\sin P}{E}\right) + F_n \sin Q \right]$	$a_{34} = a_{12}$
$a_{21} = iEG \sin P - \frac{i[(1 - G) \sin Q]}{F}$	$a_{41} = -iH \left\{ EG^2 \sin P + \frac{[(1 - G)^2 \sin Q]}{F} \right\}$
$a_{22} = (1 - G) \cos P + G \cos Q$	$a_{42} = a_{31}$
$a_{23} = -\left(\frac{i}{H}\right) \left(E \sin P + \frac{\sin Q}{F} \right)$	$a_{43} = a_{21}$
$a_{24} = a_{13}$	$a_{44} = a_{11}$
$E = \frac{\kappa_z}{\kappa_t}, F = \frac{\kappa_z}{\kappa_t}, G = \frac{2\kappa_t^2}{\kappa^2}, H = \frac{\rho\omega}{\kappa_t}, P = \kappa_z d, Q = \kappa_z d$	
<p>ρ and d are the density and thickness of each layer</p>	

Table 2: Values of the four by four elastic solid transfer matrix a_{ij}

Sandwich structures can be modelled this way, as continuity of shear stress and velocity at the boundaries between solids is accounted for.

4.1.6 Porous layers

Porous media are discussed in more depth in Section 4.2. Porous materials can be modelled in two ways:

- As equivalent fluids
- As poroelastic materials (that is, including waves travelling in the solid portion of the material)

If they are treated as equivalent fluids, the transfer matrix is exactly the same as that for a fluid, except the impedance and wavenumber will generally be complex, in order to account for energy loss within the material, through viscosity and other mechanisms.

If they are treated as a poroelastic medium, material properties of the frame are required and play an active role in the transmission of sound. In addition to longitudinal waves in the fluid portion, longitudinal and shear waves in the solid portion must be accounted for. This, in total, leads to three stress variables (longitudinal stress in the fluid, and longitudinal and shear stress in the framework), and three components of velocity:

$$V^{pe} = [v_x^s \quad v_z^s \quad v_z^f \quad \sigma_{zz}^s \quad \sigma_{xz}^s \quad \sigma_{zz}^f]^T \quad (4.12)$$

The superscripts *s* and *f* indicate, respectively, solid and fluid components, and superscript *pe* indicates the layer is poroelastic. The transfer matrix for a poroelastic layer, T^{pe} , is a 6 by 6 matrix, relating field variables either side of the layer. The elements of the matrix can be found in the appendix to Lauriks et al. (1990).

4.1.7 Thin plates

Within the transfer matrix scheme, thin plates can be modelled with a two by two matrix, similarly to a fluid. The elements of the matrix include the *wall impedance* term, Z_p :

$$\begin{bmatrix} p_0 \\ v_0 \end{bmatrix} = \begin{bmatrix} 1 & Z_p \\ 0 & 1 \end{bmatrix} \begin{bmatrix} p_1 \\ v_1 \end{bmatrix} \quad (4.13)$$

The wall impedance term and the vibration of thin plates using Kirchhoff theory is discussed in more detail in Section 4.3.

The bottom row of the transfer matrix enforces the condition that normal velocity is equal either side of the plate, $v_0 = v_1$. There is no continuity of shear stress and velocity, meaning two or more plates bonded to each other cannot be modelled this way as the shear stress continuity condition is not enforced.

4.1.8 Interface matrices

In systems of layers with different types of media (e.g. solids and fluids) with differing length of field variable vectors, the transfer matrices cannot be simply matrix multiplied. The system of equations can instead be solved with the use of interface matrices. These change the size of each transfer matrix to fit the neighbouring layers and enforce the appropriate continuity conditions between different media. At the interface between two layers, i and j , continuity conditions are applied with the following matrix equation:

$$V^i I_{ij} + V^j J_{ij} T^j = 0 \quad (4.14)$$

Where I and J are the interface matrices.

For the boundary between a fluid and a solid, shear stress is set to zero, and longitudinal pressure and velocity are preserved, resulting in the following matrices:

$$I_{fs} = \begin{bmatrix} 0 & -1 \\ 1 & 0 \\ 0 & 0 \end{bmatrix}, \quad J_{fs} = \begin{bmatrix} 0 & 1 & 0 & 0 \\ 0 & 0 & 1 & 0 \\ 0 & 0 & 0 & 1 \end{bmatrix} \quad (4.15)$$

The fs subscript indicates an interface from a fluid to a solid.

For brevity, the reader is referred to Brouard et al. (1995) for a list of interface matrices.

4.1.9 Termination conditions

In order to solve the system of equations, appropriate termination conditions must be set, depending on whether the system is rigidly backed or if surrounded on both sides by semi-infinite air layers.

A rigid termination can be enforced by setting particle velocity to zero at the rigid end of layer. This will be relevant to modelling conditions in an impedance tube measurement setup (see Section 4.2.6 for its application in this work), as well as, for instance, for modelling the sound absorption characteristics of wall-mounted panels. The condition is expressed with a binary matrix Y , applied to the field at the point B (as per Figure 15):

$$Y \times V_f(B) = 0 \quad (4.16)$$

For an arbitrary layered configuration using the full elastic, poroelastic or fluid transfer matrix, the rigid termination condition depends on whether the final layer is poroelastic, elastic or fluid.

$$\begin{aligned}
& Y_p \\
& = \begin{bmatrix} 1 & 0 & 0 & 0 & 0 & 0 \\ 0 & 1 & 0 & 0 & 0 & 0 \\ 0 & 0 & 1 & 0 & 0 & 0 \end{bmatrix} \quad Y_s = \begin{bmatrix} 1 & 0 & 0 & 0 \\ 0 & 1 & 0 & 0 \end{bmatrix} \quad Y_f = [0 \quad 1] \quad (4.17)
\end{aligned}$$

When it is necessary to obtain the sound transmission through an element, the model must instead include semi-infinite fluid layers either side of the structure. For this purpose, an additional condition is included:

$$\left[1 \quad \frac{Z_0}{\cos \theta} \right] \times V_f(B) = 0 \quad (4.18)$$

Where Z_0 is the characteristic impedance of the surrounding fluid (air): $Z_0 = \rho_0 c_0$, and θ the angle of incidence. The $\frac{1}{\cos \theta}$ term applies to radiation of an infinite structure; the radiation of a laterally infinite system into a finite sized opening is discussed in Section 4.1.11.

4.1.10 Impedance, Transmission, Reflection and Absorption coefficients

A global matrix D' is formed which satisfies all boundary conditions. The elements of the matrix (which depend on the number and types of layers) can be found in Brouard et al. (1995), and contain all transfer matrices and interface matrices, as well as the termination conditions. D' is used to determine the surface impedance, Z_s :

$$Z_s = -\frac{|D'_1|}{|D'_2|} \quad (4.19)$$

Where $|D'_1|$ and $|D'_2|$ are the determinants of the D' matrix where, respectively, the first and second columns have been removed. From Z_s , three commonly measured acoustic properties can be obtained:

- The reflected pressure amplitude R ,

$$R = \frac{Z_s \cos \theta - Z_0}{Z_s \cos \theta + Z_0} \quad (4.20)$$

where Z_0 is the characteristic impedance of the surrounding medium (generally, air)

- The absorption coefficient α ,

$$\alpha = 1 - |R|^2 \quad (4.21)$$

- The transmitted pressure amplitude T ,

$$T = (1 + R) \frac{|D'_{N-1}|}{|D'_1|} \quad (4.22)$$

where $|D'_{N-1}|$ is the determinant of the D' matrix with column $N - 1$ (second to last) has been removed.

The transmission coefficient, the ratio of incident to transmitted power, is given by the square of the transmitted pressure amplitude:

$$\tau = |T|^2 \quad (4.23)$$

The diffuse field transmission loss is obtained by integrating the transmission coefficient over a hemisphere:

$$\tau_{\text{diff}}(\omega) = \frac{\int_0^{2\pi} \int_0^{\pi} \tau(\omega, \theta, \phi) \sin \theta \cos \theta \, d\theta d\phi}{\int_0^{2\pi} \int_0^{\pi} \sin \theta \cos \theta \, d\theta d\phi} \quad (4.24)$$

Finally, the transmission loss in decibels, of particular interest to this thesis in making comparisons with available measured values, is given by the base ten logarithm of the transmission coefficient (either diffuse or angle dependent).

$$TL = -10 \log_{10} \tau \quad (4.25)$$

4.1.11 Finite size corrections

The transmission loss calculated using the transfer matrix method for infinite layers is generally much lower compared to laboratory diffuse field measurements, with differences in the order of 20 or 30 decibels, especially for dual leaf structures (see Figure 17). One cause of these differences is the fact that the source room pressure field is not perfectly diffuse, another is the particular radiation characteristics of the panels.

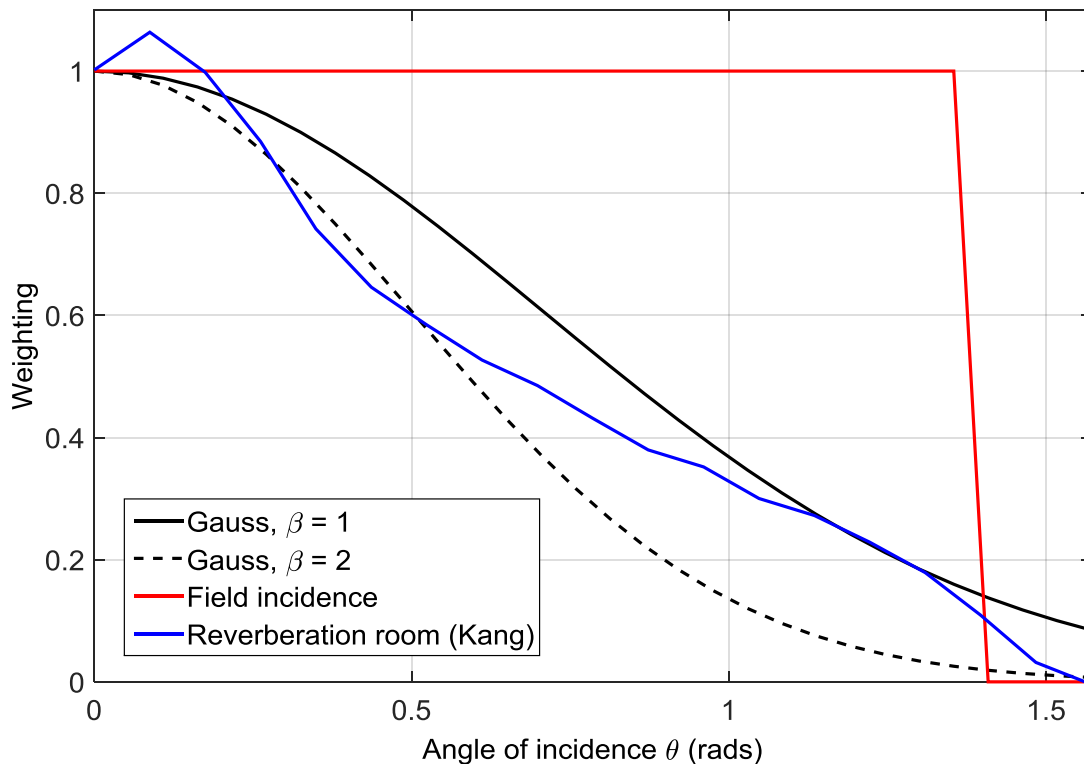


Figure 16: Angle of incidence correction factor (Gauss) with two different values of β , compared to field incidence, and a

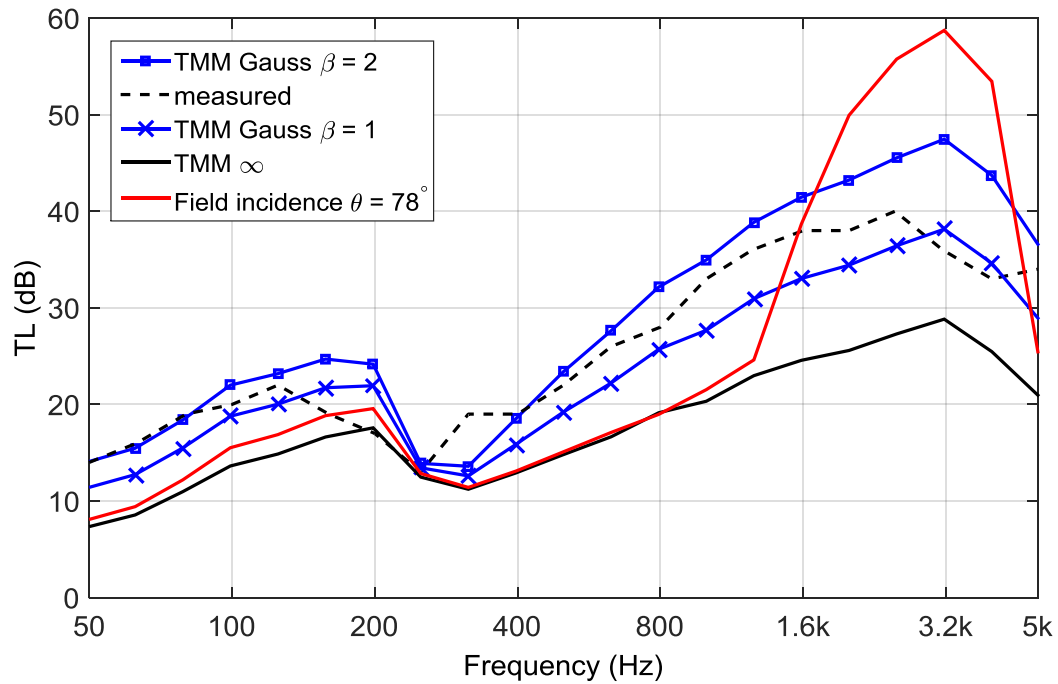


Figure 17: Double glazing 1/3 octave band transmission loss; laboratory measurement versus TMM with no corrections (∞), Gaussian incidence ($\beta = 1$ and 2), and field incidence with a limiting angle of 78 degrees.

A commonly used method of bringing the calculated transmission loss (or absorption coefficient) into agreement with laboratory measurement results is to limit the angle of incidence to an arbitrary angle close to grazing incidence. An angle of $\theta = 78^\circ$ is often used, referred to as a *field incidence* correction, with some evidence suggesting it provides the a good fit with results. However, for dual leaf partitions and other multilayer systems it can give rise to unrealistic results, as shown in Figure 17 (red curve). Kang et al. (2000) proposed a distribution in incidence angles based on ray tracing models of rooms of different geometries, obtaining a Gaussian formula for weighting transmission loss:

$$G(\theta) = e^{-\beta\theta^2} \quad (4.26)$$

Where $G(\theta)$ is the weighting as a function of incidence angle θ . The term β has a value between 1 and 2 depending on room characteristics. There is no formula to determine this value, although Kang obtained values for a small selection of room sizes.

This term is applied to transmission loss when integrating over the hemisphere, resulting in the formula:

$$\tau_{\text{diff, Gauss}} = 2 \int_0^{\frac{\pi}{2}} G(\theta) \tau(\theta) \cos \theta \sin \theta d\theta \quad (4.27)$$

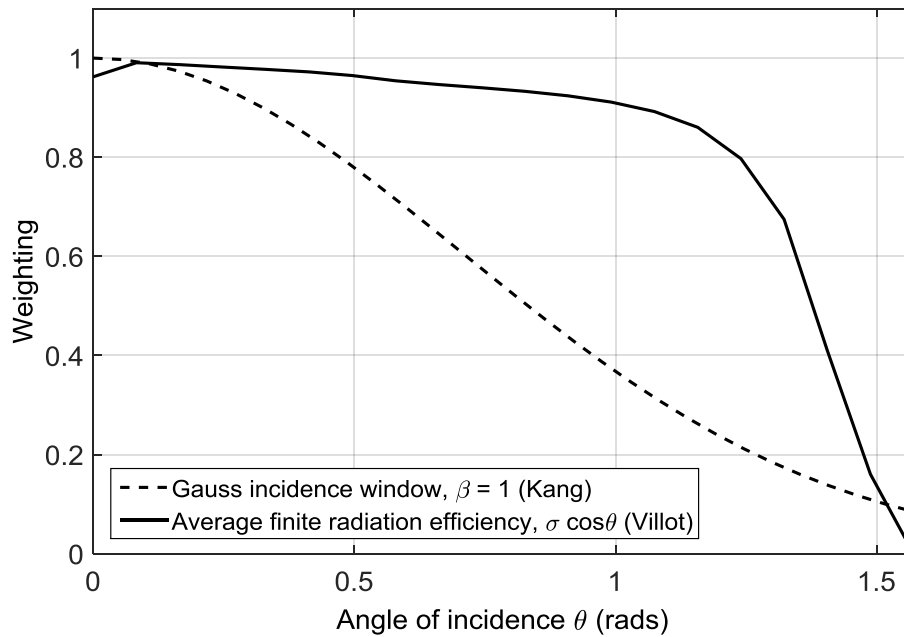


Figure 18: Gaussian incidence (H. Kang et al. 2000) versus radiation efficiency correction (Villot et al. 2001)

An approach taken by Villot et al. (2001), but also found in Cremer (2005), has been used to account for the effect of radiation efficiency of a finite, rectangular structure. The factor is referred to as a *spatial windowing*, and is only dependent on the lateral dimensions of the radiating structure.

The window is derived by considering a laterally infinite structure radiating through a finite rectangular area on the xy plane, of dimensions L_x and L_y . The normal velocity v_n over the plane has a distribution that, for a finite structure, depends on the edge conditions and type of excitation (point, line, plane wave, etc.). Independent of the velocity distribution, the radiated power W_{rad} is obtained by integrating the pressure and velocity over the surface:

$$W_{\text{rad}} = \frac{1}{2} \text{Re} \left(\int_0^{L_x} \int_0^{L_y} p v_n dx dy \right) \quad (4.28)$$

Where p is the pressure. Villot assumed the spatial distribution of v_n to have the same form as the incident field, as is the case for infinite structures. On that basis, the expression for radiated power in terms of the trace wavenumber on the surface, k_t , and wave orientation ϕ , is:

$$\begin{aligned} \sigma_r(k_t, \phi) &= \\ &= \frac{L_x L_y}{\pi^2} \times \int_0^{k_0} \int_0^{2\pi} \frac{1 - \cos(k_r \cos \psi - k_t \cos \phi L_x)}{[(k_r \cos \psi - k_t \cos \phi) L_x]^2} \frac{1 - \cos(k_r \cos \psi - k_t \cos \phi L_y)}{[(k_r \cos \psi - k_t \cos \phi) L_y]^2} d\psi dk_r \end{aligned} \quad (4.29)$$

The integration over wavenumber k_r is up to k_0 , to include all wavenumbers of propagating waves. The transmission coefficient obtained via the TMM (or other method) can then be adjusted by including σ_r into the diffuse field integration:

$$\tau_{\text{diff, Gauss}} = 2 \int_0^{\frac{\pi}{2}} (\sigma_r \cos \theta) \tau(\theta) \cos \theta \sin \theta d\theta \quad (4.30)$$

The frequency averaged radiation efficiency correction is compared to the incidence correction $G(\theta)$ in Figure 18. Both corrections have been applied simultaneously for comparisons with laboratory measurement results in Chapters 6 and 7.

4.1.12 Excitation mechanism

The incident field in the TMM can be modified to include different types of excitation. Point excitation can be introduced and used to model impact noise reduction and rainfall. A point force input is modelled by decomposing the excitation force into its plane wave components, via spatial Fourier transform, and feeding each individually into the TMM calculation. An approach to modelling rain noise excitation, including obtaining the radiated power in a diffuse field, is shown in Appendix A.

4.1.13 Conclusions

In this section, the Transfer Matrix Method was described, detailing the ways in which different material types can be modelled and interfaced to each other in a layered system. Modifications to the basic formulation (Brouard et al. 1995) in order to produce a better fit with diffuse field laboratory measurements were shown, with spatial and incident angle windowing.

4.2 POROUS MATERIAL MODELLING

4.2.1 Introduction

Porous materials feature in most cladding constructions, partly for acoustic and partly for thermal reasons, and it is therefore important to include their effect in any acoustic model. In this section, the main approaches are discussed.

The solid portion of a porous material is referred to as its frame. An important characteristic of these materials is their porosity, ϕ , which is a value from 0 to 1 indicating the ratio of fluid to frame, where 0.99 would indicate a high porosity material with 99% fluid and 1% frame.

This value is typical for commercially available “acoustic” foams and mineral fibres, and is not far from the value for even the highest density materials ($>200 \text{ kg/m}^3$) measured over the course of this work.

Some relevant existing theoretical and empirical models for porous materials are described in this section. There are broadly two approaches: rigid-frame models and porous-elastic (or poroelastic) models. Rigid-frame models only deal with transmission through the fluid portion of the material. Poroelastic models include movement of the frame and interactions between fluid and frame. A simple experimental method was used to determine many material properties of fibrous materials from a single impedance tube measurement.

4.2.2 Measurement method

The acoustic properties of absorbent materials, such as effective wavenumber and impedance, surface impedance, transmission loss etc. are generally measured on a small scale using an impedance tube. Surface impedance and, consequently, the absorption coefficient can be obtained with the use of a single microphone, one frequency at a time, as detailed in ISO 10534-1, or with two-microphones, over a broad frequency range, as described in ISO 10534-2, with the sample in both cases being placed on one end of the tube. The effective impedance and wavenumber can also be measured directly using four microphones (Jung et al. 2008), where two microphones are placed either side of the sample, and obtaining the properties via a transfer matrix, knowing the transmitted and reflected pressure amplitudes. The measured properties are for a normal incidence wave, as the geometry of the tube dictates. In practice, this limits determination of elastic properties to locally reacting isotropic materials. Nevertheless, the impedance tube results can be imported into TMM models of layered systems as will be described later.

4.2.3 Equivalent fluids

An equivalent fluid model uses an adjusted speed of sound and density based on either theoretical considerations or empirical curve fitting. This type of model usually assumes that the frame is rigid, thereby neglecting transmission of shear and longitudinal sound waves through the frame itself. Unlike lossless fluids described in 2.1, porous layers have complex impedance and wavenumber, which give rise to losses within the material.

4.2.4 Simple approaches

At a first approximation, a porous absorber can be modelled as a series of parallel tubes. The resulting impedance and wavenumber based on the Rayleigh model (based on solutions to the Navier-Stokes equation for waves in a narrow tube) are:

$$z = \frac{z_0}{\phi} \sqrt{1 - j \frac{\sigma \phi}{\rho_0 \omega}} \quad (4.31)$$

$$k = k_0 \sqrt{1 - j \frac{\sigma \phi}{\rho_0 \omega}} \quad (4.32)$$

k_0 , z_0 , and ρ_0 are, respectively, the wave number, impedance and density of air (or of the surrounding fluid) and σ and ϕ are the flow resistivity (in Nsm^{-4}) and porosity of the material.

Delany and Bazley (1970) developed an empirical equivalent fluid model that is based on the observed relationship between measured surface impedance and airflow resistivity for a range of low-density, high porosity mineral fibres. The impedance and wavenumber of such materials can be predicted from the flow resistivity of the material.

$$z = z_0(1 + 0.0571E^{-0.754} - j0.087E^{-0.732}) \quad (4.33)$$

$$k = k_0[0.0978E^{-0.7} - j(1 + 0.189E^{-0.595})] \quad (4.34)$$

Where $E = \frac{f\rho_0}{\sigma}$. The model has enjoyed extensive use in the field, and has been improved upon since its inception. Mechel (1988) split the parameters into low and high frequency regions for a better fit. Further corrections to the original model were introduced by Miki (1990), by constraining the values to be causal (important for time domain simulations), improving at the same time low frequency asymptotic behaviour

Other rigid-frame analytical models, such as those proposed by Attenborough (1983; 2014), are not discussed here. While there is scope for increasing accuracy in modelling different types of porous materials, simpler models were considered sufficient. The drawback of fluid models, including the more advanced ones, is that mechanical coupling to adjacent materials, which can be important in the layered structures studied here, is not allowed for. Additionally, the improvement in accuracy from using more complex models would be overshadowed by other uncertainties when forming part of a multilayer structure.

4.2.5 Poroelastic behaviour

High stiffness mineral wool placed in a wall cavity affects the vibration of adjacent panels, and consequently transmission loss, in a way that cannot be predicted with equivalent fluid models. Only by including motions of the solid frame can this be addressed. Poroelastic models include frameborne waves in the material, and can account for mechanical coupling between solid and porous media in a multilayer configuration.

Three different types of waves can propagate in a poroelastic medium, and they derive from the solution to three wave equations: two longitudinal waves in the fluid and solid

respectively, with wavenumber k_{l_1} and k_{l_2} , and one rotational wave k_s , due to the elastic solid nature of the frame.

$$k_{l_1}^2 = \frac{\omega^2}{2(PR - Q^2)} (P\rho_{22} - R\rho_{11} - 2Q\rho_{12} - \sqrt{\Delta}) \quad (4.35)$$

$$k_{l_2}^2 = \frac{\omega^2}{2(PR - Q^2)} (P\rho_{22} - R\rho_{11} - 2Q\rho_{12} + \sqrt{\Delta}) \quad (4.36)$$

$$\Delta = (P\rho_{22} + R\rho_{11} - 2Q\rho_{12})^2 - 4(PR - Q^2)(\rho_{11}\rho_{22} - \rho_{12}^2) \quad (4.37)$$

$$k_s^2 = \frac{\omega^2}{\mu} \left(\frac{\rho_{11}\rho_{22} - \rho_{12}^2}{\rho_{22}} \right) \quad (4.38)$$

Symbols and their meanings are shown in Table 3, along with formulae to determine poroelastic properties assuming the material has an incompressible frame, which is valid for typical mineral wools consisting of either glass or rock fibres. In Table 4, further approximations are shown that are valid for fibrous materials.

Property	Symbol/Equation
Atmospheric pressure	$P_0 = 101.32 \text{ kPa}$
Density of air	$\rho_a = 1.213 \text{ kgm}^{-3}$
Ratio of specific heats (air)	$\gamma = 1.4$
Prandtl number (air)	$Pr = 0.71$
Shear viscosity (air)	$\eta = 1.84 \times 10^{-5}$
Speed of sound (air)	$c_0 = 343$
Elastic modulus	E
Poisson ratio	ν
Density of frame material	ρ_1
Static tortuosity	α_0
Porosity	ϕ
Flow resistivity	σ
Shear modulus	$\mu = \frac{E}{2(1 + \nu)}$
Viscous characteristic length	$\Lambda = \frac{1}{c} \left(\frac{8\eta\alpha_0}{\sigma\phi} \right)^{0.5}$ (Johnson et al. 1987) With c close to 1
Thermal characteristic length	Λ'
Static viscous permeability	$q_0 = \frac{\eta}{\sigma}$
Elasticity coefficients (incompressible frame material)	$P = \frac{4}{3}N + K_b + \frac{(1 - \phi)^2}{\phi}K_f$ $Q = K_f(1 - \phi)$ $R = \phi K_f$
Bulk modulus of frame	$K_c = \frac{2N(\nu + 1)}{3}$

Property	Value for fibrous materials
Fibre length per unit volume	$L = \frac{1 - \phi}{\pi R^2}$
Static tortuosity	$\alpha = \frac{1}{\phi}$
Viscous Characteristic Length	$\Lambda = \frac{1}{2\pi LR}$
Thermal Characteristic Length	$\Lambda' = 2\Lambda$

Table 4: Approximation of properties for fibrous materials

Of the properties requiring measurement, material and framework density are straightforward to obtain. Fibre radius can be obtained from the manufacturer, or measured with an Optical Fibre Diameter Analyser or similar instrument. Flow resistivity can be measured directly in a specialised rig, or can be estimated using an empirical formula based on fibre radius and material density (Bies & Hansen 1980):

$$\sigma = \frac{0.79 \times 10^{-9}}{R^2 \rho_1^{-1.53}} \quad (4.39)$$

The remaining parameters are discussed in the following sections.

4.2.6 Determining porous material properties

The Young's modulus, Poisson ratio and flow resistivity remain to be measured. Assuming a Poisson ratio equal to zero is a reasonable assumption at least for common mineral fibres (Tarnow 2005). Current measurement methods of determining the Young's modulus can be

measured using a shaker, applying a preload to the material (Pritz 1980), affecting its mechanical properties; this may be useful in the case of dual leaf systems in which the cavity infill is compressed between the two sheets.

When the material is bonded to the rigid termination of the impedance tube, it will exhibit a quarter wavelength frame-borne resonance, dependant on its bulk modulus K and its density ρ , of frequency.

$$f = \frac{1}{4l} \sqrt{\frac{\Re(K)}{\rho}} \quad (4.40)$$

where l is the thickness of the sample. The resonance is noticeable in the measured surface impedance of stiffer and low damping samples and provides a way to access the mechanical properties of a porous material without introducing a static preload which would alter its stiffness.

The iterative method used in this work to determine Young's modulus and flow resistivity is shown schematically in *Figure 19*. A transfer matrix model for a single layer of mineral wool with a rigid termination (Section 4.1.9) is used to simulate the impedance tube measurement conditions.

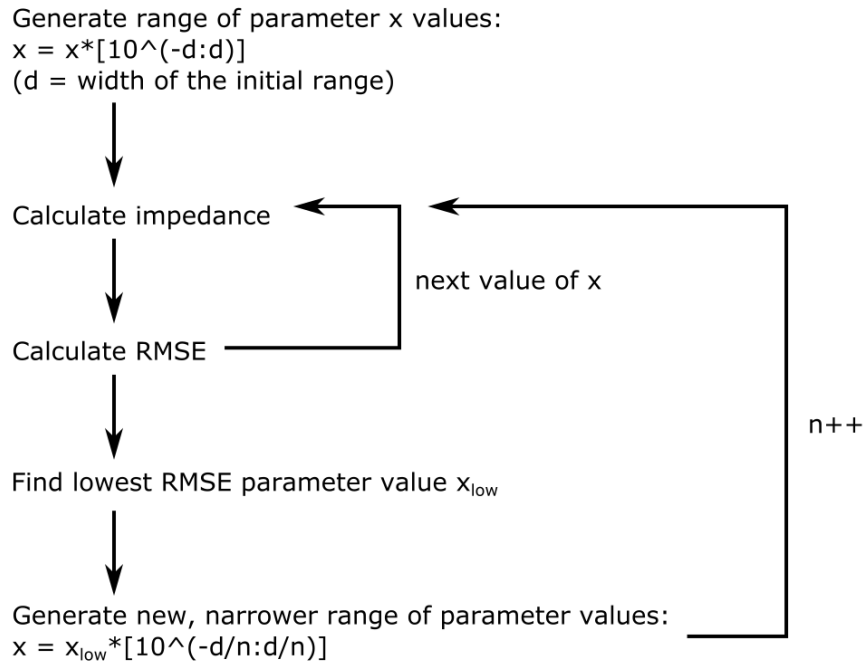


Figure 19: Diagram of an iterative method used to determine Young's modulus and flow resistivity of fibrous materials. RMSE = root mean square error.

First, a broad range of flow resistivity and Young's modulus values are determined. Then, the surface impedance is calculated for each of the input parameter values. The parameter values with the lowest root mean square error (RMSE) are chosen as the centres of a new, narrower range of input values. The impedance is then recalculated and the smallest error values chosen again. The process is repeated n times, or until it converges so that there is no further significant reduction in RMSE. The process must be guided as the frame-borne resonance frequency is not always automatically identified. The loss factor of each sample was estimated by the size of the resonant dip. The Delany-Bazley formulas cannot account for the frame-borne resonance, as can be seen in Figure 20, though the high frequency impedance is close to the measurement. A full poroelastic model correctly replicates the resonance, as in Figure 21.

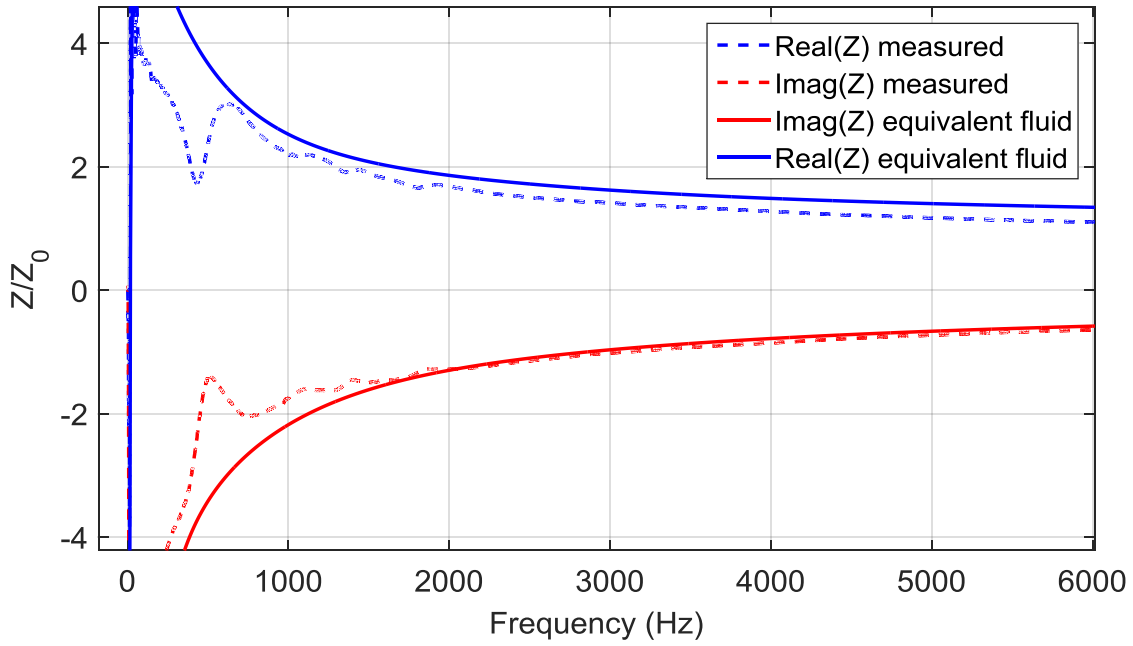


Figure 20: Real and imaginary parts of normalised surface impedance of high density mineral wool (140 kg/m^3); comparison of impedance tube measurement (dashed lines) with transfer matrix model using Delany-Bazley equivalent fluid formulation (solid lines)

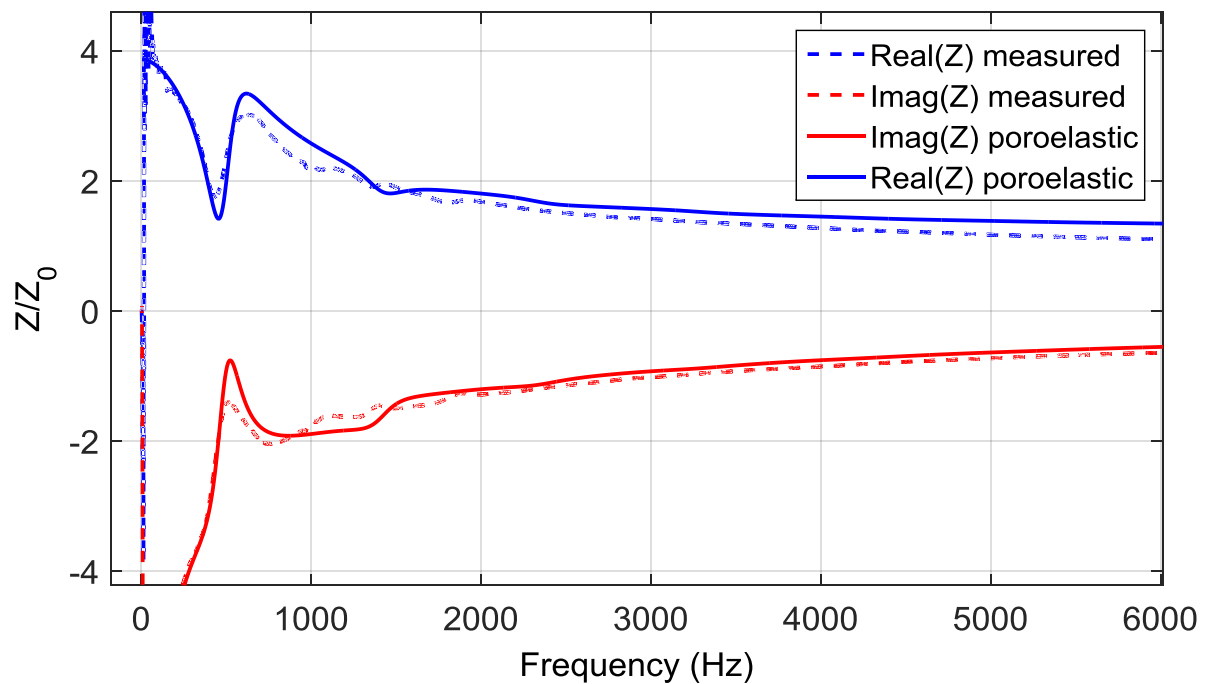


Figure 21: Real and imaginary parts of normalised surface impedance of high density mineral wool (140 kg/m^3); comparison of impedance tube measurement (dashed lines) with transfer matrix model using a poroelastic layer (solid lines)

The method described has clear limitations and relies on several assumptions, in this case applicable to fibrous materials. The method could be extended to other kinds of porous materials, with several caveats. First of all, the size of the sample in the impedance tube influences the location of solid wave resonances, which are crucial in determining the properties of the solid frame. Solids are strongly affected by their size and mounting conditions; it's therefore difficult to accurately quantify the difference between behaviour of a small 100 mm radius sample mounted in a tube, and a large scale partition.

Higher density materials (over 60 kgm^{-3}) tend to be stiffer and have a lower loss factor, resulting in a pronounced resonance which is easy to identify. Low density materials on the other hand tend to exhibit a broader and fainter resonance (if at all visible) due to their high loss factor and low stiffness in the solid portion. For this reason, poroelastic properties of low density materials are more difficult to determine with the method described in this section. With these materials, it's best to assume a rigid, fixed frame and fluid motion only.

This method of determining material properties still requires substantial user input as the results need to be evaluated on a case by case basis to determine if the frame-borne resonance has been correctly identified. The relationship between Young's modulus and density for a range of mineral wool samples measured over the course of this work, so that they may be used to model full roof and partition structures, can be seen in Figure 22 and Figure 23. The Young's Modulus and flow resistivity were both found to correlate with material density. The values of flow resistivity obtained with the reverse method are lower than what is given with the Bies-Hansen empirical formula, Equation (4.39).

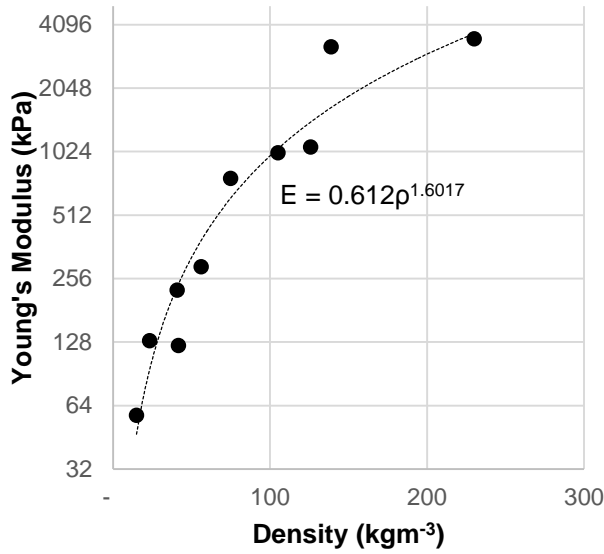


Figure 22: Relationship between density and Young's Modulus of mineral wool samples, with a fitted curve

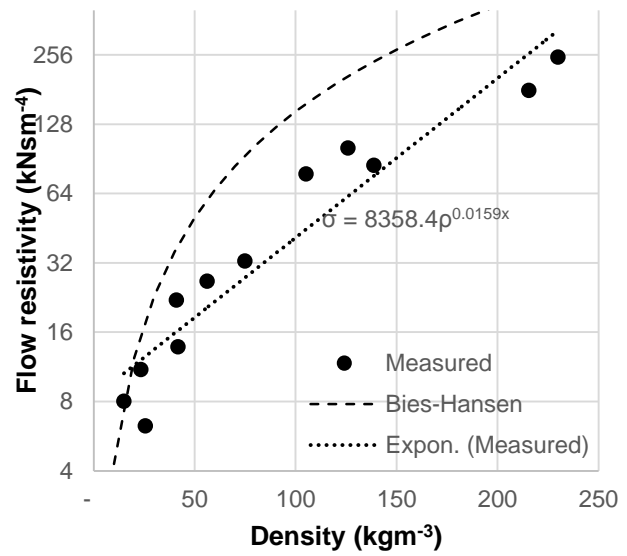


Figure 23: Relationship between density and flow resistivity of mineral wool samples, showing an exponentially fitted curve to the measured data, and the Bies-Hansen empirical formula (Equation (4.39))

4.2.7 Conclusions

In this section, available porous material models were described, with both fluid and poroelastic approaches. Formulas for the poroelastic properties of fibrous materials are given, based on assumptions about their geometry. A best-fit, inverse method of obtaining flow resistivity and Young's Modulus of fibrous materials was described, based on measuring the surface impedance of a sample and obtaining the closest match to a TMM model with a rigid termination condition. The values obtained with this method will be used to model full roof and partition systems with glass or mineral wool infill.

4.3 PLATES

In this section, thin plate theory is briefly presented, which is required to model metal sheets and other panels in full roof and partition systems. The following methods of modelling plates with periodic profiles are outlined, to be later compared in Chapter 6:

- The equivalent orthotropic plate model, as an approximation of corrugated and ribbed panels
- A classically derived periodic ribbed plate model
- The Finite Element Method, using Comsol

4.3.1 Thin plate theory

For a thin plate in free vibration lying along the xy plane, the normal displacement along the plate, w_z , obeys the Kirchhoff-Love bending wave equation:

$$(B\nabla^4 + \delta_t^2 m')w_z = 0 \quad (4.41)$$

Where B is the bending or flexural stiffness, and m' is the mass of the plate, both per unit area. The second order time derivative of displacement can be replaced by $\delta_t^2 = -\omega^2$ assuming time harmonic motion. The fourth order Laplacian ∇^4 can be replaced by $\nabla^4 = (k_x^2 + k_y^2)^2$ assuming the displacement is space harmonic. The bending stiffness is the product of elastic modulus, E , and area moment of inertia, I :

$$B = EI \quad (4.42)$$

The area moment of inertia of a flat plate about its neutral axis is:

$$I = \frac{h^3}{12} \quad (4.43)$$

where h is the plate's thickness. The bending stiffness is then given by:

$$B = \frac{E}{(1 - \nu^2)} \frac{h^3}{12} \quad (4.44)$$

where ν is the Poisson ratio of the material. For a plate immersed in a fluid, displacement along the plate is proportional to the pressure difference across the plate, $p_0 - p_1$.

$$\left(B_p (k_x^2 + k_y^2)^2 - \omega^2 m_p \right) \frac{v_z}{i\omega} = p_0 - p_1 \quad (4.45)$$

Here normal displacement from Equation (4.41) was replaced by normal velocity, v_z , assuming time-harmonic displacement, $w = W e^{i\omega t}$. An important assumption in bending plate theory is that normal velocity is the same either side of the plate, $v_0 = v_1$. With this in mind, p_0 and v_0 can be expressed in terms of p_1 and v_1 , giving rise to a formulation compatible with the transfer matrix scheme.

$$\begin{bmatrix} p_0 \\ v_0 \end{bmatrix} = \begin{bmatrix} 1 & Z_p \\ 0 & 1 \end{bmatrix} \begin{bmatrix} p_1 \\ v_1 \end{bmatrix} \quad (4.46)$$

Z_p is known as the *plate or wall impedance*, being the ratio of pressure difference across the plate and velocity along the plate:

$$Z_p = \frac{(p_0 - p_1)}{v_z} = \left(B_p (k_x^2 + k_y^2)^2 - \omega^2 m_p \right) \quad (4.47)$$

Damping is introduced by a complex Young's modulus E_μ :

$$E_\mu = E(1 + j\mu) \quad (4.48)$$

Where μ is the dimensionless loss factor. Equation (4.45) can be rearranged in terms of velocity:

$$v_z = i\omega \frac{p_0 - p_1}{Z_p} \quad (4.49)$$

The poles in the velocity function, i.e. where plate impedance is zero, represent specific combinations where the plate is no obstacle to sound transmission; this happens when the trace wavenumber on the plate, $k_t = \sqrt{k_x^2 + k_y^2}$, matches the *bending wavenumber*, $k_B = \sqrt{\omega^4 \frac{m}{B}}$. This results in the so called *coincidence* or *critical frequency*, which only occurs at oblique incidence. At grazing incidence, $\theta = \frac{\pi}{2}$, the trace wavenumber is $k_t = k_0$, and the coincidence occurs at the lowest frequency:

$$f_c = \frac{c_0^2}{2\pi} \sqrt{\frac{m}{B}} \quad (4.50)$$

where c_0 is the speed of sound in the surrounding medium. For an incident plane wave in air, there is one such frequency for every angle of incidence. Below this frequency, the plate does not couple efficiently with air, and the response to an incident wave is dominated by mass; this sub-critical frequency behaviour is known as *mass law*. As long as the plate's thickness is smaller than 1/6 of the bending wavelength, this type of thin plate theory is considered adequate (Cremer et al. 2005).

4.3.2 Orthotropic plate model

Profiled plates were modelled as equivalent flat, orthotropic plates. Orthotropic materials are defined as having distinct properties in each orthogonal spatial dimension. This approach is compatible with the transfer matrix method, requiring only an adjustment to the plate impedance term Z_p in the 2 by 2 transfer matrix described in Section 4.1.7. Profiled panels,

for example periodically rib-stiffened plates, are an example of a transversely orthotropic structure, as their bending stiffness varies depending on the bending axis.

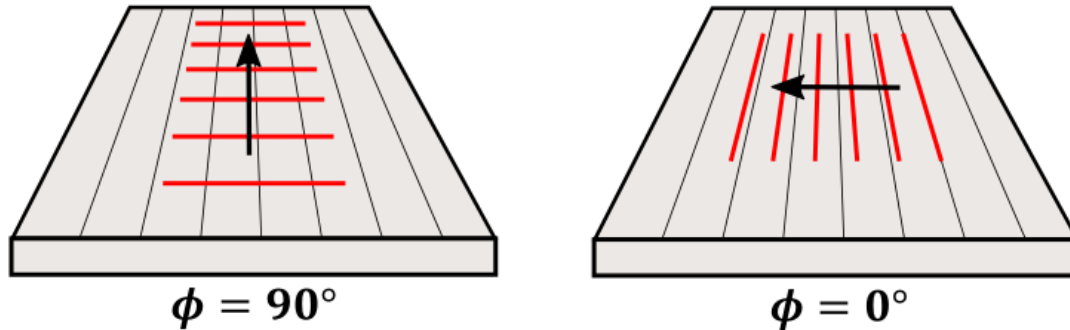


Figure 24: Incident wave orientation with respect to panel corrugations; the wave fronts on the surface of the plate are shown in red.

The first analysis that can be carried out is to determine the bending stiffness from the geometry. The bending stiffness of a structure about an axis is the product of the Young's modulus and area moment of inertia. For a flat, homogeneous, laterally infinite plate the area moment of inertia about the x and y axes is the same. For profiled plates, the area moment of inertia is different with respect to each axis. Transfer matrices for orthotropic plates are the same as for isotropic plates, except bending stiffness differs in each dimension, making the plate impedance, Z_p , vary with incident wave orientation:

$$Z_p = B_x k_x^4 + B_y k_y^4 + B_{xy} k_x^2 k_y^2 - \omega^2 m' \quad (4.51)$$

The mixed B_{xy} term is often approximated to $B_{xy} = \sqrt{B_x B_y}$. The mass per unit area m' requires adjusting based on the profile shape. A profiled plate is stiffest when bent in the direction parallel to its ribs or corrugations, $\phi = 90^\circ$ in Figure 24. It is then expected that such a plate would exhibit a lower critical frequency, as the bending wave speed c_B , will also be greater. Bending stiffness normal to the ribs is similar to the stiffness of the flat plate, meaning a second critical frequency is also expected closer to (but still lower than) the flat

plate critical frequency. In measurements of profiled panels of thicknesses close to 1 mm these features are difficult to identify, and numerous additional dips can be seen in the frequency response; this point will be examined in more detail in Chapter 6.

The following are the equations used to obtain the bending stiffness of trapezoidal and ribbed plates.

The bending stiffness of trapezoidal profiles, a diagram of which is shown in Figure 25, is found in (Bies et al. 1996). Their key dimensions are pitch (or period), crown, valley and depth.

$$B_x = \frac{Eh}{(1-\nu^2)} \sum_{i=1}^N b_i \left(z_i^2 + \frac{h^2 + b_i^2}{24} + \frac{h^2 - b_i^2}{24} \cos 2\theta_i \right)$$

$$B_y = \frac{Eh^3}{12(1-\nu^2)l} \sum_n b_n$$

$$B_{xy} \approx \sqrt{B_x B_y}$$

The neutral axis z_n can be obtained from the reference axis:

$$z_n = \frac{\sum_{i=1}^N x_i b_i h_i}{\sum_{i=1}^N b_i h_i}$$

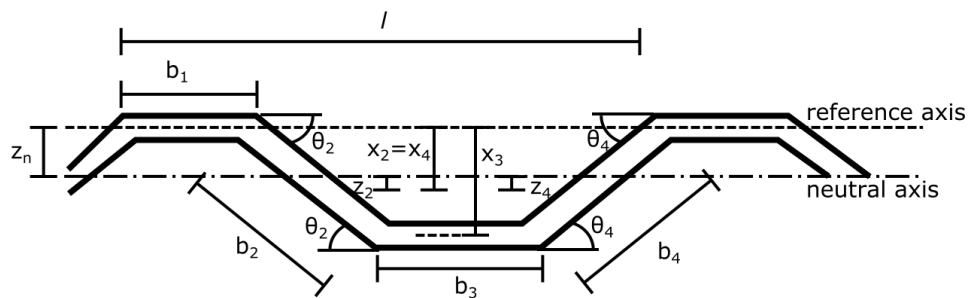


Figure 25: Trapezoidal plate geometry

The orthotropic stiffness of periodically ribbed plates can be found in (Cremer et al. 2005), and reproduced below, with reference to the diagram in Figure 26.

$$B_x = EI$$

$$I = \frac{a_a}{3} (s_1^2 - s_2^2) + \frac{a_R}{3} (s_2^2 + s_3^2)$$

$$s_1 = \frac{1}{2} \frac{a_a h_w^2 + (a_a - a_R) h^2}{a_a h_w + (a_a - a_R) h}, \quad s_2 = s_1 - h, \quad s_3 = h_w - s_1$$

$$B_y = \frac{E h^3}{12} \frac{a_a}{a_a - a_R \left(1 - \frac{h^3}{h_w^3}\right)}$$

$$B_{xy} \approx \frac{E}{3(1 + \mu)} \left(h^3 + \frac{h_w^3 a_R}{a_a} \right)$$

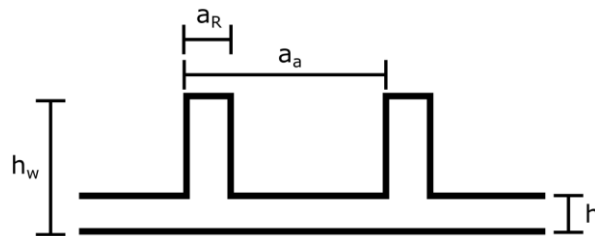


Figure 26: Ribbed plate dimensions; h_w is the total depth, a_R the rib width, a_a the pitch, and h the plate thickness

4.3.3 Conclusions

In this section, classical theory for modelling thin plates in bending was outlined. The equivalent orthotropic plate theory was also described, being required to model profiled plates within the TMM and analytical models presented in Chapter 5, and the orthotropic bending stiffness values for corrugated and ribbed plates were given.

4.4 RIBBED PLATE: PERIODIC MODEL

Corrugated panels can be thought of as periodically stiffened plates, where the ridges in the profile act as stiffening elements. This is particularly the case for standing seam profiles, described in Table 1. In the following section, an analytical model of an infinite, periodically ribbed plate is derived, following the method and notation produced by Smirnov (2015), included in full in Appendix B, a classical approach using Fourier series to represent Floquet periodic fields. These decompositions are known as space-harmonics. In this approach, the orthogonality of the Fourier basis functions is exploited to solve the system harmonic by harmonic in relatively few steps, in contrast to other established models by Mace (1980) and Mead (1978), which make use of Fourier transforms. The outputs of this model are the transmitted and reflected plane wave coefficients, which can be easily manipulated to obtain effective fluid properties and arrange the ribbed plates into layers.

4.4.1 Floquet periodicity and pressure fields

Before moving to the system equations for a periodically ribbed plate, the technique used to model a geometrically periodic system excited by plane waves will be outlined.

When a system is periodic in x and y with periods L_x and L_y , and excited by a wave of x and y wavenumber components of k_{x_0} and k_{y_0} ; the solution and all fields must satisfy the Floquet principle, so that any field f is periodic, in x and y , down to a phase shift $e^{i(k_{x_0}x+k_{y_0}y)}$ introduced by the excitation:

$$f(x + mL_x, y + nL_y) = e^{i(k_{x_0}mL_x+k_{y_0}nL_y)}f(x, y) \quad (4.52)$$

In all following derivations, harmonic time dependence $e^{-i\omega t}$ is assumed for all fields, so that solutions are presented in the frequency domain. Any Floquet periodic three-dimensional pressure field $p(x, y, z)$ in a fluid medium can be written in terms of a Fourier series with unknown coefficients A_{mn} to represent the component that is periodic in L_x and L_y , multiplied by the phase offset term $e^{i(k_{x_0}x+k_{y_0}y)}$:

$$\begin{aligned} p(x, y, z) &= e^{i(k_{x_0}x+k_{y_0}y)} \sum_{m,n} A_{mn}(z) e^{i\left(\frac{2\pi m}{L_x}x+\frac{2\pi n}{L_y}y\right)} \\ &= \sum_{m,n} A_{mn}(z) \psi_{mn}(x, y) \end{aligned} \quad (4.53)$$

The exponential terms dependent on x and y have been lumped into the variable ψ_{mn} :

$$\psi_{mn} = e^{i(k_{x_0}x+k_{y_0}y)} e^{i\left(\frac{2\pi m}{L_x}x+\frac{2\pi n}{L_y}y\right)} = e^{i(k_{x_m}x+k_{y_n}y)} \quad (4.54)$$

where $k_{x_m} = k_{x_0} \pm \frac{2\pi m}{L_x}$ and $k_{y_n} = k_{y_0} \pm \frac{2\pi n}{L_y}$. ψ_{00} is the phase offset term $e^{i(k_{x_0}x+k_{y_0}y)}$.

The z dependence of A_{mn} is obtained by knowing that the field must satisfy the Helmholtz equation, (4.4):

$$(\nabla^2 + k^2) \sum_{m,n} A_{mn}(z) \psi_{mn}(x, y) = 0 \quad (4.55)$$

where k is the wavenumber in the medium. The Laplacian operator can be replaced with its Cartesian components $\delta_{x,y,z}$: $\nabla^2 = \delta_x^2 + \delta_y^2 + \delta_z^2$. The derivatives of ψ_{mn} with respect to x and y are known, given the periodicity of the pressure distribution, and are $\delta_x^2 \psi_{mn} = -k_{x_m}^2 \psi_{mn}$ and $\delta_y^2 \psi_{mn} = -k_{y_n}^2 \psi_{mn}$, leading to the following:

$$\left(-k_{x_m}^2 - k_{y_n}^2 + \delta_z^2 + k^2\right) \sum_{m,n} A_{mn}(z) \psi_{mn}(x, y) = 0 \quad (4.56)$$

The orthogonality of complex exponentials can be invoked to easily solve equations that contain these kinds of infinite series. Integrating the product of exponential functions $e^{\frac{i2\pi mx}{L_x}} e^{\frac{i2\pi py}{L_x}}$, where p is an integer, over their period L_x returns a value of 1 when $m = p$ and $n = q$, and zero everywhere else, as the functions are orthogonal:

$$\int_0^{L_x} e^{\frac{i2\pi mx}{L_x}} e^{\frac{i2\pi py}{L_x}} dx = \begin{cases} 1, & m = p \\ 0, & m \neq p \end{cases} \quad (4.57)$$

When an equation is composed of such series, then both sides of the equation can be multiplied by a function ψ_{pq} , with p and q being integers, and integrated over the unit cell so that the unknown coefficients can be solved for mode for mode. Applying this process to Equation (4.56) gives the values of A_{mn} for each mode combination of m and n :

$$\int_0^{L_x} \int_0^{L_y} \left(-k_{x_m}^2 - k_{y_n}^2 + \delta_z^2 + k^2\right) \sum_{m,n} A_{mn}(z) \psi_{mn}(x, y) \psi_{pq}(x, y) dx dy = 0 \quad (4.58)$$

$$\delta_z^2 A_{mn}(z) + k_{z_{mn}}^2 A_{mn}(z) = 0 \quad (4.59)$$

where $k_{z_{mn}}^2 = k^2 - k_{x_m}^2 - k_{y_n}^2$, and is the z component of wavenumber in the medium.

Equation (4.59) amounts to a one dimensional Helmholtz equation, the solution to which is:

$$A_{mn}(z) = A_{mn}^+ e^{-ik_{z_{mn}} z} + A_{mn}^- e^{ik_{z_{mn}} z} \quad (4.60)$$

A_{mn}^+ are the coefficients for the waves travelling in the positive z direction, while A_{mn}^- for waves in the negative direction. Substituting this solution back into Equation (4.53), the pressure field p is now represented in terms of forward and backward travelling waves:

$$p(x, y, z) = \sum_{mn} A_{mn}^+ e^{-ik_{zmn}z} \psi_{mn}(x, y) + \sum_{mn} A_{mn}^- e^{ik_{zmn}z} \psi_{mn}(x, y) \quad (4.61)$$

The A coefficients are constant in x , y and z .

This process will be applied to solve the system equations in the following section, as well as in Chapter 5 for periodic dual leaf structures.

4.4.2 Geometry and definitions

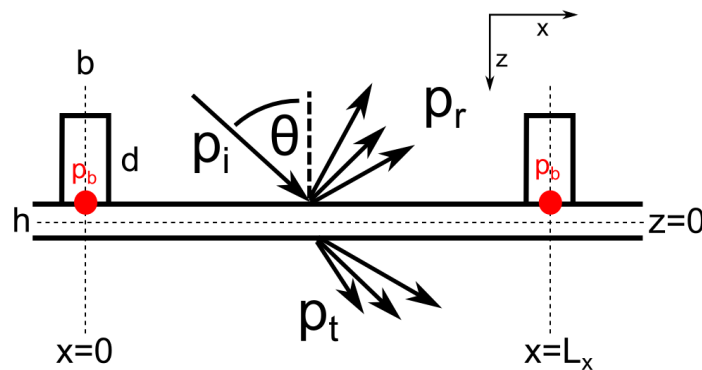


Figure 27: Periodically beam-stiffened plate geometry, showing incident, reflected and transmitted pressure wave vectors

The geometry of the beam stiffened plate is shown in Figure 27. The structure is periodic in x with period L_x . The top and the bottom of the plate are homogeneous fluids (in this case, both air), that obey the Helmholtz equation. The incident plane wave has a wavenumber $k_0 = \frac{\omega}{c_0}$, where c_0 is the speed of sound in air.

The pressure above the plate is the sum of incident and reflected (or scattered) pressure waves p_i and p_r . As the geometry is periodic, the fields are Floquet periodic and take the form shown in the previous section with summations over m and coefficients I_m and R_m :

$$p_{top} = p_i + p_r = \sum_m (I_m e^{ik_{z_0m}z} + R_m e^{-ik_{z_0m}z}) \psi_m \quad (4.62)$$

where $I_m = \begin{cases} 1 & \text{for } m = 0 \\ 0 & \text{for } m \neq 0 \end{cases}$ and $\psi_m = \psi_0 e^{\frac{i2\pi mx}{L_x}} = e^{i\left(\left(k_{x_0} + 2\frac{m\pi}{L_x}\right)x + k_{y_0}y\right)} = e^{i(k_{x_m}x + k_{y_0}y)}$

It is important to note that the wavenumber in the x direction, $k_{x_m} = k_{x_0} + 2\frac{m\pi}{L_x}$, is an infinite series of values, which also leads the z direction wavenumber in the surrounding fluid k_{z_0m} having an infinite number of terms, given the relations between wavenumber components to satisfy the Helmholtz equation: $k_{z_0m}^2 = k_0^2 - k_{x_m}^2 - k_y^2$.

The transmitted pressure is likewise a Fourier series, this time with a single term, as there are no waves travelling back towards the plate:

$$p_t = \sum_m T_m \psi_m \quad (4.63)$$

The normal velocities, which must be matched either side of the plate, are obtained by applying Euler's equation:

$$\Delta p = -\rho i \omega \vec{v} \quad (4.64)$$

To obtain the z direction velocity, v_z , the z component of the pressure gradient is used. At $z = 0$, the location of the plate, the z velocity is given by the pressure gradients immediately above and below the plate:

$$v_{z_{top}} = \sum_m \frac{1}{Z_m} (-I_m + R_m) \psi_m \quad (4.65)$$

$$v_{z_{bottom}} = \sum_m \frac{-T_m}{Z_m} \psi_m \quad (4.66)$$

Here the impedance term Z_m is introduced for simplicity:

$$Z_m = \frac{\rho_0 \omega}{k_{zm}} \quad (4.67)$$

4.4.3 The forced plate equation

The inhomogeneous, time-harmonic, bending wave equation for a plate, lying on the xy plane at $z = 0$, with an incident and transmitted sound pressure, p_i and p_t , and the pressure applied by a beam p_b is:

$$\begin{aligned} (B_p \nabla^4 - \omega^2 m_p) \frac{v_z(x, y, 0)}{i\omega} \\ = p_i(x, y, 0) + p_r(x, y, 0) - p_t(x, y, 0) - p_b(x, y, 0) \end{aligned} \quad (4.68)$$

Here m_p is the mass per unit area of the plate, B_p is the bending stiffness of the plate, given by its area moment of inertia I and Young's Modulus E :

$$B_p = EI \quad (4.69)$$

Given the known spatial distribution of velocity v_z being ψ_m , the spatial derivative ∇^4 term is given by:

$$\nabla^4 = k_{x_m}^4 + k_{y_0}^4 + 2k_{x_m}^2 k_{y_0}^2 \quad (4.70)$$

This value is replaced on the left hand side of Equation (4.68) (all terms are at $z = 0$):

$$\left[B_p \left(k_{x_m}^4 + k_{y_0}^4 + 2k_{x_m}^2 k_{y_0}^2 \right) - \omega^2 m_p \right] \frac{v_z}{i\omega} = p_i + p_r - p_t - p_b \quad (4.71)$$

For convenience, the term in square brackets on the left hand side of this equation is collected into a single term, the *plate impedance*, Z_{p_m} :

$$Z_{p_m} = \frac{\left[B_p \left(k_{x_m}^4 + k_{y_0}^4 + 2k_{x_m}^2 k_{y_0}^2 \right) - \omega^2 m_p \right]}{i\omega} \quad (4.72)$$

Replacing this term into Equation (4.71) results in more manageable notation:

$$Z_{p_m} v_z = p_i + p_r - p_t - p_b \quad (4.73)$$

This formulation neglects matching moments and angular velocity of the plate at the interfaces between the plate and the beams (Cremer et al. 2005).

The beam term p_b remains to be derived.

4.4.4 Beam forces

Reaction force due to a single beam at $x = 0$, which obeys the bending wave equation, is given by:

$$p_{b,1} = (B_b k_y^4 - \omega^2 m_b'') \frac{v_z(0, y)}{i\omega} \quad (4.74)$$

Where m_b'' is the mass per unit length of the beam, and B_b its bending stiffness.

The total force for a series of such beams $p_{b_{tot}}$ at intervals of L_x is given by the force for a single beam repeated at spatial offsets of L_x to infinity, i.e. multiplied by the Dirac comb function $\Pi\left(\frac{mx}{L_x}\right) = \sum_m \delta(x - mL_x)$, and multiplied by the phase offset determined by the incident wave $\psi_0 = e^{i(k_{x_0}x + k_{y_0}y)}$:

$$p_{b_{tot}} = \psi_0 \Pi\left(\frac{mx}{L_x}\right) p_{b,1} \quad (4.75)$$

Applying the Poisson summation formula, the Dirac comb function can be expressed as a Fourier series:

$$\Pi\left(\frac{mx}{L_x}\right) = \frac{1}{L_x} \sum_{m=-\infty}^{\infty} e^{\frac{i2\pi mx}{L_x}} \quad (4.76)$$

Replacing this equation into Equation (4.75) leads to the value of $p_{b_{tot}}$ in terms of the familiar Fourier expansion:

$$p_{b_{tot}} = \psi_0 \frac{p_{b,1}}{L_x} \sum_{m=-\infty}^{\infty} e^{\frac{i2\pi mx}{L_x}} = P_b \sum_m \psi_m(x) \quad (4.77)$$

where $P_b = \frac{p_{b,1}}{L_x}$ and $\psi_m = \psi_0 e^{\frac{i2\pi m}{L_x}x} = e^{i(k_{x_0}x + k_{y_0}y)} e^{\frac{i2\pi m}{L_x}x}$.

The value of the beam reaction pressure must exhibit Floquet periodicity, as every other field. This can be shown by verifying that $p_{b_{tot}}$ is periodic at intervals of L_x with a phase shift of $e^{ik_{x_0}x}$, i.e. that the following condition is met:

$$p_{b_{tot}}(x + m'L_x) = p_{b_{tot}}(x)e^{ik_{x_0}m'L_x} \quad (4.78)$$

where m' is an integer. The value of $p_{b_{tot}}(x + m'L_x)$ is:

$$\begin{aligned} p_{b_{tot}}(x + m'L_x) &= e^{ik_{x_0}(x+m'L_x)} \frac{p_{b,1}}{L_x} \sum_{m=-\infty}^{\infty} e^{\frac{i2\pi m(x+m'L_x)}{L_x}} \\ &= e^{ik_{x_0}x} e^{ik_{x_0}m'L_x} \frac{p_{b,1}}{L_x} \sum_{m=-\infty}^{\infty} e^{\frac{i2\pi mx}{L_x}} e^{i2\pi mm'} \end{aligned} \quad (4.79)$$

$e^{i2\pi mm'}$ is equal to 1, given that m and m' are integers, leading to:

$$p_{b_{tot}}(x + m'L_x) = e^{ik_{x_0}x} \frac{p_{b,1}}{L_x} \sum_{m=-\infty}^{\infty} e^{\frac{i2\pi mx}{L_x}} e^{ik_{x_0}m'L_x} \quad (4.80)$$

Since the value of $p_{b_{tot}}(x)$ is the following:

$$p_{b_{tot}}(x) = e^{ik_{x_0}x} \frac{p_{b,1}}{L_x} \sum_{m=-\infty}^{\infty} e^{\frac{i2\pi mx}{L_x}} \quad (4.81)$$

It follows that, by replacing this value into Equation (4.80):

$$\therefore p_{b_{tot}}(x + m'L_x) = p_{b_{tot}}(x)e^{ik_{x_0}m'L_x} \quad (4.82)$$

4.4.5 Transmission and Reflection coefficients

Finally, replacing (4.62), (4.63) and (4.77) into (4.73) gives the forced bending equation of the plate in terms of Fourier series:

$$\begin{aligned}
& \sum_m \frac{1}{Z_m} (-I_m + R_m) \psi_m Z_p \\
&= \sum_m (I_m + R_m) \psi_m - \sum_m T_m \psi_m \\
&\quad - P_b \sum_m \psi_m
\end{aligned} \tag{4.83}$$

Using the principle of orthogonality, multiplying both sides by ψ_p and integrating between 0 and L_x , results in a series of equations, one for each m , given that ψ_m and ψ_p are orthogonal to each other when $p \neq m$, resulting in $\int \psi_m \psi_p = 0$ for $p \neq m$, and $\int \psi_m \psi_p = 1$ for $p = m$:

$$0 = (Z_m + Z_p)I_m + (Z_m - Z_p)R_m - Z_m T_m - Z_m P_b \tag{4.84}$$

Matching z-velocity above and below the panel gives the following equation:

$$\begin{aligned}
v_{z_{top}} = v_{z_{bottom}} &= \sum_m \frac{1}{Z_m} (-I_m + R_m) \psi_m \\
&= \sum_m \frac{1}{Z_m} (-T_m) \psi_m
\end{aligned} \tag{4.85}$$

Again applying orthogonality, this equation can be broken down in to a series of equations:

$$T_m = I_m - R_m \tag{4.86}$$

The two equations, (4.84) and (4.86), are solved for R_m and T_m :

$$T_m = \frac{2Z_m I_m - Z_m P_b}{2Z_m - Z_p} \tag{4.87}$$

$$R_m = \frac{Z_m P_b - Z_p I_m}{2Z_m - Z_p} \quad (4.88)$$

P_b can be found by replacing the expression for normal velocity v_z into Equation (4.77):

$$v_z(0,0,0) = - \sum_m \frac{T_m}{Z_m} = - \sum_m \frac{1}{Z_m} \frac{2Z_m I_m - Z_m P_b}{2Z_m - Z_p} \quad (4.89)$$

$$\frac{B_b(k_y^4 - \omega^2 m_b/B_b)}{i\omega} \sum_m \frac{2I_m - P_b}{2Z_m - Z_p} = -P_b L_x \quad (4.90)$$

To simplify this equation, a *beam impedance* term Z_b is introduced:

$$Z_b = \frac{B_b(k_y^4 - \omega^2 m_b/B_b)}{i\omega} \quad (4.91)$$

Finally the P_b term, the contribution from the beam array, can be found:

$$P_b = \frac{\sum_m \frac{2I_m}{2Z_m - Z_p}}{\left(\sum_m \frac{1}{2Z_m - Z_p} - \frac{L_x}{Z_b} \right)} \quad (4.92)$$

Replacing this term into equations (4.87) and (4.88) yields the reflection and transmission coefficients, T_{mn} and R_{mn} , from which transmission loss and effective properties can be determined. Setting the P_b term to zero will yield the transmission through a flat plate. To obtain the far field wave amplitudes, modes m in which k_{z_m} is imaginary are neglected, as they represent evanescent waves.

The outputs of this model are shown in comparison to FEM simulations and the equivalent orthotropic plate formulation in Chapter 6.

4.4.6 Conclusions for ribbed plates

In this section, a periodic analytical model of a ribbed plate was classically derived, with notation and methodology provided by Smirnov (2015), a classical approach based on Fourier expansions. This model will be applied in Chapter 6, to understand the behaviour of profiled panels, and the limitations of the equivalent orthotropic plate representation.

4.5 CONCLUSIONS

In this chapter, the elements involved in modelling a full roof system or partition were described. All models assume a laterally infinite structure. The components of a roof system are: corrugated or flat metal sheets, high density boards such as plasterboard, structural framework such as point-to-point connections or supporting beams, and thermo-acoustic insulation, such as mineral or glass wool.

The transfer matrix method is used to model layered media; an approach by Brouard (1995) was used, which describes a method of coupling together layers of different material types: solid, fluid and porous. Because the model assumes that the system is laterally infinite, corrections are applied by weighting the incidence angle with a Gaussian distribution (H. Kang et al. 2000) that rolls off the contributions at more oblique incidence angles. Another correction is introduced to improve low frequency estimation of transmission loss by calculating the radiation efficiency over the finite area of the structure (Villot et al. 2001).

Thin plate theory is used to model metal sheets. Corrugated panels in this framework are treated as equivalent orthotropic plates. The orthotropic model is simple and can be included

in the TMM with minor adjustments; the limitations of this approach will be discussed in Chapter 6. A periodic analytical model of a ribbed plate was also developed, based on a classical approach, and will be used to evaluate the performance of the equivalent orthotropic plate.

In the next chapter, models of point-connected double plate structures are developed, and the integration of these with the TMM is described.

5 POINT-CONNECTED PLATE MODELS

In the following sections, an analytical model of two parallel plates connected by periodically spaced thin elastic rods is developed, and subsequently modified to include internal beams in the framework. This method forms the basis of the model used to calculate the transmission loss of dual leaf roof constructions with framework.

These periodic models are then combined with the Transfer Matrix Method in order to account for multiple layers of infill, by deriving the effective fluid properties of the cavity layers. The strengths and limitations of this approach are discussed.

5.1 POINT CONNECTED PLATES

5.1.1 Introduction

The following derivation was developed by Smirnov (Appendix B) and is based on classical theory for modelling geometrically periodic systems using Fourier series expansions. This method differs from existing approaches in that the orthogonality of pressure fields is exploited to solve the equations of motion of each system, as opposed to the Fourier transform approach found in Takahashi (1983) and Mace (1980).

In this section, an analytical model for double plates connected by rods is derived, as an approximation of a dual leaf roof system with point-to-point connectors. The rods will have a compressional stiffness which will allow modelling different connector designs.

The approach is here extended by including point-to-point connector stiffness, a distinct cavity fluid and plates, and orthotropic bending stiffness.

5.1.2 System description

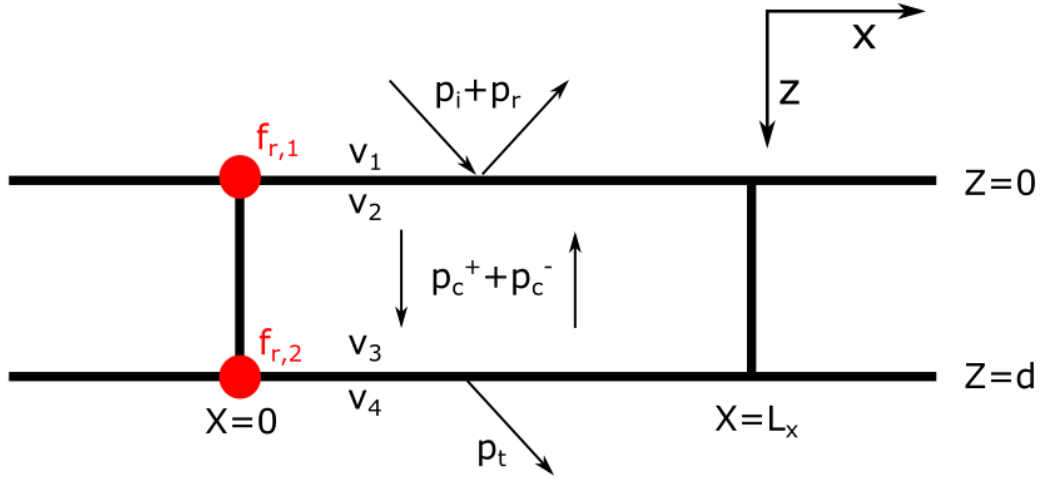


Figure 28: Double plate model diagram

The modelled structure consists of two parallel laterally infinite thin plates in the xy plane, at locations $z = 0$ and $z = d$, connected by periodically spaced thin rods in a rectangular grid, with spacing L_x and L_y (so that a unit cell is a rectangular section of lengths L_x and L_y), with semi-infinite layers of air (or a generic inviscid fluid) either side of the plates, and a fluid filling the cavity, of depth d , with a specified wavenumber and density. A diagram of the system is shown in Figure 28.

A plane wave is incident on the top plate, and is represented as a pressure field p_i of amplitude I :

$$p_i = I e^{-i(k_{x_0}x + k_{y_0}y + k_{z_0}z)} \quad (5.1)$$

Harmonic time dependence $e^{-i\omega t}$ is assumed; solutions are presented in the frequency domain.

The reader is referred to 4.4.1 for the Floquet principle, used as a basis for the following derivation.

5.1.3 Pressure in the fluid spaces

The total sound pressure everywhere above the top plate will be the sum of the incident field p_i and the scattered (or reflected) field p_r .

p_i is a Fourier series with all m and n harmonics equal to zero except for $m = 0$ and $n = 0$, where $I_{00} = 1$, so that it matches the defined incident wave:

$$p_i = \sum_{m,n} I_{mn} e^{ik_{z_0 mn} z} \psi_{mn} = I_{00} e^{i(k_{x_0} x + k_{y_0} y + k_{z_0} z)} \quad (5.2)$$

The total pressure in the top semi-infinite space is $p_{\text{top}} = p_i + p_r$

$$\begin{aligned} p_{\text{top}} &= p_i + p_r \\ &= \sum_{m,n} I_{mn} e^{-ik_{z_0 mn} z} \psi_{mn} \\ &\quad + \sum_{m,n} R_{mn} e^{ik_{z_0 mn} z} \psi_{mn} \end{aligned} \quad (5.3)$$

The coefficient R_{mn} is the complex amplitude of the reflected waves; the squared amplitude is the reflection coefficient.

The pressure in the cavity space p_c also consists of forward and backward travelling waves, with unknown coefficients A_{mn} and B_{mn} :

$$p_c = \sum_{mn} A_{mn} e^{-ik_{zc_{mn}}z} \psi_{mn} + \sum_{mn} B_{mn} e^{ik_{zc_{mn}}z} \psi_{mn} \quad (5.4)$$

where $k_{zc_{mn}}$ is the z direction wavenumber in the cavity space, given by:

$$k_{zc_{mn}} = \sqrt{k_c^2 - k_{x_m}^2 - k_{y_n}^2}$$

In the space below the bottom plate, from $z = -d$, the transmitted pressure field p_t only has one z wave direction (there are no reflections from $z = -\infty$):

$$p_t = \sum_{mn} T_{mn} e^{-ik_{z_0mn}(z-d)} \psi_{mn} \quad (5.5)$$

Here a phase shift of $k_{z_0}d$ has been introduced so that the value of the exponential function would be zero at $z = 0$, simplifying later operations. The value T_{mn} is the amplitude of the transmitted waves, the squared value of it being the transmission coefficient of each mode.

Velocities normal to the plates (i.e. the z components v_z) are found by way of Euler's equation:

$$v_z = \frac{i}{\omega\rho} \delta_z p \quad (5.6)$$

Following this equation, the normal velocity on the surface of the top plate, v_{z_1} , at $z = 0$, can be written in terms of the z gradient of the pressure above and below the plate, p_{top} and p_c :

$$\begin{aligned}
v_{z_1} &= \frac{i}{\omega\rho_0} \delta_z p_{top} \\
&= \frac{k_{z_0mn}}{\omega\rho_0} \sum_{mn} (I_{mn} e^{-ik_{z_0mn}^0} - R_{mn} e^{ik_{z_0mn}^0}) \psi_{mn} \\
&= \frac{k_{z_0mn}}{\omega\rho_0} \sum_{mn} (I_{mn} - R_{mn}) \psi_{mn}
\end{aligned} \tag{5.7}$$

$$v_{z_1} = \frac{i}{\omega\rho_0} \delta_z p_c = \frac{1}{\omega\rho_c} \sum_{mn} k_{z_cmn} (A_{mn} - B_{mn}) \psi_{mn} \tag{5.8}$$

The same process is applied to the normal velocity of the bottom plate, v_{z_2} :

$$v_{z_2} = \frac{i}{\omega\rho_c} \delta_z p_c = \frac{1}{\omega\rho_c} \sum_{mn} k_{z_cmn} \left(\frac{A_{mn}}{\xi_c} - B_{mn} \xi_c \right) \psi_{mn} \tag{5.9}$$

$$v_{z_2} = \frac{i}{\omega\rho_c} \delta_z p_t = \frac{1}{\omega\rho_0} \sum_{mn} k_{z_0mn} T_{mn} \psi_{mn} \tag{5.10}$$

The cavity phase term $\xi_{c_{mn}}$ is dependent on the cavity depth, and is given by:

$$\xi_{c_{mn}} = e^{ik_{z_cmn}d}$$

The velocities either side of each plate are then matched:

$$\begin{aligned}
&\frac{1}{\omega\rho_0} \sum_{mn} k_{z_0mn} (I_{mn} - R_{mn}) \psi_{mn} \\
&= \frac{1}{\omega\rho_c} \sum_{mn} k_{z_cmn} (A_{mn} - B_{mn}) \psi_{mn}
\end{aligned} \tag{5.11}$$

$$\sum_{mn} \frac{k_{z0mn}}{\omega\rho_0} \left(\frac{A_{mn}}{\xi_c} - B_{mn}\xi_c \right) \psi_{mn} = \sum_{mn} \frac{k_{z0mn}}{\omega\rho_0} T_{mn} \psi_{mn} \quad (5.12)$$

Using the principle of orthogonality by multiplying both sides of equations (5.11) and (5.12) by ψ_{pq} and integrating over the unit cell, the values of A_{mn} and B_{mn} in terms of I_{mn} , R_{mn} and T_{mn} are found:

$$A_{mn} = \frac{\xi_{c_{mn}}}{(1 - \xi_{c_{mn}}^2)} \frac{z_{c_{mn}}}{z_{0_{mn}}} (T_{mn} + R_{mn}\xi_{c_{mn}} - I_{mn}\xi_{c_{mn}}) \quad (5.13)$$

$$B_{mn} = (R_{mn} + T_{mn}\xi_{c_{mn}} - I_{mn}) \frac{z_{c_{mn}}}{z_{0_{mn}}} \frac{1}{(1 - \xi_{c_{mn}}^2)} \quad (5.14)$$

For simplicity, the term $\frac{k_{z0mn}}{\omega\rho_0}$ was replaced by $\frac{1}{z_{0mn}}$ and likewise $\frac{k_{zc_{mn}}}{\omega\rho_c}$ by $\frac{1}{z_{c_{mn}}}$. The zeroth terms z_{000} and z_{c00} are the characteristic impedances of the fluid media. These values will be used in the next section so that the equations of motion of the plates may be solved for R and T .

No forcing terms from the rods appear in these equations, as the assumption is that the rods in the cavity are sufficiently thin that they do not cause significant interference with the cavity pressure field. If the size of the connectors is of the order of the wavelength, then it would be necessary to account for reflections from the connectors themselves. For example, dual leaf systems with beams connecting both plates, commonly drywall partitions, would separate the cavity into smaller sections; the effect of these kinds of structures has been investigated by Brunskog and Xin & Lu (Brunskog 2005; Xin & Lu 2011).

5.1.4 Plate equations of motion

Both plates are represented physically as thin plates in bending. For this kind of plate, the assumption is that normal velocity is the same above and below the layer. This condition is used to determine the amplitudes of the scattered pressure.

The bending wave equation takes this form:

$$(B\nabla^4 - \omega^2 m') \frac{v_n}{i\omega} = f \quad (5.15)$$

where B is the bending stiffness per unit area, m' the mass per unit area, f is the forcing function per unit area. Forces f per unit area acting on the plate are the pressure fields either side of them, and the rods at periodic intervals.

The top plate is forced by the incident and reflected pressure on top, and the cavity forward and backward travelling pressure on the bottom, as well as the rod forces at L_x and L_y spacing.

$$(B_1\nabla^4 - \omega^2 m'_1) \frac{v_{z1}}{i\omega} = p_{top} - p_c - p_1 \quad (5.16)$$

$$(B_2\nabla^4 - \omega^2 m'_2) \frac{v_{z2}}{i\omega} = p_c - p_t - p_2 \quad (5.17)$$

p_1 and p_2 are the values of pressure contributed by the rods on the top and bottom plates, and will be derived in the next section; at this point all that can be said about these terms is that they also obey the Floquet principle, and can therefore be represented with the familiar Fourier expansions, with coefficients W_{1mn} and W_{2mn} :

$$p_{1,2} = \sum_{m,n} W_{1,2,mn} \psi_{mn} \quad (5.18)$$

By substituting pressures and velocities in Equation (5.16) with their respective Fourier series, we obtain the equation in terms of the unknown coefficients $A_{mn}, B_{mn}, R_{mn}, T_{mn}$ and the known properties of the materials, and the amplitude of the incident wave I_{mn} .

$$\begin{aligned} z_{B_1mn} \frac{k_{zc}}{\omega \rho_c} \sum_{mn} (A_{mn} - B_{mn}) \psi_{mn} \\ = \sum_{mn} I_{mn} e^{-ik_{z_0}z} \psi_{mn} + \sum_{mn} R_{mn} e^{ik_{z_0}z} \psi_{mn} \\ - \sum_{mn} A_{mn} e^{-ik_{z_0}z} \psi_{mn} - \sum_{mn} B_{mn} e^{ik_{z_0}z} \psi_{mn} \\ - \sum_{m,n} W_{1mn} \psi_{mn} \end{aligned} \quad (5.19)$$

where $z_{B_1mn} = \frac{(B_1(k_{x_m}^2 + k_{y_n}^2)^2 - \omega^2 m_1')}{i\omega}$, being the plate impedance; the differential operator ∇^4 applied to the quasi-periodic velocity field results in $\nabla^4 = (k_{x_m}^2 + k_{y_n}^2)^2$.

Both sides of the equation are multiplied by ψ_{pq} and integrated over the unit cell to solve for each mode individually:

$$\frac{z_{B_1mn}}{z_{c mn}} (A_{mn} - B_{mn}) = I_{mn} + R_{mn} - A_{mn} - B_{mn} - W_{1mn} \quad (5.20)$$

The same process is carried out for the bottom plate equation (5.17) resulting in:

$$\frac{z_{B2mn}}{z_{c mn}} \left(\frac{A_{mn}}{\xi_c} - B_{mn} \xi_c \right) = \frac{A_{mn}}{\xi_c} + B_{mn} \xi_c - T_{mn} - W_{2mn} \quad (5.21)$$

where $z_{B2mn} = \frac{(B_2(k_{x_m}^2 + k_{y_n}^2) - \omega^2 m_2')}{i\omega}$, being the impedance of the bottom plate, and $W_2 = \frac{f_2}{L_x L_y}$.

Combining equations (5.13), (5.14), (5.20) and (5.21) gives the values of the transmitted and reflected waves, T_{mn} and R_{mn} :

$$R_{mn} = \frac{(2Q_{2mn} + a_{mn})I_{mn} - Q_{2mn}W_{1mn} - b_{mn}W_{2mn}}{a} \quad (5.22)$$

$$T_{mn} = \frac{2b_{mn}I_{mn} - W_{1mn}b_{mn} + W_{2mn}Q_{1mn}}{a_{mn}} \quad (5.23)$$

The values of variables collected for simplicity are:

$$\begin{aligned} a_{mn} &= (b_{mn}^2 + Q_{1mn}Q_{2mn}) \\ b_{mn} &= 2 \left(\frac{z_{c mn}}{z_{0mn}} \frac{\xi_{c mn}}{(1 - \xi_{c mn}^2)} \right) \\ Q_{1mn} &= \left(\frac{\xi_{c mn}^2 + 1}{(1 - \xi_{c mn}^2)} \frac{z_{c mn}}{z_{0mn}} - \frac{z_{B1mn}}{z_{0mn}} - 1 \right) \\ Q_{2mn} &= \left(\frac{z_{B2mn}}{z_{0mn}} - \frac{z_{c mn}}{z_{0mn}} \frac{\xi_{c mn}^2 + 1}{(1 - \xi_{c mn}^2)} + 1 \right) \end{aligned}$$

Now that the R and T terms are known, the only unknown terms remaining are the rod pressure terms W_{1mn} and W_{2mn} which will be obtained in the next section.

5.1.5 Rod forces

The total reaction pressure on each plate due to the rods, can be expressed as a comb function applied to the reaction force of a single rod at coordinates $x=0$ and $y=0$ multiplied by the phase offset of the incident wave ψ_{00} to meet the Floquet condition; with f_1 and f_2 denoting respectively the forces at the top and bottom the rod, $p_{1,2}$,

$$p_{1,2} = \psi_{00} f_{1,2}(0,0) \sum_{m,n} \delta(x - mL_x, y - nL_y) \quad (5.24)$$

Using the Poisson sum formula, the comb functions that apply to the rod forces f_1 and f_2 can be written as Fourier series:

$$\sum_{m,n} \delta(x - mL_x, y - nL_y) = \frac{1}{L_x L_y} \sum_{m,n} e^{\frac{i2\pi m}{L_x} x} e^{\frac{i2\pi n}{L_y} y} \quad (5.25)$$

The total pressure contributed by the rods can then be equated to its Fourier expansion to reveal the value of $W_{1,2,mn}$:

$$\begin{aligned} p_{1,2} &= \psi_{00} f_{1,2} \frac{1}{L_x L_y} \sum_{m,n} e^{\frac{i2\pi m}{L_x} x} e^{\frac{i2\pi n}{L_y} y} = \frac{f_{1,2}}{L_x L_y} \sum_{m,n} \psi_{mn} \\ &= \sum_{m,n} W_{1,2,mn} \psi_{mn} \end{aligned} \quad (5.26)$$

Thus $W_{1,2,mn} = \frac{f_{1,2}}{L_x L_y}$; this means that the rod coefficients $W_{1,2}$ are independent of m and n .

Their values are obtained by determining the relationship between the forces f_1 and f_2 at the top and bottom of a single rod at location $x = 0$ and $y = 0$. Only longitudinal forces and velocities in the z direction were accounted for. A generic stiffness matrix K_{ij} was employed

to relate forces and velocities either side of the rod, so that values could be easily obtained with several methods, either by simulations, analytical models or measurements. This allows modelling different types of connectors.

$$\begin{bmatrix} W_1 \\ W_2 \end{bmatrix} = \frac{1}{i\omega L_x L_y} \begin{bmatrix} K_{11} & K_{12} \\ K_{21} & K_{22} \end{bmatrix} \times \begin{bmatrix} v_{z_1}(x=0, y=0) \\ -v_{z_2}(x=0, y=0) \end{bmatrix} \quad (5.27)$$

The top and bottom velocities v_1 and v_2 at $x=0$ and $y=0$ (the location of the rod within the unit cell) in terms of R_{mn} and T_{mn} , previously derived, are then substituted into this equation. It is possible to extend the matrix to include rotations too, by including additional forcing terms in the bending plate equations (5.16) and (5.17).

The value of ψ_{mn} at $x=0$ and $y=0$ is equal to 1, so the term does not appear:

$$v_{z_1}(0,0,0) = \sum_{m,n} \frac{1}{z_{0mn}} (I_{mn} - R_{mn}) \quad (5.28)$$

$$v_{z_2}(0,0,-d) = \sum_{mn} \frac{1}{z_{0mn}} T_{mn} \quad (5.29)$$

Substituting these values for the velocities yields:

$$\begin{bmatrix} W_1 \\ W_2 \end{bmatrix} = \frac{1}{i\omega L_x L_y} \begin{bmatrix} K_{11} & K_{12} \\ K_{21} & K_{22} \end{bmatrix} \times \begin{bmatrix} -2\beta_0 + f_2\gamma + f_1\beta \\ -2\gamma_0 + f_1\gamma - f_2\alpha \end{bmatrix} \quad (5.30)$$

The values of α , β and γ are shown below:

$$\alpha = \sum_{mn} \frac{Q_{1mn}}{a_{mn} z_{0mn}}$$

$$\beta = \sum_{mn} \frac{Q_{2mn}}{a_{mn}z_{0mn}}$$

$$\beta_0 = \frac{Q_{200}}{a_{00}z_{000}}$$

$$\gamma = \sum_{mn} \frac{b_{mn}}{a_{mn}z_{0mn}}$$

$$\gamma_0 = \frac{b_{00}}{a_{00}z_{000}}$$

Solving the matrix equation gives the values of the rod coefficients W_1 and W_2 in terms of all known variables:

$$W_1 = 2 \frac{q_5 q_1 - q_3 q_6}{q_1 q_2 - q_3 q_4} \quad (5.31)$$

$$W_2 = 2 \frac{q_6 q_2 + q_4 q_5}{q_1 q_2 - q_3 q_4} \quad (5.32)$$

where collected terms are:

$$q_1 = (i\omega L_x L_y + \alpha K_{22} - \gamma K_{21})$$

$$q_2 = (i\omega L_x L_y - \gamma K_{12} - \beta K_{11})$$

$$q_3 = (\gamma K_{11} - \alpha K_{12})$$

$$q_4 = (\beta K_{21} + \gamma K_{22})$$

$$q_5 = (-\beta_0 K_{11} - \gamma_0 K_{12})$$

$$q_6 = (\gamma_0 K_{22} + \beta_0 K_{21})$$

These are then substituted into the equations for R_{mn} and T_{mn} , (5.22) and (5.23), to complete the derivation. The process was carried out numerically, by calculating W_1 and W_2 separately, and using those values as inputs to equations (5.22) and (5.23).

5.1.6 Profiled panels

The orthotropic plate model is used to account for profiled panels, and all panel geometries (see Table 1) were approximated as an equivalent trapezoidal profile. As already outlined in Section 4.3.2, the impedance z_B of each plate changes with the trace wavenumber, which is different for each mode combination m and n , and bending stiffness varies with wave orientation, with values of B_x , B_y and B_{xy} :

$$z_{B_{mn}} = \frac{B_x k_{x_m}^4 + B_y k_{y_n}^4 + B_{xy} k_{x_m}^2 k_{y_n}^2 - \omega^2 m'}{i\omega} \quad (5.33)$$

Different panel orientations can be accounted for by switching the x and y bending stiffnesses, so that systems such as Spec. 4 and 5 (Section 2.4) can be modelled more accurately, given that the panels profiles are at 90 degrees to each other. Figure 29 shows a comparison of two panel orientations of a TMM modelled roof system with profiled metal sheets and mineral wool infill. When the panels are rotated, the TL is higher above 250 Hz, the lower critical frequency of the panels, by up to 20dB. In this arrangement, when the incident wave is oriented along the stiffest dimension of one panel, at the location of its lower critical frequency the second panel is more compliant, and exhibits mass-law behaviour, with a higher transmission loss. The minimum transmission loss is, as a result, overall greater at and above the lower critical frequencies, so that the average over all incidence angles is higher.

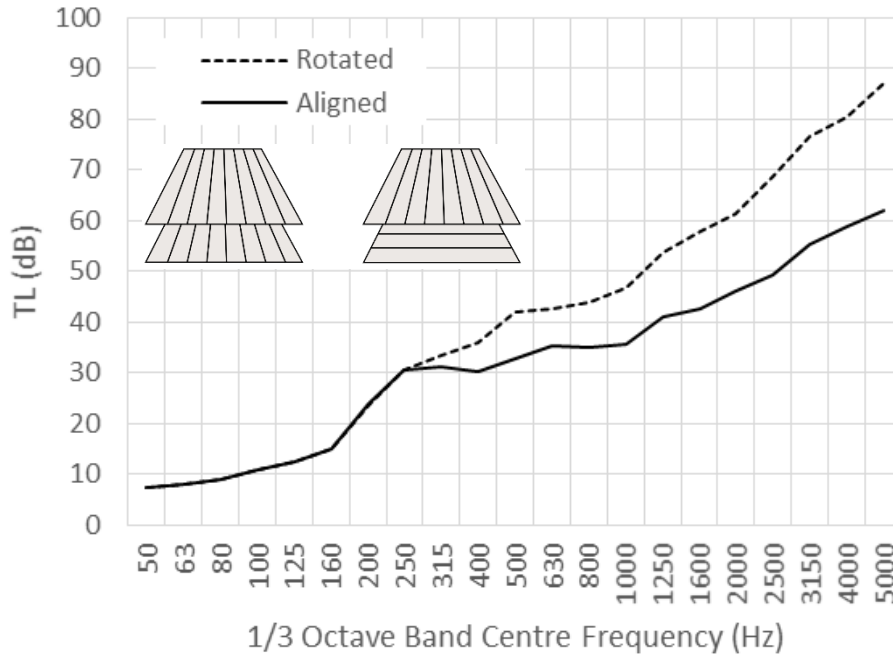


Figure 29: TMM modelled transmission loss of corrugated dual leaf structure with different panel orientations

5.1.7 Considerations on applicability and limitations

As the thickness of the plates is increased, the thin plate assumption that velocity is the same either side breaks down (as the thickness approaches around 1/6 of the bending wavelength). As most roof panels are in the region of 1 mm thick, this is not a significant issue in this work.

Another limitation is in the way the connectors are modelled. Only movements in the z direction are considered, and rotational stiffness of the connectors is neglected. In dual leaf roofs with halters, the fact that the connectors are inserted into the ridges of the top sheet means that moments may play a greater role. At the same time, the connector may not be tightly fastened in this arrangement, so that edge conditions are hard to define. Similarly, bar and bracket spacer kits are mounted in ways which would reduce stiffness, by screwing the top sheet to the bar at a distance from the bracket.

5.1.8 Conclusions

In this section, a classical analytical model based on Fourier expansions (Smirnov 2015) of periodically connected plates was derived and extended, as an approximation to a dual leaf structure with point-to-point connectors of arbitrary stiffness, with orthotropic plate properties. This model will be used to account for the common point-to-point connectors in roof systems, halters and brackets.

5.2 POINT CONNECTED PLATES WITH INTERMEDIATE BEAMS

To simulate spacer kits with top-hat purlins in roof systems (see Section 2.3 for a description), periodically spaced beams were introduced in the derivation in Section 5.1 by adding a periodic beam force and moment to the bottom plate equation, (5.17). The effect of the beam is a similar approach to Maxit (2008) combined with the ribbed plate model described in Section 4.4.

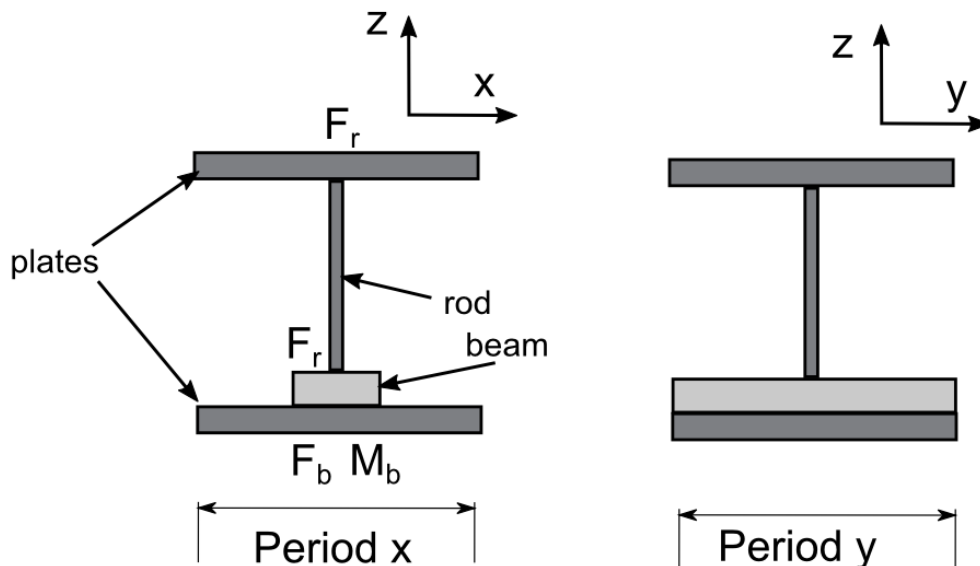


Figure 30: Point connected plates with intermediate beams

The modelled system is the same as the two plate system described in Section 5.1, with the addition of periodically spaced beams of width w and height h on the bottom plate, between the plate and the point-to-point connectors. A diagram is shown in Figure 30.

5.2.1 Beam equations

The forces f and M applied by the plate on a single beam at location $x = 0$, contributed by force and moment respectively, are shown below:

$$f_1 = \frac{(B\delta_y^4 - \omega^2 m'')}{i\omega} v_{z_2}(0, y) \quad (5.34)$$

$$M_1 = (GJ\delta_y^2\delta_x + \delta_x\omega^2\rho I_0) \frac{v_{z_2}(0, y)}{\omega} \quad (5.35)$$

where B is the bending stiffness, m'' is the mass per unit length, G is the shear modulus, J is the torsion constant, and I_0 is the polar moment of inertia of the beam.

The distribution of beam forces $f_{b_{tot}}$ is that of a single beam repeated in the x direction in intervals of L_x , as previously done for the rods (Section 5.1.5), with the appropriate phase offset $e^{ik_{x_0}x}$ to satisfy the Floquet condition:

$$f_{b_{tot}}(x, y) = e^{ik_{x_0}x} f_1(0, y) \sum_m \delta(x - mL_x) \quad (5.36)$$

The difference here is that the beams extend to infinity along y , so that no additional summations are introduced in the y direction. f_1 is dependent on y and includes the Floquet periodicity in the y direction of the velocity field. The velocity $v_{z_2}(0, y)$ is given by

$v_z(0, y) = \sum_{m,n} \frac{T_{mn}}{z_{0mn}} e^{ik_{y_0}y} e^{\frac{i2\pi ny}{L_y}}$. This value is replaced into Equation (5.36), and the fourth order derivative with respect to y can be replaced by $k_{y_n}^4$:

$$\begin{aligned} f_1 &= \frac{(B\delta_y^4 - \omega^2 m'')}{i\omega} v_{z_2}(0, y) \\ &= \sum_m \sum_n \frac{(Bk_{y_n}^4 - \omega^2 m'')}{i\omega} \frac{T_{mn}}{z_{0mn}} e^{\frac{i2\pi ny}{L_y}} e^{ik_{y_0}y} \end{aligned} \quad (5.37)$$

Substituting this value of f_1 into Equation (5.36) gives the total beam forces in terms of the velocity Fourier coefficients T_{mn} , and the term ψ_{00} appears by combining $e^{ik_{x_0}x}$ and $e^{ik_{y_0}y}$:

$$\begin{aligned} f_{b_{tot}}(x, y) &= e^{ik_{x_0}x} \sum_m \sum_n \frac{(Bk_{y_n}^4 - \omega^2 m'')}{i\omega} \frac{T_{mn}}{z_{0mn}} e^{\frac{i2\pi ny}{L_y}} e^{ik_{y_0}y} \sum_{m'} \delta(x - m'L_x) \\ &= \psi_{00} \sum_m \sum_n \frac{(Bk_{y_n}^4 - \omega^2 m'')}{i\omega} \frac{T_{mn}}{z_{0mn}} e^{\frac{i2\pi ny}{L_y}} \sum_{m'} \delta(x - m'L_x) \end{aligned} \quad (5.38)$$

Equating this to a Fourier series with unknown coefficients F_{mn} , for convenient handling of the system equations later, gives:

$$\begin{aligned}
\psi_{00} \sum_m \sum_n \frac{(Bk_{y_n}^4 - \omega^2 m'')}{i\omega} \frac{T_{mn}}{z_{0mn}} e^{\frac{i2\pi ny}{L_y}} \sum_{m'} \delta(x - m'L_x) \\
= \psi_{00} \sum_m \sum_n F_{mn} e^{\frac{i2\pi mx}{L_x}} e^{\frac{i2\pi ny}{L_y}}
\end{aligned} \tag{5.39}$$

A different set of integers m' is used for the series of Delta functions, as these are an additional infinite sum. Dropping the phase component ψ_{00} from both sides and multiplying both sides by $e^{-\frac{i2\pi py}{L_y}}$ and integrating between 0 and L_y allows separate equations for each mode n , via the usual orthogonality principle:

$$\begin{aligned}
\int_0^{L_y} \sum_m \sum_n \frac{(Bk_{y_n}^4 - \omega^2 m'')}{i\omega} \frac{T_{mn}}{z_{0mn}} e^{\frac{i2\pi ny}{L_y}} e^{-\frac{i2\pi py}{L_y}} \sum_{m'} \delta(x \\
- m'L_x) dy \\
= \int_0^{L_y} \sum_m \sum_n F_{mn} e^{\frac{i2\pi mx}{L_x}} e^{\frac{i2\pi ny}{L_y}} e^{-\frac{i2\pi py}{L_y}} dy
\end{aligned} \tag{5.40}$$

$$L_y \sum_m \frac{(Bk_{y_n}^4 - \omega^2 m'')}{i\omega} \frac{T_{mn}}{z_{0mn}} \sum_{m'} \delta(x - m'L_x) = L_y \sum_m F_{mn} e^{\frac{i2\pi mx}{L_x}} \tag{5.41}$$

Further multiplying both sides by $e^{-\frac{i2\pi qx}{L_x}}$ and integrating between 0 and L_x eliminates the series of Delta functions (L_y is dropped from both sides below):

$$\begin{aligned}
& \int_0^{L_x} \sum_m \frac{(Bk_{y_n}^4 - \omega^2 m'')}{i\omega} \frac{T_{mn}}{z_{0mn}} \sum_{m'} \delta(x - m'L_x) e^{-\frac{i2\pi qx}{L_x}} dx \\
& = \int_0^{L_x} \sum_m F_{mn} e^{\frac{i2\pi mx}{L_x}} e^{-\frac{i2\pi qx}{L_x}} dx
\end{aligned} \tag{5.42}$$

Integrating the left hand side yields the value of $e^{-\frac{i2\pi qx}{L_x}}$ at $x = 0$, which is 1, only when $m' = 0$, and 0 for all other values of m' . On the right hand side, the orthogonality of the exponential functions results in solutions for each mode m :

$$\sum_m \frac{(Bk_{y_n}^4 - \omega^2 m'')}{i\omega} \frac{T_{mn}}{z_{0mn}} = F_{mn} \tag{5.43}$$

The coefficients F_{mn} are thus only dependent on n :

$$\frac{B \left(k_{y_n}^4 - \frac{\omega^2 m''}{B} \right) \sum_m \frac{T_{mn}}{z_{0mn}}}{i\omega L_x} = F_n \tag{5.44}$$

The same process is applied to the moment term M ; the pressure contributed by the moment of all beams is that of a single beam at $x = 0$ multiplied by a comb function, and then equated to a Fourier series with coefficients M_{mn} :

$$\begin{aligned}
M_{b\text{tot}} = \frac{1}{\omega} \sum_{mn} & \left(GJk_y^2 k_{xm} \right. \\
& \left. + k_{xm} \omega^2 \rho I_0 \right) \frac{T_{mn}}{z_{0mn}} e^{\frac{i2\pi ny}{L_y}} e^{-\frac{i2\pi py}{L_y}} \sum_p \delta(x \\
& - pL_x) = \sum_{mn} M_{mn} \psi_{mn}
\end{aligned} \tag{5.45}$$

The derivatives with respect to x and y have been replaced by k_{xm} and k_{yn} . Both sides of the equation are multiplied by $e^{-\frac{i2\pi qx}{L_x}} e^{-\frac{i2\pi ry}{L_y}}$ and integrated over the unit cell:

$$\begin{aligned}
& \int_0^{L_x} \int_0^{L_y} \frac{1}{\omega} \sum_{mn} \left(GJk_y^2 k_{xm} \right. \\
& \left. + k_{xm} \omega^2 \rho I_0 \right) \frac{T_{mn}}{z_{0mn}} e^{\frac{i2\pi ny}{L_y}} \sum_p \delta(x \\
& - pL_x) e^{-\frac{i2\pi qx}{L_x}} e^{-\frac{i2\pi ry}{L_y}} dx dy \\
& = \int_0^{L_x} \int_0^{L_y} \sum_{mn} M_{mn} e^{\frac{i2\pi mx}{L_x}} e^{\frac{i2\pi ny}{L_y}} e^{-\frac{i2\pi qx}{L_x}} e^{-\frac{i2\pi ry}{L_y}} dx dy
\end{aligned} \tag{5.46}$$

The integration gives the values of the coefficient M_{mn} , which is once again constant in m :

$$\frac{\sum_m \left(GJk_y^2 k_{xm} + k_{xm} \omega^2 \rho I_0 \right) \frac{T_{mn}}{z_{0mn}}}{\omega L_x} = M_n \tag{5.47}$$

The combination of force and moment contributions can be grouped into a single coefficient G_n for simplicity:

$$G_n = M_n + F_n = \sum_m \frac{T_{mn}}{z_{0mn}} \frac{Y_{mn}}{L_x \omega} \quad (5.48)$$

where $Y_{mn} = GJk_{y_n}^2 k_{x_m} + k_{x_m} \omega^2 \rho I_0 - iB \left(k_{y_n}^4 - \frac{\omega^2 m''}{B} \right)$

The total reaction from the beams is now given, in terms of G_n :

$$f_{b_{tot}} + M_{b_{tot}} = \sum_{m,n} G_n \psi_{mn}$$

5.2.2 Forced plate equations

The forced bending wave equation for the bottom plate, Equation (5.17), is modified to add the pressure introduced by periodic beam forces and moments:

$$\begin{aligned} (B_2 \nabla^4 - \omega^2 m'_2) \frac{v_{z_2}}{i\omega} \\ = p^+ + p^- - p_t - p_{r_{tot}} + f_{b_{tot}} + M_{b_{tot}} \end{aligned} \quad (5.49)$$

As done previously, the terms in the two plate equations are replaced with Fourier series, including the derived beam series with coefficients G_n in Section 5.2.25.2.1. Again, exploiting orthogonality, each mode combination is solved for individually:

$$\frac{z_{B1mn}}{z_{c_{mn}}} (A_{mn} - B_{mn}) = I_{mn} + R_{mn} - A_{mn} - B_{mn} - W_1 \quad (5.50)$$

$$\frac{z_{B2mn}}{z_{c_{mn}}} \left(\frac{A_{mn}}{\xi_c} - B_{mn} \xi_c \right) = \frac{A_{mn}}{\xi_c} + B_{mn} \xi_c - T_{mn} - W_2 - G_n \quad (5.51)$$

The coefficients R_{mn} and T_{mn} are obtained by combining the above equations:

$$R_{mn} = \frac{(2Q_{2mn} + a_{mn})I_{mn} - Q_{2mn}W_1 - b_{mn}(W_2 + G_n)}{a_{mn}} \quad (5.52)$$

$$T_{mn} = \frac{2b_{mn}I_{mn} - bW_1 + Q_{1mn}(W_2 + G_n)}{a_{mn}} \quad (5.53)$$

5.2.3 Rod forces

Now that the expressions for R and T are known, the rod pressure terms W_1 and W_2 are still to be obtained. This can be done, as per Section 5.1.5, by replacing normal velocities v_z on the right hand side of Equation (5.27):

$$\begin{aligned} & \begin{bmatrix} W_1 \\ W_2 \end{bmatrix} \\ &= \frac{1}{i\omega L_x L_y} \begin{bmatrix} K_{11} & K_{12} \\ K_{21} & K_{22} \end{bmatrix} \begin{bmatrix} (-2\beta_0 + W_1\beta + W_2\gamma + 2\zeta_{20} - W_1\zeta_2 + W_2\epsilon_2) \\ (-2\gamma_0 + W_1\gamma - W_2\alpha - 2\zeta_{10} + W_1\zeta_1 - W_2\epsilon_1) \end{bmatrix} \end{aligned} \quad (5.54)$$

where terms were collected for simplicity:

$$\epsilon_1 = \sum_{mn} \frac{Q_{1mn}}{a_{mn}z_{0mn}} \frac{\alpha_{g_n}}{(1 - \alpha_{g_n})}$$

$$\zeta_1 = \sum_{mn} \frac{Q_{1mn}}{a_{mn}z_{0mn}} \frac{(\gamma_{g_n})}{(1 - \alpha_{g_n})}$$

$$\epsilon_2 = \sum_{mn} \frac{b_{mn}}{a_{mn}z_{0mn}} \frac{\alpha_{g_n}}{(1 - \alpha_{g_n})}$$

$$\zeta_2 = \sum_{mn} \frac{b_{mn}}{a_{mn}z_{0mn}} \frac{\gamma_{g_n}}{(1 - \alpha_{g_n})}$$

$$\gamma_{g_n} = \sum_m \frac{b_{mn}}{a_{mn}z_{0mn}} Y_{mn}$$

$$\alpha_{g_n} = \sum_m \frac{Q_{1mn}}{a_{mn}z_{0mn}} Y_{mn}$$

In this case, the values of W_1 and W_2 will also be dependent on the terms related to the beams:

$$W_1 = 2 \frac{\gamma_{20}\gamma_1 - \gamma_{40}\gamma_3}{\gamma_1\gamma_2 - \gamma_3\gamma_4} \quad (5.55)$$

$$W_2 = 2 \frac{\gamma_{20}\gamma_4 - \gamma_2\gamma_{40}}{\gamma_1\gamma_2 - \gamma_3\gamma_4} \quad (5.56)$$

where variables collected for simplicity are:

$$\gamma_1 = (\epsilon_1 K_{22} - \gamma K_{21} - \epsilon_2 K_{21} + \alpha K_{22} + i\omega L_x L_y)$$

$$\gamma_2 = (\beta K_{11} - \zeta_2 K_{11} + \gamma K_{12} + \zeta_1 K_{12} - i\omega L_x L_y)$$

$$\gamma_3 = (-\epsilon_2 K_{11} + \alpha K_{12} + \epsilon_1 K_{12} - \gamma K_{11})$$

$$\gamma_4 = (\beta K_{21} - \zeta_2 K_{21} + \gamma K_{22} + \zeta_1 K_{22})$$

$$\gamma_{20} = (\beta_0 K_{11} - \zeta_{20} K_{11} + \zeta_{10} K_{12} + \gamma_0 K_{12})$$

$$\gamma_{40} = (\beta_0 K_{21} - \zeta_{20} K_{21} + \gamma_0 K_{22} + \zeta_{10} K_{22})$$

The solved W_1 and W_2 terms can now be replaced into equations (5.52) and (5.53) to obtain the transmission and reflection coefficients.

5.2.4 Beam compressional stiffness

So far the beam has been modelled with the assumption that the velocity above and below it is the same, i.e. that it does not undergo compression. To account for beam compression, an additional longitudinal stiffness was introduced in series with the rod stiffness. For static stiffness, the values of the K matrix are the same, obtained as two series stiffnesses:

$$K_{ij} = \frac{k_1 k_2}{k_1 + k_2} \quad (5.57)$$

where k_1 and k_2 are the static compressional stiffness values of the rod and beam respectively. Waves travelling in the sections can also be accounted for by modelling both rod and beam as thin elastic rods, and obtaining the combined stiffness via transfer matrices.

The stiffness matrix for a series of rods is given by:

$$K = \begin{bmatrix} \frac{T_{22}}{T_{21}} & \frac{1}{T_{21}} \\ \frac{T_{11}T_{22}}{T_{21}} - T_{12} & \frac{T_{11}}{T_{21}} \end{bmatrix} \quad (5.58)$$

where T_{ij} values are the elements of the combined transfer matrix. For a single rod, the transfer matrix is given by:

$$T = \begin{bmatrix} \cos kl & iz \sin kl \\ \frac{i}{z} \sin kl & \cos kl \end{bmatrix} \quad (5.59)$$

where $k = \omega \sqrt{\frac{\rho}{E}}$ and $z = \sqrt{\rho E}$, with ρ being the density, E the Young's Modulus, and l is the length of the rod.

5.2.5 Considerations on applicability and limitations

The spaced beams are modelled in such a way that the bottom plate effectively acts as a ribbed panel, given that the beams are in continuous contact with the plate. The issue with this approach is that in roof structures with top hat purlin spacer kits, the top-hat beams are screwed to the liner sheets at regular or irregular intervals. If the beams are not in full contact along their length, their stiffening effect on the liner is reduced. In this situation, waves would travel along the beams and interact with the liner at the locations of the screws, which would act as line connections only where the bending wavelength is much greater than the spacing.

5.2.6 Conclusions

In this section, the sound transmission through two parallel plates connected periodically by rods has been derived using classical wave-based approach based on Fourier expansions, in order to model the behaviour of dual leaf roof structures with halters onto top-hat purlins, where point-to-point connectors are placed between the top sheet and a top-hat beam screwed to the bottom sheet.

5.3 MODEL OUTPUTS AND COMBINATION WITH THE TMM

In this section, the method of obtaining diffuse transmission loss from the outputs of the models described in this chapter is shown. As the models contain a single cavity fluid layer, the effective properties of multiple layers of insulation need to be derived using the TMM. The effective fluid approach is described with the relevant formulas, and complications

related to the propagation of multiple modes introduced by the periodic geometry are outlined. As often in roof structures high density boards are in contact with the corrugated metal sheets, the sandwich theory for obtaining the bending stiffness of multiple plates is described, and includes orthotropic stiffness. Transmission loss

The transmitted pressure field derived in all geometrically periodic derivations is an infinite sum of plane waves, over modes m and n :

$$p_t = \sum_{m,n} T_{mn} e^{-ik_{z0mn}(z-d)} \psi_{mn}(x, y)$$

Not all modes travel into the far field, however. Some represent evanescent waves, as the wavenumber in the z direction k_{zmn} for some modes is imaginary. This happens when the trace wavenumber $k_t = \sqrt{k_x^2 + k_y^2}$ is greater than the wavenumber in air, k_0 .

All modes interfere with each other to produce the total pressure, which does not converge in the far field. In order to get a measure of the total transmission loss, the energy in each mode is summed (and phase is discarded):

$$\tau_{tot} = \sum_{m,n} |T_{mn}|^2$$

This approach is a fair approximation of the transmission loss in an ideal diffuse field, in which energy from each wave adds incoherently. All modes in which k_{zmn} is imaginary are evanescent, and are thus removed from the summation above, as they do not travel into the far field.

As a low frequency approximation, one can consider only the zeroth mode T_{00} . An effective fluid can be then easily constructed, which would then allow modelling layered point

connected plate systems, if required. When including higher order modes, the transmission loss is much lower at high frequency as more transmitted energy is included. To obtain the diffuse field transmission coefficient τ_{diff} , a double integration of the transmission coefficient τ over angle of incidence θ and orientation ϕ must be carried out, with the integral in Equation (4.24). The convergence of the diffuse TL is discussed in Section 5.3.4.

Values of transmission loss are also averaged over third octave bands to compare the model output with available laboratory measurements of sound insulation.

5.3.1 Combination with the TMM via effective properties

To model roof systems (or dual leaf systems generally) with multiple infill materials within the point-connected plate framework, it becomes necessary to reduce the multilayer insulation to a single material with properties equivalent to the assembly. To do that, one needs to know the effective wavenumber k_c and characteristic impedance z_c of the multilayer system treated as a single fluid of thickness d . These properties can be obtained from the complex transmission and reflection coefficients (T and R), calculated with the TMM. The properties are obtained by reversing the equations for R and T for the transmission of sound through a single homogeneous fluid layer of thickness d with semi-infinite layers of air on either side. The formulation found in Fokin et al. (2007) is used to avoid the issue of picking a branch number when inverting a cosine function.

The refractive index n and the impedance ratio ξ , and consequently the wavenumber and impedance, are shown here in terms of R and T:

$$n = \frac{k_c}{k_0} = \frac{-i \log x + 2\pi m}{dk_0}, m \in \mathbb{Z} \quad (5.60)$$

$$\xi = \frac{z_c}{z_0} = \frac{r}{(1 - 2R + R^2 - T^2)} \quad (5.61)$$

where $r = \pm\sqrt{(R^2 - T^2 - 1)^2 - 4T^2}$ and $x = \frac{1 - R^2 + T^2 + r}{2T}$. The root of r is chosen so that the real part of the impedance ratio ξ is positive. The value of $\log x$ needs to be unwrapped numerically so that the correct branch numbers m are chosen, otherwise the wavenumber function will not be realistic and will have numerous discontinuities. This happens because several different wavenumbers can result in the same transmission and reflection coefficients at each frequency; the branch numbers m are chosen in order to make the index n a continuous function.

For multiple layers that include elastic solids and poroelastic materials as well as fluids, the values of k_c and z_c will have to be calculated for each angle of incidence θ_0 , as they would change as the trace wavenumber changes. Figure 31 shows the effective refractive index for layered systems with poroelastic materials at normal incidence (up to three layers).

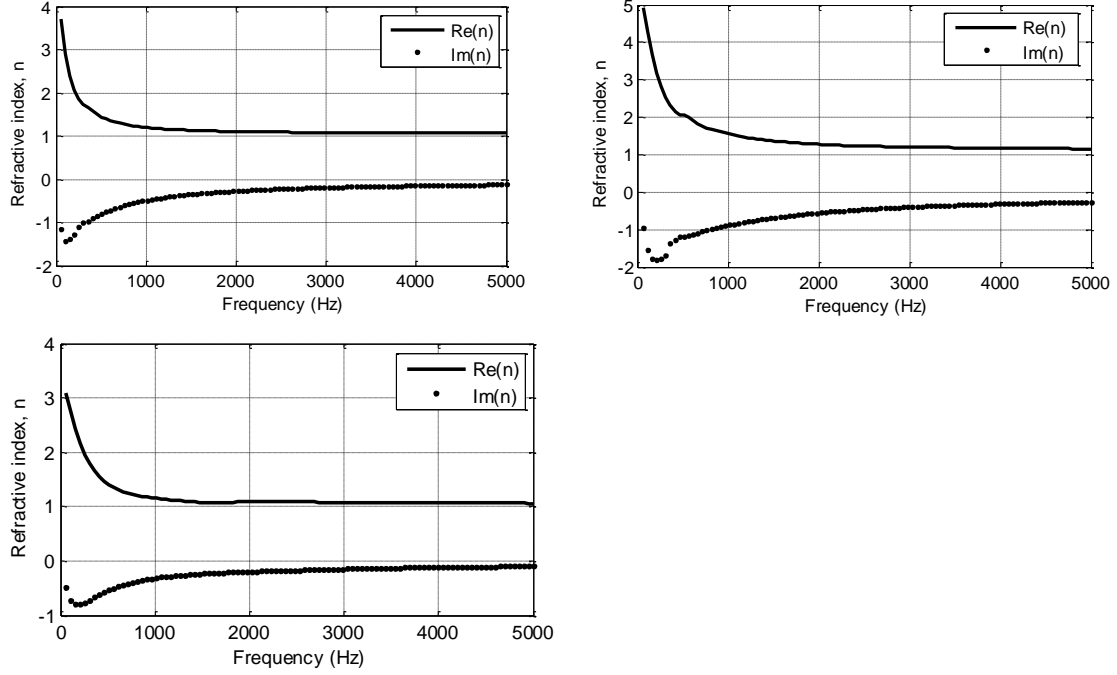


Figure 31: Refractive index obtained with the reverse method, for a single poroelastic layer (top left), two poroelastic layers of different properties (top right) and three layers, with an air gap between two poroelastic layers (bottom)

In the systems with Floquet periodicity described in this Chapter, each mode of the system has an associated trace wavenumber $k_{t_{mn}}$ for the same angle of incidence, which means that the equivalent fluid layer in the cavity space is excited at different trace wavelengths for the same, single incident wave. The cavity z direction wavenumber $k_{z_{c_{mn}}}$ is an infinite series of values dependent on m and n:

$$k_{z_{c_{mn}}} = \sqrt{k_c^2 - k_{x_m}^2 - k_{y_n}^2} \quad (5.62)$$

And since the effective wavenumber k_c obtained by reversing R and T is different for every input excitation trace wavenumber for a multilayer configuration or for a solid or poroelastic material, a transfer matrix calculation must be carried out for each mode combination, which is computationally expensive. However, at a first approximation, the effective properties for

the zeroth mode can be used, provided that the effective wavenumber does not vary sharply with angle of incidence. For layered mineral wool, even modelled using a poroelastic approach for common materials, the difference between the effective wavenumber obtained over all trace wavenumbers up to k_0 was minimal, indicating that obtaining the properties for the zeroth modes could be sufficient. The same cannot be said, however, for solid materials, meaning that for increased accuracy it is necessary to run a TMM model for all mode combinations, which is computationally taxing, increasing the number of operations by a factor of 10^4 (allowing for m and n values between -50 and +50).

Additionally, the trace wavenumber for the series of modes, which includes the terms $\frac{2\pi m}{L_x}$ and $\frac{2\pi n}{L_y}$, will often become larger than the wavenumber in a given medium; in this case, the sign of the z direction wavenumber k_z , which is obtained via the square root as per Equation (5.62), must be chosen in order to ensure that the wave is exponentially decaying (evanescent), rather than exponentially increasing. Specifically this applies to the phase term for the cavity layers $\xi_{c_{mn}}$, which must be exponentially decaying if $k_{z_{c_{mn}}}$ is imaginary:

$$\xi_{c_{mn}} = e^{i(k_{z_{c_{mn}}} d)}.$$

5.3.2 Combining plates

As outlined in Chapter 2, in many modern cladding constructions the profiled metal panels may be backed by one or more layers of plasterboard, and/or acoustic matting. A schematic representation of this kind of system is shown in Figure 32. A method of accounting for multiple solid layers either side of the cavity is required to reduce multiple plates to a single plate, so that the point-connected plate approaches may be used to predict transmission through such structures. If point connections are neglected, the TMM is capable of modelling

sandwich structures. The approach adopted here is to obtain the bending stiffness of the combined plates, which is then to be used in the plate impedance terms in the derivation.

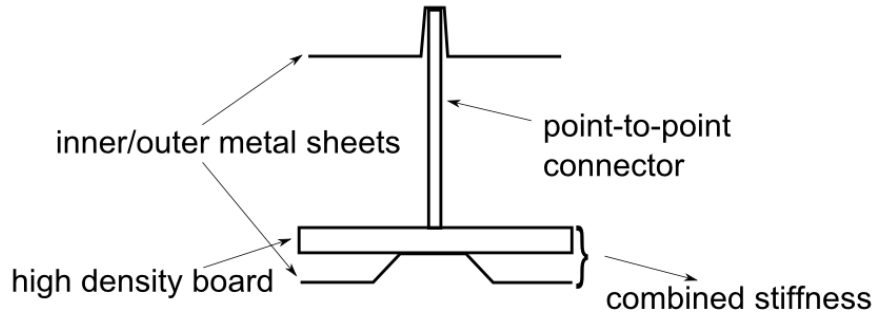


Figure 32: Diagram of roof structure with high density board

The combined bending stiffness of multiple joined sheets can be obtained by a simple equivalent area moment of inertia, by obtaining the neutral axis, and working out the total area moment of inertia. The combined stiffness per unit area B for a number n of plates in contact, of thicknesses h_n , as shown in Figure 33 for two plates, is:

$$B = \sum_n E_n I'_n \quad (5.63)$$

where E_n is Young's modulus of each plate, I'_n the area moments of inertia of each plate with respect to the global neutral axis, y . The area moment of inertia I' is found by applying the parallel axis theorem:

$$I' = I + Ay_n^2 \quad (5.64)$$

where A is the surface area of the plate, I is the area moment of inertia of the plate relative to its own neutral axis ($I = \frac{h^3}{12}$ for a flat plate of thickness h), and y_n is the distance between the

neutral axis of the plate and the neutral axis of the combined system. The neutral axis of the system y is given by imposing the following condition:

$$\sum_n E_n y_n = 0 \quad (5.65)$$

The distances y_n are now given in terms of y :

$$y = y'_n + y_n$$

Here y'_n is the location of the neutral axis of each plate with respect to the coordinate $z = 0$ of the global system, which is known based on the plate geometry. For two flat plates, three equations are produced to solve for y , y_1 and y_2 :

$$y = \frac{h_1}{2} + y_1$$

$$y = h_1 + \frac{h_2}{2} + y_2$$

$$E_1 y_1 + E_2 y_2 = 0$$

The neutral axis of this system is:

$$y = \frac{E_1 y'_1 + E_2 y'_2}{(E_1 + E_2)} \quad (5.66)$$

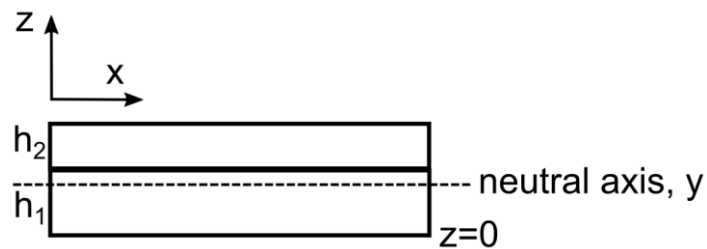


Figure 33: Two plates in contact, showing global neutral axis

The combined bending stiffness of two orthotropic plates is given here in terms of the area moment and Young's modulus of each plate:

$$B_x = \frac{E_1}{1 - \nu_1^2} (I_{x_1} + \alpha_1 h_1 (y - y'_1)^2) + \frac{E_2}{1 - \nu_2^2} (I_{x_2} + \alpha_2 h_2 (y - y'_2)^2) \quad (5.67)$$

$$B_y = \frac{E_1}{1 - \nu_1^2} (I_{y_1} + \alpha_1 h_1 (y - y'_1)^2) + \frac{E_2}{1 - \nu_2^2} (I_{y_2} + \alpha_2 h_2 (y - y'_2)^2) \quad (5.68)$$

where α is the ratio of surface area per unit width to plate thickness, which is equal to 1 for a flat plate, whereas for a trapezoidal profile plate it is:

$$\alpha = \frac{c + v + 2\sqrt{(p - c - v)^2 + d^2}}{p} \quad (5.69)$$

where p , c , v , and d are, respectively, the pitch, crown valley and depth of a corrugated plate.

There are several limitations to this approach. Firstly, shear deformations are not included. Thin plate theory also limits the thickness of the combined system to a fraction of the bending wavelength. For most existing roof systems this is acceptable, as the thickest panels tend to be plasterboard sheets which tend to be 15 mm or less, connected to steel sheets of around 1 mm thickness. The main issue in this case is in the characterisation of the panels as fully

bonded, which is unlikely to be the case. The more realistic option is that panels are fully connected only at the locations of screws, so that a fully bonded representation would only be valid at low frequencies, where the wavelength is much larger than the spacing between screws or other connection points.

5.3.3 Programming

A program was developed in Python, using the *numpy* library for calculations and the *PyQt4* library for the GUI. The program allows the user to choose layers in the system, specifying materials, thicknesses and profile dimensions, as well as details of point-to-point connections, and outputs transmission loss in third octave bands.

A flow diagram of the complete program is shown in Figure 35.

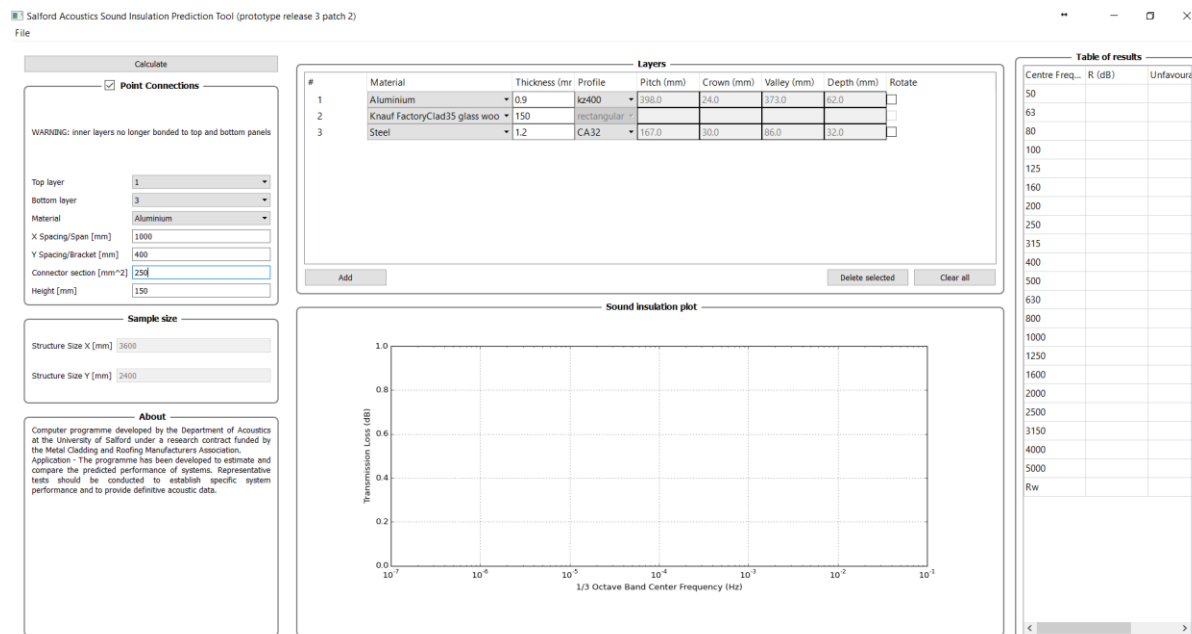


Figure 34: Sound reduction index modelling tool main window

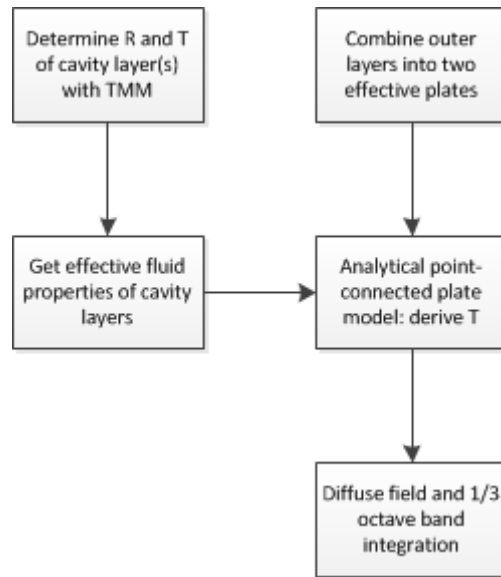


Figure 35: Flow diagram of calculation program

If point-to-point connections are disabled, the transmission loss through the layers is calculated using the TMM only, with corrections for sample size and laboratory diffusivity.

When point connections are enabled, the user must select on which layers the connections start and end, as well as the properties and spacing of the connectors (which are modelled as thin elastic rods); the inner cavity layers are modelled using the TMM, from which the equivalent fluid properties are obtained for each angle of incidence. Then, layers above and below the connectors are combined into two equivalent plates (if there is more than one plate either side), using sandwich theory (Section 5.3.2). Finally, the transmission loss is calculated with the analytical model in Section 5.1.

5.3.4 Convergence and truncation

Initially, the integration to obtain the diffuse field transmission coefficient, Equation (4.24), was carried out with a simple trapezoidal integration over both θ and ϕ at regularly spaced intervals, in a rectangular grid. If the angular resolution is too low, however, large fluctuations in transmission loss appear at high frequency, in particular above the critical

frequency of individual plates, where it is likely that the minima occur between chosen points and so are missed.

The Monte Carlo method was used to address this issue and enable convergence to be easily achieved. Pairs of values of θ and ϕ were picked randomly in the interval between 0 and $\pi/2$, with a Halton distribution, to ensure uniform sampling and avoid clustering. The transmission coefficient was obtained for each pair, $\tau_{\theta,\phi}$. The total transmission loss at each frequency f was then obtained by averaging over all pairs and multiplying by the integration area, $\frac{\pi^2}{4}$:

$$\begin{aligned}\tau_{diff}(f) &\approx \frac{\pi^2}{4} \frac{\sum_{\theta,\phi} \sin \theta \cos \phi \tau_{\theta,\phi}(f)}{N \int_0^{2\pi} \int_0^{\frac{\pi}{2}} \sin \theta \cos \theta d\theta d\phi} \\ &= \frac{\pi}{4} \frac{\sum_{\theta,\phi} \sin \theta \cos \phi \tau_{\theta,\phi}(f)}{N}\end{aligned}\tag{5.70}$$

where N is the number of θ, ϕ pairs. It is more useful, however, to carry out the averaging cumulatively with each iteration n :

$$\bar{\tau}_n = \frac{\left(\frac{\pi}{4} \sum_{\theta,\phi} \sin \theta \cos \theta \tau_{\theta,\phi} + n\bar{\tau}_{n-1}\right)}{n+1}\tag{5.71}$$

This approach is more convenient than regularly spaced values and trapezoidal integration: pairs can be added one at a time until convergence is achieved, and variance can be estimated with each additional pair.

The frequency values f were picked from an array of 120 logarithmically spaced values between 44.7 Hz and 5623 Hz, so that each octave band contained approximately the same number of frequency points.

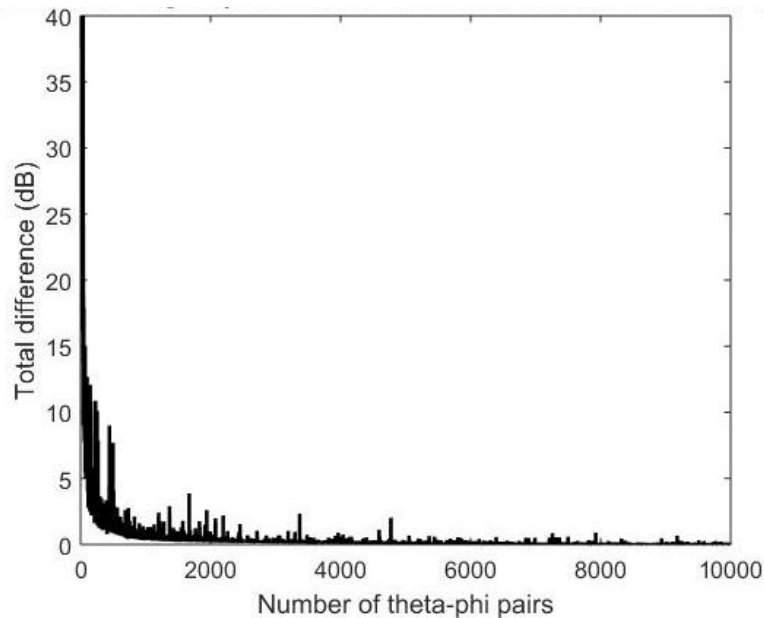


Figure 36: Sum across frequencies of difference between consecutive τ values with increasing number of θ, ϕ pairs

Convergence was defined as the point at which the error, the square root of the estimated variance calculated with each successive pair n , is within 0.1dB at each frequency. Figure 37 shows the required number of pairs N for convergence of the TL of a dual leaf corrugated roof structure with 145 mm cavity filled with mineral wool (modelled with poroelastic properties). An upper limit of 10000 pairs was chosen to reduce calculation time; this limit is reached typically above 300 Hz for a dual leaf structure with mineral wool infill, while the final estimated error values are still within 3dB at the highest frequencies, as can be seen in Figure 38, which shows the error margins in red for the calculated transmission loss. Figure 36 shows the total relative change in the diffuse transmission loss value (across all frequency bins) in dB as more theta-phi pairs are added.

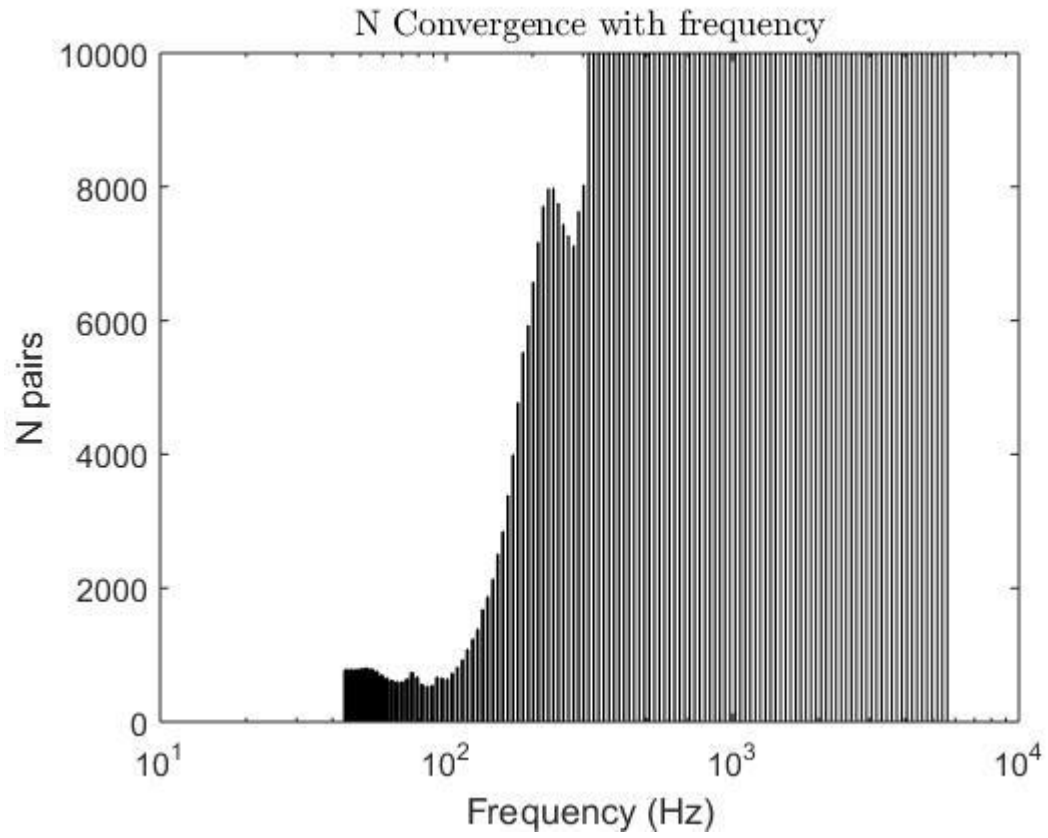


Figure 37: Number of θ, ϕ pairs required for convergence for each frequency bin ($\sqrt{\text{Var}(\tau)} < 0.1\text{dB}$)

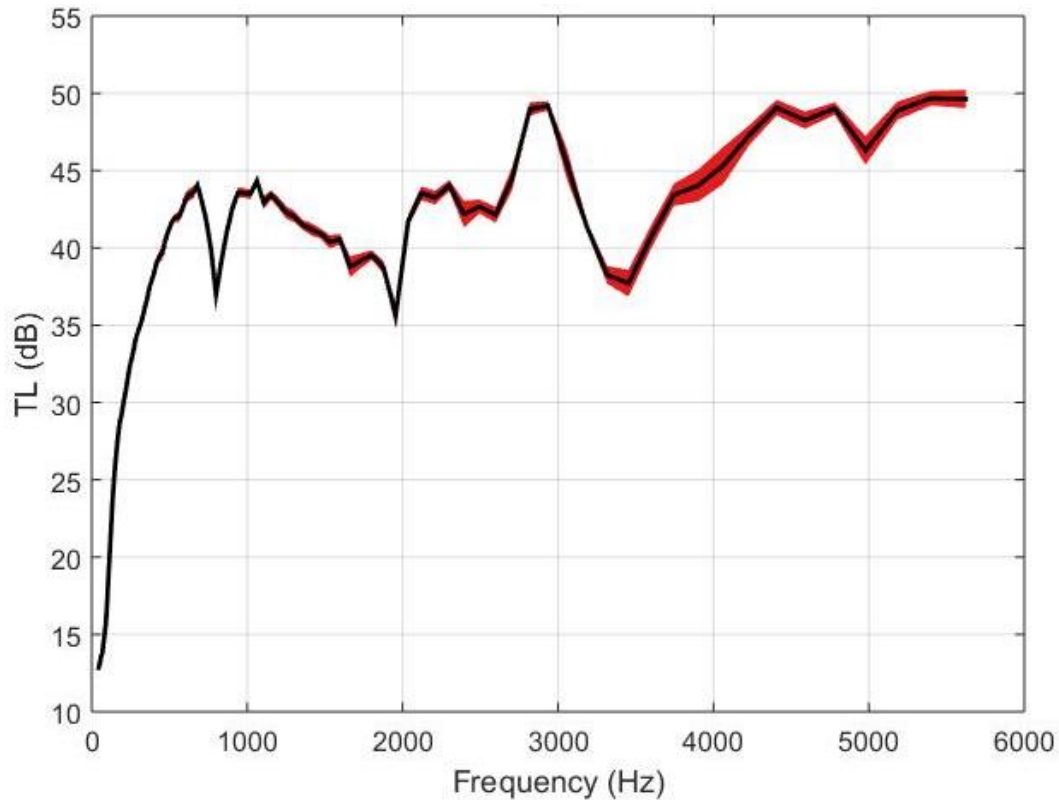


Figure 38: Transmission loss of dual leaf corrugated roof structure with connections spaced at 1m and 0.4 m, showing error margins in red

Refinements of the method would be to implement adaptive variance reduction to give greater weight to pick optimal distributions of θ and ϕ .

Further, the transmission loss in periodic models is dependent on the number of m and n modes included in the summations; it was therefore necessary to choose a practical truncation number based on convergence data. Figure 39 shows the relative change in transmission loss of a dual leaf corrugated roof system with point connections as the truncation number N is increased from 15 to 60 ($m = -N$ to $m = +N$, likewise for n), summed across all frequency bins between 44.7 Hz and 5623 Hz. A truncation number of $N=50$ was considered sufficient to capture the behaviour of a typical structure.

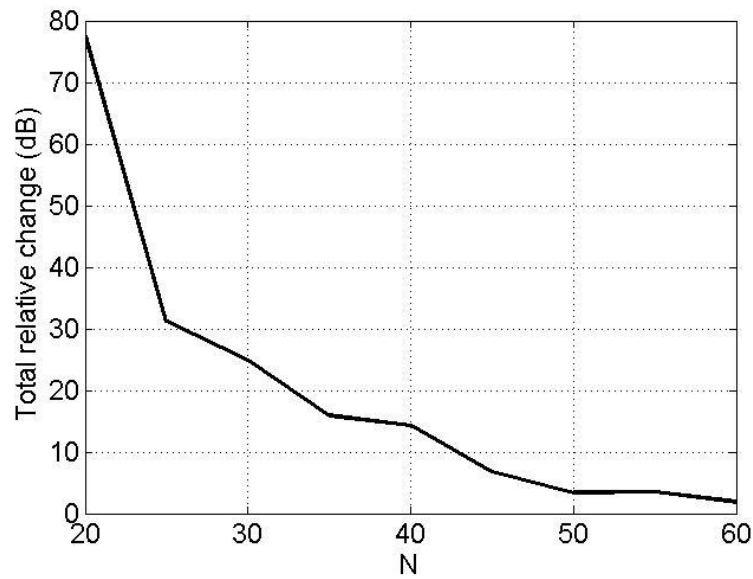


Figure 39: Change in TL summed over 120 frequency bins with increasing m and n truncation number N for dual leaf wall with mineral wool infill and point connections

5.4 CONCLUSIONS

In this chapter, two analytical models of parallel plates connected by periodically spaced point-to-point connectors were presented. The first derivation has two plates connected by simple rods of arbitrary compressional stiffness. The second derivation includes internal beams onto which the rods are mounted, in order to simulate spacer kits with halters onto top-hat purlins.

This method is what is primarily used to calculate the transmission loss of dual leaf roof constructions.

The process to combine the analytical models with the Transfer Matrix Method was described, and basic details of the software created for the purpose of modelling roof and partition systems were given. In order to account for multiple layers of infill between the two

plates, using equivalent fluid properties for the layer between the two leaves, and the strengths and limitations of this approach are discussed.

Convergence data was also shown for the Monte Carlo integration approach used in this work to evaluate the diffuse transmission loss.

The following chapters are presentations of results, validation and parametric studies based on the developed models.

Chapter 6 contains comparisons between the periodic ribbed plate model and FEM simulations carried out in Comsol, for the purpose of validation. The analytical model is compared to the equivalent orthotropic plate model in the same chapter, including diffuse field TL comparisons.

Chapter 7 deals with dual leaf systems; TMM models of simpler dual leaf structures are compared to laboratory measurements, then the periodic point-connected plate models are validated against FEM simulations, and finally laboratory measurements of various categories of corrugated roof structures are compared to the combined TMM and point-connection model.

6 RESULTS: PROFILED PLATES

This chapter is a presentation and discussion of comparisons between analytical models, numerical simulations and laboratory measurements of single profiled metal panels. This stage is necessary to understand the practical limitations of the equivalent orthotropic plate model described in Section 4.3.2. The strengths of this approach are its simplicity, computational efficiency and, most importantly, its direct compatibility with the TMM.

FEM analysis of periodic profiled plates, both ribbed and trapezoidal, was carried out in Comsol, by modelling a single unit cell and applying Floquet periodicity conditions at the boundaries. The FEM models were compared to equivalent orthotropic plates, and used to validate the periodically ribbed plate model developed in Section 4.4. The ribbed plate model is then used to compare the performance of the orthotropic plate in predicting diffuse transmission loss.

A number of diffuse field laboratory measurements of single profiled sheets were drawn from the available literature and measurements carried out at the University of Salford. Attention is also given to standing seam structures – cladding sheets with high depth and narrow crowns – which are compared with the ribbed plate and equivalent orthotropic plate models to evaluate their ability to capture its observed features.

6.1 RIBBED PANELS

Ribbed panels were used as an equivalent of a corrugated plate, as they are simpler to model and present similar features, having a similar geometry to standing seam profiles. The periodic model involves terms with infinite summations in determining the transmission loss; it is therefore not trivial to extract useful design parameters. The following comparisons have

shone a light on the limits of the equivalent orthotropic representation and illustrate some of the features introduced by the profile.

6.1.1 Ribbed panels as equivalent orthotropic plates

In this section, the analytical ribbed plate model is compared to an equivalent orthotropic plate model of four ribbed panels with different dimensions, shown in Table 5. The transmission loss of these panels was predicted using the periodic model described in Section 4.4, an equivalent orthotropic model based on calculating the area moment of inertia of the plate cross section, as per Section 4.3.2, and with FEM in Comsol (only for panel A and B). This, and further FEM simulations in are carried out over a frequency range between 50 and 2000 Hz. The meshes were tetrahedral, and the maximum mesh element size chosen was one fifth of the wavelength in air at the highest frequency, 0.0343 m.

The material properties chosen are those of aluminium, though the loss factor was set to 0.1, reducing resonant dips, making the response smoother.

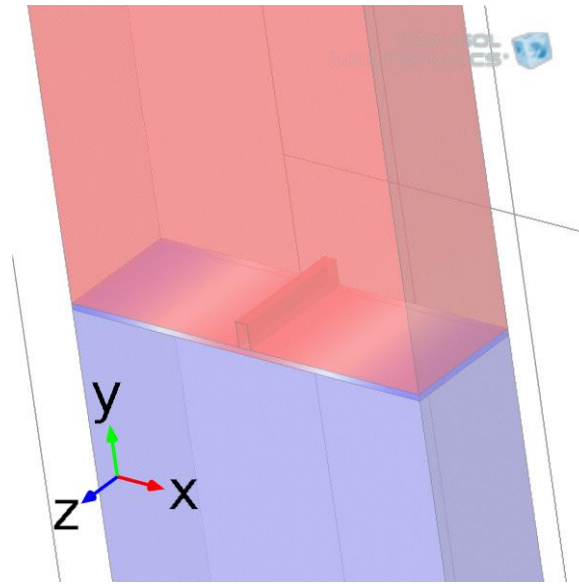


Figure 40: Ribbed plate geometry in Comsol

Dimensions in mm	Panel A	Panel B	Panel C	Panel D	
Pitch (p)	100	300	100	300	
Plate thickness (h)	5	5	1	1	
Rib width (b)	10	10	2	2	
Rib depth (d)	20	20	40	40	

Table 5: Dimensions of modelled ribbed panels A and B

6.1.1.1 Panel A and FEM validation

Panel A is 5 mm thick, and has large, closely spaced ribs at 100mm. This is considerably thicker than the plates found in any cladding construction, however, it has been included for

the purposes of numerical validation. This panel has been modelled in Comsol, and comparisons between the full analytical model and FEM, shown in Figure 42, are favourable, especially at low frequency. The evanescent modes of the analytical model have been included in this comparison, as the transmitted power in the FEM model was obtained on the surface of the plate. Convergence of the FEM model was achieved with 5 elements per wavelength at 2 kHz, with Figure showing the relative difference between 5 and 8 elements per wavelength lower than 0.1dB throughout the frequency range of interest, as shown in Figure 41.

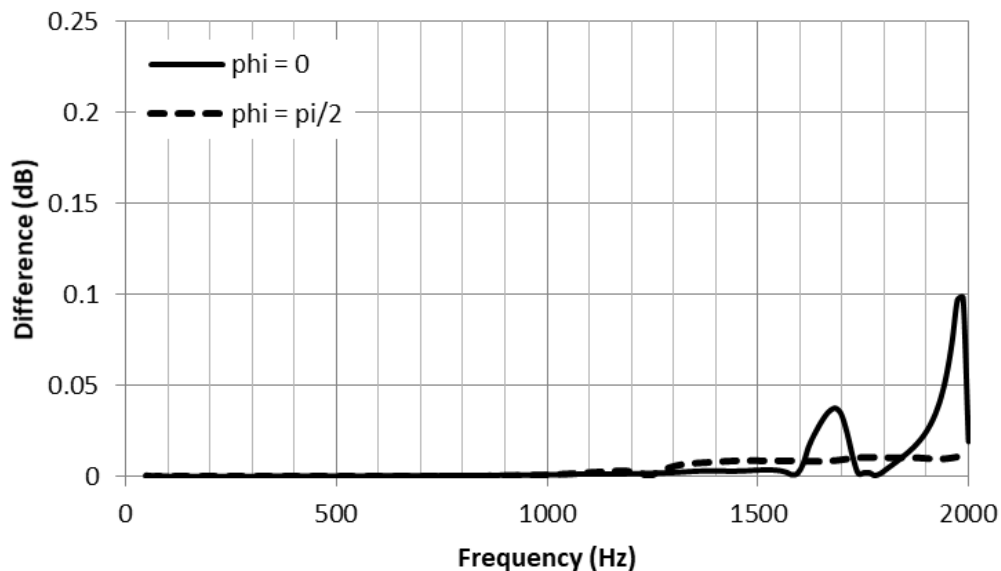


Figure 41: Relative difference in FEM modelled TL of panel A between 5 and 8 elements per wavelength at 2 kHz.

The analytical model excludes matching of in-plane and rotational velocity at the interface between the plate and its ribs, which explains the deviations from the FEM simulation. The equivalent orthotropic plate performs well when the wave orientation is $\phi = 0$, i.e. travelling in the direction perpendicular to the ribs, however it performs badly when the wave travels along the ribs, the stiffest direction, where it greatly underestimates the critical frequency dip

which, in reality, is approximately four times greater, suggesting the effective bending stiffness of a real ribbed plate is lower.

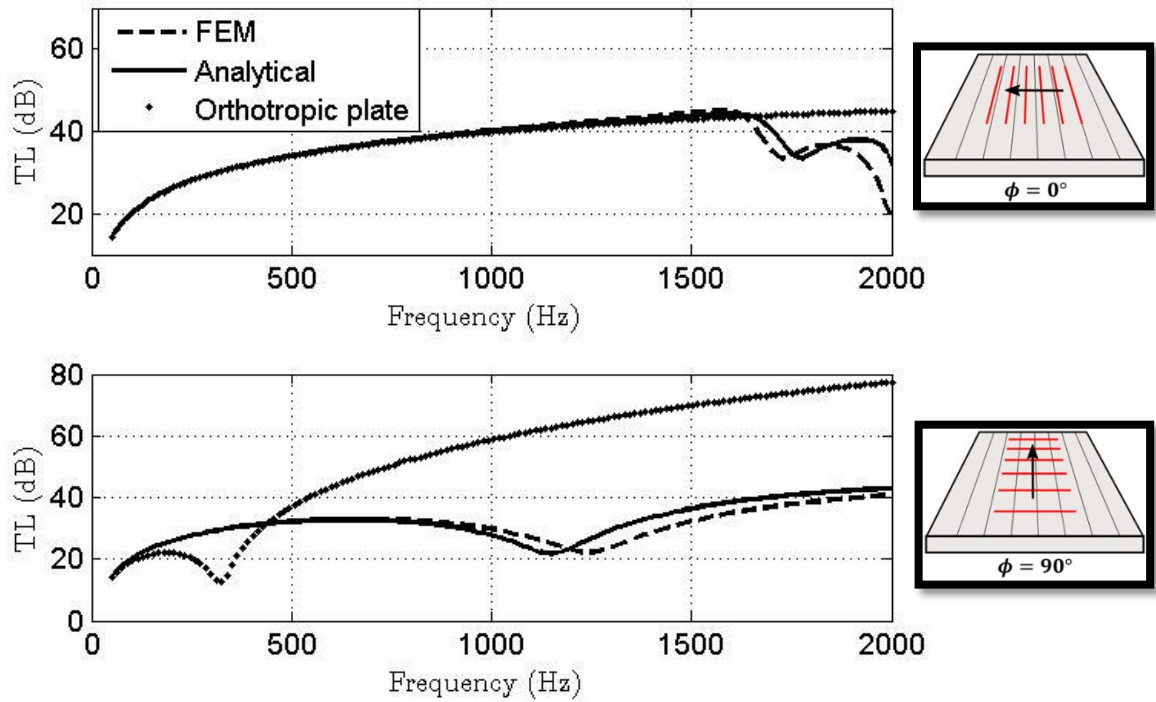


Figure 42: Transmission loss of panel A for incident angle $\theta = \frac{\pi}{4}$ and two wave orientations, $\phi = 0^\circ$ (top) and $\phi = 90^\circ$ (bottom), showing FEM, analytical and equivalent orthotropic results

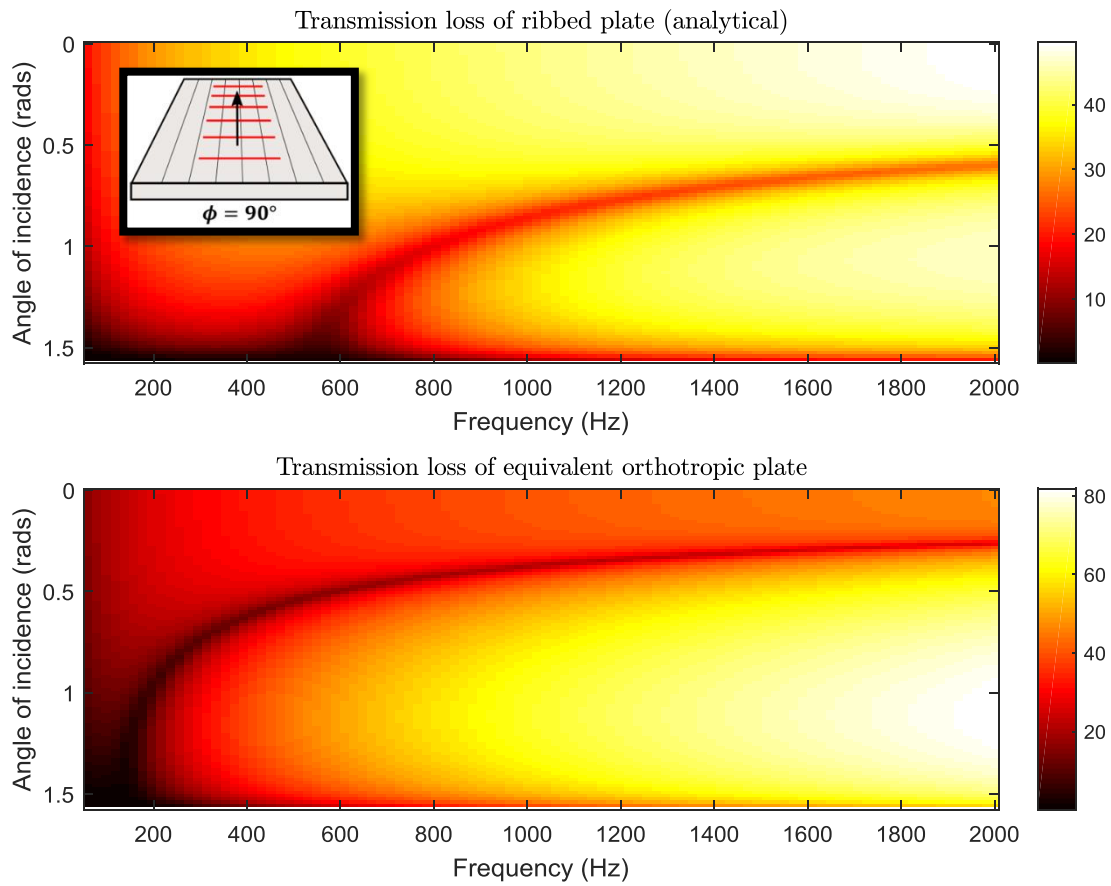


Figure 43: TL of panel A calculated with ribbed plate analytical model (top) compared to an equivalent orthotropic plate (bottom), showing all angles of incidence, with a wave oriented in the stiffest dimension

Figure 43 shows the TL variation with angle of incidence and frequency for a single wave orientation ($\phi = \frac{\pi}{2}$). The equivalent orthotropic plate and the ribbed plate both have similar features; the dark red areas represent high transmission, and the critical frequency can be seen forming an arc from grazing incidence, at 450 Hz for the ribbed plate, and below 200 Hz for the equivalent orthotropic plate. This means that the bending stiffness obtained with the equivalent orthotropic model appears to be much greater than the full analytical model predicts. The equivalent orthotropic model includes the added mass per unit area of the ribs, which is significant for this geometry, so that at low frequency, below 100 Hz, the curves are close. As can be seen in Figure 44, which shows the diffuse field transmission loss of both models, the results begin to diverge at 100 Hz, where the lower orthotropic plate critical

frequency dip is located. The main difference is caused by the underestimation of the lower critical frequency by the orthotropic plate. Both diffuse TL curves show a further dip at 3150 Hz, which is the critical frequency associated with incident wave along the most compliant direction, $\phi = 0^\circ$.

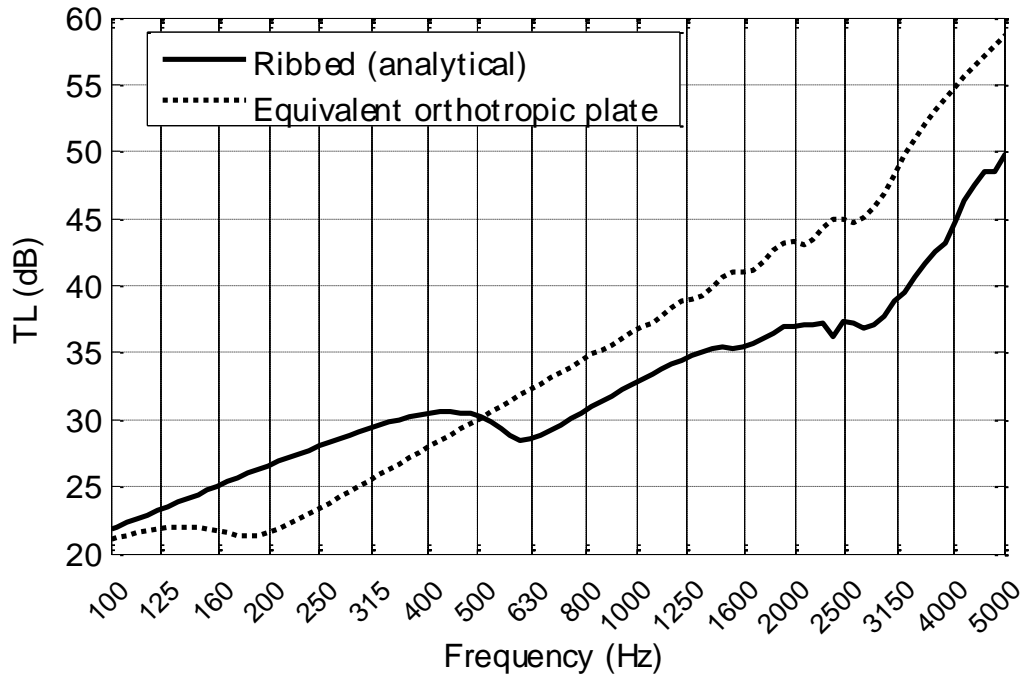


Figure 44: Comparison of diffuse field transmission loss of panel A for analytical ribbed plate model and equivalent orthotropic plate

6.1.1.2 Panel B

Panel B has a larger profile period L_x of 300 mm compared to panel A. In this case, the bending wavelength approaches the profile period at a lower frequency; a greater number of profile-related resonances are expected.

Figure 45 shows the TL at incidence $\theta = \frac{\pi}{4}$ for two wave orientations, $\phi = 0$ and $\phi = 90^\circ$. Along the least stiff dimension, where the bending stiffness does not differ much from a flat plate, the orthotropic model deviates little from the periodic model, with the latter showing

additional profile-related resonances. These were made more pronounced by reducing the loss factor of the material from 10^{-1} to a more realistic 10^{-4} for aluminium. Along the stiffer dimension, the orthotropic plate model does not adequately capture the physical behaviour. Figure 46, with the TL of both representations for all angles of incidence along the stiffest dimension, shows how the profile-related resonances for the analytical ribbed plate model vary sharply with angle of incidence and have their lowest frequency for a normal incidence excitation. Along with these, a critical frequency starting at 2.5 kHz, at grazing incidence, can be seen, and is close to that for a flat panel of the same material and thickness; in the orthotropic model TL, a much lower critical frequency of 100 Hz can be seen, and is the only identifiable feature in the plot. When obtaining the diffuse field transmission loss, both models identify the higher critical frequency at 2.5 kHz, however the orthotropic plate model underestimates transmission loss at the low end due to the additional critical frequency.

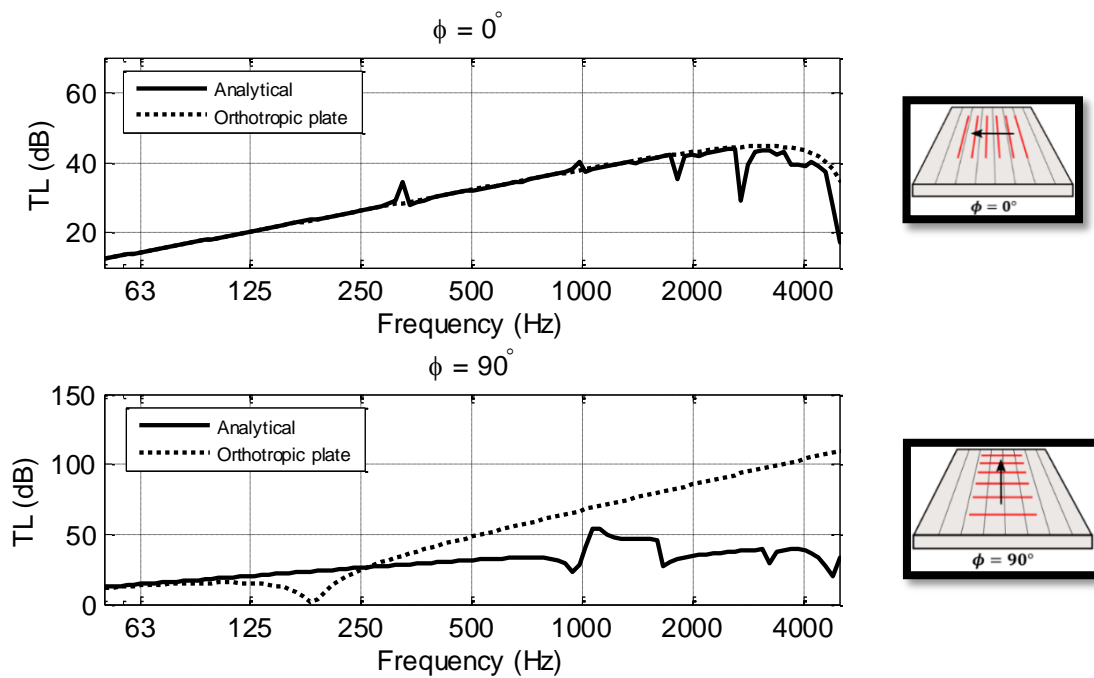


Figure 45: Transmission loss of panel B for incident angle $\theta = \frac{\pi}{4}$ and two wave orientations, $\phi = 0^\circ$ (top) and $\phi = 90^\circ$

(bottom), showing analytical and equivalent orthotropic results

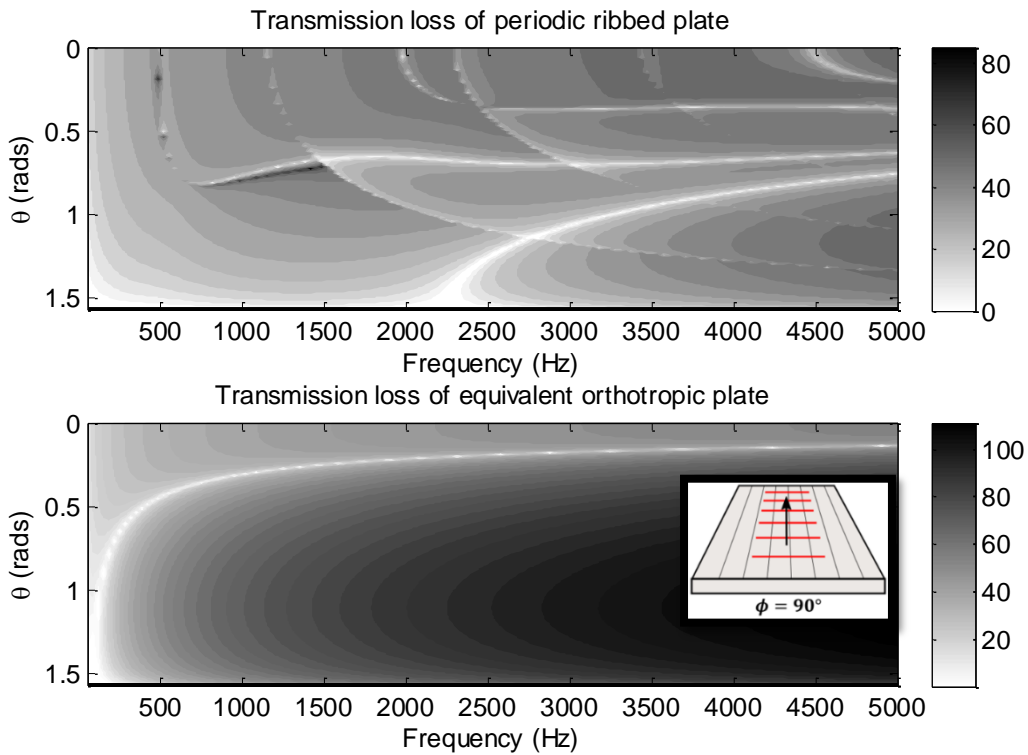


Figure 46: TL of panel B calculated with ribbed plate analytical model (top) compared to an equivalent orthotropic plate (bottom), showing all angles of incidence, with a wave oriented in the stiffest dimension

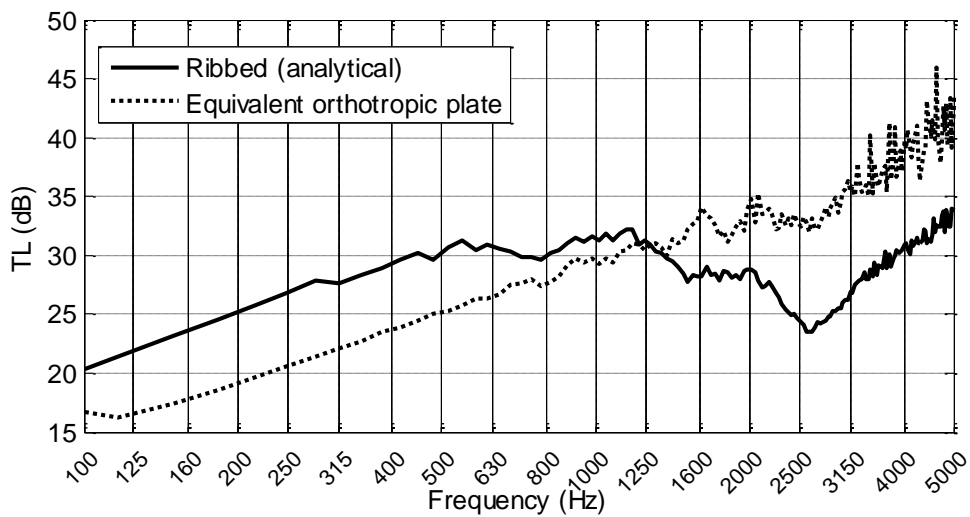


Figure 47: Comparison of diffuse transmission loss of panel B for analytical ribbed plate model and equivalent orthotropic plate

6.1.1.3 Panel C

Panel C is 1 mm thick, which is in the typical thickness range of commercially available trapezoidal profile metal roofs, and a pitch p of 100mm. Profile related resonances and anti-resonances are both more pronounced, and lower in frequency than panel A and B, as are the result of the great decrease in effective bending stiffness compared to the thicker plates. There is smaller difference in the diffuse field transmission loss between analytical and orthotropic, though, again, the latter ignores the detail of profile resonances, and can be clearly seen to strongly differ when looking at individual angles, especially in the stiffer dimension (bottom plot in *Figure 48*).

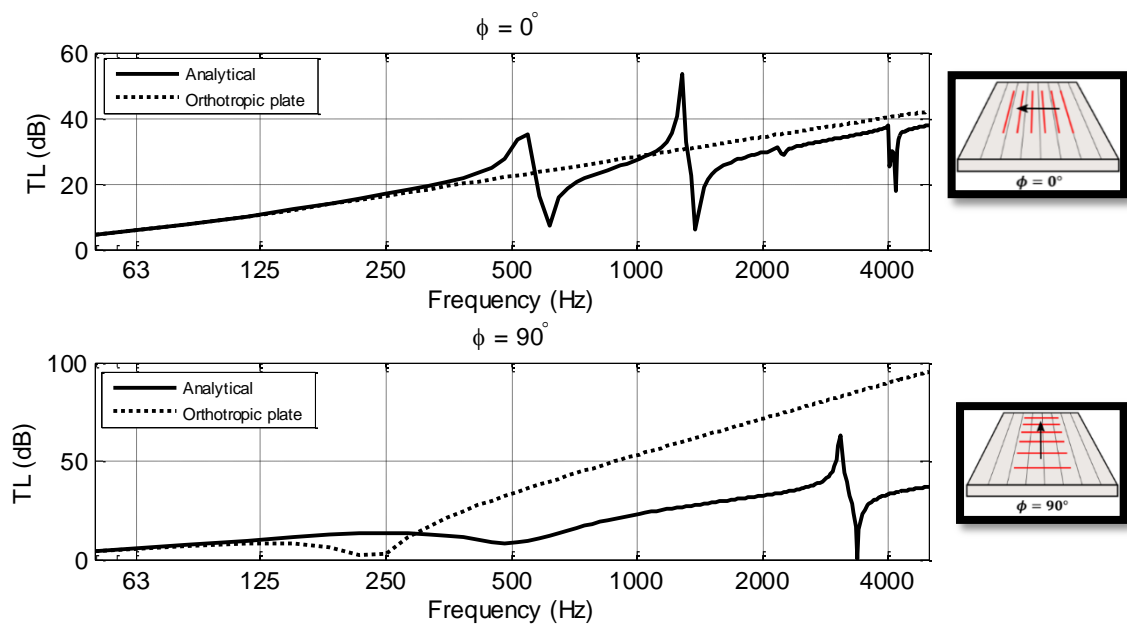


Figure 48: Transmission loss of panel C for incident angle $\theta = \frac{\pi}{4}$ and two wave orientations, $\phi = 0^\circ$ (top) and $\phi = 90^\circ$ (bottom), showing analytical and equivalent orthotropic results

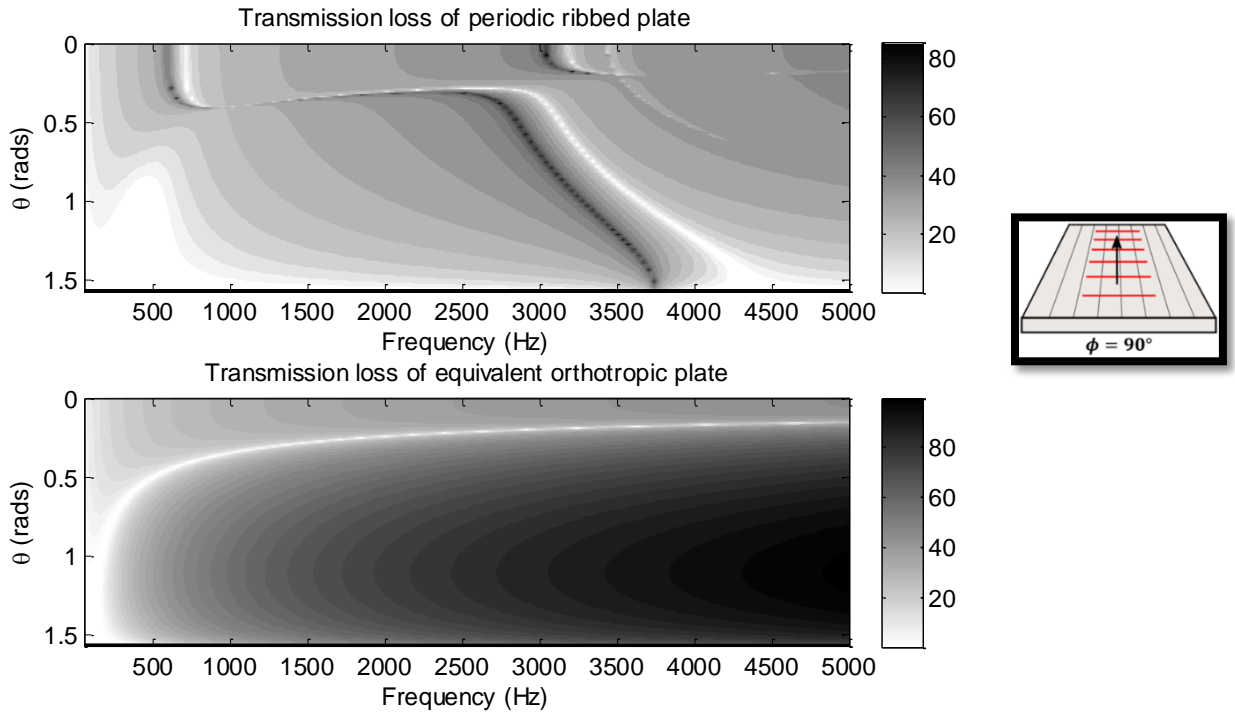


Figure 49: TL of panel C calculated with ribbed plate analytical model (top) compared to an equivalent orthotropic plate (bottom), showing all angles of incidence, with a wave oriented in the stiffest dimension

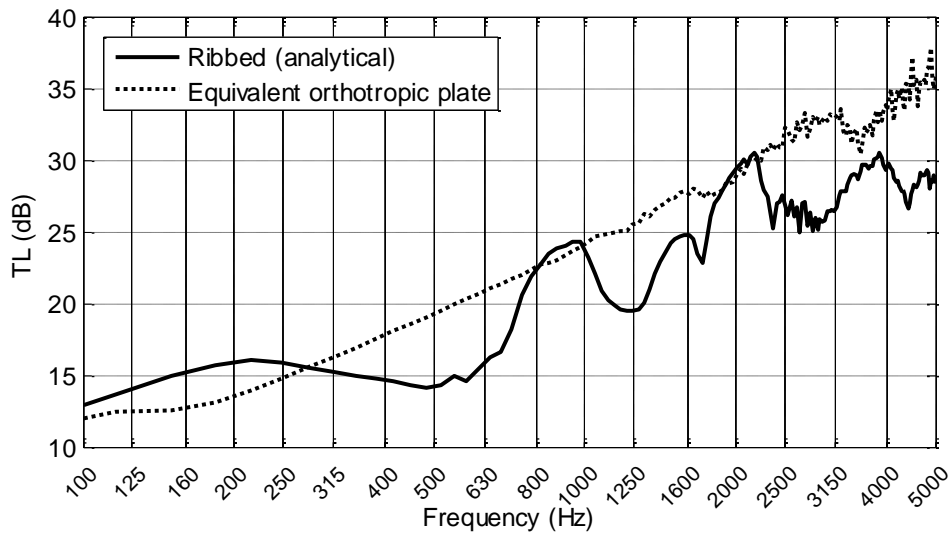


Figure 50: Diffuse transmission loss of panel C, analytical ribbed plate model versus equivalent orthotropic plate

6.1.1.4 Panel D

Panel D is 1 mm thick, and has a relatively large pitch of 300mm. The profile-related resonances start at a much lower frequency, resulting in higher density of such resonances in the frequency range of interest. In the diffuse field, Figure 53, resonances are largely averaged out and no longer visible, and the differences between orthotropic and analytical model solutions can almost entirely be explained by the added mass of the ribs. The resonances are strongly dependent on stiffness, meaning the Young's modulus of the material itself is just as important as profile characteristics in determining the diffuse field transmission loss.

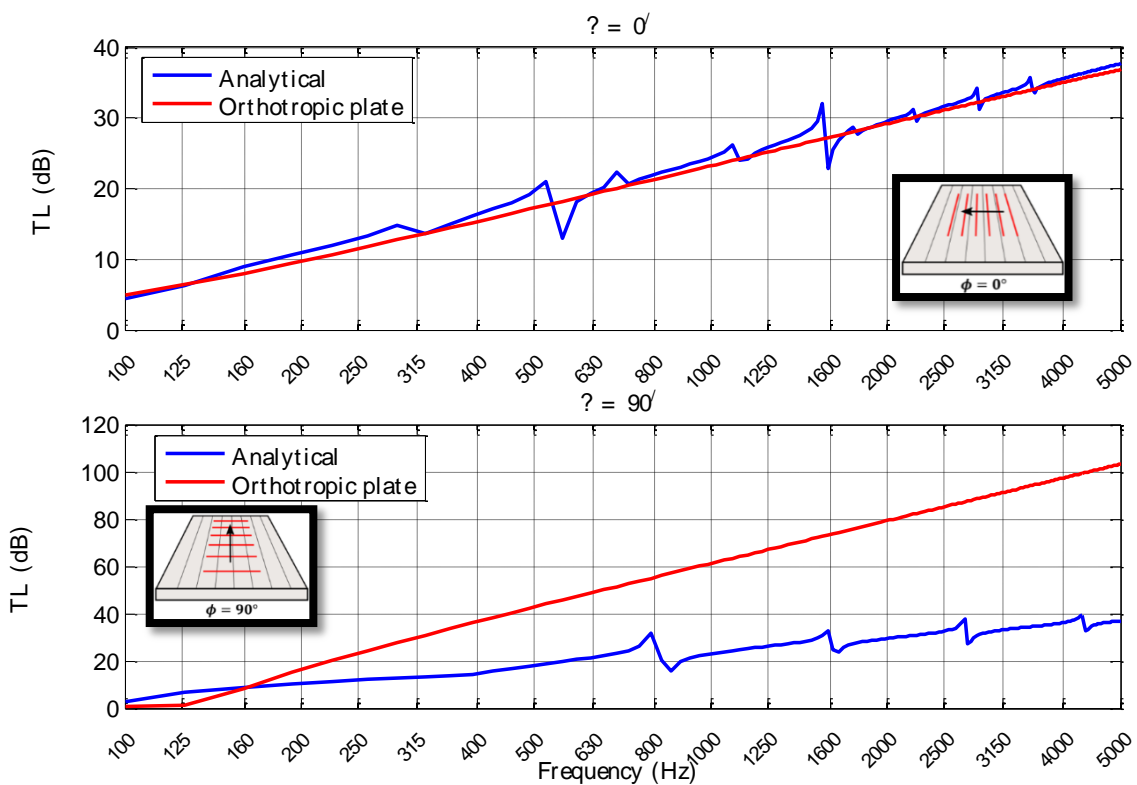


Figure 51: Transmission loss of panel D for incident angle $\theta = \frac{\pi}{4}$ and two wave orientations, $\phi = 0^\circ$ (top) and $\phi = 90^\circ$ (bottom), showing analytical and equivalent orthotropic results

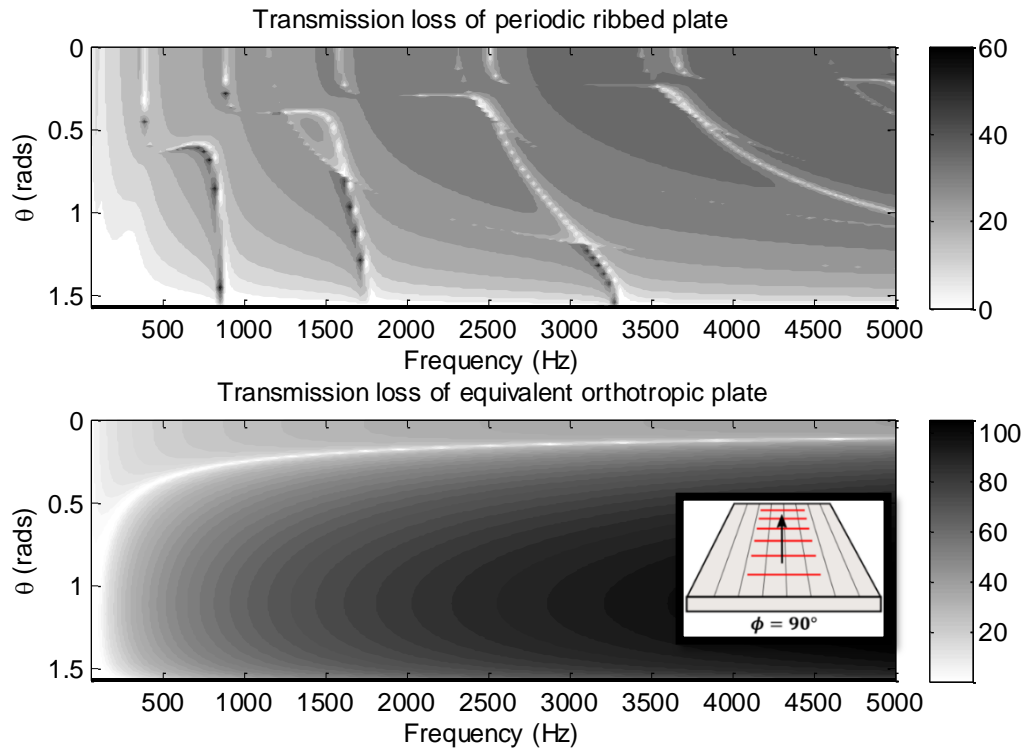


Figure 52: TL of panel D calculated with ribbed plate analytical model (top) compared to an equivalent orthotropic plate (bottom), showing all angles of incidence, with a wave oriented in the stiffest dimension

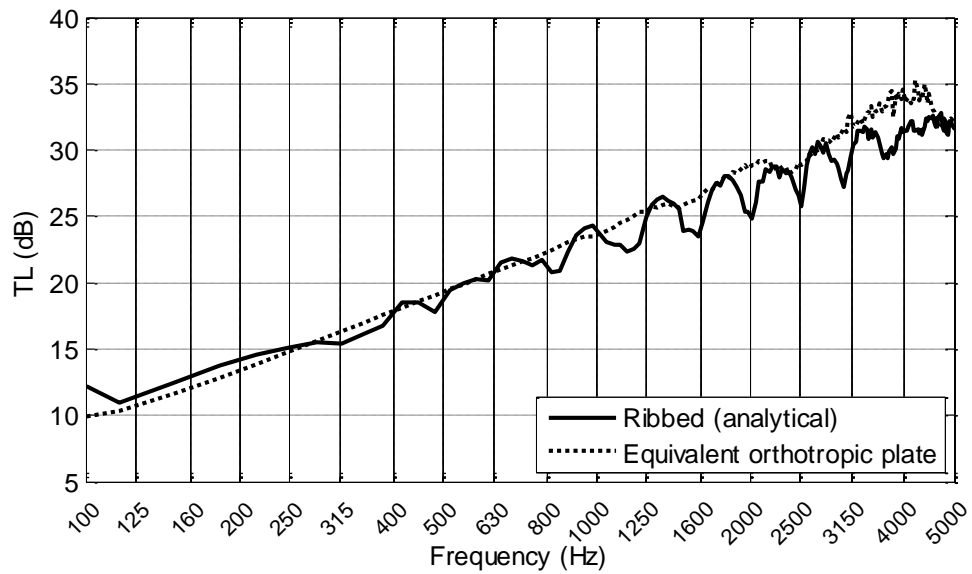


Figure 53: Diffuse field transmission loss of panel D for analytical ribbed plate model and equivalent orthotropic plate, full resolution (top) and averaged in third octave frequency bands (bottom)

6.1.2 Profile resonances

The behaviour of periodically ribbed plates is complex, and analytical solutions in the form presented in this work, containing infinite summations, make it difficult to extract useful relationships between inputs and outputs. In this section, the outputs of the periodic ribbed plate model are used to illustrate some of its features.

Figure 54 shows the transmission loss through a 1 mm thick periodically ribbed plate, with geometric period of 400mm, for incident waves in two orientations, along and across the ribs; in this figure, the y axis is the value of trace wavenumber k_t , and includes values greater than the natural wavenumber in air k_0 , at which there would be no propagation into the far field. When the incident wave travels across the ribs ($\phi = 0^\circ$), where the stiffness is lowest, strong resonances occur in harmonic multiples of the bending wavenumber of the plate. These resonances occur at normal incidence, and increase in frequency as the trace wavenumber increases. In the vibration of a flat plate the opposite occurs: above coincidence frequency the natural wavenumber on the plate is always lower than the natural wavenumber in air, so that there is always a combination that results in high transmission. If, in this case, the trace wavenumber on the plate is zero (i.e. normal incidence), no bending motion occurs, as there is no variation in normal velocity along the plate.

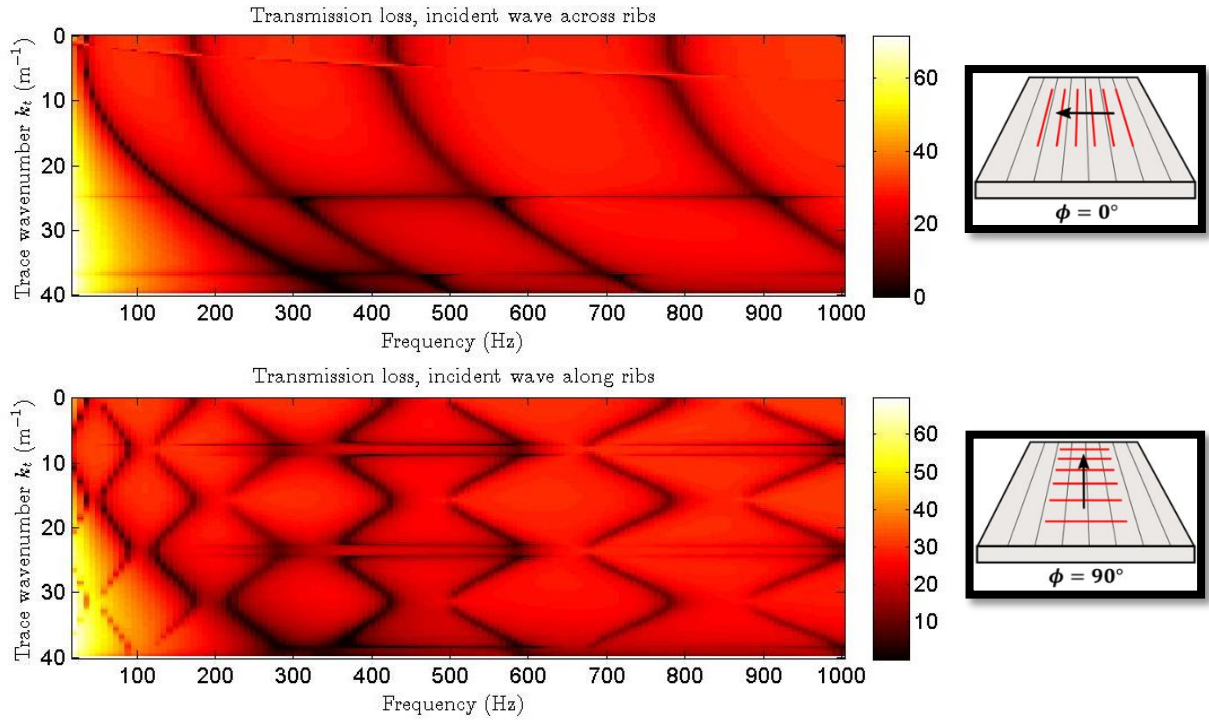


Figure 54: Transmission loss through periodically ribbed plate, with period of 400mm. Top graph shows incident wave across ribs, bottom graph incident wave along ribs

The wavenumbers k_{B_n} at which the profile-related resonances occur for each of the harmonics can be found by the following equation, derived empirically:

$$k_{B_n} = \sqrt{\omega - \omega_n} \sqrt[4]{\frac{m'}{B}} \quad (6.1)$$

The resonant frequencies ω_n were found to correspond approximately to the odd harmonics of the vibrations of a free-free beam of the length of the rib period. The resonant frequencies of a free-free beam can be obtained in the solutions to the following equation:

$$\cosh(kL) \cos(kL) - 1 = 0$$

where L is the length of the beam, and k is its natural wavenumber. The values of kL are an infinite series and can be found numerically. This was carried out in Matlab using the function *fzero*. Table 6 shows the values of kL for the first ten modes.

Mode number	kL
1	4.73
2	7.85
3	11.00
4	14.14
5	17.28
6	20.42
7	23.56
8	26.70
9	29.85
10	32.99

Table 6: Values of kL for the first ten modes of a free-free beam obtained numerically

The resonant frequencies ω_n can then be obtained by substituting k with the known natural bending wavenumber of the plate:

$$k_n L_x = \sqrt{\omega}^4 \sqrt{\frac{m'}{B}} L_x = \alpha_m \quad (6.2)$$

$$\omega_n = \left(\frac{\alpha_n}{L_x}\right)^2 \sqrt{\frac{B}{m'}} \quad (6.3)$$

where $\alpha_n = k_n L$.

Figure 59 shows the transmission loss of the plate for a normal incidence plane wave. The mode frequencies are slightly underestimated.

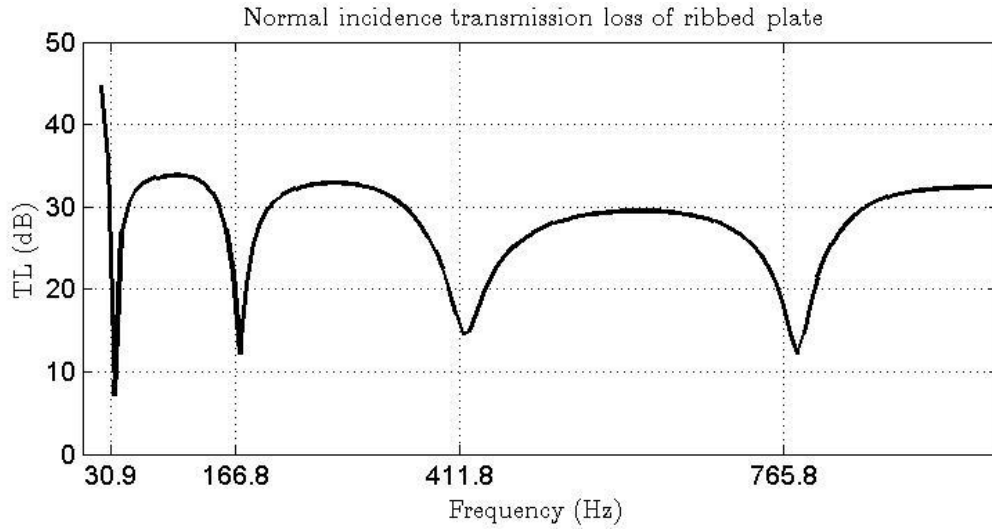


Figure 55: Normal incidence transmission loss of ribbed plate showing mode frequencies

Figure 56 shows the transmission loss as per Figure 54 with overlaid wavenumber harmonics k_{B_n} (odd numbered only). The wavenumber in air k_0 is also shown, as any transmitted wave above that value is evanescent and does not propagate in the far field.

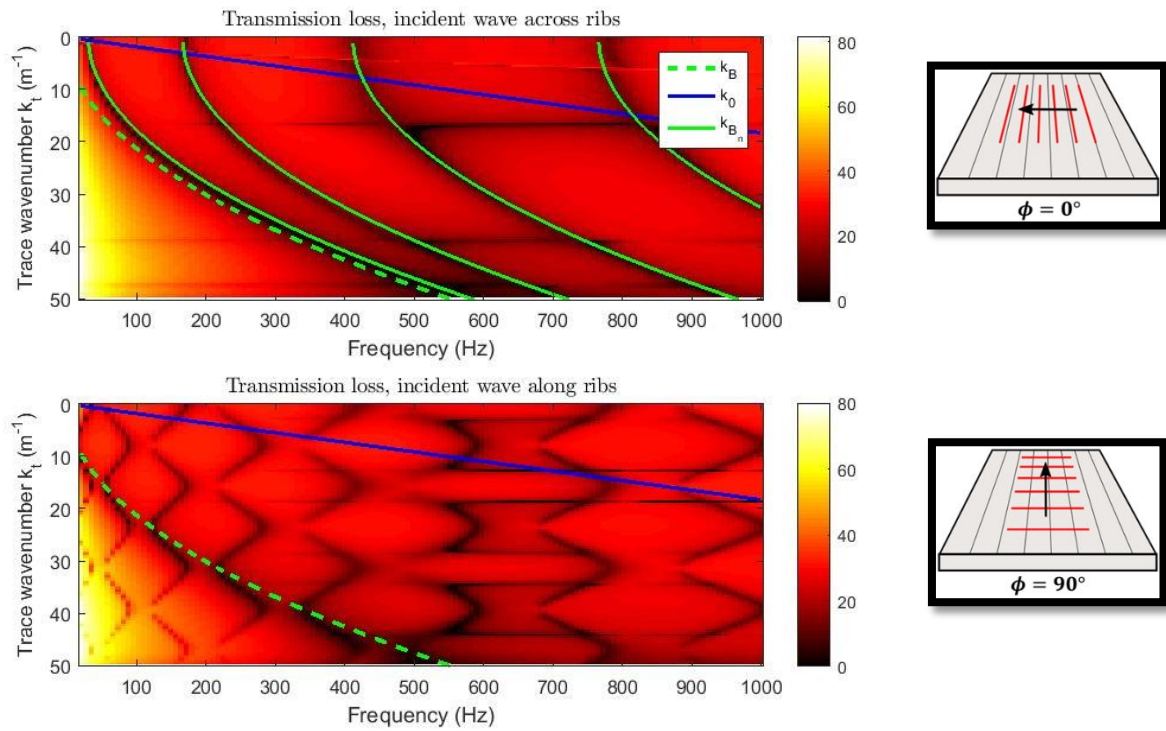


Figure 56: Transmission loss of analytical ribbed plate model for a range of trace wavenumbers, plotted with the wavenumber in air k_0 , the bending wavenumber of the plate k_B and the wavenumber multiples k_{B_n}

In the same figure, resonances can also be seen that are frequency independent, corresponding to fixed wavenumber values at regular intervals of $\frac{\pi m}{L_x}$, and can be seen as straight lines running horizontally, occurring when the excitation matches the period.

6.1.3 Ribbed plates compared to standing seam corrugations

A standing seam plate, simplified to a top-hat corrugated plate, and a beam stiffened plate of the 20 mm depth and 1 mm thickness, were modelled using FEM in Comsol, with a two-dimensional geometry. Both types of panel were modelled with aluminium and also with steel properties. Figure 57 and Figure 58 are plots of pressure in air and displacement of the aluminium plates for a plane wave incident at angle $\theta = \frac{\pi}{4}$ and frequency of 1200 Hz; the displacement amount of the plates is amplified. These plots are used to illustrate how some in-plane motion occurs at the ridges of the corrugated plate as opposed to the beam stiffened

case. Figure 59 and Figure 60 show the transmission loss of, respectively, the aluminium and steel plates produced in FEM. Both figures show similar results, though the steel has an overall higher transmission loss due to its greater mass. The two curves in each figure are in good agreement, and present similar features. The resonances appear at slightly different frequencies, with the lowest being for the beam stiffened plate. The differences are thought to be due to the reduced stiffness of the top hat construction in comparison to the solid beam. These results indicate the possibility of using an equivalent beam stiffness approach which could account for profile-related resonances of corrugated sheets without resorting to a more complex model.

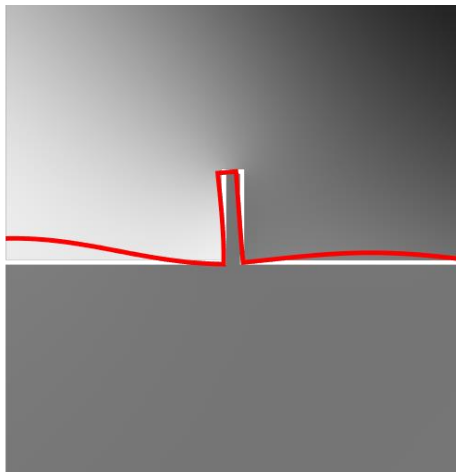


Figure 57: Comsol model of top hat corrugated aluminium plate with incident wave at $\theta = \frac{\pi}{4}$ and $f = 1.2$ kHz, showing in-plane motion

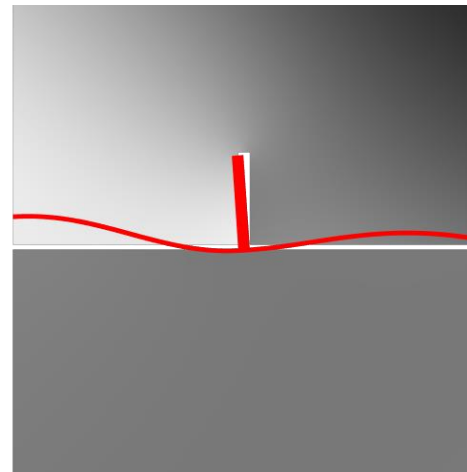


Figure 58: Comsol model of beam stiffened aluminium plate with incident wave at $\theta = \frac{\pi}{4}$ and $f = 1.2$ kHz, showing bending of plate and beam

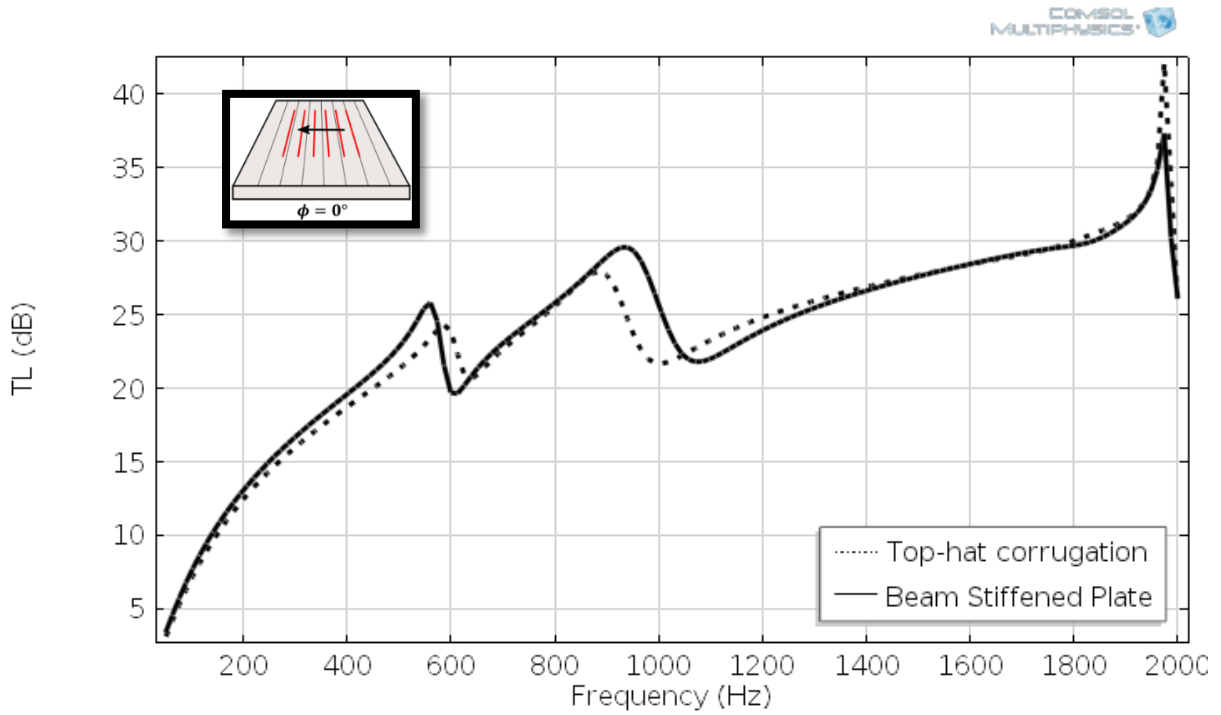


Figure 59: Transmission loss of beam stiffened **aluminium** panel and top-hat corrugated panel of 1 mm thickness and 20 mm depth for incident angle $\theta = \frac{\pi}{4}$

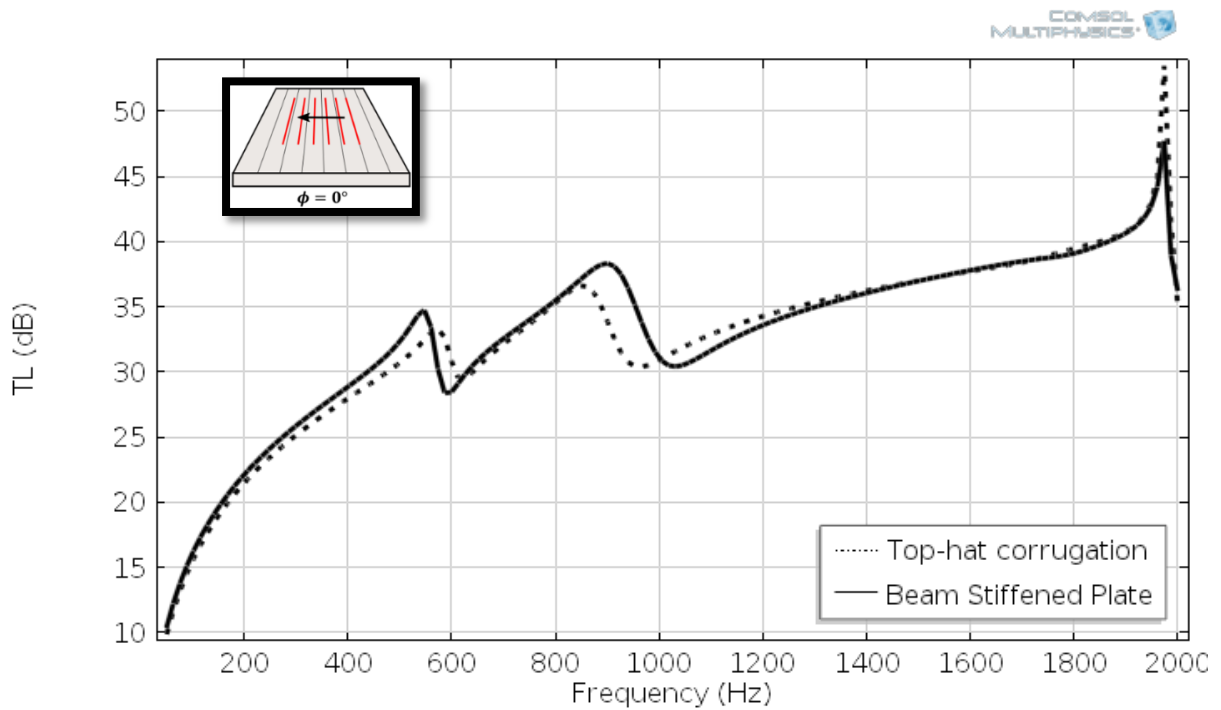


Figure 60: Transmission loss of beam stiffened **steel** panel and top-hat corrugated panel of 1 mm thickness and 20 mm depth for incident angle $\theta = \frac{\pi}{4}$

6.1.4 Periodically ribbed plate as a TMM layer

The effective fluid properties of the ribbed plate can be obtained and used within a TMM framework to model multilayer structures with ribbed plates.

The transmitted pressure obtained with the periodic ribbed plate model is in the form of an infinite sum of travelling waves of different amplitudes and wavenumbers:

$$p_t(x, y, \omega) = \sum T_{mn}(\omega) \psi_{mn}(x, y)$$

The total energy can be obtained by summing the energy from each component independently, as the square of the amplitude T_{mn} . However, in the case where there are multiple layers besides the ribbed plate, the direction and phase of each wave needs to be taken into account. In this case, then, to introduce the ribbed plate into a TM framework requires an infinite number of separate transfer matrices, one for each mode. For each mode, then, equivalent fluid properties k and ρ can be obtained from the values of R_{mn} and T_{mn} , and its properties can then be used in the usual four by four fluid transfer matrix:

$$T^f = \begin{bmatrix} \cos k_z d & j \frac{\omega \rho}{k_z} \sin k_z d \\ j \frac{k_z}{\omega \rho} \sin k_z d & \cos k_z d \end{bmatrix} \quad (6.4)$$

The total transmitted energy is then going to be the sum of the transmitted energy in each mode. This results in complications when modelling multi-layered systems with multiple periodic plates, as each plate would have its own corresponding infinite series. This is the issue with coupling together any number of resonant systems. In a system of two plates separated by a cavity, for each input wavenumber vector of the incident wave there would be a corresponding series of wavenumbers resulting from the geometric periodicity of the first

plate, and each of these would in turn result in an infinite series of wavenumbers from the second plate. A simpler method, which would be valid only at low frequency, would be to construct an equivalent fluid from the zeroth order mode only (from T_{00} and R_{00}), so that only waves with a single trace wavenumber (equal to the incident trace wavenumbers k_{x_0} and k_{y_0}) are considered. Moreover, the cost of introducing periodic point connections between two periodic plates, while not impossible to do, would increase in much the same way. The issue is completely sidestepped by using the orthotropic plate formulation, at the expense of accuracy.

6.2 TRAPEZOIDAL PROFILE PANELS: DIFFERENCES BETWEEN FEM MODEL AND ORTHOTROPIC PLATE FORMULATION

To understand the limitations of the equivalent orthotropic model, compared to the behaviour of corrugated panels, several trapezoidal profile sheets were modelled in Comsol. The combinations of modelled panels are shown in Table 7, and cover a range of profile depths, pitches and thicknesses. Additionally, measurement results for some of the profiled panels of similar thickness (0.7mm) already discussed in the previous section were used to illustrate the effects of profile characteristics on the TL.

Ref.	Material properties	Thickn.	Pitch	Crown	Valley	Depth
Panel 1	$\rho = 2700 \frac{\text{kg}}{\text{m}^3},$ $E = 7 \times 10^{10} \text{Pa},$ $\nu = 0.3,$ $\eta = 0.1,$	4mm	100mm	10mm	80mm	10mm 20mm 30mm 40mm
Panel 2		2mm	150mm	10mm	120mm	10mm 20mm 40mm 60mm
Panel 3		2mm	200mm 300mm 400mm	10mm	140mm 240mm 340mm	20mm

Table 7: List of modelled corrugated panels with dimensions and material properties

The equivalent orthotropic plate model generally predicts that the equivalent bending stiffness increases with profile depth, as the area moment of inertia of the structure increases. Lower depth structures approach the sound transmission of flat panels, as the lower critical frequency associated with the stiffest dimension increases in frequency. This holds true for a real corrugated panel, as FEM calculations show that the lower critical frequency shifts upward with decreased profile depth (precisely what is expected as the area moment of the profile as a whole changes); for this effect see Figure 61, which shows a plot of FEM modelled transmission loss of a 2 mm thick trapezoidal profile panel of depth between 10 and 60mm, ‘Panel 2’: in this graph the lower dip in transmission loss shifts to the right as depth is reduced. On the other hand, the FEM calculations also show that modes related to the profile periodicity, caused by reflections from the discontinuities of the profile itself, can still provide regions of high transmission in the frequency range of interest even for low depth panels, as can be seen in Figure 62, which compares the transmission loss of a corrugated plate for a normal incidence wave over a range of profile depths from 10 mm to 60mm.

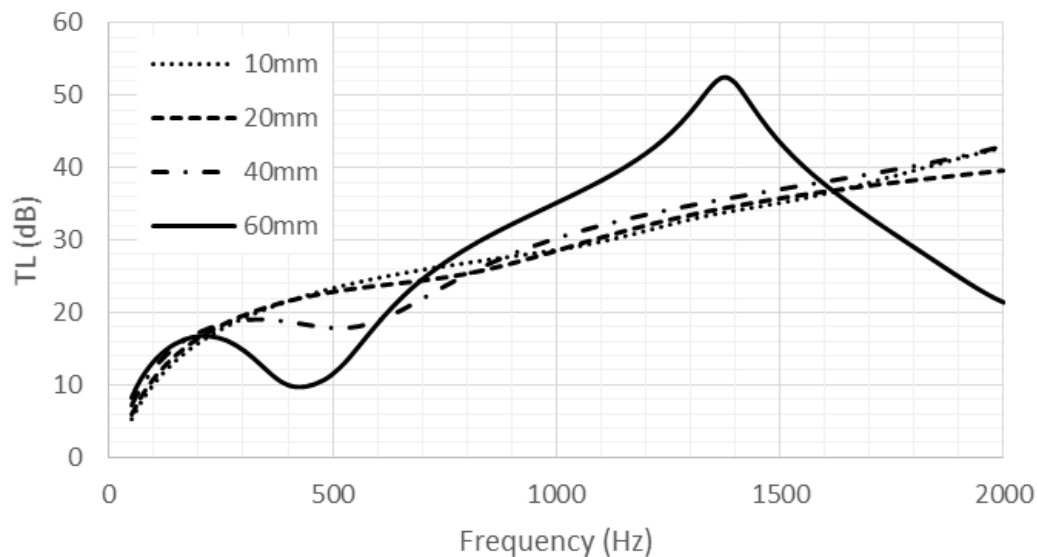


Figure 61: Transmission loss through a single trapezoidal corrugated sheet of varying depth, incidence $\theta = \frac{\pi}{4}$ and wave direction along corrugations (stiffest dimension)

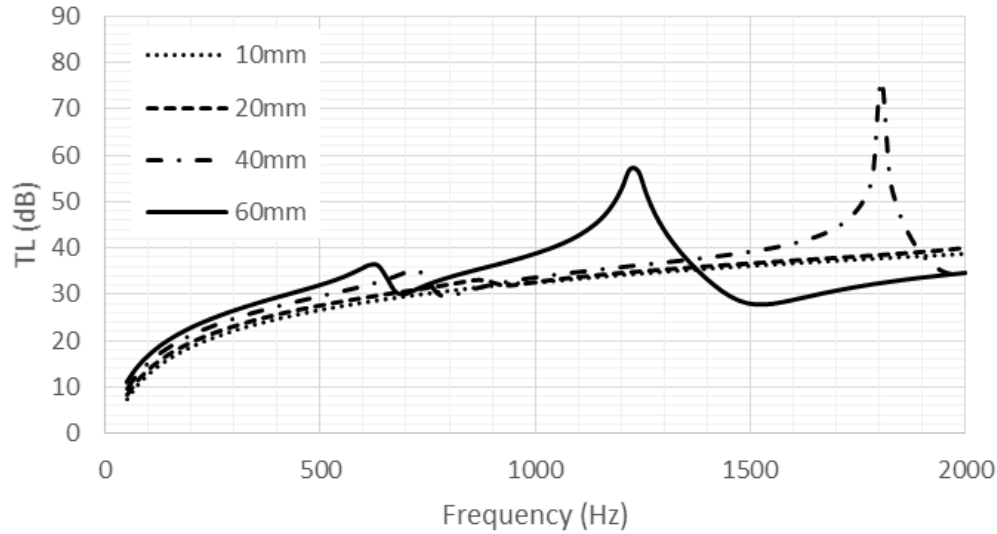


Figure 62: Transmission loss through a single 2 mm thick corrugated sheet of varying depth, normal incidence wave

Figure 63 and Figure 64 show the comparisons between transmission loss of a trapezoidal profile plate predicted with orthotropic plate theory ('analytical') and obtained numerically in Comsol ('FEM') for, respectively, Panel 1 and Panel 2, including depth variations and wave orientation. For the 4 mm thick plate, the lower critical frequency is visible when the wave orientation is $\phi = 0$, i.e. along the corrugations, and is underestimated in frequency by around 20% in the orthotropic plate model, suggesting again that, as for the ribbed plate case, the bending stiffness is slightly overestimated. The peak transmitted energy is modelled correctly, as the dip in TL is in the same order. When the wave travels in the orientation $\phi = \frac{\pi}{2}$, i.e. across the corrugations, the behaviour is similar to a flat plate and at low frequency matches the orthotropic plate model, except for additional resonances and anti-resonances at higher frequencies. For the 2 mm plate, with a 50% greater pitch, the lower critical frequency in the FEM case for $\phi = 0$ is not as strong and appears to be near inexistent for lower depth panels, indicating that the orthotropic plate theory is not valid in this case: it predicts a large dip as it does for the thicker plate. In the orientation $\phi = \frac{\pi}{2}$, a similar result to the 4 mm plate can be seen. This indicates that while the orthotropic plate

formulation is overall preferable to a flat plate model, thin sheets with larger periods require a more complex model.

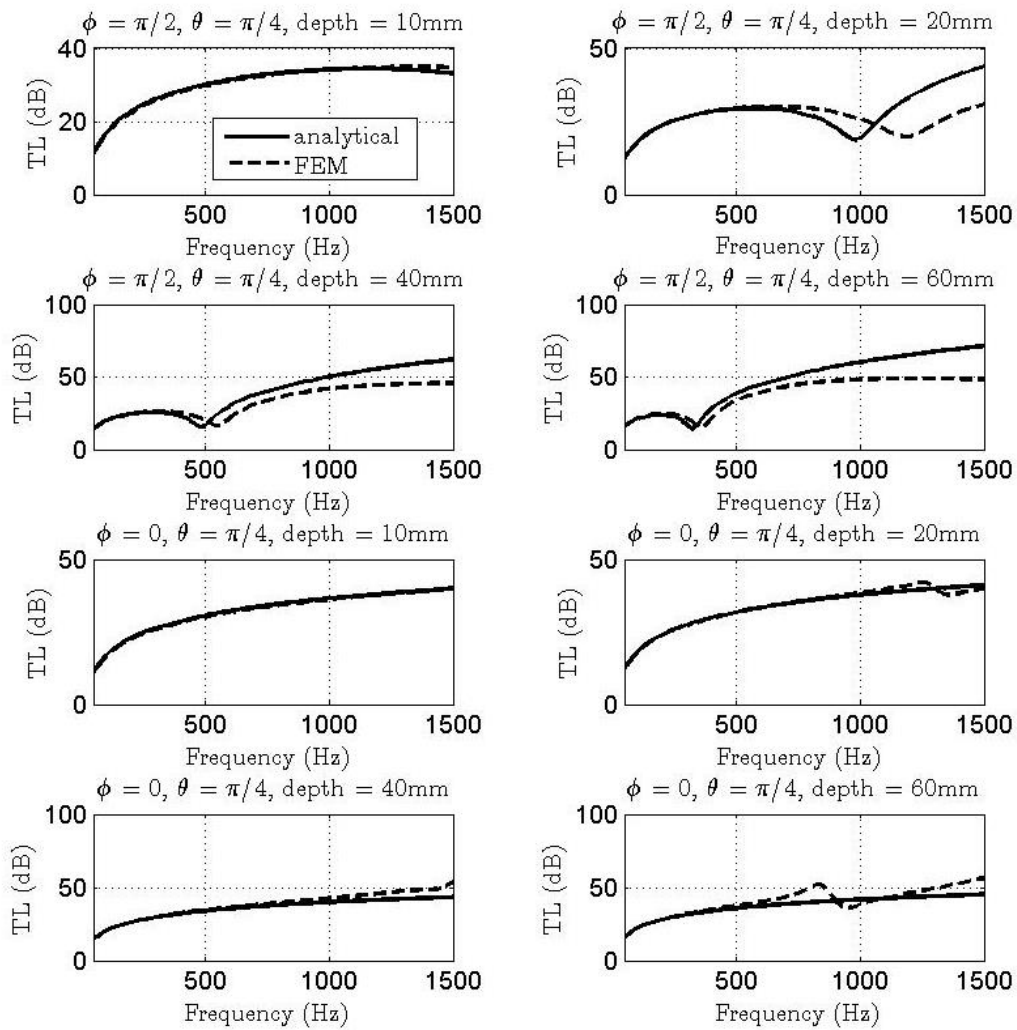


Figure 63: Transmission loss through a single 4 mm thick corrugated sheet (100 mm pitch) – Panel 1 – of varying depth and wave direction (along and across corrugations); comparison with equivalent orthotropic ('analytical') model

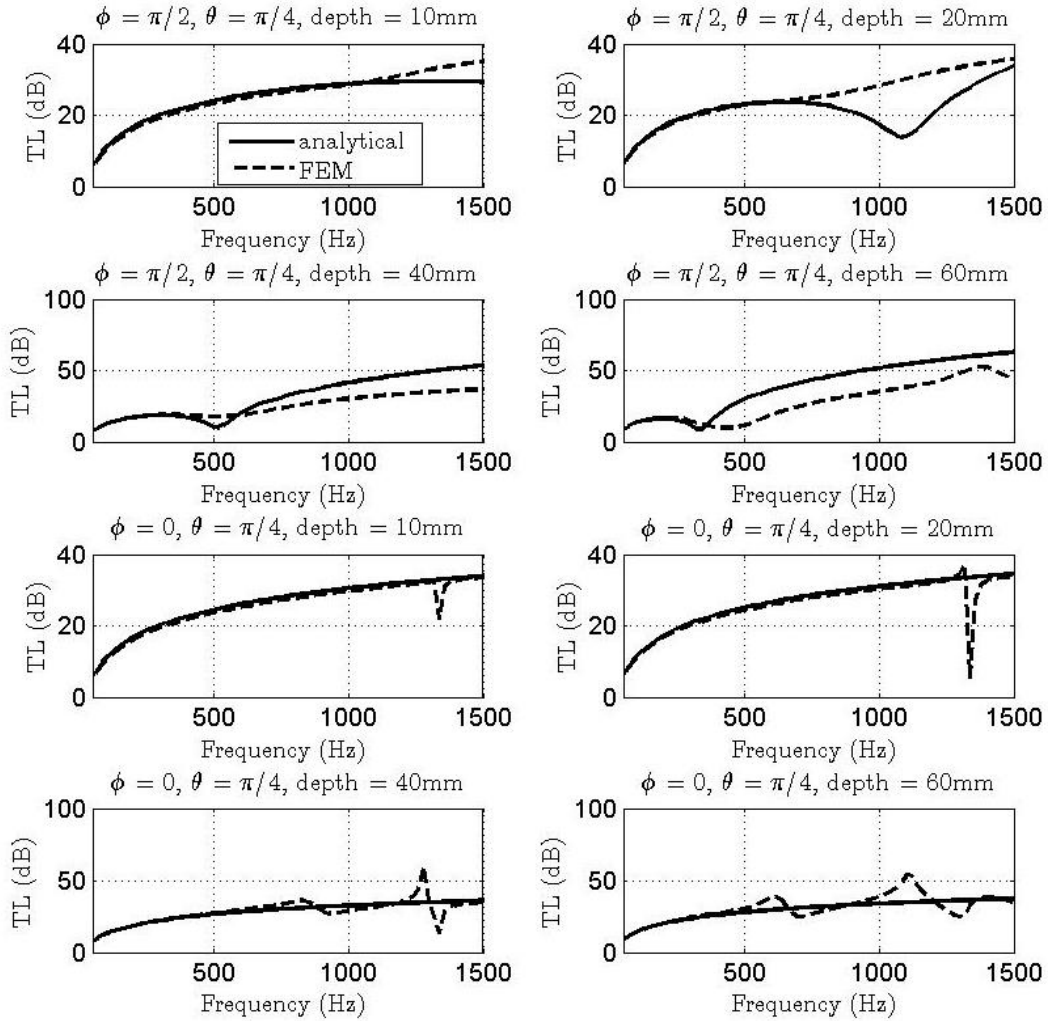


Figure 64: Transmission loss through a single 2 mm thick corrugated sheet (150 mm pitch) – Panel 2 – of varying depth and wave direction (along and across corrugations); comparison with equivalent orthotropic ('analytical') model

6.3 CORRUGATED METAL SHEETS: COMPARISONS WITH MEASURED DATA

This section is a presentation of comparisons between measured transmission loss and predictions using the output from the TMM, with a single solid layer with orthotropic Young's Modulus based on the profile area moment of inertia. The TMM output includes the Villot finite size correction (Section 4.1.11) and a Gaussian angle of incidence window with factor $\beta = 1$. Laboratory measurements of sound transmission loss of individual corrugated

sheets were drawn from available literature and previous measurements carried out at the University of Salford laboratories – with panel depths ranging from 30 mm to 70 mm. Panel profiles with drawings and approximated trapezoidal dimensions (pitch, crown, valley and depth) are shown in Table 9. In modelling these panels, the effect of smaller stiffening ribs was neglected.

Reference and description	Pitch (mm)	Crown (mm)	Valley (mm)	Depth (mm)
CF750 0.6 mm steel (Lam 1995)	250	20	202	47
KZ400 0.9 mm aluminium (Lam 1995)	400	24	373	65
SS1200 0.7 mm steel (Lam 1995)	400	41	322	70
SS600 0.7 mm steel (Lam 1995)	600	51	480	70
NG1998 0.5 mm steel (Ng & Zheng 1998)	190	30	130	30
KL200 0.7 mm corrugated steel sheet (INSUL database)	203	30	160	41

Table 8: Types of corrugated panels, showing approximate trapezoidal dimensions

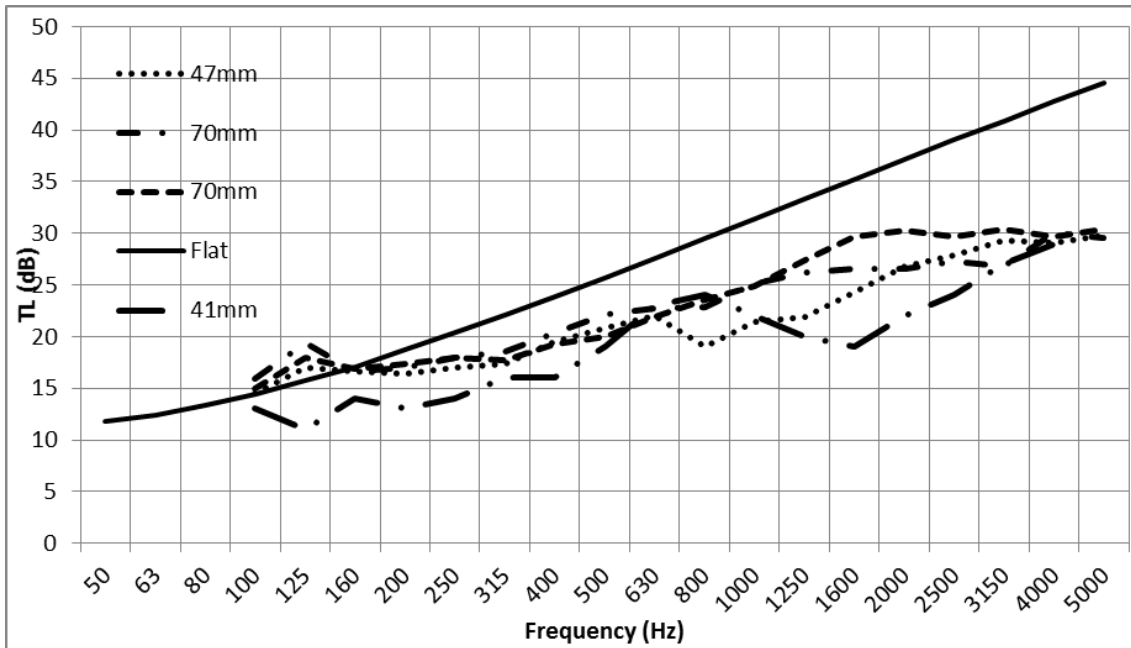


Figure 65: Measured diffuse sound transmission loss of 0.7mm gauge corrugated steel sheets of varying depth (47mm deep sheet is 0.6 mm gauge) compared to a TMM prediction for a 0.7mm thick flat steel panel ('Flat')

The measured transmission loss of all the 0.7 mm thick steel corrugated panels in Figure 65 shows no distinct lower critical frequency shift with depth. The low frequency response of panels of different depth is largely similar, whereas orthotropic plate theory predicts a clearly shifting critical frequency, which would make the TL below the critical frequency higher, something that does not happen in practice, as evidenced in Figure 65. Lower depth panels (41 mm and 47 mm) show dips at mid frequency which are higher than expected based on their bending stiffness.

Generally, the slope per octave and the predicted curves in Figure 66 to Figure 71, which show TL modelled using orthotropic properties against diffuse field measurements, are reasonably close to the result, and an improvement from the predictions for a flat plate of the same thickness. Where the predictions differ from the measurement, is that they tend to overestimate at high frequency, where profile modes dominate transmission; the predicted TL at low frequency varies for different profiles, as the lower critical frequency changes. In practice this does not happen, the low frequency TL is relatively close for all panels. The smaller profile periods in Figure 68, Figure 70 and Figure 71 show a greater amount of dips, while the larger pitches (400mm+) have a smoother transmission loss which is related to the higher mode density, as has been previously shown with the ribbed plate analytical model. Figure 66 and Figure 67 show how, for larger periods, there is a steady increase in TL up to around 2 kHz, where it begins to drop.

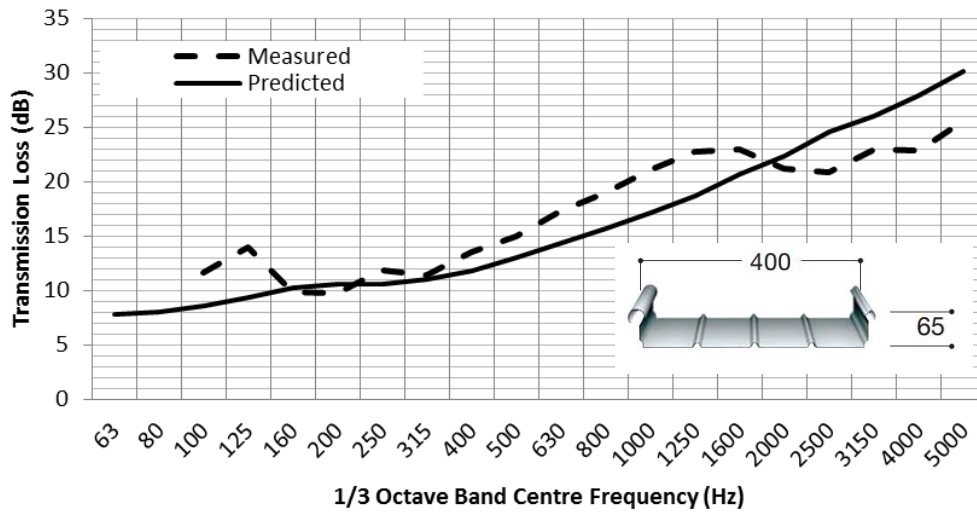


Figure 66: Measured vs predicted transmission loss of KZ400 400 mm pitch

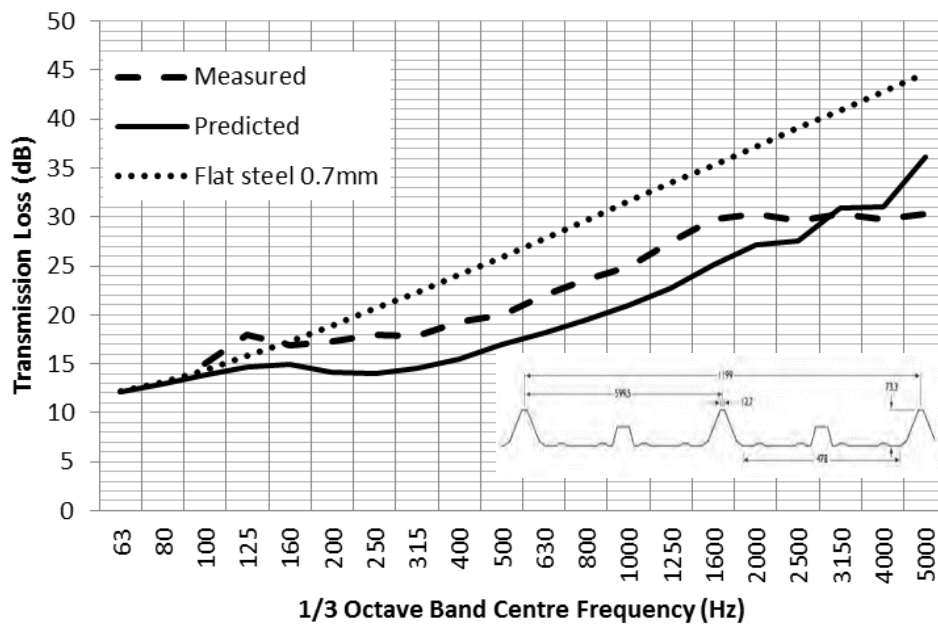


Figure 67: Measured vs predicted transmission loss of SS600 600 mm pitch

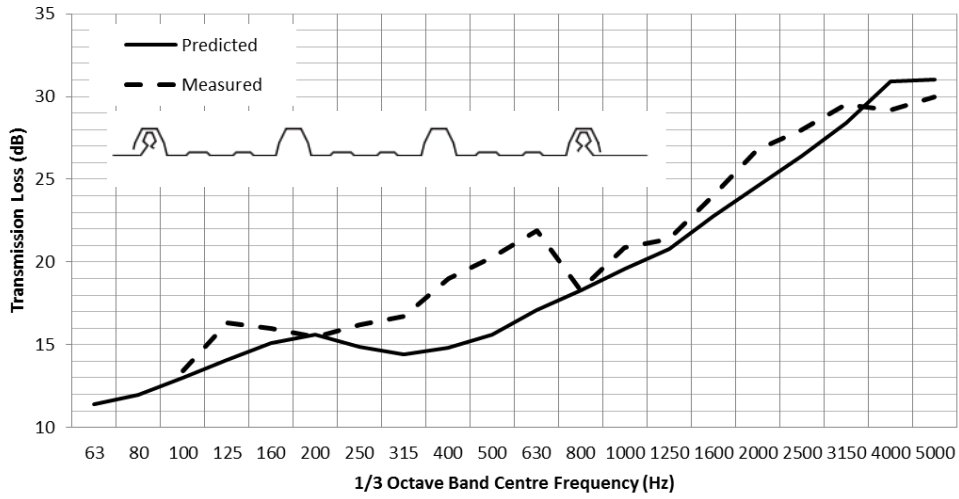


Figure 68: Measured vs predicted transmission loss of CF750 250 mm pitch

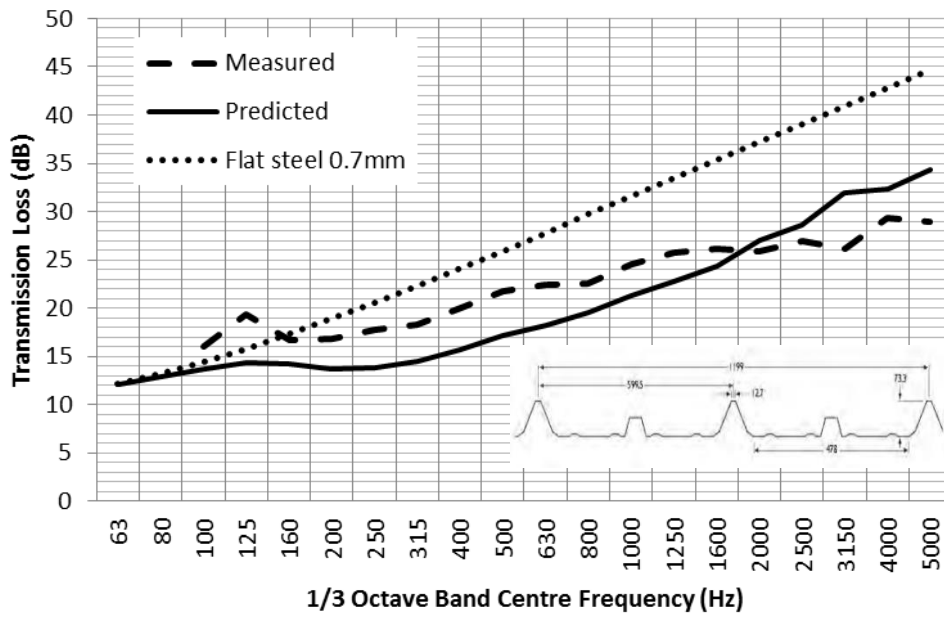


Figure 69: Measured vs predicted transmission loss of SS1200 400 mm pitch

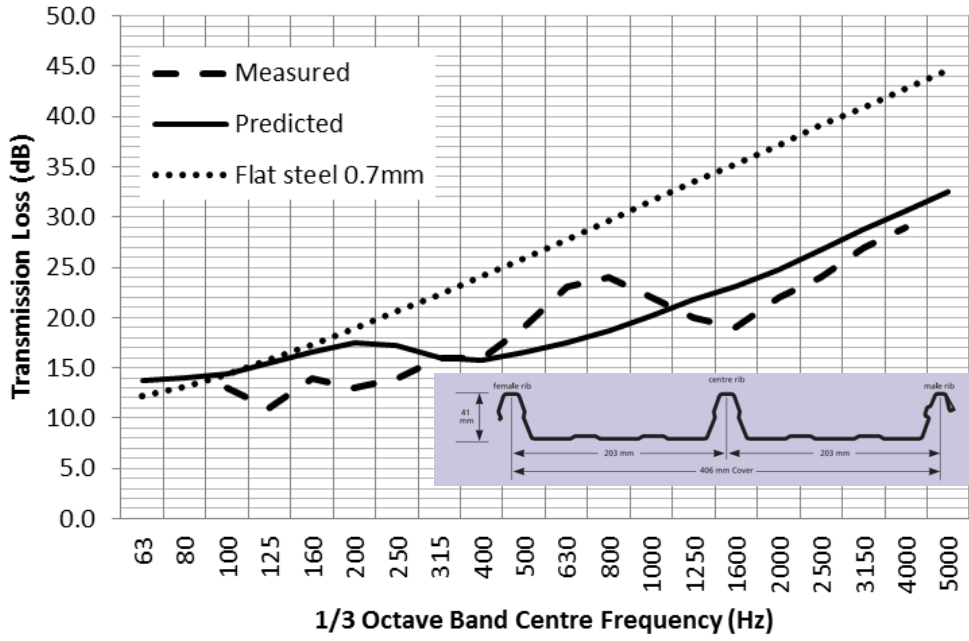


Figure 70: Measured vs predicted transmission loss of KL200 203 mm pitch (INSUL database)

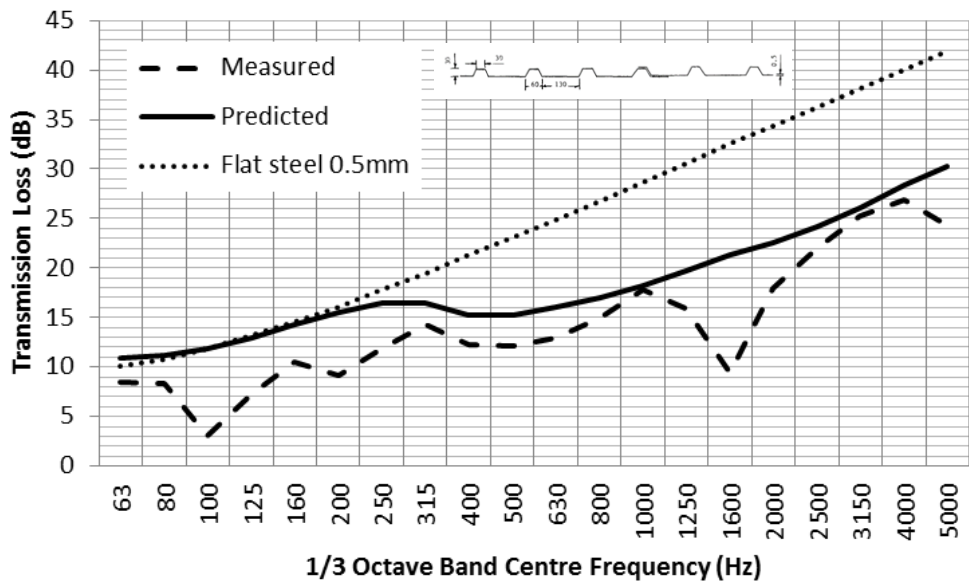


Figure 71: Measured vs predicted transmission loss of NG1997 190 mm (Ng & Zheng 1998)

6.4 CONCLUSIONS

In this chapter, single profiled sheets have been examined from different angles. By comparing the orthotropic plate representation with the periodic ribbed plate model, the differences highlighted how the orthotropic plate generally overestimates the stiffness of real panels, and most accurately captures overall behaviour when the profile period is smaller than the bending wavelength of the plate. However, for larger profile periods, while the orthotropic plate fails to replicate the observed features of a ribbed plate, the diffuse field TL is still close, as the profile-related modes are closer together and are smoothed out when integrating over multiple angles of incidence. Lower critical frequency behaviour in the ribbed plate for wide spacing is less pronounced, as the profile-related modes begin at lower frequencies. In all cases there is little difference in TL between the orthotropic plate and ribbed plate at very low frequency (as the bending wavelength approaches the profile width). Similar observations were made when comparing the orthotropic plate representation to FEM models of trapezoidal plates; the bending stiffness is slightly overestimated when obtaining the area moment of inertia of the corrugated section, and the simulated trapezoidal panels exhibit a fainter critical frequency dip as the profile period increases and the thickness decreases.

Comparisons with laboratory measurements of corrugated steel plates of thickness of 0.6 and 0.7 mm show that, for real panels, the low frequency response is relatively stable even when varying the profile depth, and high frequency behaviour is dominated by profile related resonances which are not captured by an equivalent orthotropic plate model, which consequently tends to overestimate TL.

7 RESULTS: DUAL LEAF STRUCTURES

This chapter is a presentation and discussion of the bulk of validation and applications of the point connected plates and TMM models to the prediction of transmission loss and associated parameters of full roof and partition structures. The sections are presented as much as possible in order of complexity, from single sheets, to dual leaf structures with flat panels and little framework, to roof systems with point-to-point connections, multiple layers of infill and more complex framework. In some figures containing laboratory measurement results, the y axis values have been removed; in these cases, the figure caption will give the y axis gridline step size for reference.

7.1 SINGLE AND DUAL LEAF STRUCTURES WITHOUT STRUCTURAL CONNECTIONS

Laboratory measurements of sound insulation are dependent on several parameters at once, obscuring the details of transmission at specific angles of incidence and for the individual components measured. This will be the case unless the measurements are extremely simple and heavily constrained to a handful of parameters, as in the case of a normal incidence impedance tube measurement. In this section, systems of increasing complexity are modelled with comparisons to diffuse field laboratory measurements.

7.1.1 Structures with flat panels

Large multi-layer structures with flat panels are useful tests of the TMM because they correspond most closely to its formulation. In this section, some glazing and plasterboard partitions will be considered, and comparisons made between available measured data and the TMM model, including two corrections for laboratory diffusivity discussed in

Section 4.1.11: the Gaussian incidence windowing, from Kang et al. (2000), and the spatial windowing, from Villot et al. (2001).

7.1.1.1 Single and double glazing

Glazing partitions are an ideal ‘simple’ case, in that glass sheets are commonly uniform, flat and double glazing partitions have no cavity infill. Framework is often minimal and confined to the outer edges of the structure.

Laboratory measurement results for single and double glazing partitions have been drawn from the literature.

The first single glazing partition examined is comprised of a sheet of 4 mm tempered glass. The laboratory measured TL is compared to the TMM model of a single sheet, using nominal properties of glass; these results are shown in Figure 72. The measured TL shows features expected of a single solid sheet: a mass region at low-mid frequency, with a steady 6dB per octave increase, and a critical frequency dip at high frequency which is dependent on the bending stiffness of the panel. The modelled TL shows the same features. The TMM model with a Gaussian incidence window (with factor $\beta = 1$) is closest to the measured result, while a combination of the Gaussian window and spatial window overestimates TL over most of the frequency range. At low frequency, irregularities in the TL are due to panel resonances related to its lateral dimensions, as well as the resonant behaviour of the laboratory rooms, neither of which were taken into account over the course of this work.

A similar comparison is shown in Figure 73, for a 10 mm single glazing panel of laminated glass. Laminated glass is comprised of two sheets of glass separated by a thin viscous damping layer, and are generally used for increased acoustic performance. The critical frequency dip is lower than for the 4 mm tempered panel due to the increased thickness, but

also lower than predicted with the nominal properties of glass ($\rho = 2500$, $E = 7 \times 10^{10}$ Pa, $\nu = 0.3$, $\mu = 10^{-4}$), modelling a single 10 mm sheet, suggesting the laminated glass also has greater bending stiffness. The critical frequency dip is not as sharp, as the viscous layer in the laminated glass increases its internal damping, which can be accounted for in the model by increasing the loss factor η , as shown in one of the curves in the figure. The change in loss factor does not affect the predicted TL below the critical frequency, which is expected given that the TMM models non-resonant behaviour only. Modal analysis would account for the effect of changes in internal damping on vibration below the critical frequency.

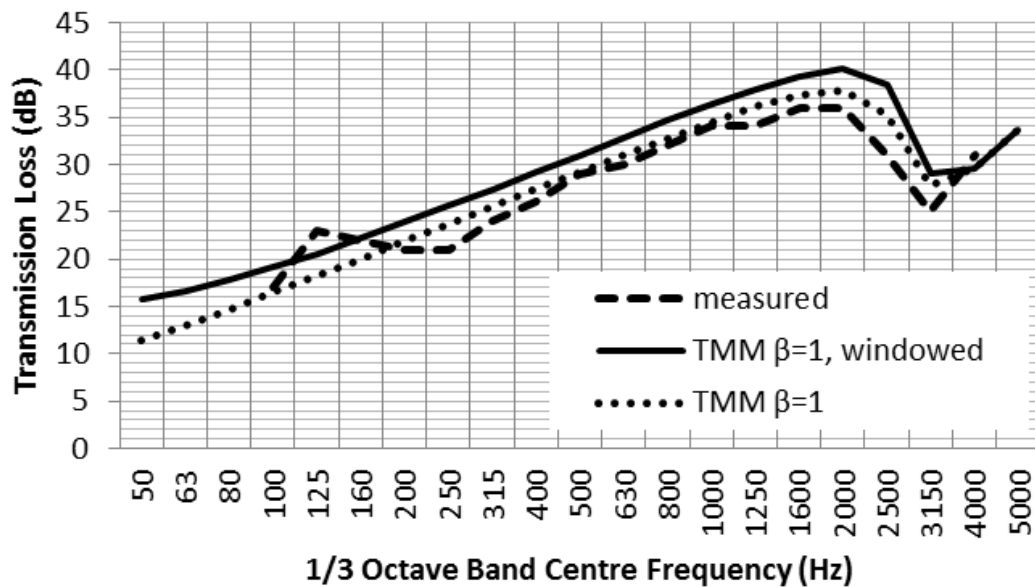


Figure 72: 4 mm single glazing, comparison of measured TL with elastic solid layer model, with corrections for incident field and spatial windowing

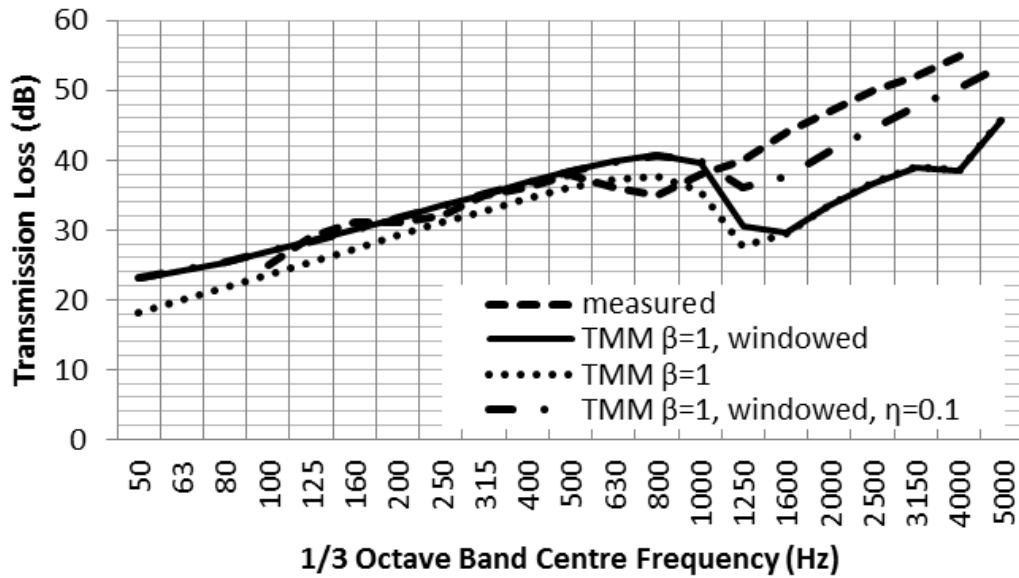


Figure 73: 10 mm laminated single glazing, comparison of measured TL with elastic solid layer model, with corrections for incident field and spatial windowing, and adjusted loss factor η

Diffuse TL of double glazing with two sheets of 6mm tempered glass separated by a 12 mm cavity are shown in Figure 74. The measured TL shows two features of dual leaf structures: the mass-air-mass resonance at low frequency (200 Hz) and the critical frequency associated with each panel (2000 Hz). The diffuse TL obtained with the TMM without adjustments greatly underestimates TL throughout the range. A combination of both the Villot spatial window and the Gaussian incidence window achieve the closest match with results at mid frequency, between the mass-air-mass resonance and the critical frequency dip, although there is some overestimation at the low end. As for the single glazing cases, low frequency results (up to around 200 Hz) tend to be dominated by features of the laboratory rooms and panel resonances which are not accounted for.

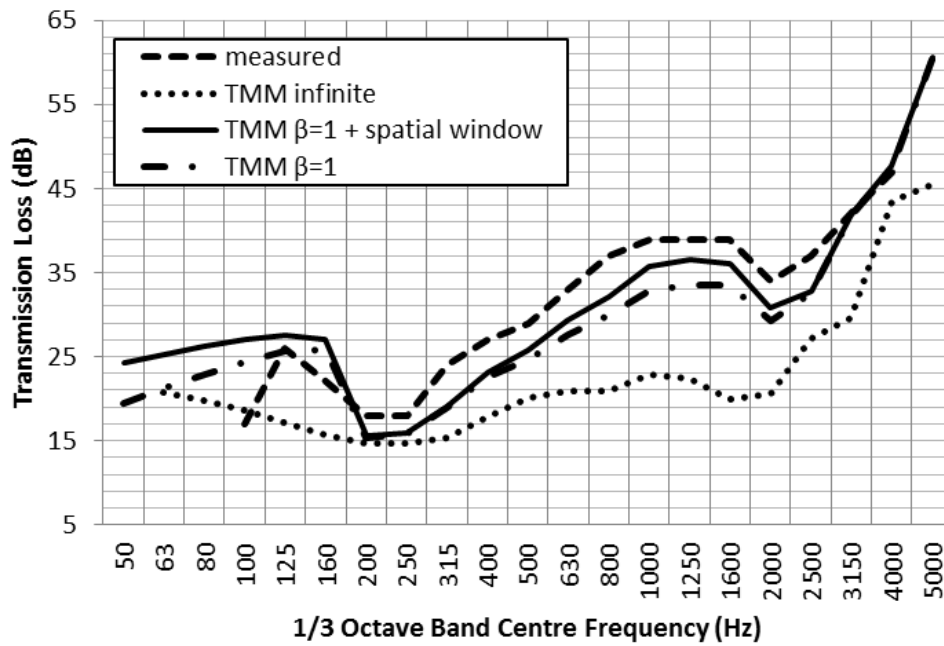


Figure 74: 6-12-6mm double glazing, comparison of measured TL with TMM results, with and without corrections for incident field and spatial windowing

7.1.1.2 Plasterboard partitions

Laboratory measurements of TL of plasterboard partitions were drawn from Stani et al. (2004) and compared with the TMM predictions. In both measurements discussed here, the structure is a dual leaf plasterboard partition with 12.5mm sheets on either side of a 115mm cavity, with aluminium framework, consisting of two 50mm wide C-shaped studs at 630mm spacing. The sectional diagram of the structure can be seen in Figure 75.

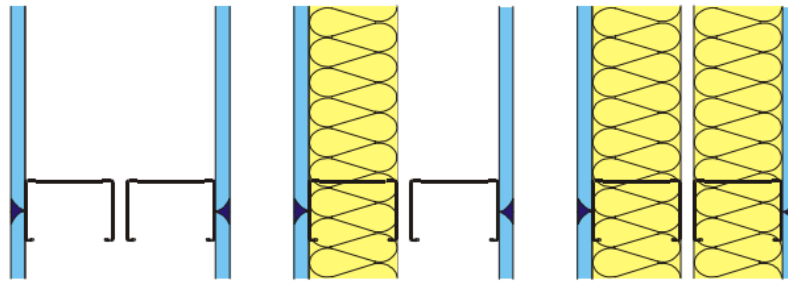


Figure 75: Cross section from Stani et al.: plasterboard partition with 12.5mm sheets and empty 115mm cavity, with double 50mm aluminium C-shaped studs separated by 15mm .

Figure 76 shows the transmission loss of the plasterboard partition with no cavity infill, while in Figure 77 mineral wool is introduced, with a flow resistivity of $5.4\text{kPa}\cdot\text{s}\cdot\text{m}^{-2}$. The measured curves in Figures Figure 76 and Figure 77 are typical, showing features present in most similar constructions. In both cases, a dip at low frequency, around 80 Hz, can be observed, which corresponds to the mass-air-mass resonance. A further dip at 2500-3150 Hz corresponds to the critical frequency of the plasterboard sheets, and is particularly pronounced as both sheets are the same material and geometry. The critical frequency drop amount is dependent on the internal damping of the sheets. The results modelled using the TMM alone predict both features. In the case of the empty cavity, Villot's correction for radiation efficiency (spatial window) improves the prediction significantly compared to the incidence window only ($\beta = 1$), increasing predicted TL by up to 10dB between the mass-air-mass resonance and the critical frequency. When 100mm of low density mineral wool is introduced in the cavity, the TL is significantly higher, as shown in Figure 77, and the slope between the mass-air-mass resonance and the critical frequency dip is much greater, and is influenced by the absorptive properties of the mineral wool. The mass-air-mass resonance frequency is also lower due to the increased damping introduced by the infill. In this case, the TMM modelled results vary little whether the spatial window is used or not. Its effect is to

increase the TL by 5dB below the mass-spring-mass resonance (as radiation efficiency of a finite panel is lower at low frequency), and by only 2-5 dB in the rest of the curve.

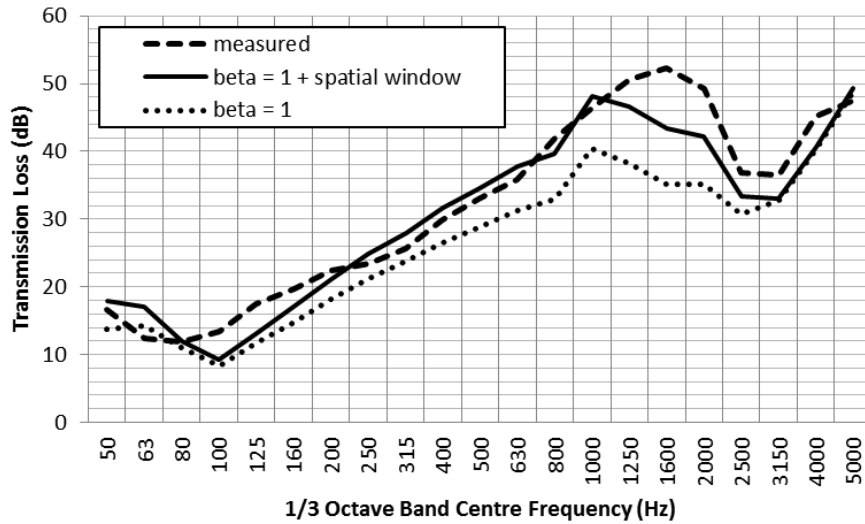


Figure 76: Plasterboard partition with 12.5mm sheets and empty 100mm cavity: laboratory measured versus modelled with incidence window and spatial window (Data from Stani et al.)

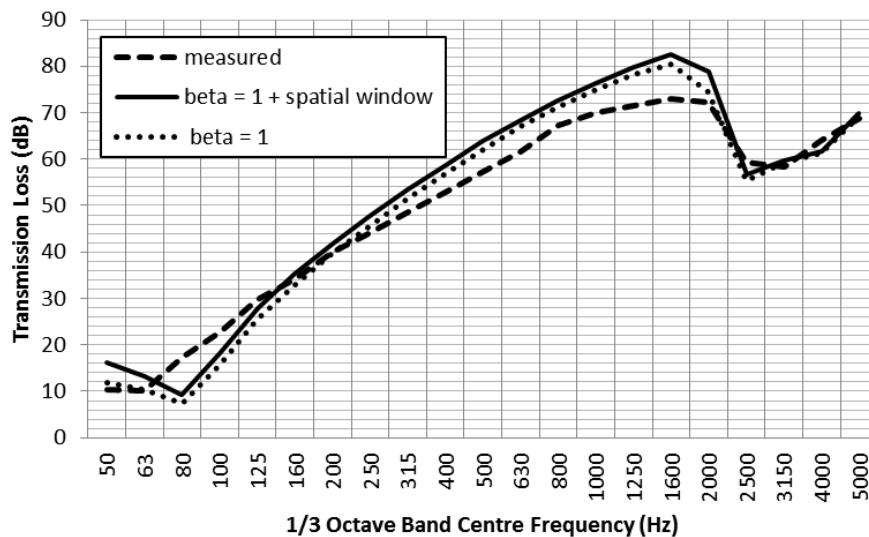


Figure 77: Plasterboard partition with 12.5mm sheets and 100mm cavity filled with mineral wool with air flow resistivity of $5.4 \text{ kPa}\cdot\text{s}\cdot\text{m}^{-2}$: laboratory measured versus modelled with incidence window and spatial window (Data from Stani et al.)

7.1.2 Interfacing layers: bonded versus unbonded solids and poroelastic materials

The behaviour of structures involving solids and high density infill materials which allow significant transmission through the solid portion is heavily dependent on the mounting conditions of each panel, which presents a challenge in modelling. The TMM predicts a large difference in transmission loss when air gaps are introduced between solid or poroelastic layers in a sandwich configuration. Separating layers by small air gaps has the effect of forcing shear stress to zero at the boundaries of the fluid, effectively decoupling solids which would otherwise be fully bonded, if modelled as consecutive layers in the transfer matrix framework. Figure 79 illustrates this effect, showing the large difference between coupling and decoupling poroelastic layers by 1mm air gaps in a sandwich panel; a similar example is found in Allard and Atalla (2009). It is harder to observe such effects in practice

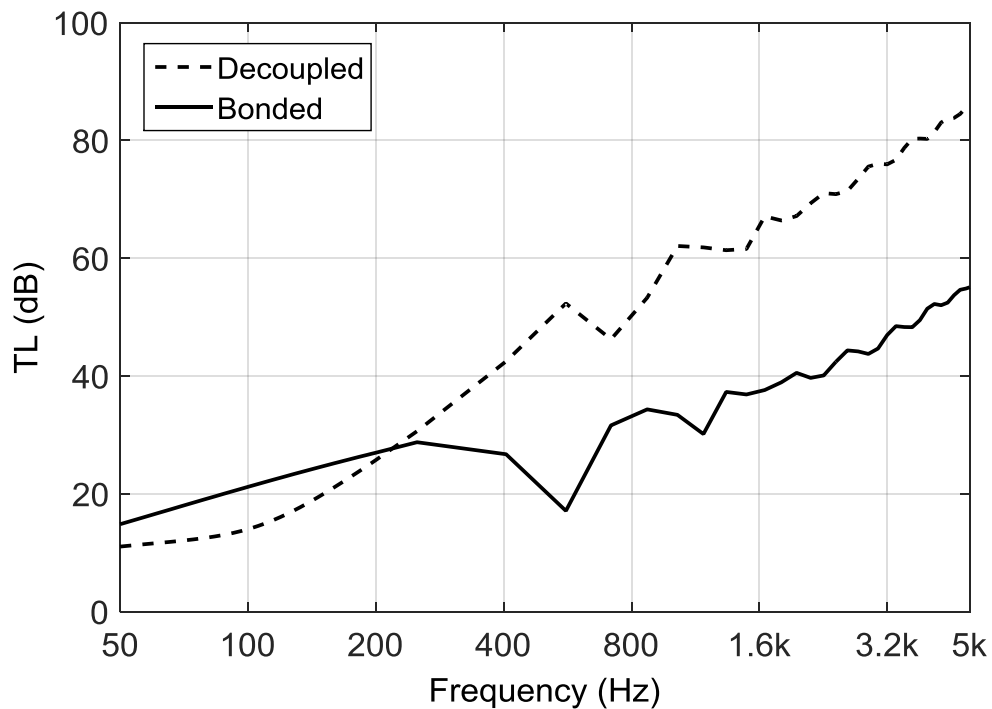


Figure 78: Sandwich plate consisting of mineral wool placed between two steel plates. Predicted transmission loss with and without 1mm air gaps between the plates and the mineral wool.

In many of the dual leaf roof systems described in Chapter 2, corrugated sheets are screwed to high density boards and mats. In this case, one modelling approach has been to obtain the bending stiffness of the combined panels moving as one, using sandwich theory, so that they are effectively bonded. However, in practice, solid panels are joined together with screws, at regular or irregular spacing, so that panels move separately except at the fixing locations. This configuration is rather more difficult to model. Two solid plates fully bonded together are much stiffer than each individual panel, and produce a critical frequency dip in TL which is lower in frequency than it is for either of the plates individually. This is shown in Figure 79, with two plates, a 6mm glass layer and a 4mm glass layer modelled using the TMM; when they are bonded, the critical frequency dip is 1.25 kHz, while it is 2.5 kHz for the unbonded case. It is often the case that dual plasterboard partitions with double plasterboard panels (screwed together) either side of the cavity have a single strong critical frequency dip

(when all panels are the same thickness) at the same frequency as for a single panel, indicating that the effective bending stiffness of each panel does not change significantly even when screwed together.

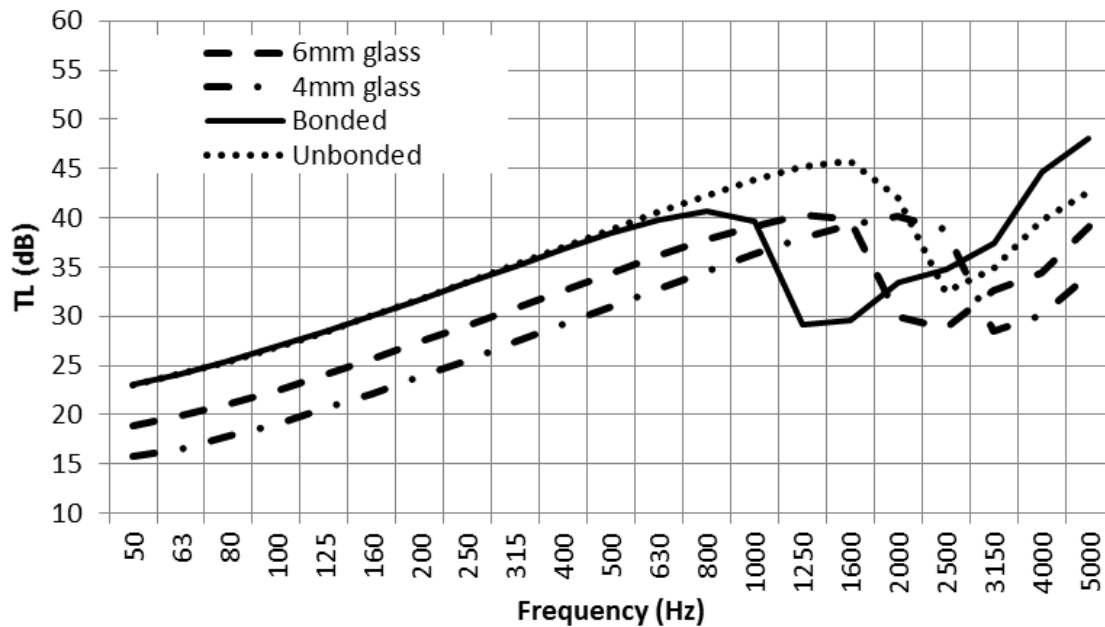


Figure 79: 6mm and 4mm glass panels modelled using the TMM, as single panels, and together, both bonded and unbonded

7.1.3 Factory-made composites

Composites are structures with two thin corrugated metal sheets, and a cavity between them filled with expanding foam, the *core*. Figure 80 is a cross-section of a factory-made composite. In this type of system, the steel sheets are effectively bonded to the core material.

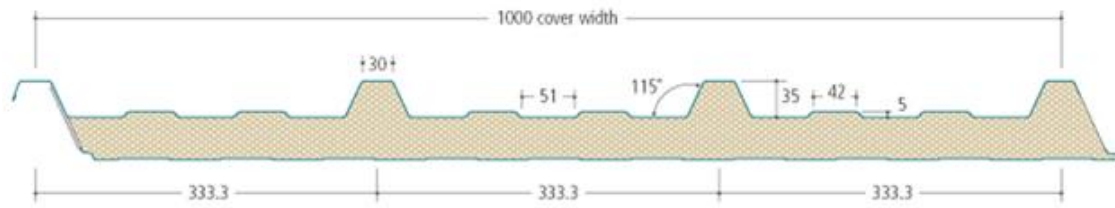


Figure 80: Factory made composite diagram. Corrugated composite panel, two steel sheets with polyisocyanurate (PIR) core

Figure 81 shows the transmission loss of the composite shown in Figure 80, with a core depth of 100mm, along with TMM predictions based on two different values of core modulus, with the appropriate adjustments for diffusivity and radiation discussed in previous sections. The nominal core static stiffness value gives poor prediction of the mass-spring-mass resonance; this is reflected by Pritz (1998), who showed that the dynamic moduli are generally higher than the static values and increase with frequency. Other important transmission mechanisms are also neglected. These are most likely related to the influence of the profile and require a detailed investigation beyond the scope of this work.

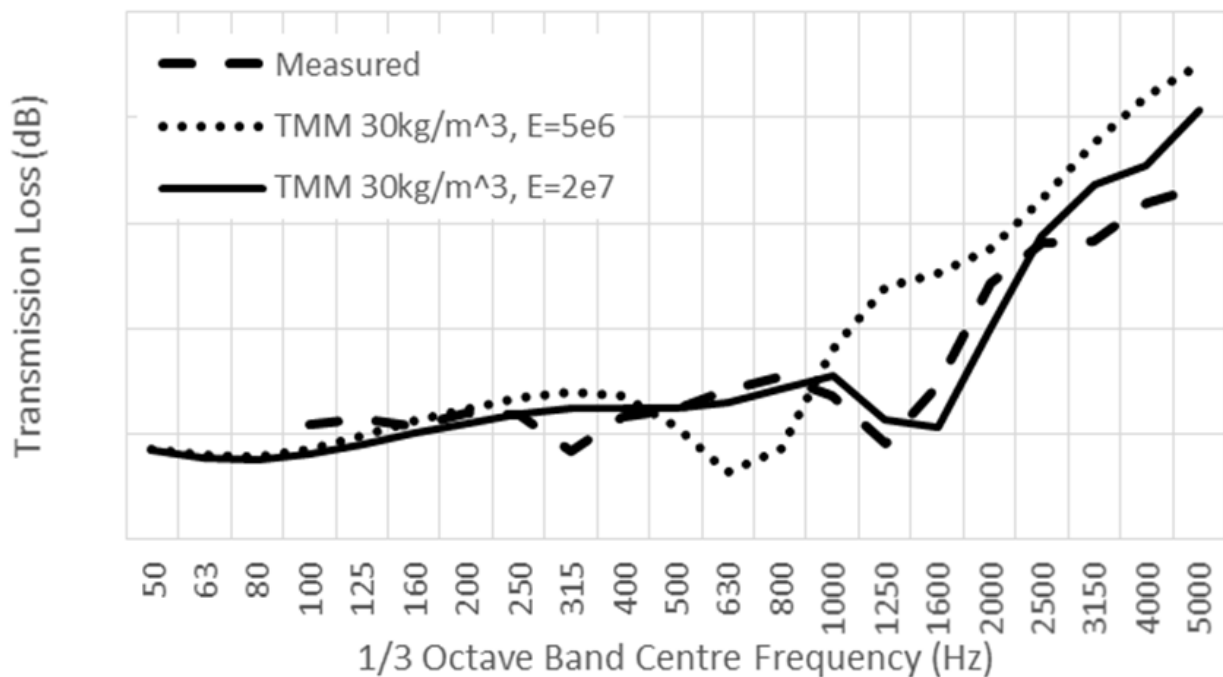


Figure 81: Diffuse TL of corrugated composite panel with polyisocyanurate (PIR) core and 100mm depth: comparison of measurements to TMM model with varying Young's modulus E of the core ($E=5e6$ nominal static value, $E=2e7$ empirical estimate) (y axis gridlines are in 10dB increments)

Measured TL was also available for a composite with a smaller 40mm core depth. In this case, the TMM predicted transmission loss overestimated the measured results by around 5dB from mid to high frequency, and underestimated in the low frequency region. These results can be seen in Figure 82. As the thickness of the core decreases, the profile depths become larger with respect to the overall depth. The impedance mismatch between the valley and crown areas of the profile becomes larger and profile modes would thus play a greater role. This suggests that effects associated with the profile are stronger and influence transmission loss to a greater degree, resulting in overestimation in the model.

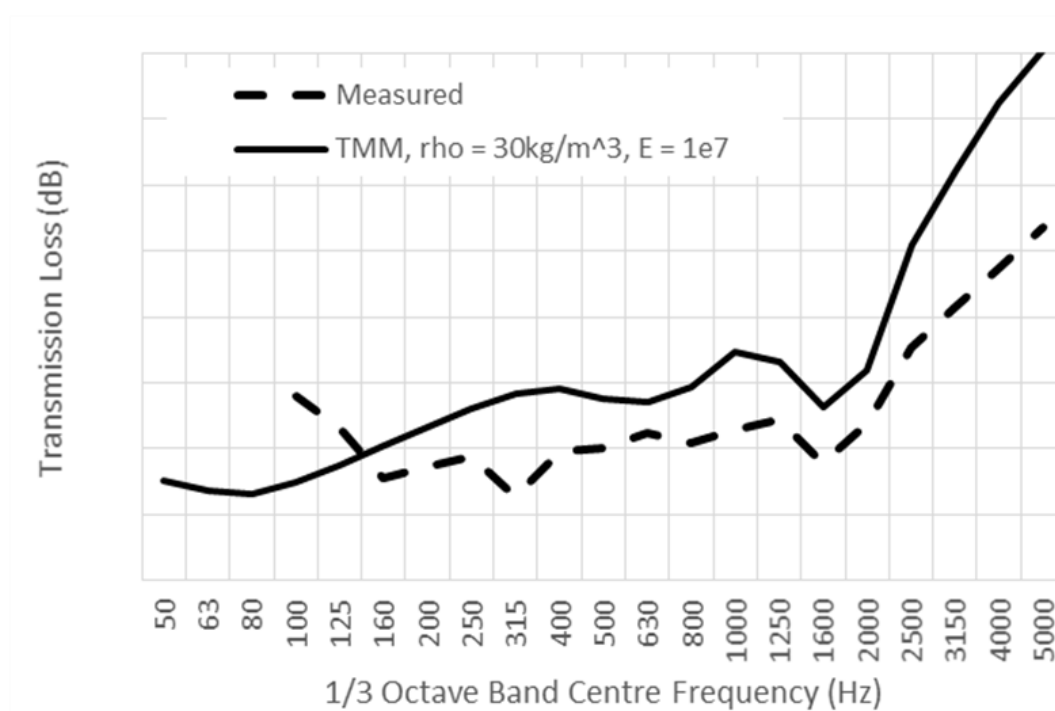


Figure 82: Diffuse TL of corrugated composite panel with polyisocyanurate (PIR) core and 40mm depth; comparison of measurement to TMM model (Young's Modulus E estimated). (y axis gridlines are in 5dB increments)

Composite panels can be represented as mass-spring-mass systems, where the two sheets are the masses and the core material provides the stiffness. The mass-spring-mass resonance then follows the usual equation:

$$f_m = \frac{1}{2\pi} \sqrt{\frac{K_b}{d} \frac{m'_1 + m'_2}{m'_1 m'_2}}$$

Where K_b is the bulk modulus of the core, and m'_1 and m'_2 are the masses per unit area of the metal sheets, and d is the thickness of the core.

The behaviour of a real composite is no doubt more complex, however the mass-spring-mass resonance is the most clearly visible feature in many measurement results, and a reasonable approximation of TL can be obtained with a simplified approach that only accounts for this. A three-layered transfer matrix approach, where all layers are modelled as elastic solids with a flat profile, captures the overall behaviour seen in measured results. However, the

mechanical properties of the core material, which are essential in determining the resonant frequency, are hard to obtain reliably. The static modulus of the core varies considerably with overall core depth (as evidenced by measurements provided by the manufacturers), and its dynamic properties have not been established. Based on reverse engineering from diffuse field measured data, the bulk modulus of the core appears effectively one order of magnitude higher than any static values for the material, nominal or measured.

7.1.4 Conclusions

In this section, single and dual leaf structures were modelled without considering framework or structural connections, using the TMM with two correction methods to approximate laboratory conditions: the incidence window and the spatial window (Villot et al. 2001; H. Kang et al. 2000). A combination of both corrections together has been found to improve prediction accuracy for dual leaf structures without absorbent infill. The use of a double correction has a smaller impact in the case of systems with high absorption, where often either the spatial window or the incidence window alone are better than both combined.

The TL of corrugated composite panels with high stiffness foam cores can be modelled with the TMM, using the equivalent orthotropic plate model for the outer metal sheets. This approach can predict the global mass-spring-mass behaviour but overestimates transmission loss for thinner composites, where the corrugation depth is a greater percentage of overall depth.

7.2 POINT CONNECTED PLATES: VALIDATION AND SURVEYS

This section will move on to discussing structures with structural point-to-point connections and spacer kits. First, the analytical model of plates connected by rods, described in

Section 5.1, is validated by comparison with FEM model of two plates connected periodically by thin rods. The influence of point connection spacing and stiffness on the transmission loss of dual leaf structures is then observed by way of a parametric survey using model outputs. The compressional stiffness of halter and bracket connectors is obtained with FEM models of typical geometries. The stiffness values are then used as inputs to the periodic point-connected plate model. Finally, spacer kits with halters onto top hat purlins (top hat section beams between the halters and the bottom plate) are examined with FEM, by obtaining the changes in stiffness compared to halters, and the point-connected plate model to shed some light on their influence within full structures.

7.2.1 FEM validation

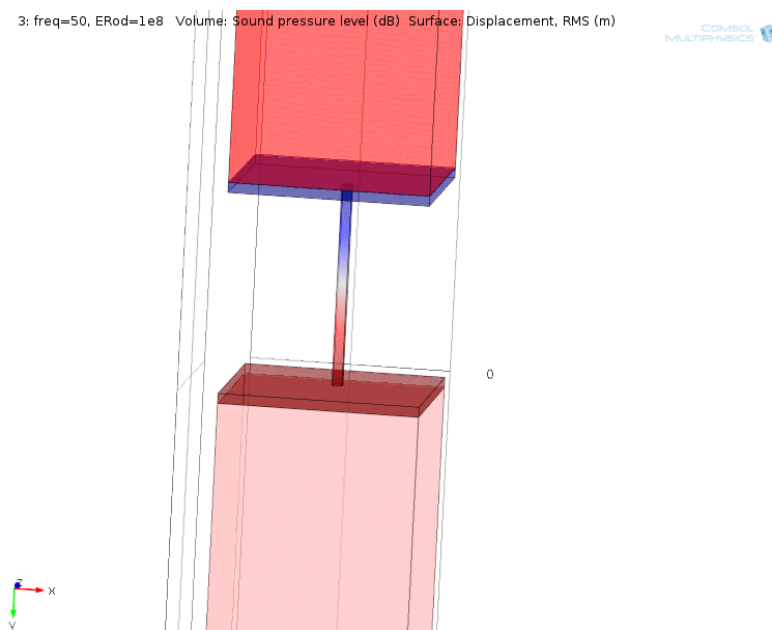


Figure 83: Dual leaf system with connecting rods, unit cell geometry produced in COMSOL

A system of two parallel infinite plates interconnected by spatially periodic thin rods and separated by an air cavity was modelled analytically, as described in Section 5.1, and with a frequency domain FEM carried out in COMSOL. Within COMSOL, a single unit cell was

modelled and Floquet periodicity was introduced at the boundaries to model the periodic system. The incident wave was modelled as a ‘background pressure field’, with a given wavenumber to determine the wave direction. The unit cell size (and consequently the spacing of rods) was 100mm by 100mm in the x and y directions. Figure 83 shows the system geometry of a single unit cell produced with COMSOL. The top and bottom plates were both 5mm thick with the commonly used properties of aluminium ($\rho = 2700 \text{ kgm}^{-3}$, $E = 7 \times 10^{10} \text{ Pa}$, $\nu = 0.3$), with an adjusted loss factor of 0.1 to produce smoother results around resonances. The rods had a density of 2700 kgm^{-3} and four values of Young’s Modulus between 10^6 and 10^9 .

Figure 84 shows the transmission loss obtained with the periodic analytical model and the FEM simulation for angle of incidence $\theta = \frac{\pi}{4}$, over the range of rod moduli. The results show good agreement throughout the range considered, between 50 Hz and 2 kHz, and for the different rod stiffness values. The analytical model predicts most features, including how the lower mass-spring-mass resonance increases from 80 Hz to 315 Hz as the modulus of the rod increases, and how higher frequency resonances shift with stiffness. The FEM model includes all degrees of freedom for the rods, so some discrepancies are expected; in particular, the TL differences are greater for lower values of rod Young’s Modulus. This could be improved by introducing additional degrees of freedom in the point-connected plate model.

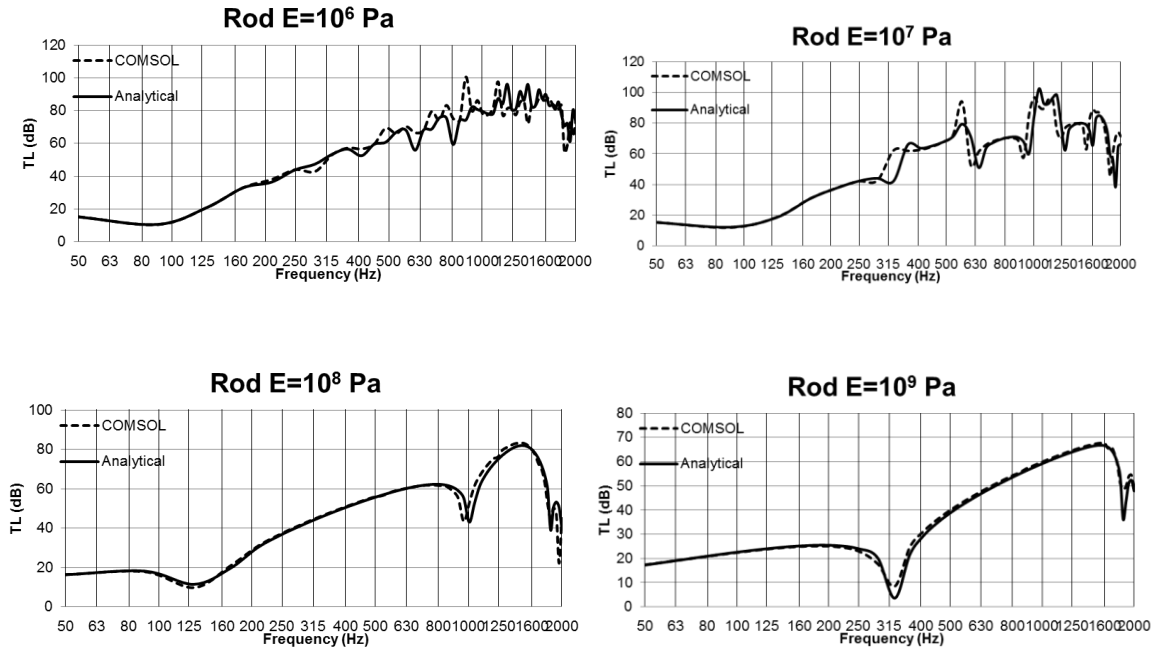


Figure 84: Comparison of analytical and FEM calculated transmission loss through the infinite periodic double plate structure with point connections at 100mm by 100mm for an incident plane wave at $\theta = \frac{\pi}{4}$, with rod Young's modulus varying from 10^6 to 10^9

7.2.2 Halters and brackets: comparison of compressional stiffness

Two common types of connectors used in spacer kits in roof systems have been examined: halters and brackets (see Section 2.3). Their compressional stiffness was obtained with FEM modelling carried out with COMSOL, so that the values could be used within the analytical model for point connected plates by replacing the stiffness matrix K_{ij} .

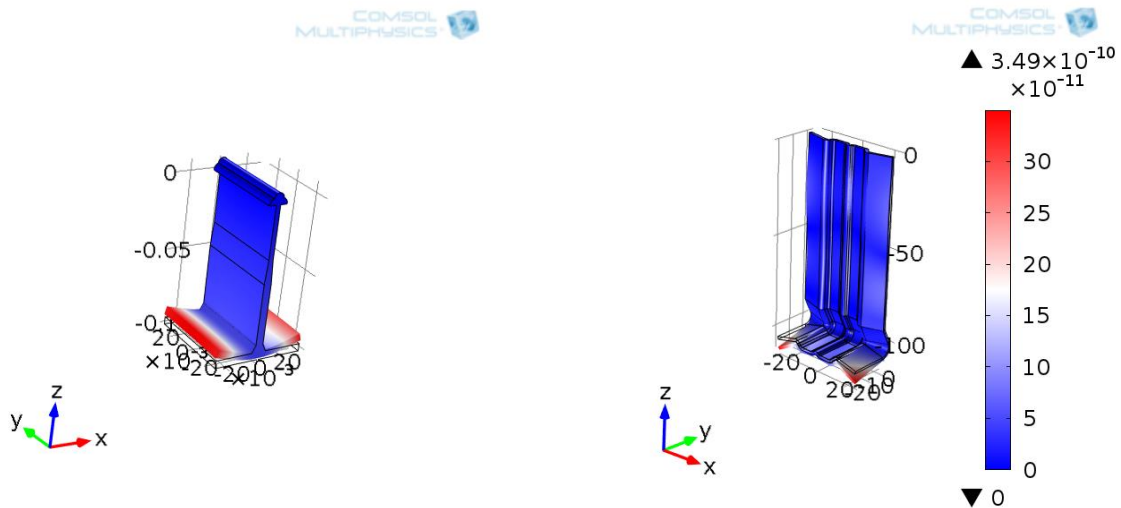


Figure 85: Comsol geometry of halter (left) and bracket (right)

The halter geometry was based on a common design (Metal Cladding and Roof Manufacturers Association 2013) . The halter is made of aluminium ($\rho = 2700 \text{ kg/m}^3$, $E = 7 \times 10^{10} \text{ Pa}$, $\nu = 0.3$), with 5mm thick base and bottom half, tapering to 3mm in the top half, and an overall height of 105mm. In an application, four screws, two either side of the base, would be used to secure the halter to the liner sheet, or top hat purlin, while the top would be inserted into a standing seam profiled panel (for the standing seam profile see Table 1).

A common bracket design was chosen. It is 1.6mm thick and made of steel ($\rho = 7800 \text{ kg/m}^3$, $E = 1.8 \times 10^{11} \text{ Pa}$, $\nu = 0.3$). In practice, it would be joined to the liner with two screws through the base, and the top inserted into the bar, screwed to the top sheet.

The boundary conditions of the connectors are not easy to characterise. The halter would only be in partial contact with the top sheet, as it is inserted into the top sheet ridges, with some rotation allowed. The bracket is inserted into a stud which in turn is screwed to the top sheet, so that there is some distance between the top of the halter and the connection point on the top plate. Accounting only for axial stiffness is a crude approximation of their real behaviour.

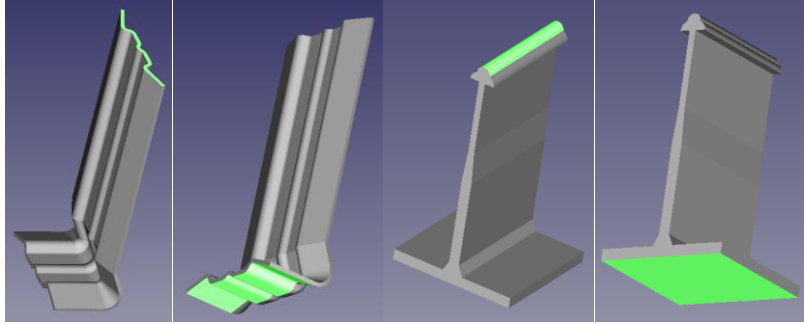


Figure 86: Prescribed displacement areas on bracket (left) and halter (right)

To obtain the stiffness matrix k_{ij} for z displacements and forces, a z direction displacement value was prescribed at the base of each connector, over the area that would be in contact with the rest of the structure (see Figure 86), while enforcing zero displacement on the top, and vice versa. The reaction forces at the top and bottom, F_{z1} and F_{z2} , are then obtained. The stiffness matrix k_{ij} is given by the ratio of the z direction reaction forces and displacements w_{z1} and w_{z2} :

$$\begin{bmatrix} F_{z1} \\ F_{z2} \end{bmatrix} = \begin{bmatrix} k_{11} & k_{12} \\ k_{21} & k_{22} \end{bmatrix} \times \begin{bmatrix} w_{z1} \\ w_{z2} \end{bmatrix} \quad (7.1)$$

The amplitudes of w_{z1} and w_{z2} were set to 0mm and 0.1mm respectively (and vice versa), so that all values of the k matrix could be obtained.

Figure 87 shows the stiffness of the two connectors derived in Comsol, with a free rotation condition either side of the connector. The bracket has a geometry such that a force on the base induces a higher degree of rotation in the element, due to its asymmetry. The first resonance of the bracket is at around 200 Hz, below which the stiffness flattens out. The stiffness of the halter is greater by about one order of magnitude, and is approximately constant throughout the frequency range. Figure 88 shows the stiffness matrices of the

connectors when rotation is constrained. The bracket and halter in this case have a similar stiffness up to 1.5 kHz, where the bracket has its lowest resonance.

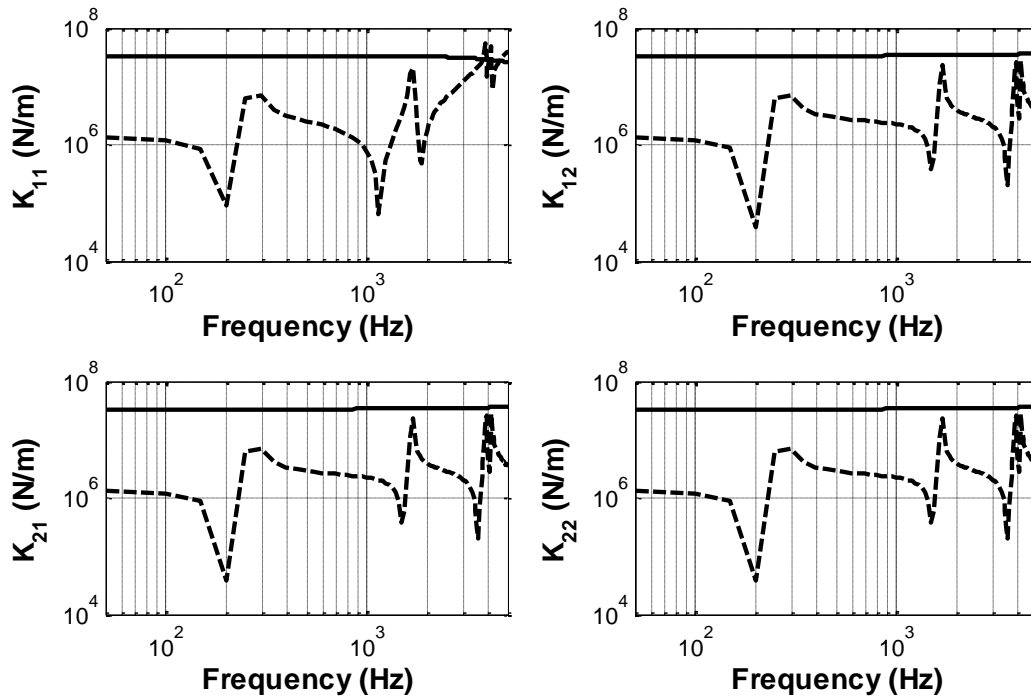


Figure 87: Comparison of FEM calculated stiffness matrix values k_{ij} between 1.6mm steel bracket (dashed line) and 3-5mm aluminium halter (solid line); free rotation

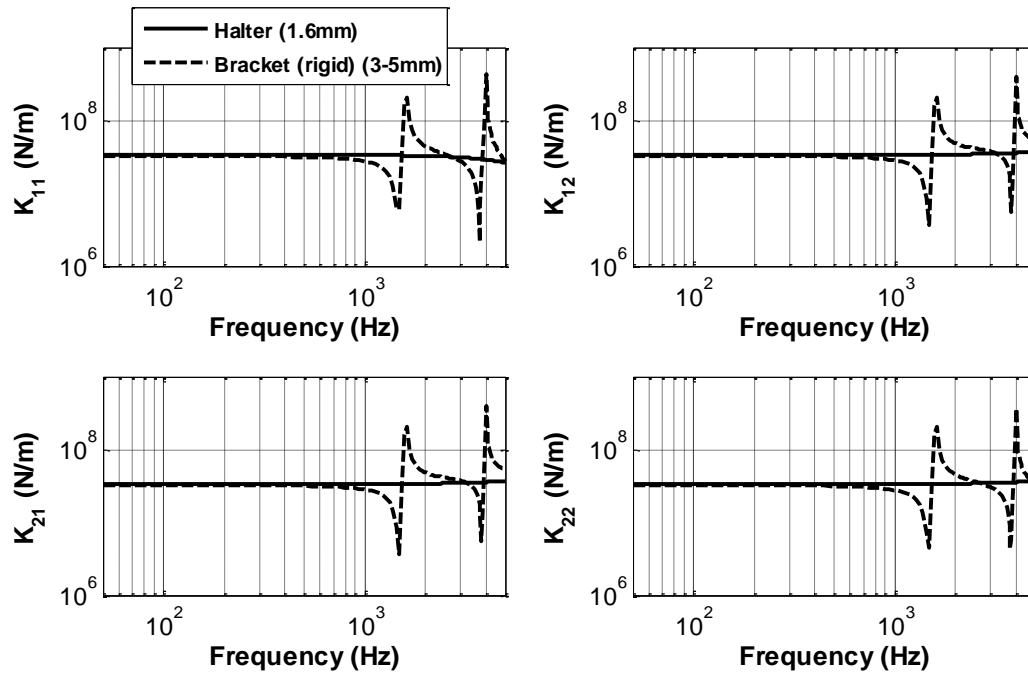


Figure 88: Comparison of FEM calculated stiffness matrix values k_{ij} between 1.6mm steel bracket (dashed line) and 3-5mm aluminium halter (solid line); constrained rotation

The dynamic stiffness of structural connectors can also be obtained by measurement. However, there are several practical issues which limit the validity of results to low frequencies, especially when dealing with high stiffness elements. With stiffness generally increasing with frequency, the differences between velocities at the top and bottom of the connector used to determine it are increasingly small and approach internal equipment noise and background noise. While stiffness values may be extrapolated to high frequency from more reliable low frequency results, these can only be a rough estimate and would neglect internal resonances.

7.2.3 Halter and bracket connectors in roof systems

In this section, the halter and bracket stiffness obtained in the previous section are introduced in the point-connected model, as described in Section 5.1, to observe their impact on diffuse TL.

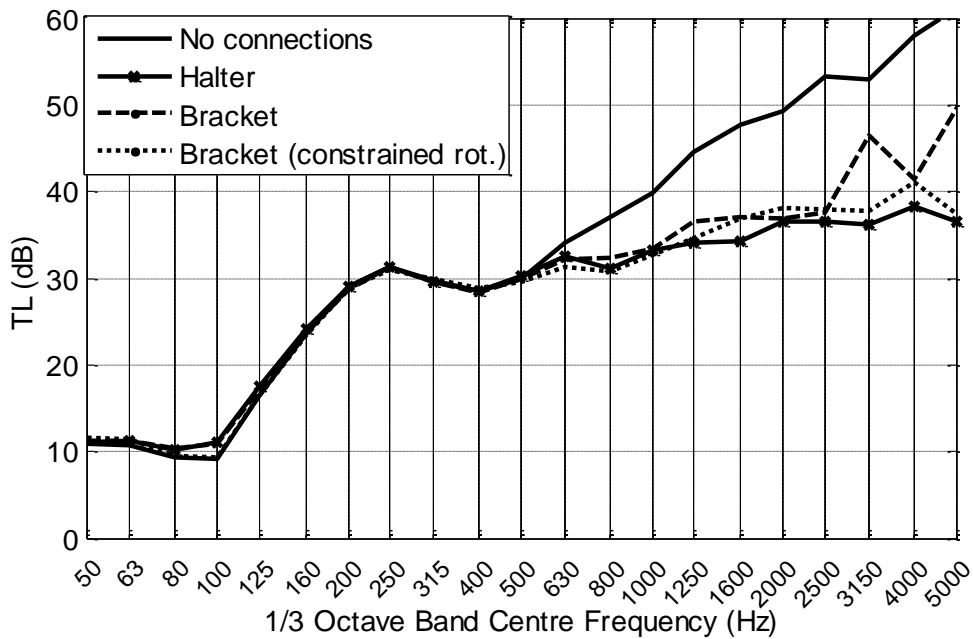


Figure 89: Modelled dual leaf corrugated roof structure with bracket and halter connectors (stiffness derived from FEM), compared to the same structure with no connectors; showing bracket with constrained and free rotation

Figure 89 shows the transmission loss of a modelled dual leaf structure with 0.7mm thick corrugated steel panels and a 100mm deep cavity filled with mineral wool. The system is modelled using the pure TMM without point connections, and with point connections at 400mm by 1000mm spacing, using the stiffness matrices of brackets and halters, obtained in Comsol as detailed in the previous section. TL is highest for the case without connections, though there is little difference between all models up to 500 Hz, the transition frequency from above which the presence of connectors causes a considerable reduction, with a difference of up to 20dB at 5 kHz. TL is on the whole similar between the connectors, though it is greater for the bracket in free rotation above 800 Hz, with a difference of up to 10dB compared with the halter. When the bracket stiffness is obtained without constraining rotation, the TL is greater than for the constrained bracket above the 2500 Hz band. The internal resonances of the bracket lead to regions of lower TL between 500 and 800 Hz, and at 2 kHz.

7.2.4 Effect of connector stiffness and spacing on dual leaf structures

While it is not trivial to extract direct relationships between diffuse field transmission loss and parameters in the analytical point-connected plate model, parametric surveys nonetheless allow some trends to be identified. In this section, broad relationships between spacing, stiffness and transmission loss are shown using modelled results.

The effect of connector spacing was examined by modelling a dual leaf system with aluminium connectors with 150mm^2 cross sectional area, modelled as static springs with stiffness matrix $K_{ij} = \frac{AE}{L}$. The structures consists of 1mm steel sheets separated by a 100mm cavity, filled with a low density porous absorber, modelled with the Delany-Bazley approach, using a flow resistivity of $6.2 \text{ kPa}\cdot\text{s}\cdot\text{m}^{-2}$. The results are shown in Figure 90. The closest spacing configuration, 100mm by 100mm, shows an overall low TL (though a higher TL up to 125 Hz compared to all other configurations). It also has a prominent dip at 315 Hz, which is a (shifted) mass-spring-mass resonance. As the spacing between the rods increases, the TL increases and the mass-spring-mass resonance is lowered, approaching the TL of the structure in the absence of connectors, also shown in the figure. The spacings of connectors in real roof systems typically exceed 300mm in both dimensions, meaning that their influence will be predominantly limited to high frequency, with a small impact on the mass-spring-mass resonance. An accurate determination of connector stiffness will be particularly important in predicting TL above 200-300 Hz.

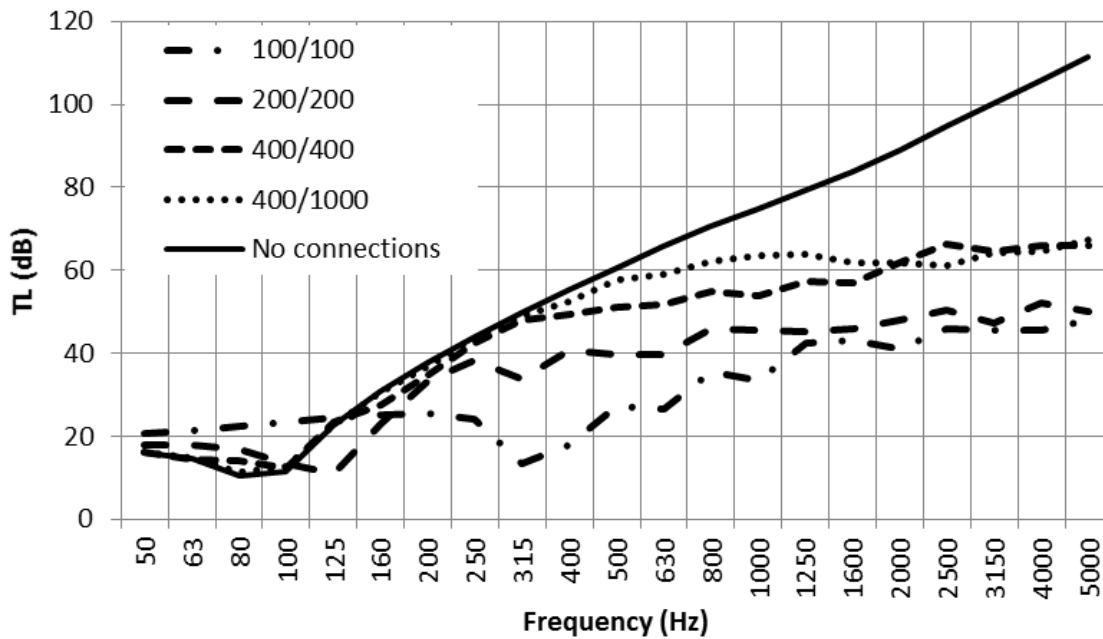


Figure 90: Transmission loss of modelled dual leaf structure with point connections of varying x/y spacing shown in mm

The influence of changes in stiffness is also important in determining what can be expected in roof structures with different spacer kits.

Figure 91 shows the transmission loss through a dual leaf structure with two sheets of 0.9mm thick steel and porous infill in a 100mm deep cavity, with connectors at 400mm by 1000mm spacing, and shows the effect on TL as the axial stiffness of the connectors – constant in frequency – is changed. Higher stiffness significantly decreases transmission loss at high frequency, and is also associated with a shift in the low frequency mass-spring-mass resonance, similarly to changing spacing, as the stiffness of the air or mineral wool in the cavity becomes negligible compared to that of the rods. This effect is described by Cremer (Cremer et al. 2005), while examining the case of floating floors, where the stiffness between two plates can be represented as parallel lumped springs, weighted by their respective surface area. As the stiffness of the connectors decreases, the TL tends to the values for a structure modelled with the TMM only, without connectors. While this holds generally, connectors will exhibit resonances as the wavelengths approach the dimensions of the connector,

providing additional regions of high transmission throughout the spectrum. The range of TL values produced by varying stiffness at high frequency suggests that an accurate determination of the connector properties is a crucial component in modelling.

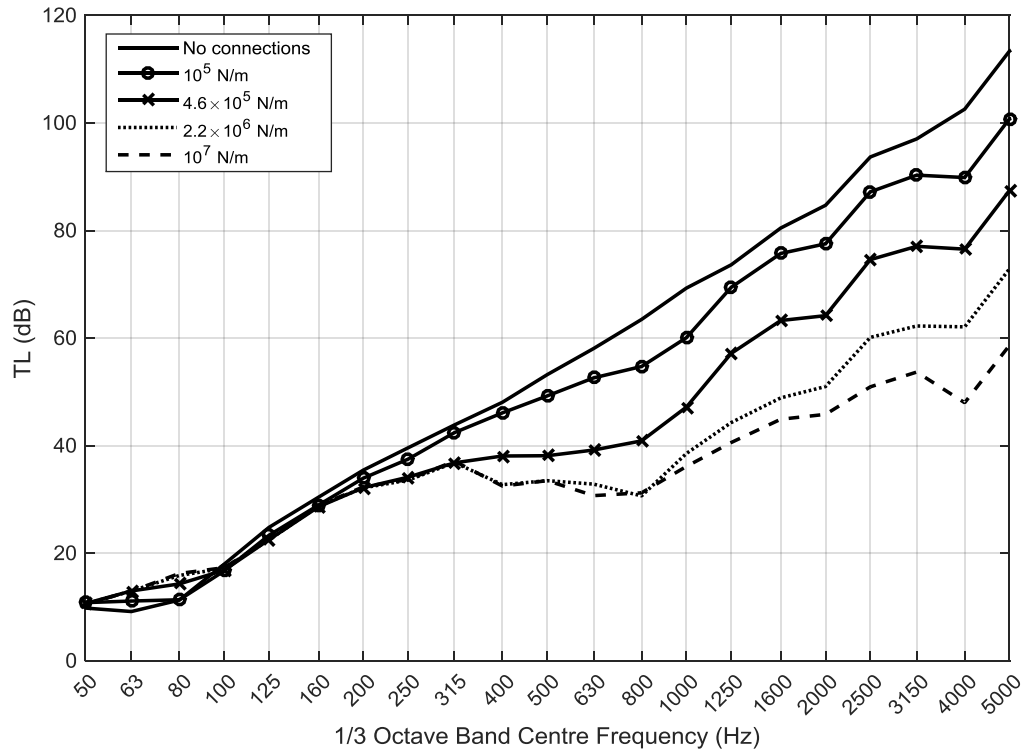


Figure 91: Diffuse field transmission loss of dual leaf roof structure with connectors of varying stiffness

7.2.5 Effect of top hat purlins

Many high performance roof structures have structural connections which run from the top metal sheet to a “top hat” beam, or purlin, as illustrated in Figure 92 (the top metal sheet is not shown). This type of structure has been modelled analytically as a point connected plate system with the addition of periodically spaced beams on the bottom plate, as described in Section 5.2. This approach assumes that the beam is in full contact with the bottom plate, acting as a constraint; however, in reality, the beam would be fixed with screws at specific points, so that this approach would likely be more applicable at low frequency. Including the

compressional stiffness of the beam was necessary to account for significant effects of varying the beam cross section and properties, which are especially important when it comes to top hat purlins, given their greater compliance than halter, as will be shown.

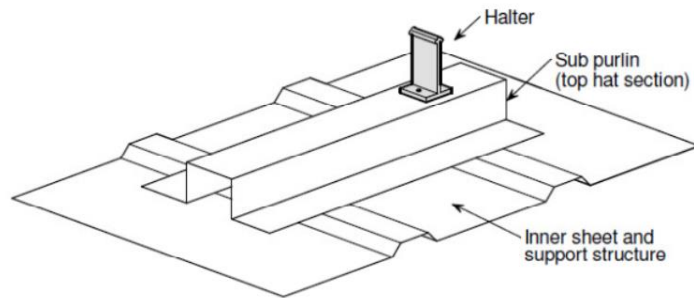


Figure 92: Halter connectors onto top hat beam, or purlin. MCRMA (2013)

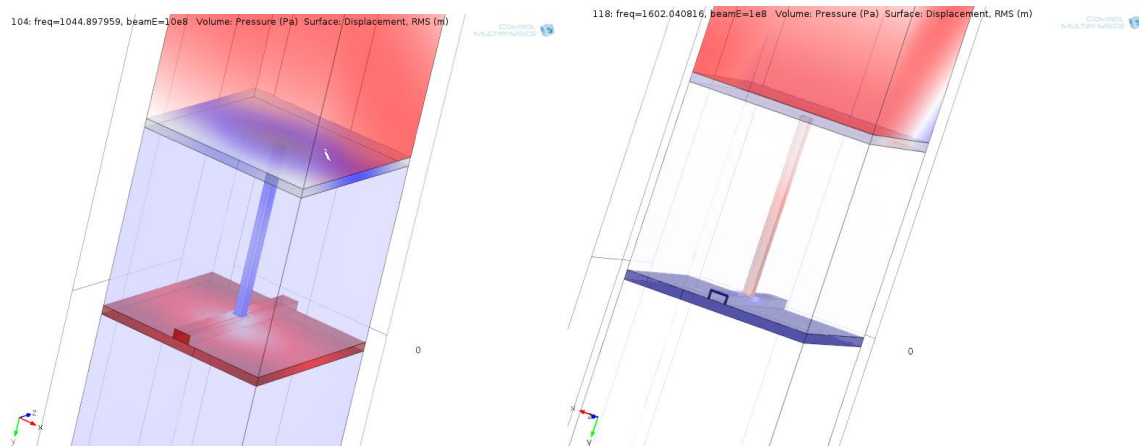


Figure 93: Geometry of point connected plates with connections onto rectangular section (left) and “top hat” section (right) beams, produced in Comsol

The system was modelled with FEM in Comsol, with both a rectangular section beam and a top hat section beam of 20 mm by 10 mm; the unit cell geometry is shown in Figure 93. Both plates in this FEM simulation are flat, 5mm thick and have the properties of aluminium ($\rho = 2700 \text{ kg/m}^3$, $E = 7 \times 10^{10} \text{ Pa}$, $\nu = 0.3$), with a loss factor of 0.1. 5mm by 5mm square section aluminium rods connect the top plate to the beam.

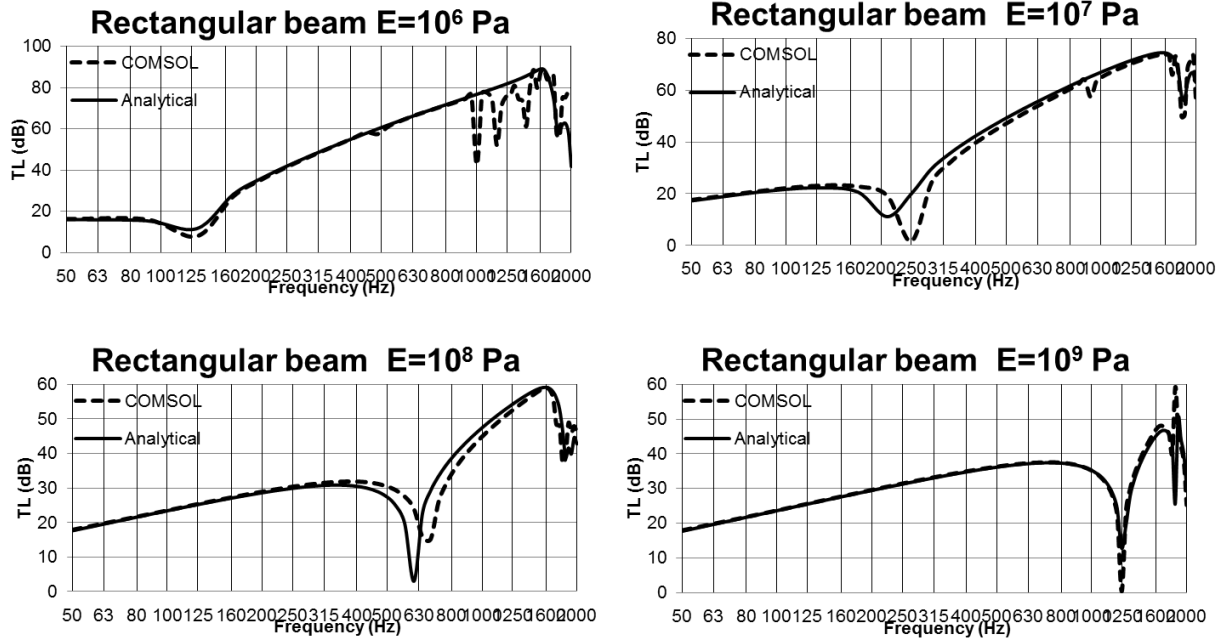


Figure 94: TL of point connected plates with intermediate rectangular section beams modelled in Comsol and analytically, varying the Young's modulus of the beam. The compressional stiffness of the beam was modelled as a stiffness value in series with that of the rod.

Figure 94 shows a comparison of FEM models of the system with a rectangular section beam of varying Young's modulus and the analytical model developed in Section, for a wave incident at $\theta = \frac{\pi}{4}$, oriented in the direction of the beam. For low values of beam Young's modulus, the analytical model fails to account for some resonant behaviour above 1 kHz. There are also differences in the predicted mass-spring-mass frequencies, which are underestimated by the model except for the lowest and highest beam Young's Modulus cases. As the purlins in real systems are not fully connected to the bottom plate, as previously mentioned, their effect cannot be easily quantified, but it is more likely that in the realistic case, being low in stiffness and not fully bonded to the bottom sheets, their stiffening effect on the panel can be neglected.

Figure 95 shows the comparison of TL between the point-connected plate system with a top hat and rectangular section aluminium beam for an incident wave at $\theta = \frac{\pi}{4}$, oriented in the

direction of the beam. What can be seen in this comparison is that the system with the “top hat” beam has a significantly lower mass-spring-mass resonance, from 650 Hz to 200 Hz. This is not a result of the change in bending stiffness of the beam, as it is not predicted by the analytical model when accounting only for the beam’s bending stiffness, neglecting its compressional stiffness.

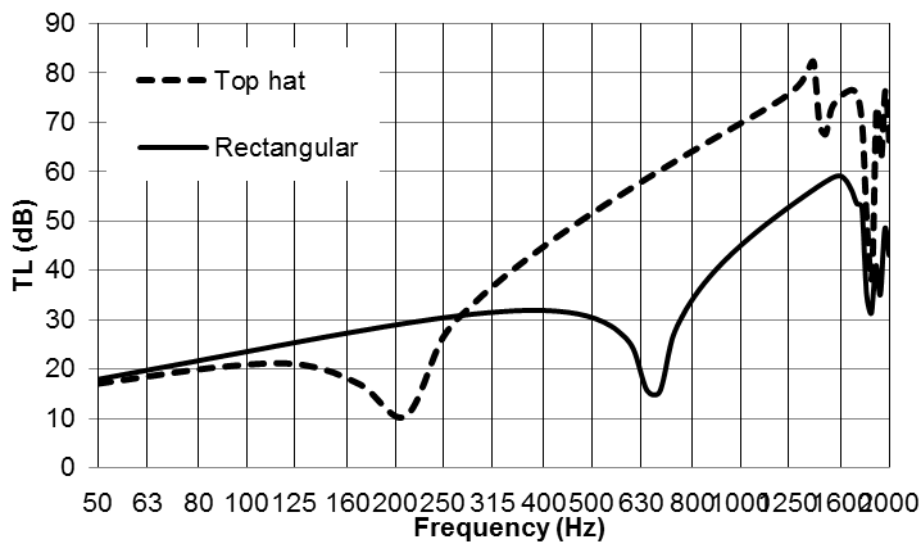


Figure 95: TL of point connected plates with intermediate beams modelled in Comsol; result of changing beam section from rectangular to top hat

In light of these results, determining the difference in compressional stiffness between a typical halter connector and a halter mounted on a top-hat beam section would help to make sense of comparisons with laboratory measurements of full structures in diffuse conditions, having observed dramatic differences.

A realistic halter on a top-hat purlin section was also modelled in Comsol, with the same method outlined in Section 7.2.2, by isolating the component and measuring its stiffness. Displacements are constrained at the top of the halter, and on the legs of the top hat purlin, where it would be joined to the liner sheet. Figure 96 shows the modelled geometry in Comsol. The halter is the same as in Section 7.2.2, and the top hat beam is 1.25mm thickness

steel of the same width as the base of the halter, 60mm. Figure 97 shows a comparison of axial stiffness between the halter alone (solid line) and the halter firmly mounted on a top-hat purlin (dashed line). The addition of the top-hat section reduces the stiffness an order of magnitude. The value of k is approximately constant in frequency up to the first resonance at 1 kHz.

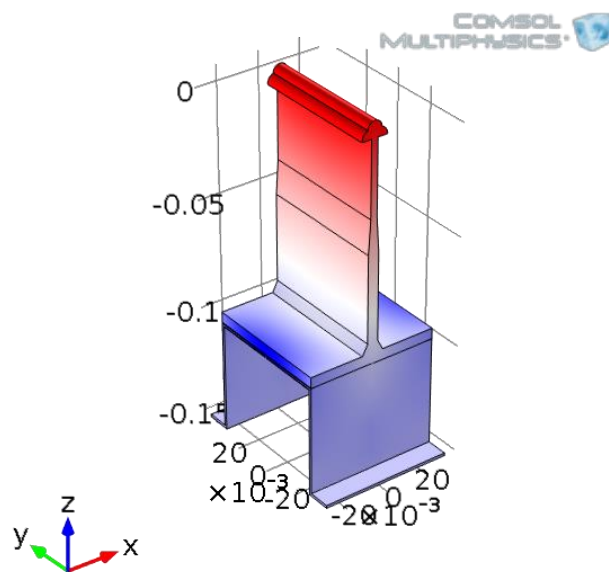


Figure 96: 100mm aluminium halter mounted on 1.25mm steel top-hat purlin, Comsol geometry

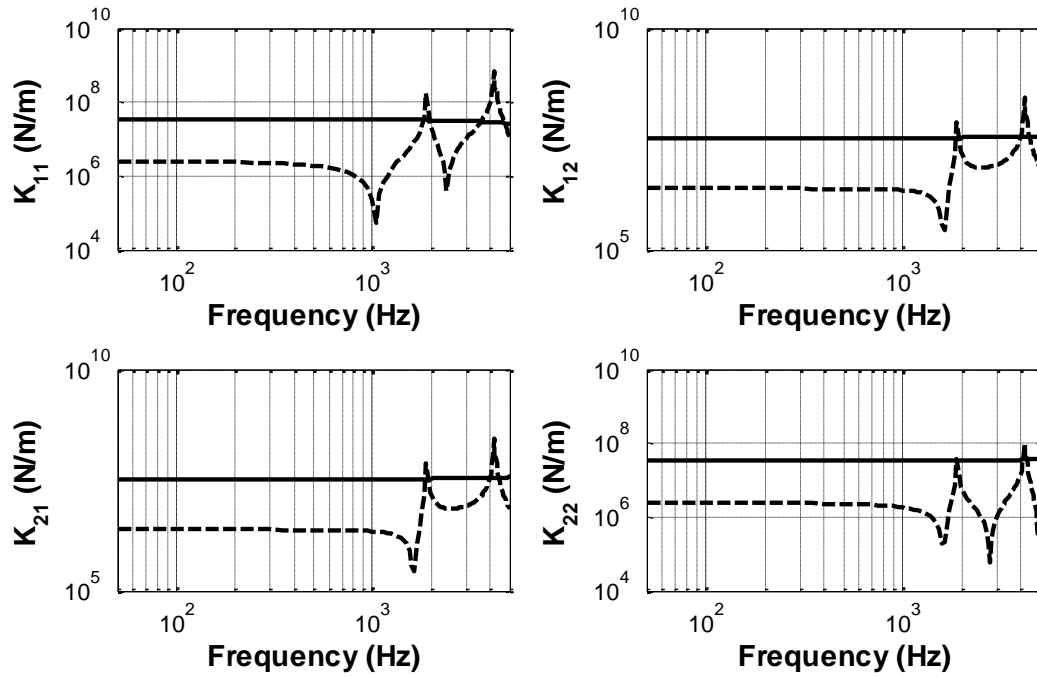


Figure 97: Axial stiffness matrix k_{ij} for a halter (solid line) and a halter + top-hat purlin (dashed line)

The stiffness matrix of the halter and top-hat beam section obtained with FEM was used to calculate the diffuse field transmission loss of the same roof structure as Section 7.2.3, and is shown in Figure 98. Compared to the modelled structure with halters alone, the diffuse transmission loss is 5-10dB greater above 800 Hz.

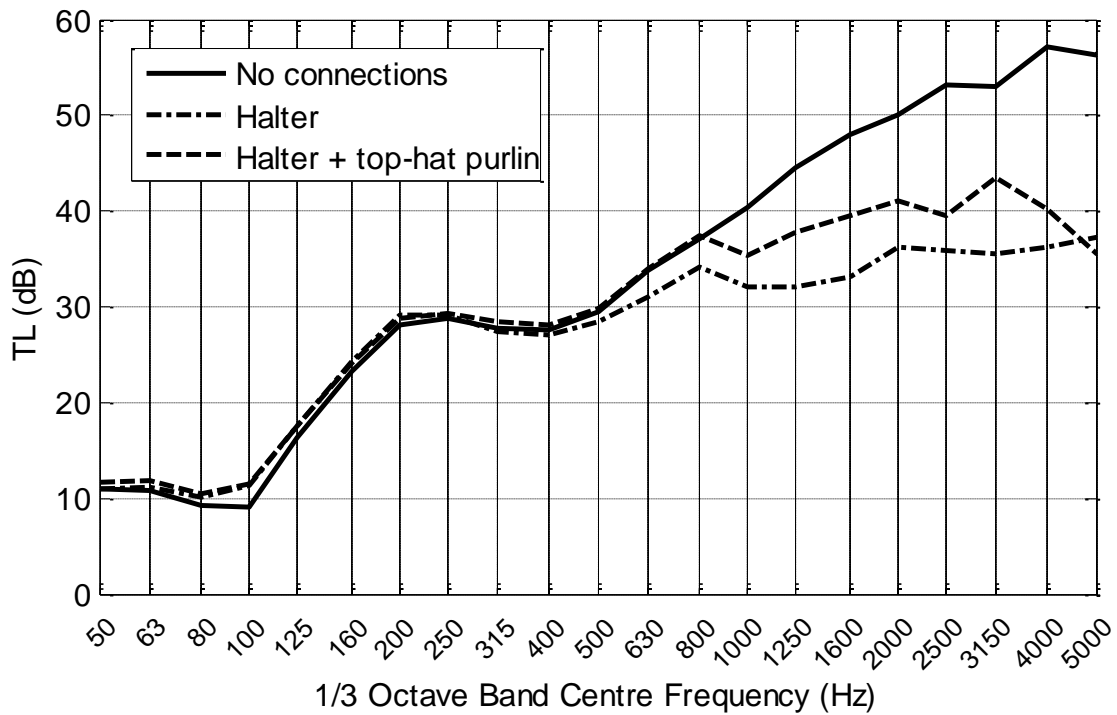


Figure 98: Modelled dual leaf corrugated roof structure with halter and halters on top-hat beam section (stiffness derived from FEM), compared to the same structure with no connectors

7.2.6 Conclusions

The point connection model was validated against FEM simulations of two flat plates connected by periodically spaced thin rods; the model accurately captured the TL features of the simulated structure, including the effect of varying connector stiffness.

Two common types of roof connectors, halters and brackets, were compared via FEM simulations, and their FEM-derived stiffness was used within the point connections model to observe their effects on overall TL of a dual leaf structure.

The effect of top hat purlins was also examined. A typical aluminium halter mounted onto a steel top hat beam was modelled with FEM; the stiffness is overall reduced by the top hat section compared to a halter by itself. The effect of the top hat purlin on the TL of a dual leaf system was also determined in FEM, showing that where the beam is more compliant than

the point-to-point connector, the compressional stiffness is an important factor in transmission and can influence the overall mass-spring-mass frequency and increase transmission loss overall. In a modelled roof structure, the transmission loss at high frequency for a typical top-hat purlin was greater by 5-10dB compared to a halter.

7.3 CORRUGATED ROOF STRUCTURES: COMPARISONS WITH LABORATORY MEASUREMENTS

Having investigated the performance of the model in comparison with that of FEM models in the previous section, as well as the influence of framework and connector details, we now go on to compare predicted results with those of laboratory tests.

The comparisons will start from the simplest available structures, to more complex ones with several layers:

1. Rooflights: structures with no infill and rigid connectors
2. Twin skin roofs with a single layer of low density infill and rigid connectors
3. Twin skin roofs with multiple layers of infill and connectors
4. Twin skin roofs with additional internal high density boards screwed to the inner metal sheets

7.3.1 Rooflights

Rooflights, described in Section 2.4, are a good example of a simple corrugated roof structure. They are most commonly dual leaf structures with corrugated polycarbonate sheets and no cavity infill. Figure 99 shows a typical rooflight, including steel fixings either side of the crown of the outer sheet. The lack of cavity infill, as they are designed to allow light to

shine through, means that the uncertainties relating to the properties of mineral fibres and other types of infill are absent.

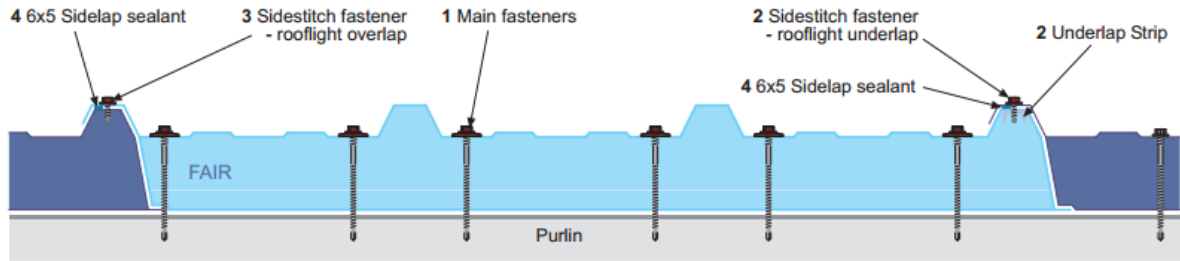


Figure 99: Rooflight diagram showing steel fixings

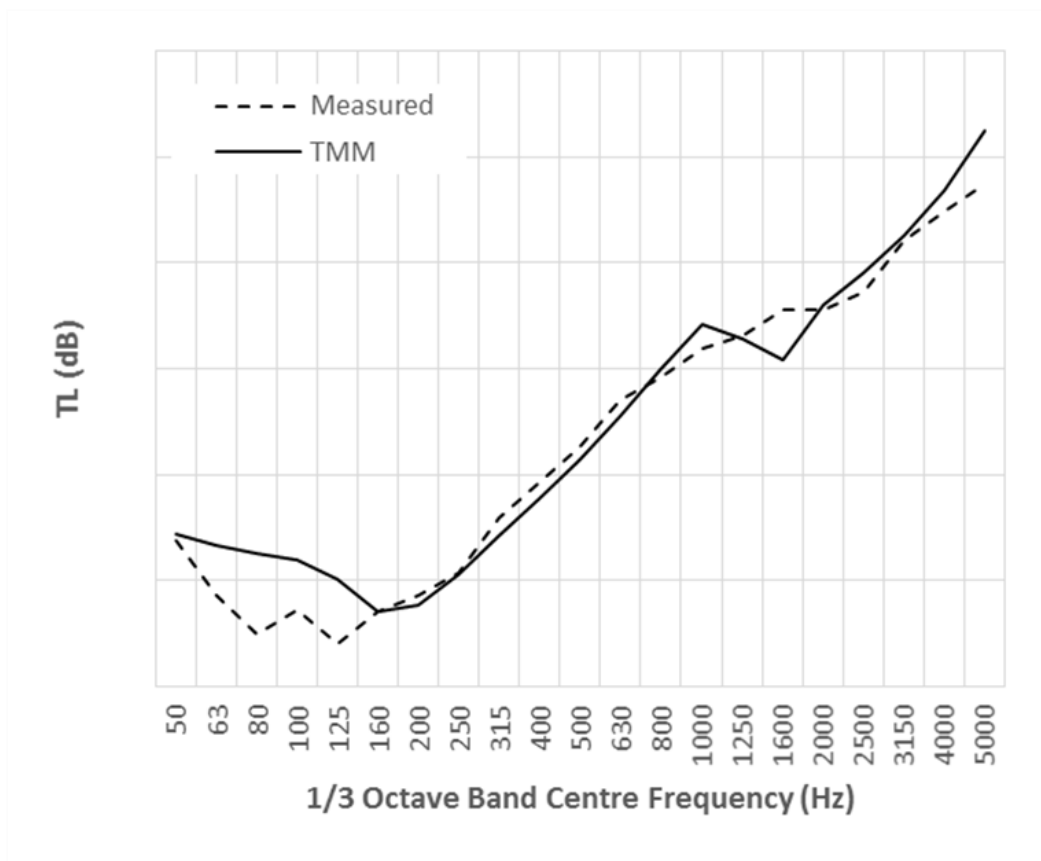


Figure 100: Comparison of TMM modelled rooflight TL with measured diffuse field transmission loss (y axis gridlines are in 10dB steps)

Figure 100 shows the measured TL of a rooflight system together with the TMM modelled TL. There is a strong mass-spring-mass resonance at low frequency, followed by a steady increase in TL. At high frequency, from 1 kHz onwards, there are resonances when the z component of the waves in the cavity k_{z_c} are half of the cavity depth (and integer multiples), $k_{z_c} = n \frac{\pi}{d}$, where d is the cavity depth and n is a positive integer. This effect is more noticeable in the modelled curve, where the damping in the cavity is zero.

Introducing even rigid point connections into this system has a relatively small effect as the transmission path through the air in the cavity is strong. Figure 101 shows the predicted transmission loss of the same rooflight for each angle of incidence θ on the y axis, and frequency on the x axis, with and without rigid point connections at 500mm x and y spacing. On the top graph of the figure, which shows the case without point connections, a dip can be seen at very low frequency, the mass-air-mass resonance, which is a line of low transmission loss values running from normal incidence to grazing incidence without much change in frequency, at around 200 Hz. Two strong critical frequencies associated with the GRP sheets can be seen running from grazing incidence ($\theta = \frac{\pi}{2}$) and describing arcs pointing in the positive frequency direction; these are the lower critical frequencies that occur along the stiffest dimension of the corrugated profiles. The resonances of the waves in the cavity can be seen from just over 1000 Hz at normal incidence (and not at grazing incidence, as the wavelength in the z direction is infinite) and at regular intervals. These features can still be seen, albeit with some difficulty, in the bottom graph, which shows the transmission loss including point connections between the GRP sheets, where additional resonances due to the connectors can be seen.

The mass-air-mass resonance is slightly higher in the point-connected model – this is clearer from Figure 102 which compares the diffuse field transmission loss of the two cases, where

the dip shifts from 150 Hz to 200 Hz. The critical frequencies occur in the same locations. The many resonances associated with the connections have an impact at high frequency, as the transmission loss begins to deviate from 500 Hz onwards.

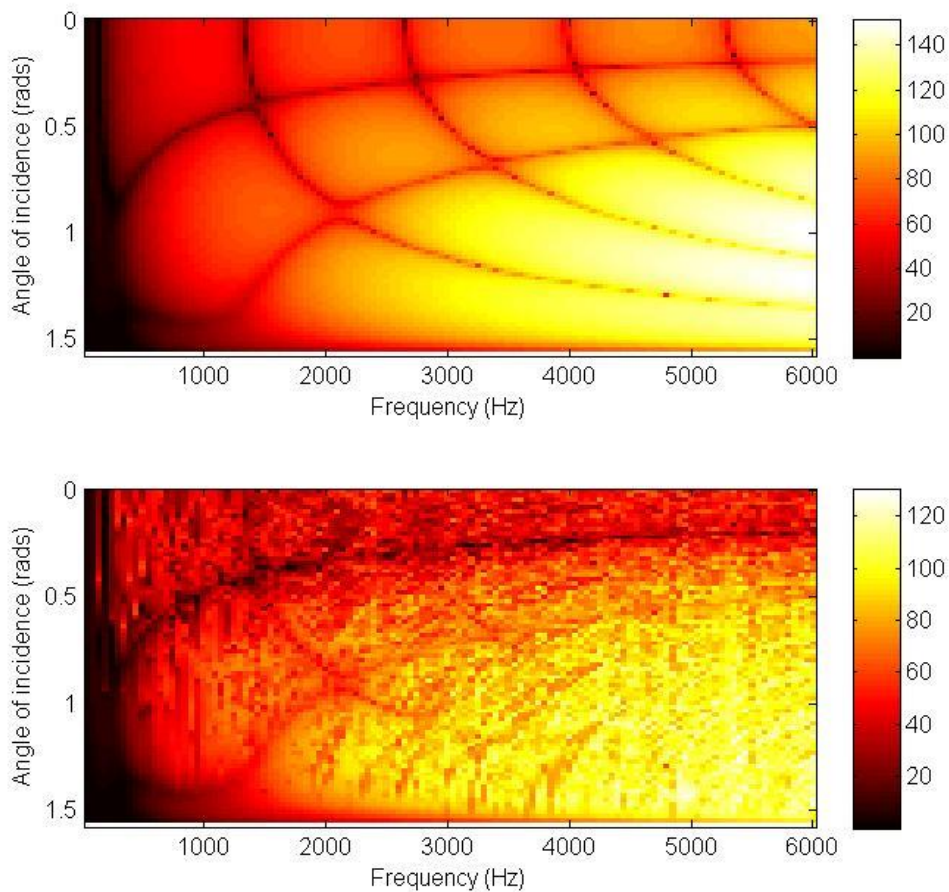


Figure 101: Predicted transmission loss of rooflight system with (bottom) and without (top) point connections at 500mm x and y spacing; wave travelling along corrugations

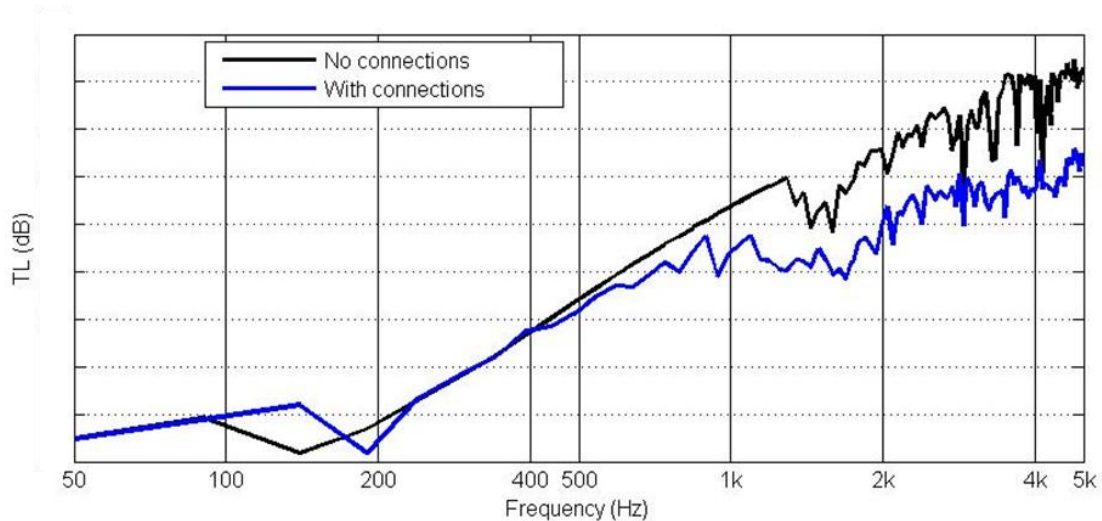


Figure 102: Diffuse field predicted transmission loss of rooflight with and without point connections at 500mm x and y spacing (y axis gridlines are in 10dB steps)

7.3.2 Roof structures with soft fibrous infill

In this section, roof structures with the addition of low density mineral wool infill are compared to the TMM and point-connected models, adding in complexity from the previous section; the results examined include roofs with both halter and bracket connectors.

7.3.2.1 Roof with halter connections: L3057

The TMM and point-connected plate model were used to predict the performance of a basic corrugated roof construction, ‘L3057’, with low density fibrous infill and stiff halter connectors, a diagram of which is shown in Figure 103. The data has been obtained from the laboratory measurement database of the MCRMA (2013). This system consists of two outer profiled metal sheets (aluminium top and steel bottom) with a low density fibrous infill (15 kg/m^3) in the cavity, and periodic aluminium halter connections.

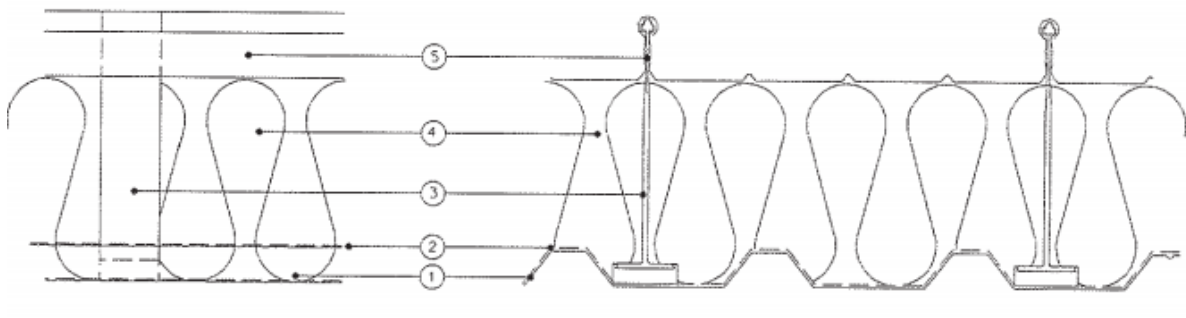


Figure 103: Diagram of simple dual leaf roof structure (L3057) with halter connectors (item 3); MCRMA (2013)

These halter connections are stiff, and as shown in the diagram, the top portion is placed inside the ribs of the top sheet. The system was modelled with and without point connections with stiffness modelled in Comsol, and using the properties of mineral wool infill measured according to the method in Section 4.2.6; the results are shown in Figure 104. The point connection model falls in line with measured values when compared to the pure TMM case without connections, with good agreement especially at low to mid frequency. A dip can be seen at around 1 kHz in the measured result, which appears to be present to a lesser extent in the predicted values with point connections. As the spacing between the connectors is relatively large (400mm by 1400mm), resonances introduced by these begin at low frequency and are closely spaced, as has been seen with rooflights in the previous section. The structure-borne energy transmission through the connections dominates at high frequency, as well as slightly increasing the transmission loss at lower frequency, where the pure TMM case greatly overestimates transmission loss, by up to 40dB. Compared to the case of rooflights, where there is no cavity infill, the introduction of point connectors has a dramatic impact on transmission loss at high frequency, as the transmission through the absorbent material in the cavity is much lower than the contribution through the connectors.

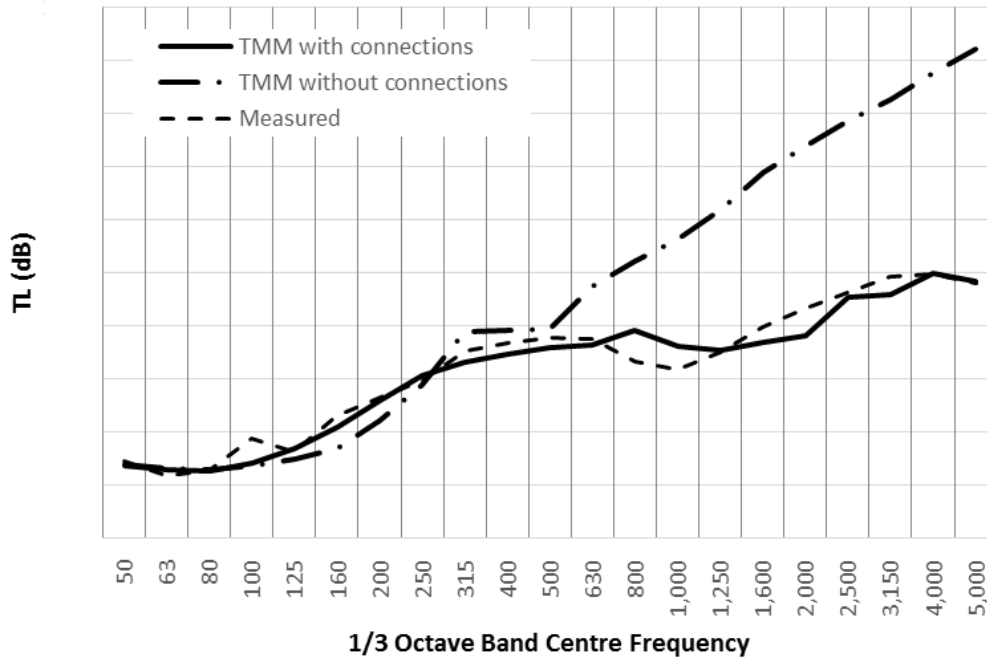


Figure 104: Transmission loss of typical commercial corrugated roof system with soft fibrous infill and halters at 1400mm by 400mm spacing; measured (dashed) versus periodic point-connected model (solid) (y axis gridlines are in 10dB steps)

7.3.2.2 Structures with bracket connectors

In this section, basic roof systems with bracket connectors are examined with comparisons to laboratory measurements.

The data was obtained from the test database of MCRMA (2013). All structures in this section follow the design shown in Figure 105, with trapezoidal profile steel panels of 0.4mm and 0.7mm thickness, mineral wool infill and bracket connectors. The properties of the structures are found in Table 9.

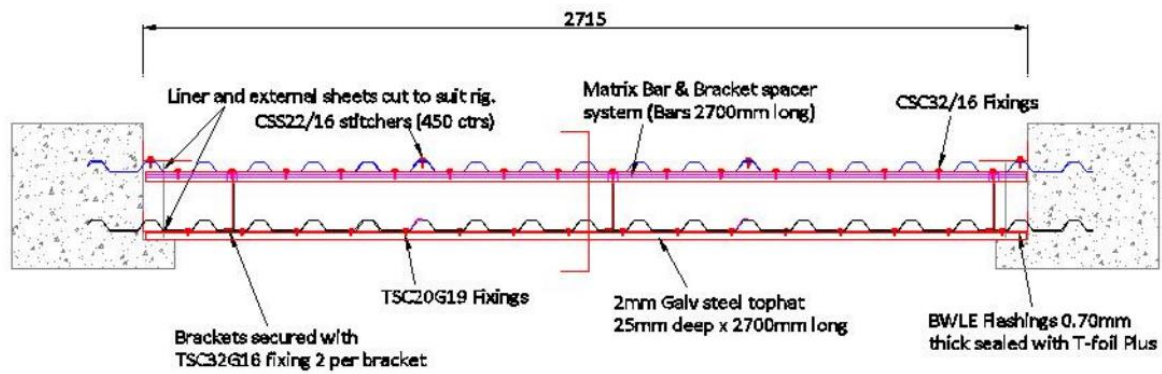


Figure 105: Corrugated metal roof with bracket connectors (cavity infill not shown); MCRMA (2013)

Structure reference	Features
R02	Mineral wool density: 11 kg/m ³ Top sheet thickness: 0.7 mm Top sheet depth: 32 mm Liner thickness: 0.7 mm Liner depth: 32 mm Cavity depth: 220 mm
R04	Mineral wool density: 26 kg/m ³ Top sheet thickness: 0.7 mm Top sheet depth: 32 mm Liner thickness: 0.7 mm Liner depth: 32 mm Cavity depth: 220 mm
R07	Mineral wool density: 11 kg/m ³ Top sheet thickness: 0.7 mm Top sheet depth: 32 mm Liner thickness: 0.7 mm Liner depth: 32 mm Cavity depth: 140 mm
R08	Mineral wool density: 11 kg/m ³ Top sheet thickness: 0.4 mm Top sheet depth: 17 mm Liner thickness: 0.7 mm Liner depth: 32 mm Cavity depth: 140 mm

Table 9: Features of corrugated roof structures with low density mineral wool

As bar and bracket spacer kits are less stiff than halters, the transmission loss of structures with brackets is expected to be slightly higher than halters at high frequency, all other parameters being equal.

The first structure examined, referenced R02, has 0.7mm thick steel inner and outer sheets, of the same 32mm deep trapezoidal profile, and mineral wool infill of density 11-12 kg/m³ in a 220mm cavity. The mineral wool was modelled as a single fluid layer using the Delany-Bazley approach based on the properties of glass wool derived using the best fit method in Section 4.2.6. The Delany-Bazley approach is suited for this type of low density infill, as transmission of solid waves through the material frame can be neglected. Figure 106 shows the measured diffuse transmission loss compared to a pure TMM model (the system without connectors) and the point-connected model, using FEM derived bracket stiffness. Both models are in good agreement up to 100 Hz. The point connected case deviates from the TMM model above 100 Hz. The measurement result is closest to the TMM case from 500 Hz onwards, though there is a 10-15 dB discrepancy around the critical frequency of the profiled metal sheets, with the model showing a pronounced dip at 630 Hz. The measured result shows no visible lower critical frequency dip at 315 Hz, though the slope of the TL curve decreases above 100 Hz, suggesting a change in behaviour related to the corrugations. As was discussed in Section 4.3.2, corrugated and ribbed sheets only present a strong critical frequency dip when the pitch dimension is near the bending wavelength of the panel, with the effect diminishing with increased pitch and reduced thickness.

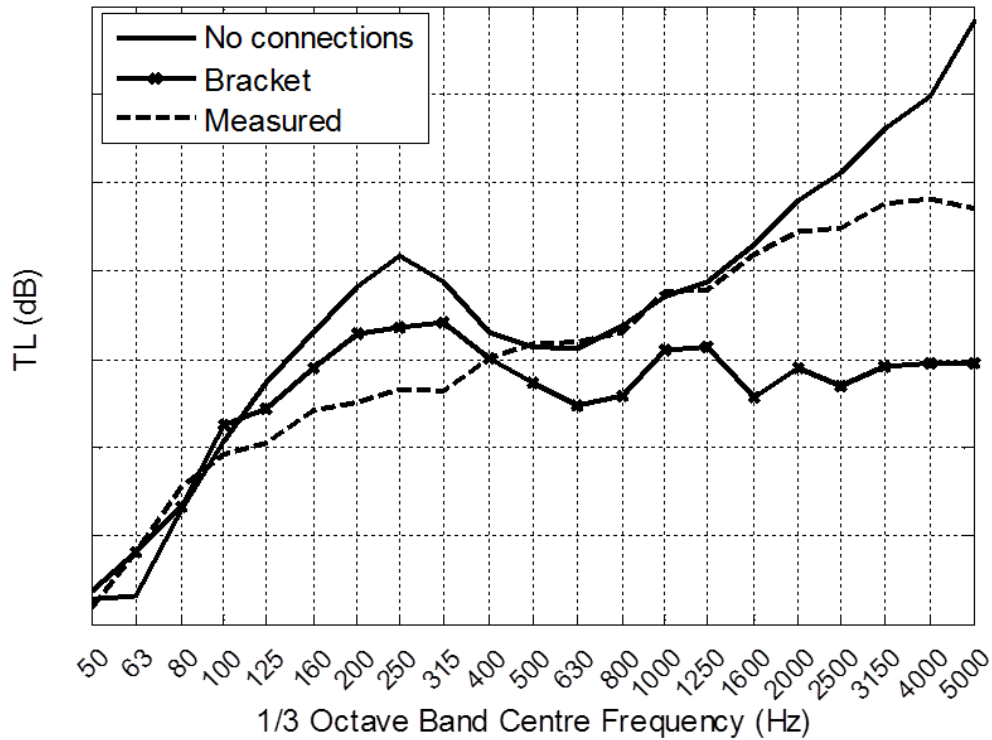


Figure 106: Diffuse transmission loss of corrugated metal roof R02 with bracket connectors against TMM model with and without rigid point connections (y axis gridlines are in 10dB steps)

Structure R04 has a higher density infill, and the same cavity depth of 220mm. The higher density infill was modelled with poroelastic properties, though the point connected model neglects mechanical coupling between the metal sheets and the infill. Results for this structure are shown in Figure 107. The comparisons are very similar to the previous case, with the same discrepancy between 100 Hz and 400 Hz, and better overall agreement from the pure TMM.

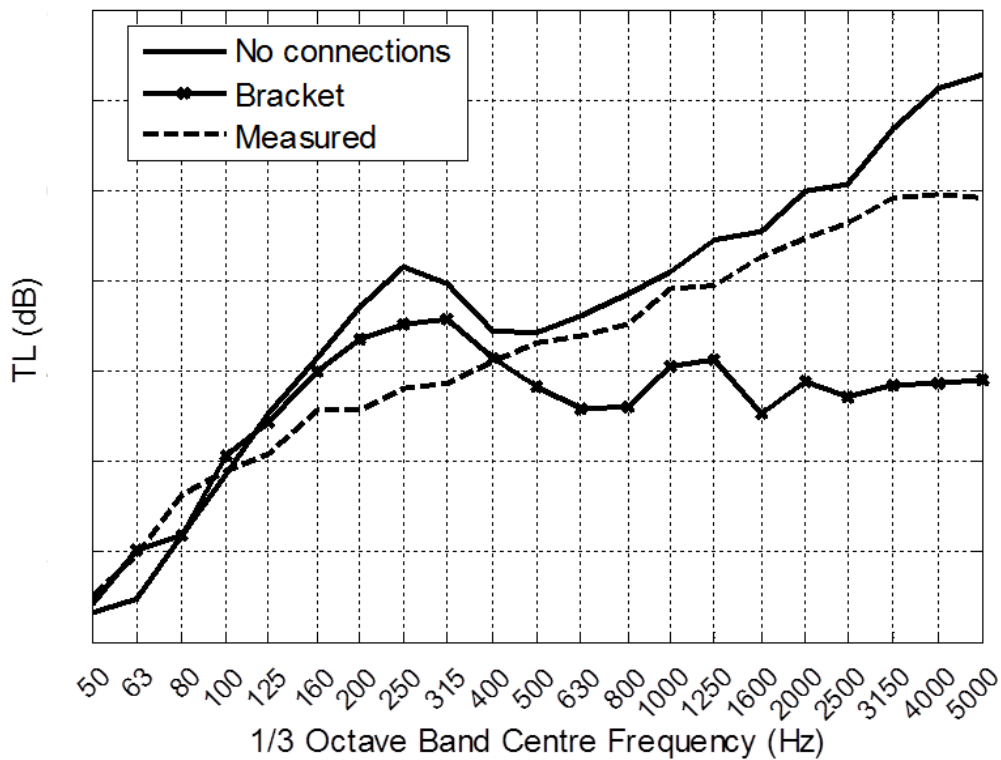


Figure 107: Diffuse transmission loss of corrugated metal roof R04 with bracket connectors against TMM model with and without FEM-derived bracket connector stiffness (y axis gridlines are in 10dB steps)

The structure referenced R07 has two 0.7 mm corrugated steel sheets with the same trapezoidal profile of 32 mm depth, and low density infill (11 to 12 kg/m³) and a smaller cavity of 140 mm. The results are shown in Figure 108. The TMM model of this structure predicts an initially rapid increase in transmission loss with frequency (immediately above the mass-air-mass resonance at 63 Hz) and subsequently a dip at the first lower critical frequency (400 Hz), which is noticeable as it is the same for both metal panels. From there on, the slope of the curve is determined by the connection stiffness; the connections tend to dominate transmission in this region, though their impact on transmission loss is smaller since the mineral wool absorption is relatively low. Once again, transmission loss is underestimated when modelling the structure with connectors, which indicates that the connector stiffness is lower in the real structure.

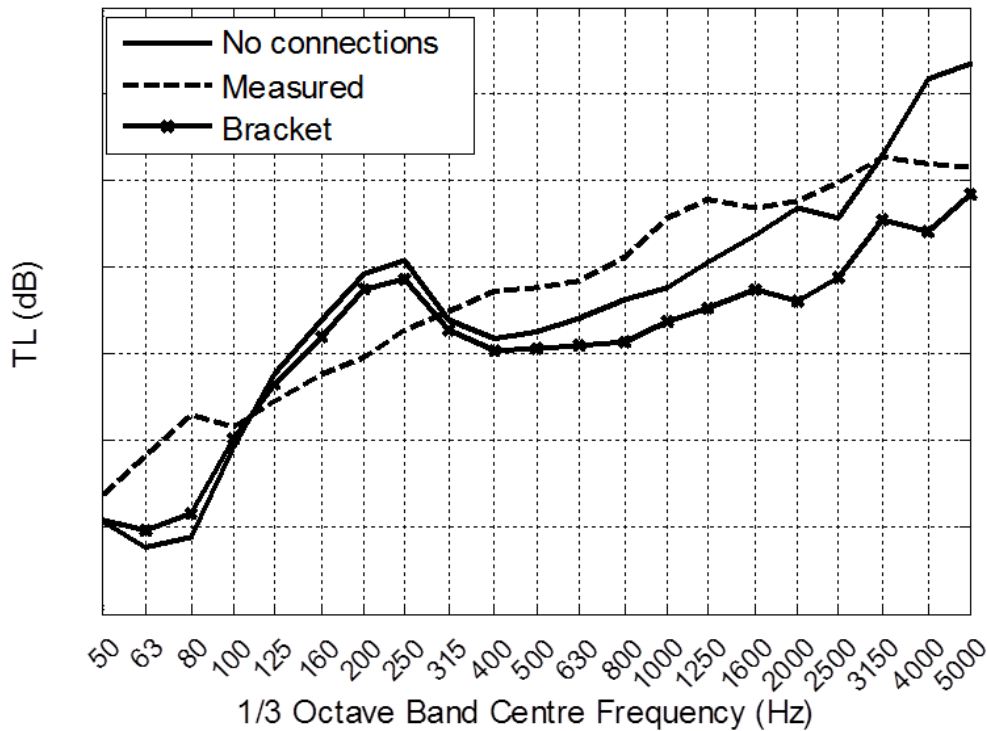


Figure 108: Diffuse transmission loss of corrugated metal roof R07 against TMM model with and without point connections (y axis gridlines are in 10dB steps)

Structure R08 has both different thicknesses and different profiles, with a 0.4 mm top sheet of 17 mm depth and a 0.7 mm liner of 32 mm depth, with a 140mm cavity. The results are shown in Figure 109. The modelled TL with the pure TMM is the highest overall, and overestimates the measured values by up to 40 dB at high frequency. The reason for this is that the mismatch in panel profiles and thicknesses results in two distinct lower critical frequencies in the model. As the critical frequencies do not overlap, their combined effect is spread over the frequency range, and transmission loss is higher. In reality, as has been shown in Section 6.3, the diffuse transmission loss of corrugated panels of different depth tends to be similar, and it does not present strong critical frequency dips except for small profile periods and high thickness. The introduction of point connectors in this case has a greater impact on overall transmission loss, reducing the high frequency response to the range observed in the measured values above 250 Hz.

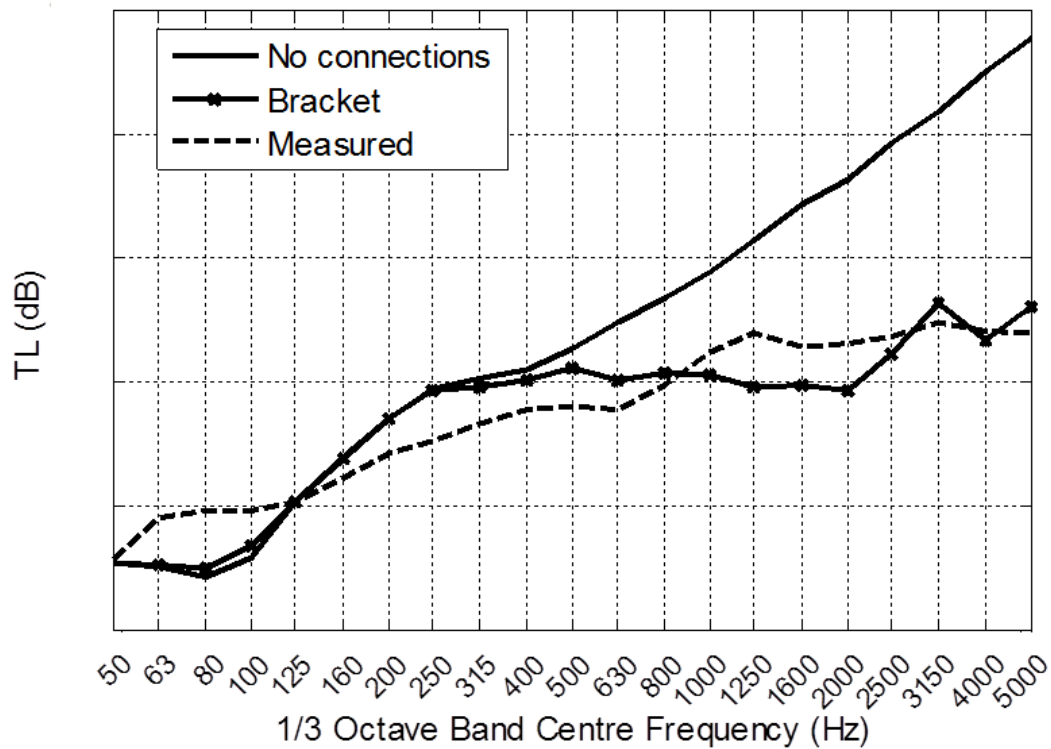


Figure 109: Corrugated metal roof (R08) with 140mm cavity and bracket connectors against TMM model with and without point connections (y axis gridlines are in 20dB steps)

7.3.3 Roof structure with high density infill and top-hat purlins

So far, structures with single layers of low density infill have been examined. Roof structures with multiple layers of high density infill further complicate modelling, as the influence of frame-borne waves in the porous infill may be significant, depending on the mounting conditions. In this section, a roof structure is considered which has multiple layers of high density mineral wool, and halter connectors onto top hat purlins.

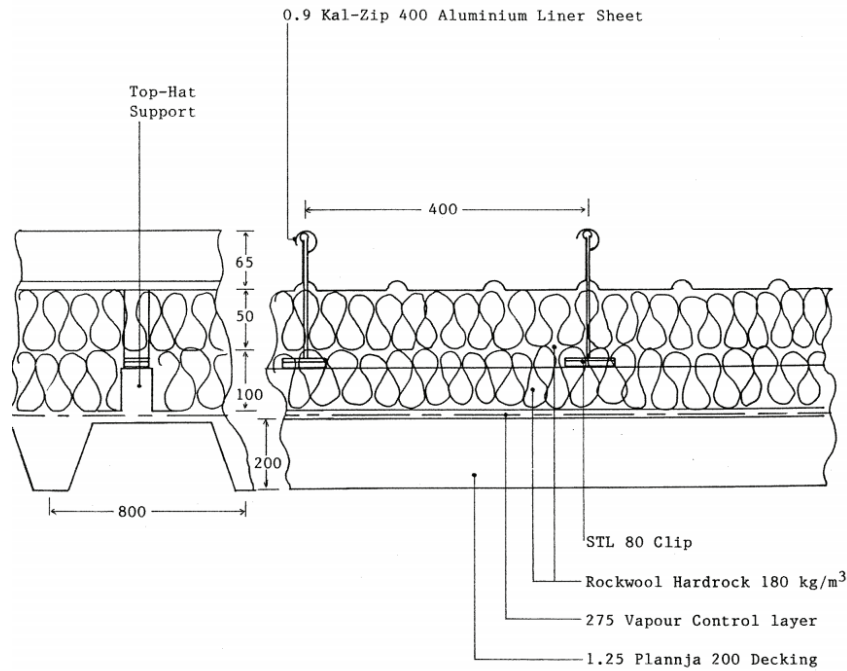


Figure 110: Roof structure L-2297 with halters and two layers of high density infill (180kg/m^2), MCRMA (2013)

The following results were chosen from data provided by the MCRMA (2013). Figure 110 is the diagram of the roof structure, L-2297, with halters onto top-hat purlins screwed to the liner sheet and two slabs of high density mineral wool (180kg/m^2), where each slab consists of two layers of different densities bonded together; the top sheet is 0.9 mm thick aluminium, the bottom sheet is 1.25 mm thick steel decking, with a large pitch of 800 mm, and a 200 mm deep profile. The combined layers of mineral wool were nominally the same thickness as the cavity. The mineral wool properties were obtained via normal incidence measurements of surface impedance of small samples (100 mm diameter) in an impedance tube, by reverse engineering the values from a poroelastic model, as described in Section 4.2.6. As each layer of mineral wool is dual density, each sample was separated into high and low density parts which were measured separately and modelled as distinct layers in the final TMM model, so that the cavity consisted of four adjacent poroelastic layers. By obtaining the effective fluid properties of these layers, they are effectively decoupled from the plates in the periodic point-

connection model. In the pure TMM, the metal sheets can be similarly decoupled, as has been previously outlined, by adding thin air layers between the metal sheets and the infill.

This structure is particularly complicated to model, and three approaches were taken:

1. With compliant point connections (the mineral wool is not in mechanical contact with both sheets, as the analytical model only accounts for longitudinal waves in the cavity space) based on FEM derived stiffness of halter onto top-hat beam (connector geometry in Section 2.3)
2. Pure TMM, without point connections, with mineral wool separated from the outer metal sheets by 1mm air layers ('unbonded')
3. Pure TMM, without point connections, with mineral wool fully in contact with both sheets ('bonded')

Figure 111 shows the laboratory measured diffuse TL compared to the TMM and point-connection models in the above arrangements. The closest modelled result to the measurement is the 'fully bonded' case (item 3 above). All other modelled scenarios overestimate TL by 10dB between 100 Hz and 500 Hz, suggesting that contact between mineral wool and the metal sheets contributes significantly to the transmitted energy. The shape of the modelled 'bonded' TL shows resonances due to the high density mineral wool layers, with a dip at 315 Hz, which can also be observed in the measured result. The dip is a mass-spring-mass resonance formed by the stiffness of the infill between the two metal sheets.

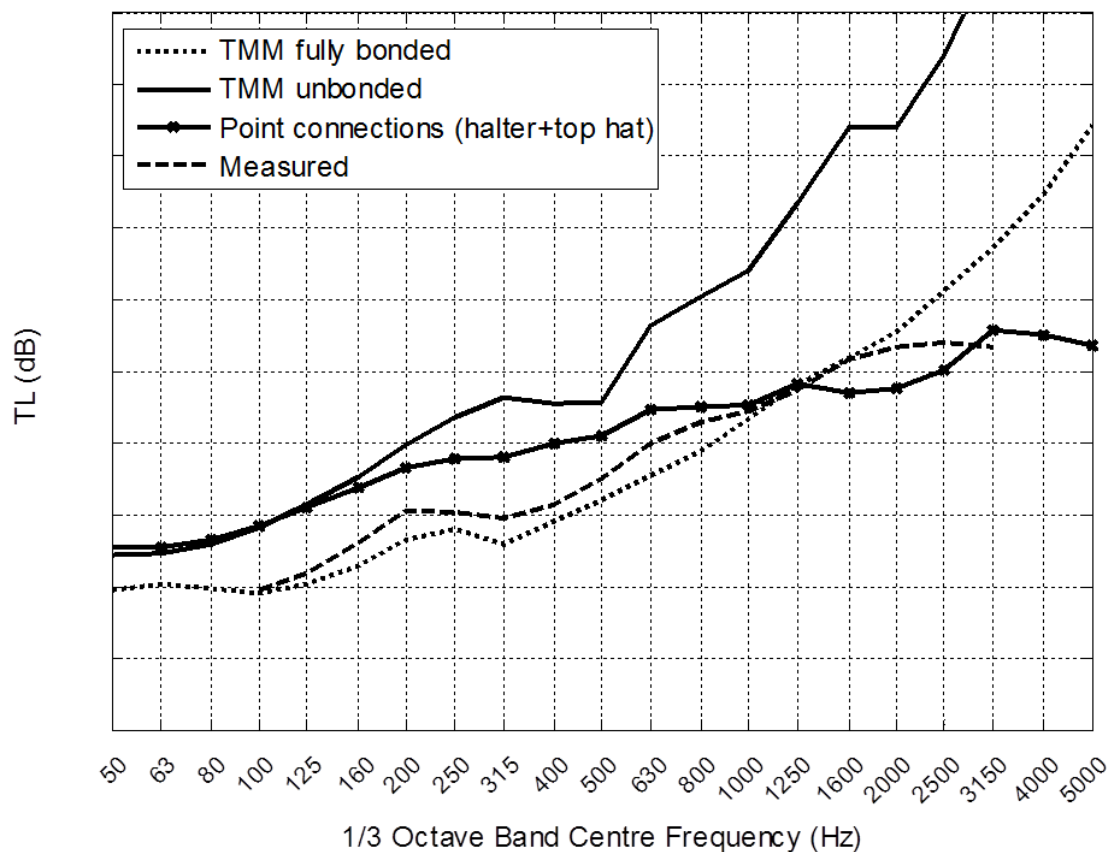


Figure 111: Comparison of measured and modelled TL of roof structure L2297 (y axis gridlines are in 10dB steps)

Without point connections, the ‘unbonded’ case also greatly overestimates transmission loss, especially above 500 Hz (up to 60dB), as it does not account for either the mechanical coupling between the solid portion of the mineral wool and the metal sheets, or the path through the structural connections. The bonded case predicts the observed dip at 315 Hz and the overall lower transmission loss observed in the measurement, while still overestimating the transmission loss above the 1250 Hz band, suggesting that connectors and other paths contribute greater energy in this region.

7.3.4 Roof structures with high density boards, multiple panels

In this section, roof structures that include multiple panels beyond the metal top sheet and liner are examined.

7.3.4.1 Structure with halters, top-hat purlins and high density board: combined plate approach

Figure 112 shows the diagram of a roof structure, ‘BG’, with two metal sheets and a cement particle board (CPB) between two rubber mats screwed to the bottom sheet, with lightly compressed mineral wool infill and halter connections from the top sheet to a top-hat purlin, which is screwed to the CPB. The transmission loss has been modelled in four ways:

1. As a structure with halter and top-hat connections running from the top sheet to the bottom sheet, where the intermediate layers (including the CPB) are modelled as a single equivalent fluid
2. As a structure with halter and top-hat connections running from the top sheet to the CPB, where the CPB and the bottom steel sheet have been combined using sandwich theory (Section 5.3.2) into a single equivalent plate.
3. As 2, but with empirically adjusted stiffness
4. As a structure without point connections, using a pure TMM.

These models are compared to the measured diffuse TL in Figure 113.

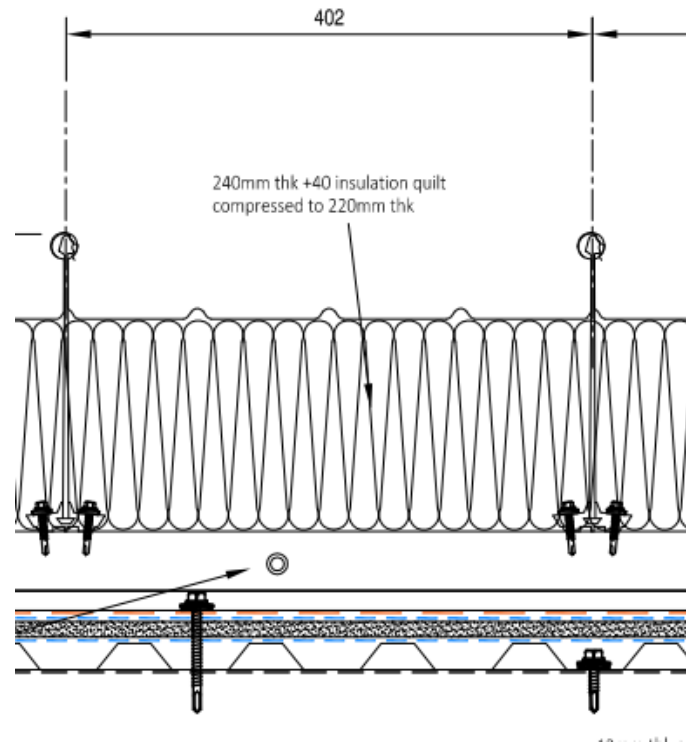


Figure 112: Diagram of roof structure 'BG' with halter connections, mineral wool infill, and high density cementitious board, MCRMA (2013)

The measured TL is, as with most of the results in this section, relatively smooth, with no particularly strong, identifiable features beyond the mass-spring-mass frequency. All models are within 5dB of the measurement at low frequency except the case where point connections run from the top sheet directly to the bottom sheet, which underestimates TL by up to 10dB. Figure 114 shows the low frequency comparisons up to 315 Hz; it can be seen that the halter and top-hat connection case predicts a dip at 160 Hz that is mirrored in the measurement; this dip is due to the increase in mass-spring-mass resonance caused by the connectors, however it is not clear whether this is the reason for the dip in the real structure without also accounting for other factors. At high frequency, the model results differ dramatically between each other and the measurement. The case without point connections has the highest TL (up to 120 dB at 5 kHz), and begins to deviate from the measurement at 125 Hz, with a constant increase per octave. The case with stiff point connections deviates from the measurement at 250 Hz and thereafter underestimates the measured values by over 20 dB. By decreasing the

stiffness of connectors in the model, the TL increases to the range found in the measurement; however, the modelled TL shows features not present in the structure, which are due to the combined plate approach, which produces a low critical frequency due to the increased bending stiffness of the bonded plates – in practice, the CPB and metal sheets are screwed at discrete locations, allowing the panels to bend more freely, resulting in a higher critical frequency.

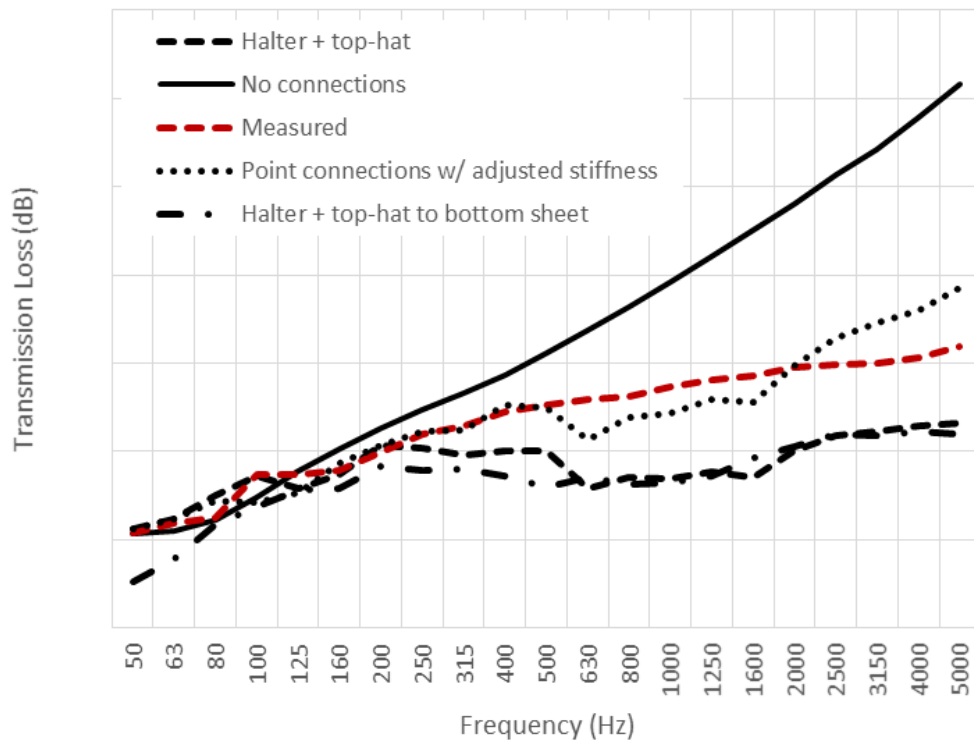


Figure 113: Measured and modelled diffuse transmission loss of 'BG' roof structure with high density board (y axis gridlines are in 20dB steps)

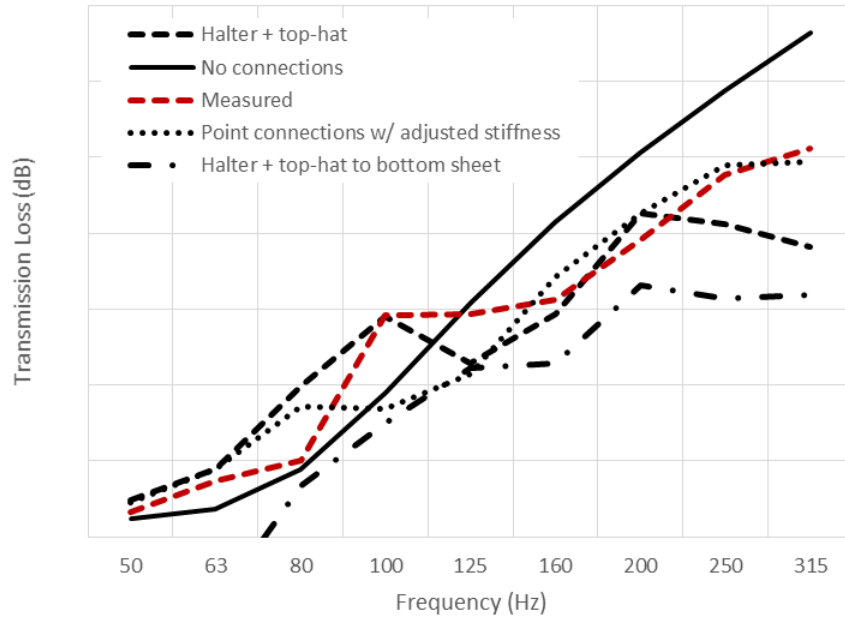


Figure 114: Measured and modelled diffuse transmission loss of 'BG' roof structure with high density board; low frequency results (y axis gridlines are in 5dB steps)

7.3.4.2 Structure with top-hat purlins and intermediate high density board

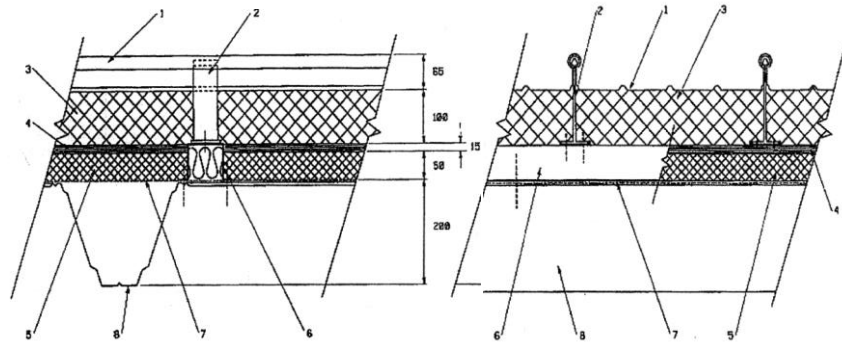


Figure 115: Roof structure diagram; 1: 0.9mm profiled aluminium sheet 2: halter connectors 3&5: 180 kg/m² mineral wool 4: 15mm plasterboard 6: top hat beam 7: vapour control film 8: profiled steel decking, MCRMA (2013)

Figure 115 shows the sectional drawings of a roof structure, referenced L-2510, with metal profile outer sheets with halter connections onto an internal 15mm layer of plasterboard, which rests between two layers of high density mineral wool. The halter connectors are screwed to a top hat purlin, which is fixed to the bottom steel decking. Modelling this structure with all layers mechanically decoupled by air layers, and without point connections

(a pure TMM model) predicts the TL loss well at low frequency, up to 200 Hz, where it begins to significantly overestimate it as structure-borne paths are ignored. This can be seen in Figure 116. The same figure shows the TL of the TMM model without air gaps, which allows continuity of shear stress between the mineral wool, plasterboard and metal sheets; this approach underestimates the TL at mid frequency, where there is a broad resonance dependent on the stiffness of the mineral wool, and overestimates TL at low frequency, as the mass-spring-mass resonance is shifted upwards. This is an indication that the materials in the cavity layers are free to move at the boundaries.

Point connections were introduced and comparisons are shown in Figure 117 between the measurement, the TMM model with unbonded layers, and the model including top hat and halter connections and point connections with empirically lowered stiffness. The top hat connection case underestimates TL at high frequency. As with the previous system, 'BG', the stiffness of the spacer kit appears to be underestimated, such that reducing the value of connector stiffness gets the TL in line with laboratory measured values.

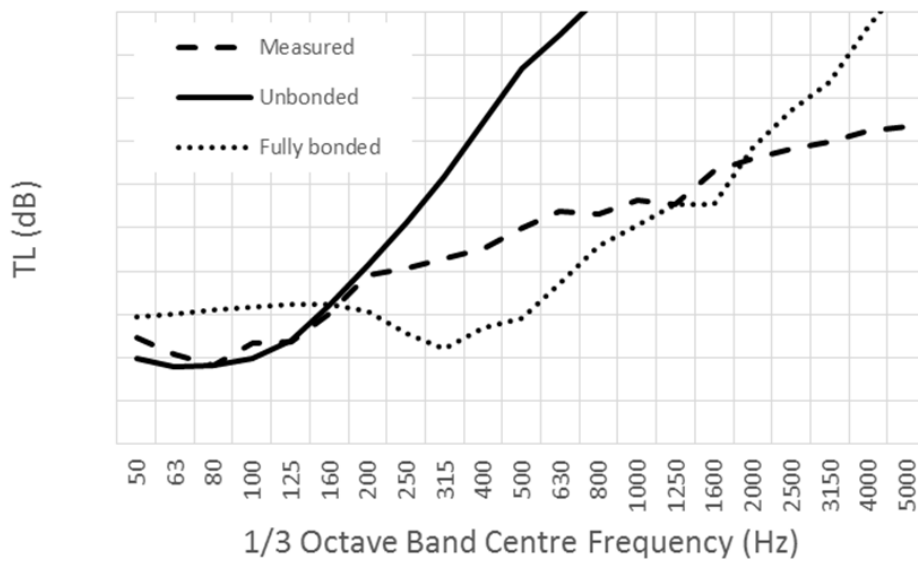


Figure 116: Comparison between TMM modelled and measured transmission loss of roof structure L2510, showing both fully bonded and decoupled TM models (y axis gridlines are in 10dB steps)

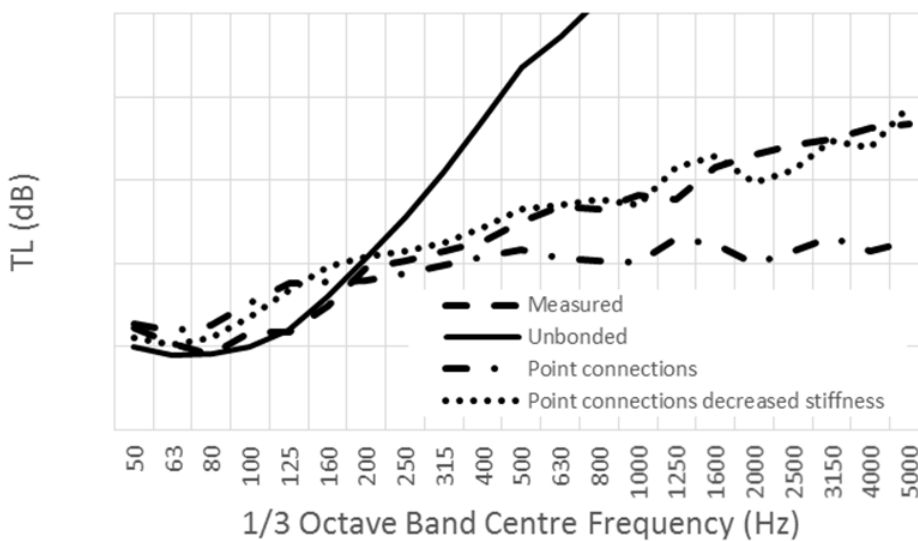


Figure 117: Comparison between TMM modelled and measured diffuse transmission loss of roof structure L2510, showing the effect of adjusted rod compressional stiffness values (y axis gridlines are in 20dB steps)

7.3.5 Roof structures with damping sheets (“acoustic matting”)

In designing high insulation products, to increase the overall transmission loss, high density sheets of rubber or other high damping materials (*acoustic matting*) are commonly added to a structure. Results were available for the structure shown Figure 105 (Section 7.3.2.2) with an

added layer of 10 kg/m^2 acoustic matting, placed over the bottom corrugated metal sheet. Figure 118 shows the laboratory measured diffuse sound transmission loss for the structure with and without the additional layer. The overall TL is increased by approximately 5dB in each band with the addition of the matting. The added mass of the membrane is significant, as the inner and outer metal sheets are only 0.7mm thick steel, with a mass per unit area of 5.5 kg/m^2 . The effect has been mirrored in a TMM model of a dual leaf roof structure, as can be seen in Figure 119, however it is overestimated by approximately 5dB. Similarly, the effect of the membrane is overestimated when modelling the TL with the periodic point connection model, as shown in Figure 120 compared to measured results; in this case, the connector stiffness was estimated from the measured data. The problem may be due to the use of static material properties of the membrane, and the complex boundary conditions of the measured system, where the membrane is neither fully bonded to nor completely separated from the metal sheet. This can be corrected empirically by reducing the effective mass of the membrane, however it is not clear whether such a correction would apply across roof systems.

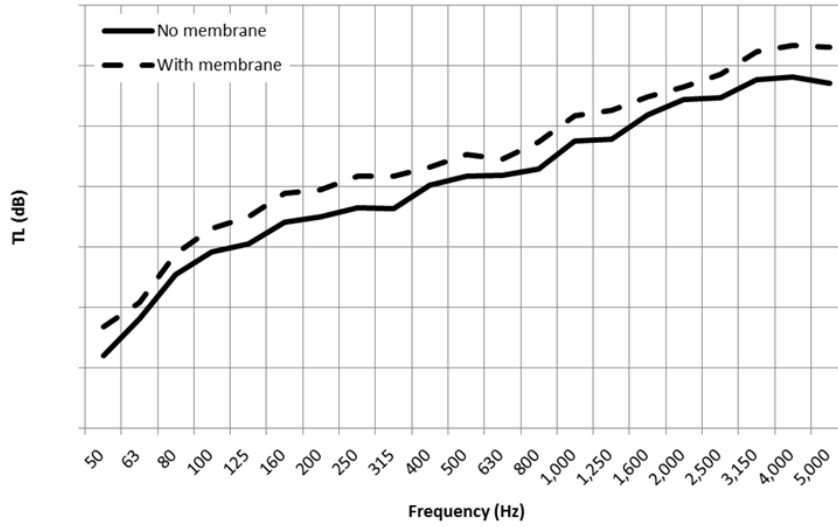


Figure 118: Measured diffuse field transmission loss of roof structure with and without a 10 kg/m² damping membrane. Mass per unit area without membrane: 14 kg/m²; with membrane: 23.8 kg/m² (y axis gridlines are in 10dB steps)

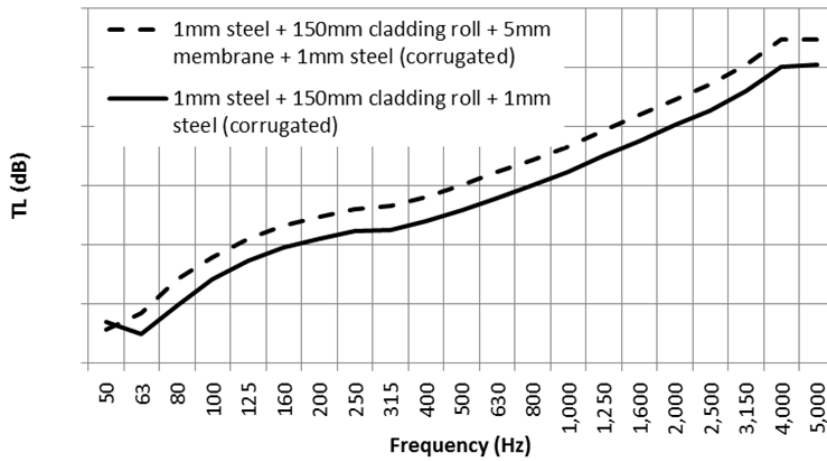


Figure 119: TMM modelled structure with and without a 5mm rubber membrane. (y axis gridlines are in 20dB steps)

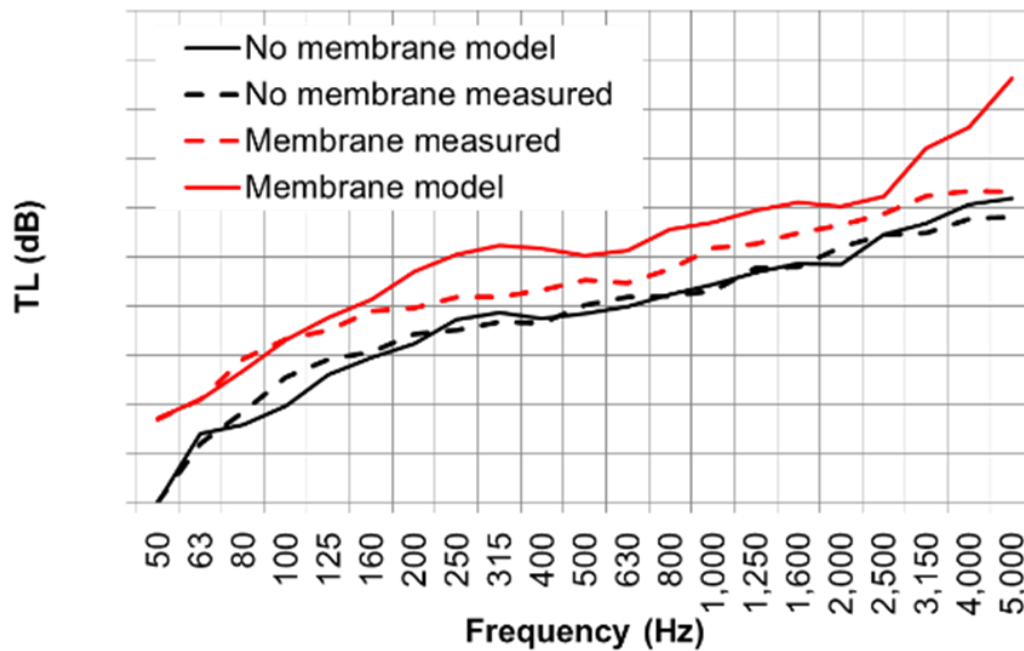


Figure 120: Modelled structure with periodic point connections with and without a 5mm rubber membrane (stiffness of point connections estimated from measurements) comparison with measurement results (y axis gridlines are in 10dB steps)

7.3.6 Conclusions for full systems

In this section, the analytical model for point connected dual leaf structures combined with the equivalent fluid properties for the infill layers, obtained via TMM, was tested against available laboratory measurements of sound insulation of corrugated roof structures, drawn from the literature and from data provided by roof manufacturers. Each system provides its own set of challenges.

Simple structures like rooflights, with empty cavities, are reasonably well modelled; point connections in these structures have a relatively small impact on transmission loss, as the energy transmitted through this path is not much greater than the energy transmitted through the air in the cavity. Conversely, the transmission loss through roof structures with fibrous infill depends strongly on the structural connections beyond a transition frequency, where it becomes greater than the energy through the mineral wool (as most is absorbed). The TM

method predicts very high values (unachievable in practice) of TL at high frequencies in the absence of connectors. The critical frequency dip is also more pronounced in the TMM modelled TL, produced by the orthotropic plate formulation. In the real case, there is a difference in slope between low and mid frequency, but no pronounced dip. This leads to a 10dB discrepancy around the critical frequency compared to measurement results, and an overall lower TL in cases where both metal sheets are the same.

Models of more complex roof structures, containing additional high density boards like plasterboard or cement boards, have been attempted but present a greater challenge in determining the exact boundary conditions between each layer. These structures can be modelled as if all consecutive layers were bonded to each other with no gaps, or small air gaps can be artificially introduced between any layers to force the shear stress at the boundaries to zero; good agreement is usually found at low to mid frequency for most combinations. For all structures examined, an accurate estimation of connection stiffness is deemed of high importance to improve high frequency accuracy.

7.4 CONCLUSIONS FOR LABORATORY MEASUREMENT COMPARISONS

This chapter has covered the bulk of verification and validation of the modelling approaches produced over the course of this work, as well as highlighting salient features and differences between some common roof and partition systems. The process of validation has been approached in successive stages, isolating individual components before arriving at comparisons of full roof structures.

Single profiled sheets were modelled via FEM in Comsol, an analytical model of a ribbed plate, and the equivalent flat orthotropic plate formulation based on obtaining the area

moment of inertia of the plate geometry. The orthotropic plate model is suitable for a limited range of geometries and fails to account for profile-related resonances. It predicts a clear lower critical frequency when waves are oriented in the stiffest dimension of the plate, however this feature is much less prominent in simulated thin trapezoidal profile plates.

Single and double glazed partitions as well as plasterboard partitions were modelled with the TMM and compared with available laboratory measured data. Correction factors were applied for laboratory diffusivity and a combination of Gaussian incidence windowing and spatial windowing techniques were found to improve prediction accuracy. Overall, salient features of the TL curves of these structures were captured by the model. Corrugated roof structures with expanding foam core (composites) were also modelled with the TMM with some success. The core stiffness was the most important factor in determining the overall response. For composites with a greater profile depth in comparison to the overall depth, the TMM overestimates transmission loss, as it does not account for profile-related resonances.

The effects of point connectors in dual leaf systems were examined; the analytical model for periodic point connected plates compared favourably with FEM simulations in Comsol, for a range of connector stiffness values. Then the stiffness of two common connectors used in roof structures, halters and brackets, were compared in Comsol, and the values thus obtained were transferred to the analytical model to observe their impact on the TL of a dual leaf structure. Brackets are considerably more compliant than halters of the same thickness, and overall increase TL of a modelled dual leaf structure.

The effect of changing stiffness and spacing of connectors was explored, and low stiffness and greater spacing were both associated with lower mass-air-mass resonant frequency, as well as higher overall TL above a transition frequency where the structural paths dominate.

Top hat purlins, i.e. beams that are screwed to the bottom sheet of roof systems, on which halter or brackets are fixed, were modelled as beams and included in a revised analytical model for point connected dual leaf structures. The purlins have a low compressional stiffness and, based on modelled scenarios, decrease the amount of energy transmitted between the two sheets in dual leaf roof systems, while likely having a small stiffening effect on the bottom sheet.

Finally, available laboratory measurements of TL of full roof systems were compared with the outputs of the analytical model combined with the TMM for the cavity layers. The TMM alone generally overestimates TL at high frequency as it does not account for structural paths. For systems with high density infill and/or other solid layers in the space between the two outer sheets, whether or not the materials are in full contact with each other (modelled as successive layers as opposed to introducing small air gaps between them) makes a large difference to results. Generally, when high density infill is bonded to the outer metal sheets the TL increases at low frequency and decreases at high frequency, as the mass-air-mass resonance shifts upward. Including point connections in the model was sufficient to predict the TL of roofs with halter connections (and no purlins), and soft fibrous infill within 5dB throughout the range. Structures with bracket connectors required adjusting the effective stiffness of connectors in the model. Similarly, roof systems with top hat purlins had a higher TL in practice than in the model with stiff connectors. For examined structures, the introduction of rubber (or similar material) damping sheets increases transmission loss by an amount roughly constant in frequency, in line with the increase in mass. This result, while overestimated by around 5dB, is mirrored in TMM modelled TL.

8 CONCLUSIONS

The aim of this work was to replicate laboratory measurements of sound insulation of dual leaf structures, and in particular of common corrugated roof structures with point-to-point structural connections, according to specifications from the Metal Cladding and Roof Manufacturers Association (2013).

The following elements of dual leaf corrugated roof structures were considered:

- Profiled metal panels, with trapezoidal or ribbed geometry
- Mineral wool and glass wool infill
- Multiple, layered materials
- High density boards
- Rubber/damping mats
- Point-to-point connectors – T-shaped halters and L-shaped brackets – in spacer kits which can include intermediate beams

A unified modelling approach was attempted, to account for as many elements as practicable, including some characteristics of the measurement environment. This was attempted by combining several modelling techniques. The Transfer Matrix Method was used to model layered materials; two analytical models of plates periodically connected by thin rods were used to determine the behaviour of common structural connections; FEM simulations were used to obtain the stiffness of real connectors; corrugated sheets were modelled as equivalent orthotropic plates; an analytical model of a periodically ribbed plate was developed; the TMM was used to derive the effective properties of layered infill materials which could be used within the double plate models.

The acoustic performance of building elements is commonly tested in an acoustic transmission suite, so that a comparison had to, as far as practicable, emulate the measurement conditions outlined in BS EN ISO 10140. The pure TMM and the periodic analytical models assume that the systems is laterally infinite, so that it was necessary to account for the effect of finite size and laboratory diffusivity. While it was not possible to account for panel resonances in the lateral dimensions, which strongly affect low frequency behaviour, an adjustment was introduced to account for the radiation efficiency of the finite radiating surface; the imperfect diffusivity of the incident sound field was simulated by applying a Gaussian distribution to the incident energy, strongly limiting grazing incidence waves.

The corrugated metal sheets found in roof constructions were modelled as equivalent orthotropic plates, by calculating the bending stiffness of the panel with its profile. Theoretically, the equivalent orthotropic plate formulation can predict the behaviour of a ribbed or corrugated plate, provided that the bending wavelength is much larger than the geometric period of the profile. Comparisons of transmission loss determined with FEM simulations of trapezoidal plates have shown that, even for small profile periods, the equivalent orthotropic formulas tend to overestimate the bending stiffness of the profiled panels, leading to consistently lower critical frequencies.

An analytical model was also developed to account for the behaviour of periodically ribbed plates, which can be implemented as layers in the TMM as effective fluids – though this was not carried out in the course of the work. The model was also validated against FEM simulations. Profile-related resonances appear in the transmission loss of the periodic plate, which depend on the rib spacing and bending stiffness of the plate. For low profile periods, the equivalent orthotropic formulation compares favourably to the periodic ribbed plate model, in terms of identifying the key aspects of behaviour (two critical frequency dips),

except, similarly to trapezoidal plates, it overestimates bending stiffness resulting in poor low frequency accuracy. For higher profile periods, the analytical model has shown that the profile-related resonances begin at lower frequency, and are closely spaced, with high mode density in the frequency range of interest (100-5000 Hz). This situation leads to a good match between the orthotropic plate and the periodic ribbed plate model when comparing diffuse transmission loss, despite the lack of a clearly identifiable lower critical frequency in the periodic model.

Comparisons between the equivalent orthotropic plate formulation and laboratory measurements of diffuse transmission loss of trapezoidal and standing seam panels have shown that the orthotropic plate model, while improving on a simple flat plate, tends to overestimate diffuse transmission loss at high frequency, and misses prominent dips throughout the frequency range. Diffuse transmission loss predictions are however still within 5-10dB of measurements at low frequency. Trapezoidal panels with the smallest profile period produce greater discrepancies, most likely due to the incorrect estimation of the lower critical frequency and failure to account for profile-related modes which are more widely spaced in frequency.

To account for dual leaf structures, two variations of an analytical model of parallel plates connected periodically by thin elastic rods, and separated by a fluid cavity, were derived, with and without intermediate beams intended to simulate top hat purlins. The connectors were characterised using two by two axial stiffness matrices, the values of which could be obtained with any number of techniques. These models were initially validated against FEM simulations carried out in Comsol. The effect of connector spacing and axial stiffness on the transmission loss through these periodic double plate models, with absorptive cavity material, was examined through parametric surveys. Increased connector stiffness was associated with lower transmission loss at mid to high frequency, and an upwards shift in the lowest mass-

spring-mass resonance of the system. Similarly, reduced spacing between the connectors also increased the mass-spring-mass resonant frequency, and reduced transmission loss at mid-high frequency.

Two types of connectors common in roof systems were examined: halters and brackets. Their axial stiffness was determined via FEM in Comsol. Aluminium halters, being thicker and with greater symmetry, are overall stiffer than steel brackets of the same height, despite being a lower modulus material. Using the stiffness values of these connectors in the periodic double plate model has shown that the bracket connectors tend to produce a higher transmission loss at high frequency, though internal resonances also lead to regions of lower transmission loss.

The diffuse transmission loss of full roof and partition systems was compared to the outputs of the TMM and the double plate models. The TMM, with the aforementioned corrections for diffusivity and sample size, captures the behaviour of double glazing and simple plasterboard partitions well throughout the frequency range of interest. The TMM is also suited to predicting the transmission loss of rooflights, where the presence of structural connectors has only a small impact, due to the high amount of energy transmitted through the air in the cavity. When it comes to corrugated roof structures with mineral wool infill and structural connections, the low frequency TMM prediction is often good, however it consistently overestimates transmission loss above 200-300 Hz, as the mineral wool will absorb most energy in the cavity space, making the structural path dominant. When the two metal sheets in a roof system share the same profile and thickness, the TMM predicts a strong lower critical frequency dip in diffuse transmission loss, which is not observed in measurements. When the two profiled panels are of different thicknesses and depth, the TMM model predicts a much greater transmission loss, as the two lower critical frequencies occur in different

locations. In practice this is not the case, given that low to mid-frequency behaviour of single panels does not change significantly with depth.

The periodic double plate model with point connections can better account for the overall behaviour of these structures, however it requires an accurate determination of the stiffness of the connectors, which is crucial to evaluating high frequency performance. In most cases, the transmission loss is underestimated at high frequency when modelling the connectors as thin elastic rods, suggesting that the structural frameworks of roof structures are generally more compliant.

Roof structures with multiple layers of infill have been modelled and compared with laboratory measurements, providing an avenue for the validation of the combined TMM and periodic double plate model. Features of the measured transmission loss curve of a roof structure with four layers of high density mineral wool were found in the modelled case with both the TMM and the combination of TMM and periodic double plate model. The TMM alone was able to predict the effect of mechanical coupling between the outer sheets and the infill. The point connected model overestimated TL, as the mechanical coupling is neglected. Structures with high density boards in the cavity space, screwed to one of the corrugated metal sheets, were modelled by obtaining the combined stiffness of the connected high density boards and metal sheets, resulting in good low frequency agreement. At high frequency, the issue of determining connector stiffness remained, and good agreement was obtained only with empirical adjustments to the connector stiffness matrix.

Roof structures with acoustic membranes were also modelled. In practice, the addition of membranes of typical thickness increases the diffuse TL by 5dB over the whole frequency range for a common corrugated roof structure, however the TMM predicts double that increase, as does the periodic double plate model.

9 REFERENCES

- Allard, J. & Atalla, N., 2009. *Propagation of Sound in Porous Media*, John Wiley and Sons.
- Attenborough, K., 1983. Acoustical characteristics of rigid fibrous absorbents and granular materials. *the Journal of the Acoustical Society of America*, 73(March 1983), pp.785–799.
- Attenborough, K., 2014. Acoustical characteristics of rigid fibrous absorbents and granular materials Po. , 73(March 1983), pp.785–799.
- Bies, D.A. & Hansen, C.H., 1980. FLOW RESISTANCE INFORMATION FOR ACOUSTICAL DESIGN. *Applied Acoustics*, 13(5), pp.357–391.
- Bies, D.H., Hansen, C.H. & Campbell, R.H., 1996. Engineering Noise Control. *The Journal of the Acoustical Society of America*, 100, p.1279.
- Biot, M. a., 1956. Theory of Propagation of Elastic Waves in a Fluid-Saturated Porous Solid. I. Low-Frequency Range. *The Journal of the Acoustical Society of America*, 28(2), p.168.
- Brouard, B., Lafarge, D. & Allard, J., 1995. A general method of modelling sound propagation in layered media. *Journal of Sound and Vibration*, 183, pp.129–142.
- Brunskog, J., 2004. Near-periodicity in acoustically excited stiffened plates and its influence on vibration, radiation and sound insulation. *Acta Acustica united with Acustica*, 90(2), pp.301–312.
- Brunskog, J., 2005. The influence of finite cavities on the sound insulation of double-plate structures. *The Journal of the Acoustical Society of America*, 117(6), p.3727.

- Brunskog, J. & Davidsson, P., 2004. Sound transmission of structures. A finite element approach with simplified room description. *Acta Acustica united with Acustica*, 90(5), pp.847–857.
- Brunskog, J. & Hammer, P., 2000. Prediction Models of Impact Sound Insulation on Timber Floor Structures; A Literature Survey. *Building Acoustics*, 7(2), pp.89–112.
- Craik, R.J.M. & Smith, R.S., 2000. Sound transmission through double leaf lightweight partitions part I: airborne sound. *Applied Acoustics*, 61(2), pp.223–245.
- Cremer, L., Heckl, M. & Petersson, B.A.T., 2005. *Structure-borne sound: Structural vibrations and sound radiation at audio frequencies*, Springer-Verlag Berlin Heidelberg.
- Delany, M.E. & Bazley, E.N., 1970. Acoustical properties of fibrous absorbent materials. *Applied Acoustics*, 3(2), pp.105–116.
- Dijkmans, a & Vermeir, G., 2013. Development of a hybrid wave based-transfer matrix model for sound transmission analysis. *The Journal of the Acoustical Society of America*, 133(4), pp.2157–68.
- Fausti, P., Pompoli, R. & Smith, R.S., 1999. An Intercomparison of Laboratory Measurements of Airborne Sound Insulation of Lightweight Plasterboard Walls. *Building Acoustics*, 6(2), pp.127–140.
- Fokin, V. et al., 2007. Method for retrieving effective properties of locally resonant acoustic metamaterials. *Physical Review B*, 76(14), p.144302.
- Folds, D. & Loggins, C., 1977. Transmission and reflection of ultrasonic waves in layered media. *The Journal of the Acoustical Society of America*, pp.1102–1109.

- Griffin, D. & Ballagh, K., 2013. a Consolidated Theory for Predicting Rain Noise. *Noise & Vibration Bulletin*, 19(4), p.46.
- Guigou-Carter, C. & Villot, M., 2003. Study of Simulated Rainfall Noise on Roofs and Glazings. In *Proceedings of EURONOISE*. pp. 2–8.
- Hopkins, C., 2007. *Sound Insulation*, Butterworth-Heinemann.
- Johnson, D.L., Koplik, J. & Dashen, R., 1987. Theory of dynamic permeability and tortuosity in fluid-saturated porous media. *Journal of Fluid Mechanics*, 176(1), p.379.
- Kang, H. et al., 2000. Prediction of sound transmission loss through multilayered panels by using Gaussian distribution of directional incident energy. *The Journal of the Acoustical Society of America*, 107(3), pp.1413–20.
- Kang, H.-J. et al., 2000. Prediction of sound transmission loss through multilayered panels by using Gaussian distribution of directional incident energy. *The Journal of the Acoustical Society of America*, 107(3), p.1413.
- Lam, Y.W., 1995. *FINAL REPORT FOR THE METAL CLADDING & ROOFING MANUFACTURERS ASSOCIATION (MCRMA)*, Salford.
- Lam, Y.W. & Windle, R.M., 1993. Prediction of the sound reduction of profiled metal cladding. In *INTER-NOISE and NOISE-CON Congress and Conference Proceedings*. Institute of Noise Control Engineering, pp. 999–1002.
- Lauriks, W., Mees, P. & Allard, J., 1992. The acoustic transmission through layered systems. *Journal of sound and vibration*, 155, pp.125–132.
- Lauriksand, W. et al., 1990. Modelization at oblique incidence of layered porous materials

- with impervious screens. *The Journal of the Acoustical Society of America*, 87(3), pp.1200–1206.
- Lin, G.-F., 1977. Sound transmission through periodically framed parallel plates. *The Journal of the Acoustical Society of America*, 61, p.1014.
- Mace, B.R., 1980. Periodically stiffened fluid-loaded plates, I: Response to convected harmonic pressure and free wave propagation. *Journal of Sound and Vibration*, 73(4), pp.473–486.
- Maluski, S.P. & Gibbs, B.M., 2000. Application of a finite-element model to low-frequency sound insulation in dwellings. *The Journal of the Acoustical Society of America*, 108(4), pp.1741–1751.
- Maxit, L., 2009. Wavenumber space and physical space responses of a periodically ribbed plate to a point drive: A discrete approach. *Applied Acoustics*, 70(4), pp.563–578.
- Mayr, a. R. & Gibbs, B.M., 2011. Point and transfer mobility of point-connected ribbed plates. *Journal of Sound and Vibration*, 330(20), pp.4798–4812.
- Mead, D.J. & Mallik, a. K., 1978. An approximate theory for the sound radiated from a periodic line-supported plate. *Journal of Sound and Vibration*, 61(3), pp.315–326.
- Mechel, F., 1988. Design charts for sound absorber layers. *The Journal of the Acoustical Society of America*, pp.1002–1013.
- Metal Cladding and Roof Manufacturers Association, 2013. Private communication.
- Miki, Y., 1990. Acoustical properties of porous materials-modifications of Delany-Bazley models. *J. Acoust. Soc. Jpn.(E)*.

- Ng, C.F. & Zheng, H., 1998. Sound transmission through double-leaf corrugated panel constructions. *Applied Acoustics*, 53(1–3), pp.15–34.
- Pritz, T., 1998. Frequency dependences of complex moduli and complex Poisson's ratio of real solid materials. *Journal of Sound and Vibration*, 214, pp.83–104.
- Pritz, T., 1980. TRANSFER FUNCTION METHOD FOR INVESTIGATING THE COMPLEX MODULUS OF ACOUSTIC MATERIALS: SPRING-LIKE SPECIMEN. *Journal of Sound and Vibration*, 72(3), pp.317–341.
- Sewell, E., 1970. Transmission of reverberant sound through a single-leaf partition surrounded by an infinite rigid baffle. *Journal of Sound and Vibration*, 12, pp.21–32.
- Sharp, B., 1978. Prediction methods for the sound transmission of building elements. *Noise Control Engineering*, pp.53–63.
- Smirnov, D., 2015. Sound transmission through two elastic plates interconnected by rods. *Internal document*.
- Stani, M., Muellner, H. & Plotizin, I., 2004. Sound insulation of plasterboard walls and airflow resistance: An empirical examination with respect to practical applications. *INTER-NOISE ...*, pp.1987–1992.
- Takahashi, D., 1983. Sound radiation from periodically connected double-plate structures. *Journal of Sound and Vibration*, 90, pp.541–557.
- Takahashi, D., 1983. Sound radiation from periodically connected double-plate structures. *Journal of Sound and Vibration*, 90(4), pp.541–557.
- Tarnow, V., 2005. Dynamic measurements of the elastic constants of glass wool. *The Journal*

of the Acoustical Society of America, 118(6), p.3672.

Vigran, T., 2008. *Building acoustics*, Taylor & Francis.

Villot, M., Guigou, C. & Gagliardini, L., 2001. Predicting the Acoustical Radiation of Finite Size Multi-Layered Structures By Applying Spatial Windowing on Infinite Structures. *Journal of Sound and Vibration*, 245(3), pp.433–455.

Xin, F.X. & Lu, T.J., 2011. Transmission loss of orthogonally rib-stiffened double-panel structures with cavity absorption. *The Journal of the Acoustical Society of America*, 129(4), pp.1919–34.

APPENDIX A: RAIN NOISE

Rain noise excitation within the TMM can be modelled by modifying the amplitude of the incident plane wave, and obtaining the radiated power from the output velocity; the method has been previously implemented by Guigou-Carter & Villot (2003).

The force applied by a rain drop onto a flat surface, P_i , acting on a single point located at coordinates $x = 0$ and $y = 0$, can be approximated using a Dirac delta:

$$P_i(x, y, \omega) = F(\omega)\delta(x, y) \quad (9.1)$$

Where F is the time-frequency Fourier transform of the impact force for a single drop.

The spatial Fourier transform of the impact force is simply the amplitude of the force:

$$P_i(k_x, k_y, \omega) = F(\omega) \quad (9.2)$$

The incident field comprises plane waves of equal amplitude, of all wavenumbers k_x and k_y .

The force $F(\omega)$ depends on the size and shape of the drop, and on its velocity at the time of the impact. For a paraboloidal drop, the force function is given by the following equation (Griffin & Ballagh 2013):

$$F(\omega) = -\rho_w \pi r^2 v_0^2 \left[\frac{3v_0}{8r\omega^2} \left(1 - \cos \frac{8r\omega}{3v_0} \right) - \frac{i}{\omega} \left(1 - \frac{3v_0}{8r\omega} \sin \frac{8r\omega}{3v_0} \right) \right] \quad (9.3)$$

Where ρ_w is the drop density, r is the drop radius, and v_0 is the fall velocity. The function in the time domain is shown in Figure 121, and in the frequency domain in Figure 122. The incident power onto the surface, in 1/3 octave bands, is shown in Figure 123.

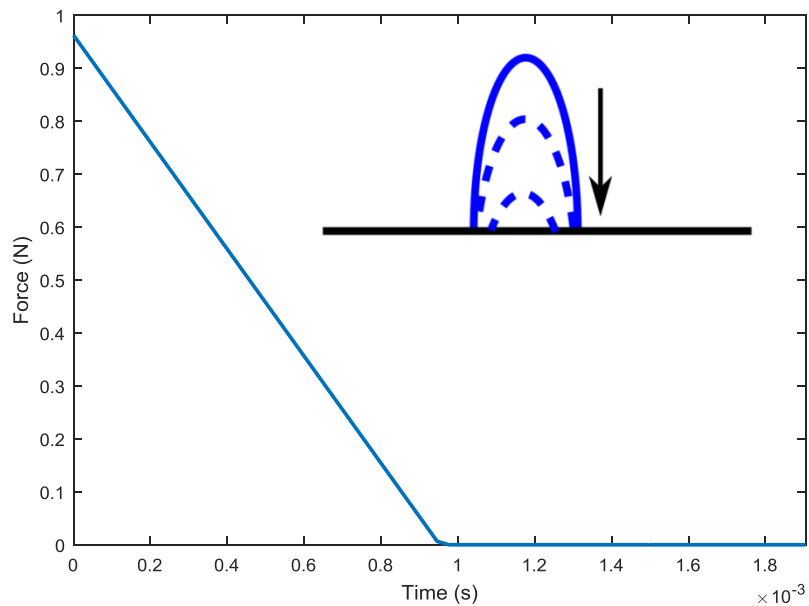


Figure 121: Paraboloidal rain drop force in the time domain

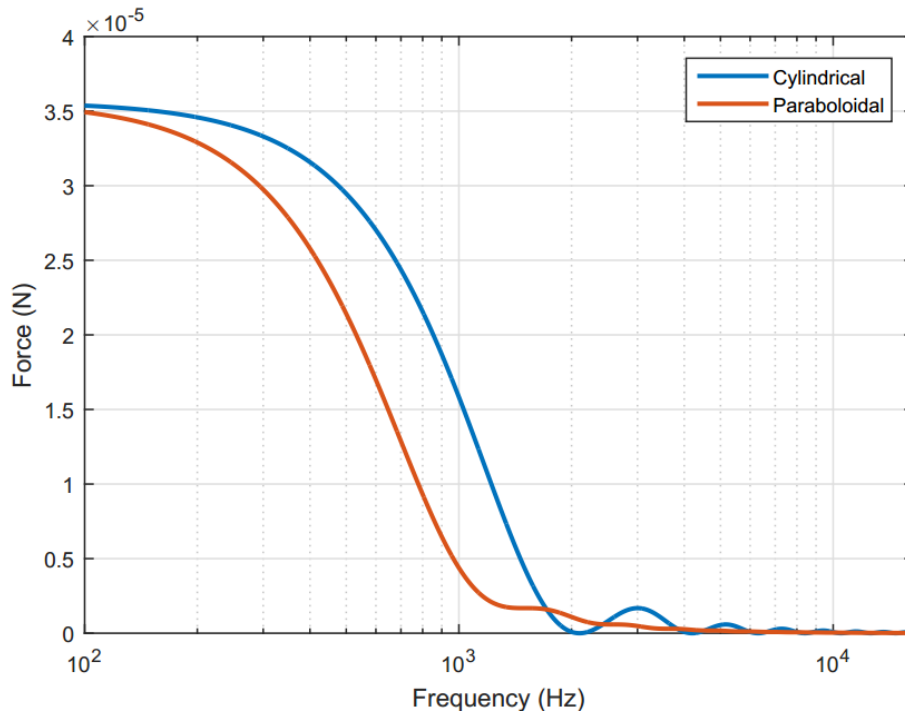


Figure 122: Rain drop force $F(\omega)$ in the frequency domain

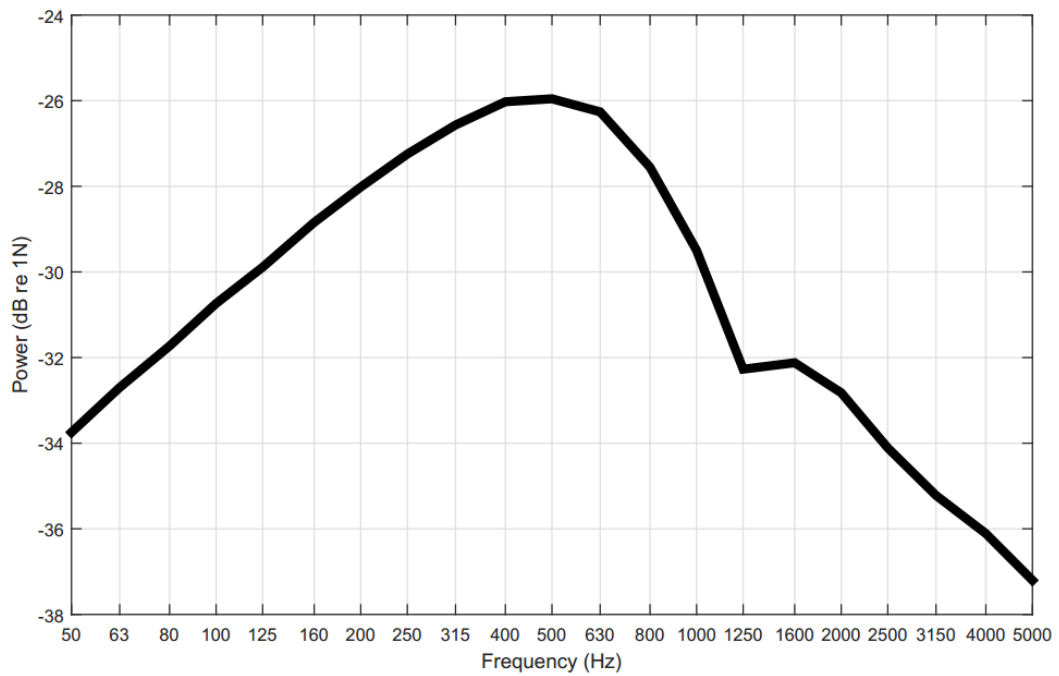


Figure 123: Incident sound power of simulated standard rainfall

The incident sound power of rain fall is proportional to the number of rain drops per unit area per unit time n :

$$P_i = n \times |F|^2$$

Figure 123 shows the incident power from simulated heavy rainfall, with terminal velocity of 7 m/s, drop size of 5mm and rainfall rate of 40mm/h, as per the requirements in BS EN ISO 140-18.

The radiated power from a laterally infinite surface on the xy plane is obtained by integrating the spatial Fourier transform of the normal velocity field v_z at the output over all wavenumbers up to the natural wavenumber in air, k_0 (Cremer et al. 2005):

$$\Pi_{rad} = \frac{k\rho c}{8\pi^2} \iint \frac{\omega^2 |w(k_x, k_y)|^2}{\sqrt{k^2 - k_x^2 - k_y^2}} dk_x dk_y \quad (9.4)$$

The equation can be written in terms of the trace wavenumber k_r , where $dk_x dk_y = k_r dk_r d\phi$ and $k_x = k_r \sin \phi$ and $k_y = k_r \cos \phi$:

$$\Pi_{rad}(\omega) = \frac{\rho c}{8\pi^2} \int_0^{2\pi} \int_0^k \frac{k k_r |v_z(k_r, \phi)|^2}{\sqrt{k^2 - k_r^2}} dk_r d\phi \quad (9.5)$$

Given that the velocity shares the same periodicity of the excitation for any given combination of x and y wavenumbers, $e^{i(k_x x + k_y y)}$, the spatial Fourier transform of velocity is easily obtained, and is related to the derivative of the transmitted pressure in the z direction via Euler's equation, with the complex transmitted amplitude T obtained with the TMM:

$$v(k_x, k_y) = -\frac{k_z}{\omega\rho_0} T(k_x, k_y) \quad (9.6)$$

The radiated sound power can also be adjusted to account for the finite size of the structure, as in Section 4.1.11.

The TMM predicted sound intensity of 4/16/4mm double glazing against laboratory measurements reproduced from Guigou-Carter & Villot (2003), in Figure 124, shows good agreement above 250 Hz, identifying peaks around mass-spring-mass resonance and at the critical frequency of the glass panels (2500-3150 Hz), however sound intensity is underestimated at low frequency, which can be attributed to the difference in radiation efficiency between the infinite TMM case and the finite structure.

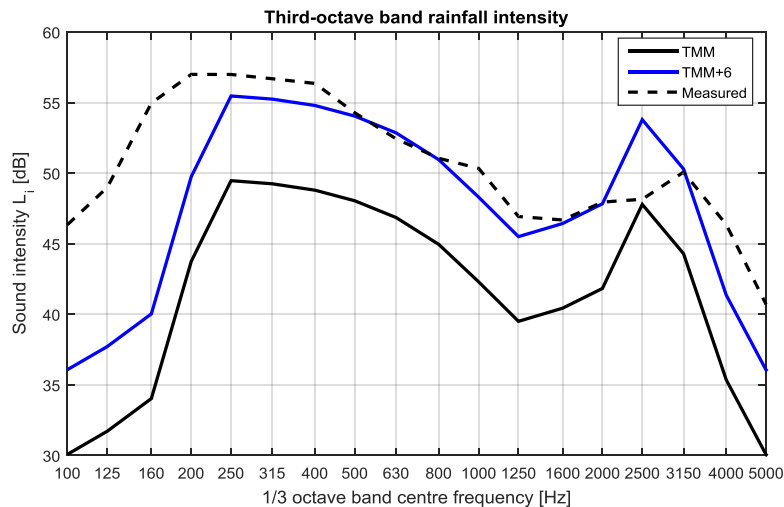


Figure 124: TMM modelled sound intensity of 4/16/4mm double glazing, compared to measurement (Guigou-Carter & Villot 2003)

APPENDIX B: PLATES INTERCONNECTED BY RODS

The following pages contain an internally circulated document produced by Dmitry Smirnov, which details the derivation of a periodically point-connected double plate system.

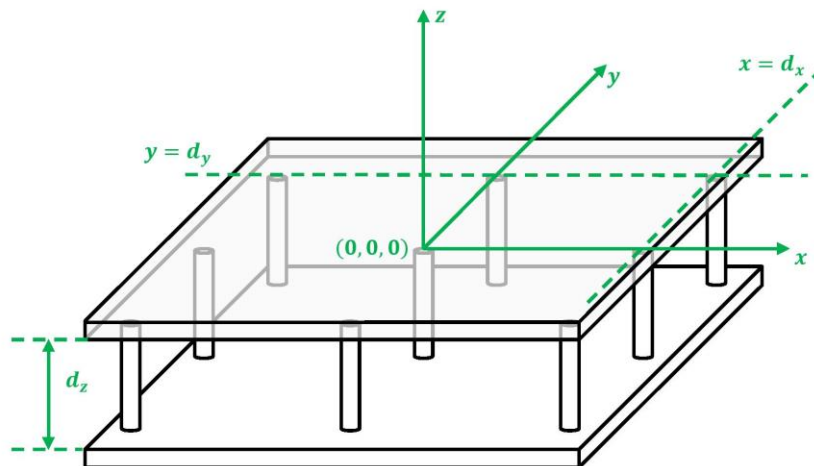
Sound transmission through two elastic plates interconnected by rods

1. Introduction to the problem

In this section, the problem geometry is defined and a list of the initial assumptions is presented. The solution is derived in [Section 5](#), following prerequisite theory covered in [Section 2](#), [Section 3](#) and [Section 4](#). Subsequently, some properties of the solution are discussed and sample numerical results are presented in [Section 6](#).

1.1 Geometry

The problem consists of a plane wave incident on two elastic plates aligned with the horizontal xy plane and spanning to infinity in both x and y directions, spaced at distance d_z apart along the vertical z axis. The plates are interconnected by an infinite rectangular grid of rods spaced at a distance of d_x apart in the x direction, and d_y in the y direction. The Cartesian coordinate system origin is placed on the top plate at the point of connection to one of the rods. A section of the infinite geometry is shown in the diagram below, indicating coordinate system relations:



1.2 Incident pressure field

The scattered wave formulation is used to solve for the pressure in the semi-infinite air-filled domain above the top plate, meaning the total field in that domain is a superposition of the incident field p_{inc} which would exist without the structure, and a scattered field p_{scat} which is determined by the introduction of the structure to give the correct total response when added to the incident field. The derivation uses the $e^{-i\omega t}$ time-dependence convention, if conversion to the $e^{+j\omega t}$ convention is required then the complex conjugate of all expressions presented here must be used. The incident

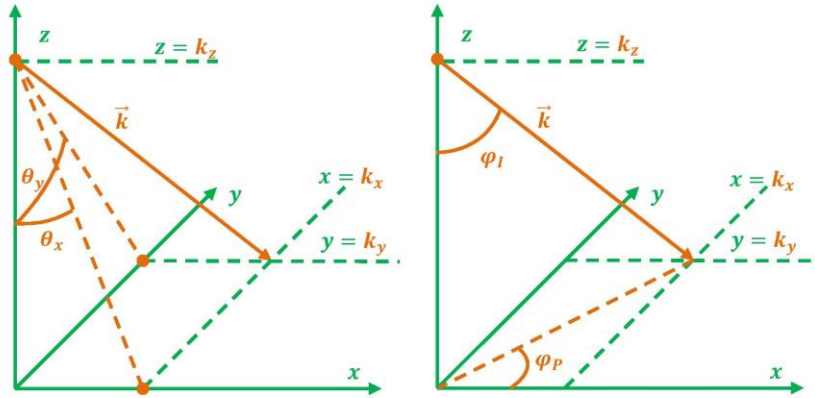
pressure is defined as a time-harmonic plane wave with wave vector \vec{k}_0 where all components are real and the z component is negative:

$$\vec{k}_0 = \begin{bmatrix} k_x^0 \\ k_y^0 \\ -k_z^0 \end{bmatrix} \quad (1.1)$$

$$p_{inc} = e^{i(k_x^0 x + k_y^0 y - k_z^0 z)} \quad (1.2)$$

The wavenumber of the incident wave is $k = \|\vec{k}\| = \sqrt{(k_x^0)^2 + (k_y^0)^2 + (k_z^0)^2}$, i.e. p_{inc} satisfies the homogeneous Helmholtz equation $(\nabla^2 + k^2)p_{inc} = 0$.

The components k_x^0 and k_y^0 can be expressed in terms of angle components θ_x and θ_y which the projections of the wave vector onto the xz and yz planes respectively make with the inwards-pointing plate normal (negative z axis). Alternatively, a definition using an incidence angle φ_I which the wave vector makes with the inwards plate normal, and a "polarisation" angle φ_P which is the angle the projection of the wave vector onto the xy plane (plate surface) makes with the x axis, defining a plane of incidence:



$$\vec{k}_0 = k \begin{bmatrix} \sin(\theta_x) \\ \sin(\theta_y) \\ -\sqrt{1 - \sin^2(\theta_x) - \sin^2(\theta_y)} \end{bmatrix} = k \begin{bmatrix} \sin(\varphi_I) \cos(\varphi_P) \\ \sin(\varphi_I) \sin(\varphi_P) \\ -\cos(\varphi_I) \end{bmatrix} \quad (1.3)$$

1.3 Assumptions and simplifications

The assumptions made to solve the problem are:

- Air pressure p in all air-filled domains satisfies the homogeneous Helmholtz equation $(\nabla^2 + k^2)p = 0$

- Plate displacement w satisfies the thin plate equation $(D\nabla^4 - M\omega^2)w = p_{top} - p_{bottom}$ where p_{top} and p_{bottom} are pressures or spatial force distributions at the top and bottom of the plate. The signs are chosen so that a positive p_{bottom} pushes the plate upwards (in the $+z$ direction)
- The rods connecting the plates are thin enough to have no scattering effect on the air inside the cavity, and are connected to the plates via infinitesimal points
- Whereas plate thickness is accounted for in the plate wave equation, the plates are treated as if they occupy an infinitely thin plane, meaning plate thickness is not accounted for in the cavity dimensions (this is easily accounted for but requires more terms in the expressions)

2. Quasi-periodic solutions in Cartesian coordinates

This section describes the concept of quasi-periodicity and how it is used to determine the interaction of periodic structures with time-harmonic waves. 2D Fourier expansions are used to obtain a representation of the quasi-periodic fields – the generic expansions defined here are used to assume the form of quantities dealt with in the rest of the derivation, such as the rod forces and plate velocities in [Section 3](#) and the air pressure in [Section 4](#).

2.1 Introduction to quasi-periodicity

The structure investigated is periodic in the x and y directions, with spatial periods d_x and d_y respectively. As with any periodic structure stimulated by a time-harmonic incident field, the functions describing any part of the structure's response over the x and y coordinates, be this the pressures in the air regions or the panel vibration, must satisfy quasi-periodicity. This means that if a region of the system's response local to a certain point in space is examined, and then a jump is made an integer number of d_x lengths in the x direction, the response looks exactly the same aside from a phase offset equal to the difference in phase of the incident field from the original to the new point; equally this is also true for integer numbers of jumps of d_y lengths in the y direction. This statement is equivalent to applying Floquet's theorem:

$$\{f(x + nd_x, y + md_y) : n, m \in \mathbb{Z}\} = e^{i(nk_x^0 d_x + mk_y^0 d_y)} f(x, y) \quad (2.1)$$

Here, $f(x, y)$ can be chosen to represent any part of the system response in the xy plane as described above. The convenience of this type of periodicity is that if one rectangular unit cell of the system with size d_x and d_y in the x and y directions respectively is selected, then quasi-periodicity can be enforced from the start, and hence from there onwards manipulations such as applying boundary conditions need only be done within the one unit cell – as the system is quasi-periodic, the changes will apply throughout the system's whole extent.

The "quasi" in quasi-periodicity refers to the fact that the fields are periodic down to a phase offset, rather than being truly periodic (unaltered by jumps equal to unit cell dimensions). The fields are only ever periodic when k_x^0 and k_y^0 are both equal to zero, that is when the incident wave vector is normal to the xy plane, otherwise they are quasi-periodic.

2.2 Quasi-periodicity in 1 dimension via Fourier series expansion

One way of enforcing quasi-periodicity is by Fourier expansion in Cartesian coordinates. Starting with quasi-periodicity in the x direction, the following is known about the function under inspection so far: the magnitude is periodic in x with period d_x , a jump of nd_x results in a phase offset of $e^{ink_x^0 d_x}$, however so far nothing is known about changes in phase resulting from movements in x not equal to nd_x . Therefore, the function can be expressed as a product of a complex exponential $e^{ik_x x}$ and an unknown complex function $g(x)$ which is periodic in x so that $g(x + nd_x) = g(x)$. The complex exponential facilitates the phase offset, and $g(x)$ provides the periodic magnitude and has whatever phase is necessary to provide the correct local phase variation of the full function $f(x)$:

$$f(x) = e^{ik_x^0 x} g(x) \quad (2.2)$$

$$g(x + nd_x) = g(x) \quad (2.3)$$

$$\therefore f(x + nd_x) = e^{ik_x^0 (x+nd_x)} g(x + nd_x) = e^{ik_x^0 (x+nd_x)} g(x) = e^{ink_x^0 d_x} f(x) \quad (2.4)$$

Now the spatial Fourier expansion is applied: a Fourier series is a convenient method of representing a periodic function, therefore $g(x)$ can be represented as a Fourier series with period d_x using as of yet unknown coefficients A_n :

$$g(x) = \sum_{n \in \mathbb{Z}} A_n e^{\frac{2in\pi}{d_x} x} \quad (2.5)$$

The full quasi-periodic function $f(x)$ is therefore represented as:

$$f(x) = e^{ik_x^0 x} \sum_{n \in \mathbb{Z}} A_n e^{\frac{2in\pi}{d_x} x} \quad (2.6)$$

The unknown coefficients are then found using a method specific to the problem by substituting this enforced form of the solution into the relevant governing equations, for instance a boundary condition or a wave equation.

This completes the process of enforcing quasi-periodicity in 1 dimension – if quasi-periodicity in a second dimension is required, then the same process is repeated again, starting from the already determined form of the function with quasi-periodicity in 1 dimension.

2.3 Quasi-periodicity in 2 dimensions: the 2D Fourier series

If $f(x)$ is replaced by $f(x, y)$, then it is expected that the unknown coefficients A_n represent the Fourier expansion along x which is valid at a specific value of y , and to a different location in the y direction would result in a different expansion along x , yielding a different set of coefficients. For this reason, the fixed expansion coefficients A_n are now made to be functions of y , $A_n(y)$:

$$f(x, y) = e^{ik_x^0 x} \sum_{n \in \mathbb{Z}} A_n(y) e^{\frac{2in\pi}{d_x} x} \quad (2.7)$$

Now, quasi-periodicity over y is simply applied to each one of these y -variable coefficients, making the whole expansion also quasi-periodic in y . This means enforcing the following condition for each A_n :

$$A_n(y + md_y) = e^{imk_y^0 d_y} A_n(y) \quad (2.8)$$

Using the same logic as explained in [Section 2.2](#), each A_n is expressed as the product of a phase offset $e^{ik_y y}$ and an unknown function $h_n(y)$ which is periodic in y :

$$A_n(y) = e^{ik_y y} h_n(y) \quad (2.9)$$

$$h_n(y + md_y) = h_n(y) \quad (2.10)$$

Now the periodic function $h_n(y)$ is represented as a new Fourier expansion with new unknown coefficients $B_{n,m}$, which in addition to the first index n used for A_n must now carry a second index m for the new expansion:

$$h_n(y) = \sum_{m \in \mathbb{Z}} B_{n,m} e^{\frac{2im\pi}{d_y} y} \quad (2.11)$$

Therefore the y -variable coefficients $A_n(y)$ for the expansions along x are represented as:

$$A_n(y) = e^{ik_y y} \sum_{m \in \mathbb{Z}} B_{n,m} e^{\frac{2im\pi}{d_y} y} \quad (2.12)$$

This form of $A_n(y)$ is now substituted back into the original expansion for $f(x, y)$, [\(2.7\)](#):

$$f(x, y) = e^{ik_x^0 x} \sum_{n \in \mathbb{Z}} \left(e^{ik_y y} \sum_{m \in \mathbb{Z}} B_{n,m} e^{\frac{2im\pi}{d_y} y} \right) e^{\frac{2in\pi}{d_x} x} \quad (2.13)$$

$$f(x, y) = e^{i(k_x^0 x + k_y^0 y)} \sum_{n \in \mathbb{Z}} \sum_{m \in \mathbb{Z}} B_{n,m} e^{2i\pi \left(\frac{nx}{d_x} + \frac{my}{d_y} \right)} \quad (2.14)$$

This form is equivalent to the 2D Fourier series (the double summation) multiplied by the incident phase term $e^{i(k_x^0 x + k_y^0 y)}$.

2.4 Orthogonality and its use in applying boundary conditions

A very useful property of expansions taking the form of [\(2.14\)](#) is orthogonality: the 2D Fourier series components indexed by n and m within the summation $e^{2i\pi(n x/d_x + m y/d_y)}$ are by definitional orthogonal with respect to one another over the extent of the cell spanning over $x \in [0, d_x)$, $y \in$

$[0, d_y)$, and multiplying the whole summation by the incident phase term $e^{i(k_x^0 x + k_y^0 y)}$ does not alter that fact. This means that if two or more expansions of this form are equated to one another, a one-to-one relationship between the expansion coefficients can be formed. For instance, suppose the following equation appears in the derivation:

$$e^{i(k_x^0 x + k_y^0 y)} \sum_{n \in \mathbb{Z}} \sum_{m \in \mathbb{Z}} B_{n,m} e^{2i\pi \left(\frac{nx}{d_x} + \frac{my}{d_y} \right)} = e^{i(k_x^0 x + k_y^0 y)} \sum_{n \in \mathbb{Z}} \sum_{m \in \mathbb{Z}} C_{n,m} e^{2i\pi \left(\frac{nx}{d_x} + \frac{my}{d_y} \right)} \quad (2.15)$$

This directly leads to the conclusion that $B_{n,m} = C_{n,m}$. This can be proven by multiplying both sides of the equation by $e^{-2i\pi(lx/d_x + qy/d_y)}$ where l and q are new integer values, and then performing an area integral over the unit cell: each side returns zero for all terms in the summation except where $l = n$ and $q = m$:

$$\int_0^{d_y} dy \cdot \int_0^{d_x} dx \cdot e^{i(k_x^0 x + k_y^0 y)} \sum_{n \in \mathbb{Z}} \sum_{m \in \mathbb{Z}} B_{n,m} e^{2i\pi \left(\frac{(n-l)x}{d_x} + \frac{(m-q)y}{d_y} \right)} = d_x d_y B_{l,q} \quad (2.16)$$

$$\int_0^{d_y} dy \cdot \int_0^{d_x} dx \cdot e^{i(k_x^0 x + k_y^0 y)} \sum_{n \in \mathbb{Z}} \sum_{m \in \mathbb{Z}} C_{n,m} e^{2i\pi \left(\frac{(n-l)x}{d_x} + \frac{(m-q)y}{d_y} \right)} = d_x d_y C_{l,q} \quad (2.17)$$

$$\therefore B_{n,m} = C_{n,m} \quad (2.18)$$

Another way of concluding that this is true is simply by recognising that a Fourier series for a given function is unique – only one combination of components represents the function, therefore when linear superpositions of different series summations with the same periods appear in equations, the individual components can be dealt with separately. The orthogonality property is useful, for instance, in applying boundary conditions when matching the fields in two regions at an interface.

2.5 Expansion terms as wave functions

It may be convenient to express the expansion (2.14) in a slightly different form:

$$e^{i(k_x^0 x + k_y^0 y)} \sum_{n \in \mathbb{Z}} \sum_{m \in \mathbb{Z}} B_{n,m} e^{2i\pi \left(\frac{nx}{d_x} + \frac{my}{d_y} \right)} = \sum_{n \in \mathbb{Z}} \sum_{m \in \mathbb{Z}} \psi_{n,m}(x, y) \quad (2.19)$$

Here, the wave functions $\psi_{n,m}(x, y)$ are defined as:

$$\psi_{n,m}(x, y) = e^{i \left(k_x^0 + \frac{2n\pi}{d_x} \right) x + i \left(k_y^0 + \frac{2m\pi}{d_y} \right) y} \quad (2.20)$$

This form is convenient for brevity, and it also helps recognise that each term in the summation $e^{2i\pi(nx/d_x + my/d_y)}$ when multiplied by the incident phase term $e^{i(k_x^0 x + k_y^0 y)}$ forms a plane wave travelling in the xy plane, with a wave vector whose x and y components are $k_x^n = k_x^0 + 2n\pi/d_x$ and $k_y^m = k_y^0 + 2m\pi/d_y$ respectively:

$$\psi_{n,m}(x,y) = e^{i(k_x^n x + k_y^m y)} \quad (2.21)$$

2.6 3D functions with 2D periodicity

The next stage in using the quasi-periodic expansions is to determine a form of expansion in 3 dimensions, which is only quasi-periodic in just 2 of those dimensions. Returning to the form of arbitrary function $f(x,y)$, a function of all 3 coordinates is now substituted, $f(x,y,z)$. There are no periodicity relations for the z coordinate, and so far nothing is known about the z dependence, therefore the only logical step is to allow the coefficients $B_{n,m}$ for the expansion over the xy plane vary z , so that in each xy plane for a given value of z a new expansion with a new set of coefficients is permitted to exist:

$$f(x,y,z) = \sum_{n \in \mathbb{Z}} \sum_{m \in \mathbb{Z}} B_{n,m}(z) \psi_{n,m}(x,y) \quad (2.22)$$

The only fields in the problem at hand defined over all 3 dimensions are the pressures, which within their domains satisfy the homogeneous Helmholtz equation $(\nabla^2 + k^2)p = 0$. If the function $f(x,y,z)$ is to satisfy the Helmholtz equation, then the form of the z -dependent expansion coefficients $B_{n,m}(z)$ can be determined by substituting (2.22) into the Helmholtz equation:

$$(\nabla^2 + k^2) \sum_{n \in \mathbb{Z}} \sum_{m \in \mathbb{Z}} B_{n,m}(z) \psi_{n,m}(x,y) = 0 \quad (2.23)$$

The Laplacian operator ∇^2 takes the form of $\nabla^2 = \partial_x^2 + \partial_y^2 + \partial_z^2$ in Cartesian coordinates:

$$(\partial_x^2 + \partial_y^2 + \partial_z^2 + k^2) \sum_{n \in \mathbb{Z}} \sum_{m \in \mathbb{Z}} B_{n,m}(z) \psi_{n,m}(x,y) = 0 \quad (2.24)$$

Due to linearity, the partial differential operators can be applied to each summation term independently:

$$\sum_{n \in \mathbb{Z}} \sum_{m \in \mathbb{Z}} \left(-(k_x^n)^2 - (k_y^m)^2 + \partial_z^2 + k^2 \right) B_{n,m}(z) \psi_{n,m}(x,y) = 0 \quad (2.25)$$

Due to orthogonality of the $\psi_{n,m}(x,y)$ terms, each term within the summation must equal 0 (consider that the 0 on the right hand side in (2.25) can be seen as another 2D Fourier expansion with each coefficient simply equal to 0):

$$\left(-(k_x^n)^2 - (k_y^m)^2 + \partial_z^2 + k^2 \right) B_{n,m}(z) \psi_{n,m}(x,y) = 0 \quad (2.26)$$

This leads to the following differential equation for $B_{n,m}(z)$:

$$\partial_z^2 B_{n,m}(z) + \left(k^2 - (k_x^n)^2 - (k_y^m)^2 \right) B_{n,m}(z) = 0 \quad (2.27)$$

This equivalent to a Helmholtz equation in 1D, along z :

$$\partial_z^2 B_{n,m}(z) + (k_z^{n,m})^2 B_{n,m}(z) = 0 \quad (2.28)$$

The new term $(k_z^{n,m})^2$ is defined as:

$$(k_z^{n,m})^2 = \left(k^2 - (k_x^n)^2 - (k_y^m)^2 \right) \quad (2.29)$$

The solution for $B_{n,m}(z)$ is a linear combination of two complex exponentials with undetermined coefficients $C_{n,m}^+$ and $C_{n,m}^-$:

$$B_{n,m}(z) = C_{n,m}^+ e^{ik_z^{n,m}z} + C_{n,m}^- e^{-ik_z^{n,m}z} \quad (2.30)$$

Here, $k_z^{n,m}$ is taken from the positive square root of (2.29), making obvious that the term represents the z component of a wave vector which has magnitude k , and x and y components k_x^n and k_y^m respectively:

$$k_z^{n,m} = +\sqrt{k^2 - (k_x^n)^2 - (k_y^m)^2} \quad (2.31)$$

Therefore the full form of the Cartesian expansion of any field defined over x , y and z which is quasi-periodic in x and y with periods d_x and d_y respectively, and satisfies the Helmholtz equation, is:

$$f(x, y, z) = \sum_{n \in \mathbb{Z}} \sum_{m \in \mathbb{Z}} (C_{n,m}^+ e^{ik_z^{n,m}z} + C_{n,m}^- e^{-ik_z^{n,m}z}) \psi_{n,m}(x, y) \quad (2.32)$$

For brevity in the same vein as using the $\psi_{n,m}(x, y)$ terms, the expansion can be expressed as:

$$f(x, y, z) = \sum_{n \in \mathbb{Z}} \sum_{m \in \mathbb{Z}} \left(C_{n,m}^+ \zeta_{n,m}(z) + \frac{C_{n,m}^-}{\zeta_{n,m}(z)} \right) \psi_{n,m}(x, y) \quad (2.33)$$

Where the terms $\zeta_{n,m}(z)$ are the z -dependent parts of the wave functions:

$$\zeta_{n,m}(z) = e^{ik_z^{n,m}z} \quad (2.34)$$

The summation now represents a superposition of plane waves travelling in all 3 dimensions:

$$\psi_{n,m}(x, y) \zeta_{n,m}(z) = e^{i(k_x^n x + k_y^m y + k_z^{n,m} z)} \quad (2.35)$$

$$\frac{\psi_{n,m}(x, y)}{\zeta_{n,m}(z)} = e^{i(k_x^n x + k_y^m y - k_z^{n,m} z)} \quad (2.36)$$

As enforced by applying the Helmholtz equation, all of the wave vectors $\overrightarrow{k_{n,m}}$ have length k :

$$\|\overrightarrow{k_{n,m}}\| = \sqrt{(k_x^n)^2 + (k_y^m)^2 + (k_z^{n,m})^2} = k \quad (2.37)$$

An important point is that $k_z^{n,m}$ is not always real – in fact, every expansion will only have a finite set of n, m combinations for which $k_z^{n,m}$ is real, outside which set $k_z^{n,m}$ is imaginary. This is obvious from examining the expression definition of $k_z^{n,m}$ in (2.37). When $(k_x^n)^2 - (k_y^m)^2 > k^2$, $k_z^{n,m}$ becomes imaginary. Since imaginary wavenumber components cause exponential growth towards infinity in either the positive or negative direction along their respective coordinate axis, this places a restriction on the terms in expansion (2.33) which can be used in domains which are either infinite or semi-infinite along z . For instance, if the domain extends to $z = +\infty$, negative imaginary z components of the wavenumber are not permitted as this causes growth towards $z = +\infty$. If in combination with this, waves approaching from $+\infty$ are also not permitted (such as is the case when only scattered or transmitted waves travelling towards $z = +\infty$ are valid), then all real negative or negative imaginary z components resulting from the $1/\zeta_{n,m}(z)$ terms are prohibited, setting all $C_{n,m}^-$ in (2.33) to zero and leaving just one side of the expansion featuring the $\zeta_{n,m}(z)$ terms:

$$f(x, y, z) = \sum_{n \in \mathbb{Z}} \sum_{m \in \mathbb{Z}} C_{n,m}^+ \zeta_{n,m}(z) \psi_{n,m}(x, y) \quad (2.38)$$

3. Behaviour and interaction of structural elements

The equations governing the behaviour of the rods and plates in the problem and their mutual interactions are determined in this section, leading to a set of expressions used in the solution in Section 5.

3.1 Behaviour of rods

The equations governing longitudinal vibration in a thin rod are:

$$\left(\partial_r^2 - \frac{E_{rod}}{\rho_{rod}} \partial_t^2 \right) \sigma_{rod}(r) = 0 \quad (3.1)$$

$$\rho_{rod} \partial_t u_{rod} = \partial_r \sigma_{rod}(r) \quad (3.2)$$

Where $\sigma_{rod}(r)$ is stress, and $u_{rod}(r)$ is the velocity of a point under deformation. The constants E_{rod} and ρ_{rod} are the elastic modulus and density of the rod material. For convenience, a new coordinate r has been defined local to the rod, where the rod extend from $r = 0$ to the rod length $r = L_{rod}$ (otherwise the solution in this section would have an excess of minus signs due to the location of the rods within the problem with one end at $z = -d_z$). The first equation (3.1) is the standard wave equation for σ_{rod} , and the second allows u to be determined, given σ . The solutions are:

$$\sigma_{rod}(r) = a e^{ik_L r} + b e^{-ik_L r} \quad (3.3)$$

$$u_{rod}(r) = -\frac{1}{Z_{rod}} (a e^{ik_L r} - b e^{-ik_L r}) \quad (3.4)$$

Here, the quantities k_L are the longitudinal wavenumber and Z_{rod} the rod impedance defined as:

$$k_L = \sqrt{\frac{E_{rod}}{\rho_{rod}}} \quad (3.5)$$

$$Z_{rod} = \rho_{rod} c_{rod} = \sqrt{\rho_{rod} E_{rod}} \quad (3.6)$$

In the given problem, the rod is known to exert forces on the upper plate and lower plate. If the rod exerts a force f_1 via its upper end upwards (pushing in the $+r$ direction) on the upper plate, an equal force downwards must be experienced by the rod's upper end, resulting in a stress of $\sigma_1 = f_1/S_{rod}$ at $r = L_{rod}$ where S_{rod} is the rod's cross-sectional area perpendicular to r . The stress σ_1 a positive sign as a positive f_1 causes compression in that end of the rod. If the rod exerts a force f_2 from its lower end upwards (pulling in the $+r$ direction) on the lower plate, an equal force downwards must be experienced by the rod's lower end, stretching the rod via a negative stress of $\sigma_2 = -f_2/S_{rod}$ at $r = 0$. This results in the following boundary conditions:

$$\sigma_{rod}|_{r=0} = \sigma_2 \quad (3.7)$$

$$\sigma_{rod}|_{r=L_{rod}} = \sigma_1 \quad (3.8)$$

Defining $\vartheta = e^{ik_L L_{rod}}$, the boundary conditions result in the following relations between a and b :

$$a + b = \sigma_2 \quad (3.9)$$

$$a\vartheta^2 + b = \sigma_1\vartheta \quad (3.10)$$

The resulting expressions for a and b are:

$$a = \frac{\sigma_1\vartheta - \sigma_2}{\vartheta^2 - 1} \quad (3.11)$$

$$b = \frac{\sigma_2\vartheta^2 - \sigma_1\vartheta}{\vartheta^2 - 1} \quad (3.12)$$

Defining $\theta = e^{ik_L r}$, The total expression for stress in the rod is therefore:

$$\sigma_{rod}(r) = a\theta + \frac{b}{\theta} = \frac{\theta(\sigma_1\vartheta - \sigma_2) + \frac{1}{\theta}(\sigma_2\vartheta^2 - \sigma_1\vartheta)}{\vartheta^2 - 1} \quad (3.13)$$

$$= \frac{\sigma_2 \sin(k_L r) + \sigma_1 \sin(k_L(L_{rod} - r))}{\sin(k_L L_{rod})} \quad (3.14)$$

The expression for point velocity in the rod is:

$$u_{rod}(r) = \frac{1}{Z_{rod}} \left(\frac{b}{\theta} - a\theta \right) = \frac{1}{Z_{rod}} \left(\frac{\frac{1}{\theta} (\sigma_2 \vartheta^2 - \sigma_1 \vartheta) - \theta (\sigma_1 \vartheta - \sigma_2)}{\vartheta^2 - 1} \right) \quad (3.15)$$

$$= \frac{k_L}{\rho_{rod} \omega} \left(\frac{\sigma_2 \cos(k_L(L_{rod} - r)) - \sigma_1 \cos(k_L L_{rod})}{i \sin(k_L L_{rod})} \right) \quad (3.16)$$

Taking the limit of the velocity expression (3.16) as k_L approaches 0 requires application of l'Hospital's rule, and results in:

$$\lim_{k \rightarrow \infty} u_{rod}(r) = \frac{\sigma_2 - \sigma_1}{i\omega \rho_{rod} L} = \frac{f_2 + f_1}{i\omega \rho_{rod} L_{rod} S_{rod}} = \frac{f_2 + f_1}{i\omega M_{rod}} \quad (3.17)$$

Therefore, the rod is seen to act as a rigid body with mass $M_{rod} = \rho_{rod} L_{rod} S_{rod}$. Taking the same limit of the stress expression (3.14) also requires l'Hospital's rule and results in:

$$\lim_{k \rightarrow \infty} \sigma_{rod}(r) = \frac{r\sigma_1 + (L - r)\sigma_2}{L_{rod}} = \sigma_2 \left(1 - \frac{r}{L_{rod}} \right) + \sigma_1 \left(\frac{r}{L_{rod}} \right)$$

Hence, the stress varies linearly from σ_2 at $r = 0$ to σ_1 at $r = L_{rod}$.

The key result of this part of the derivation relevant to the solution in Section 5 is the relationship between the rigid rod velocity u_{rod} and the two forces exerted on the plates:

$$f_2 = i\omega M_{rod} u_{rod} - f_1 \quad (3.18)$$

3.2 Forces exerted by the rods on the plates

The total upwards (+z) force exerted by a single rod on the upper plate (the rod located at $x = 0, y = 0$ in the central unit cell is taken here) is defined to be f_1 , similarly the total upwards force exerted by the same rod on the lower plate is f_2 . Force f_1 must result in an applied upwards pressure distribution $p_{rod1, single}(x, y)$ at the point connection between the rod at its upper end and the plate, and as this must be the force f_1 distributed over a certain area, the area integral of $p_{rod1, single}(x, y)$ must equal f_1 . Taking the limit as this area approaches zero justifies expressing σ_{point1} as a 2D Dirac delta multiplied by f_1 , whose area integral is f_1 :

$$p_{rod1, single}(x, y) = f_1 \delta(x) \delta(y) \quad (3.19)$$

$$\int_{x=-x_1}^{x=x_1} dx \cdot \int_{y=-y_1}^{y=y_1} dy \cdot p_{rod1, single} = f_1, \quad x_1, y_1 > 0 \quad (3.20)$$

Similarly, the applied upwards pressure at the point connection between the lower end of the rod and the lower plate is expressed by $f_2 \delta(x) \delta(y)$.

Since the combined pressure distributions on the plates due all of the rods together must satisfy quasi-periodicity, once the nature of the distribution for the rod within the central unit cell is known,

the total distribution due to all the rods is immediately known as a quasi-periodic grid consisting of the distribution to a single rod repeated with the necessary spatial and phase offsets:

$$p_{rod1,tot} = \psi_{0,0}(x, y) \sum_{n \in \mathbb{Z}} \sum_{m \in \mathbb{Z}} p_{rod1,single}(x - nd_x, y - md_y) \quad (3.21)$$

$$= f_1 \psi_{0,0}(x, y) \sum_{n \in \mathbb{Z}} \sum_{m \in \mathbb{Z}} \delta(x - nd_x) \delta(y - md_y) \quad (3.22)$$

This form is now converted to the form using the 2D Fourier expansion whose generic form is given in (2.19). First, the expression is equated to an expansion with unknown coefficients $G_{m,n}$:

$$f_1 \psi_{0,0}(x, y) \sum_{n \in \mathbb{Z}} \sum_{m \in \mathbb{Z}} \delta(x - nd_x) \delta(y - md_y) = \sum_{n \in \mathbb{Z}} \sum_{m \in \mathbb{Z}} G_{n,m} \psi_{n,m}(x, y) \quad (3.23)$$

$$f_1 \sum_{n \in \mathbb{Z}} \sum_{m \in \mathbb{Z}} \delta(x - nd_x) \delta(y - md_y) = \sum_{n \in \mathbb{Z}} \sum_{m \in \mathbb{Z}} G_{n,m} e^{2i\pi \left(\frac{nx}{d_x} + \frac{my}{d_y} \right)} \quad (3.24)$$

Now, both sides are multiplied by $e^{-2i\pi(lx/d_x + qy/d_y)}$ where $l, q \in \mathbb{Z}$, following which an area integral is performed over the unit cell. All terms in the summation on the right hand side return 0 except for the case where $n = l$ and $m = q$, in which case the result is just the coefficient $G_{n,m}$ multiplied by the unit cell area:

$$f_1 \sum_{n \in \mathbb{Z}} \sum_{m \in \mathbb{Z}} \delta(x - nd_x) \delta(y - md_y) e^{-2i\pi \left(\frac{lx}{d_x} + \frac{qy}{d_y} \right)} = \sum_{n \in \mathbb{Z}} \sum_{m \in \mathbb{Z}} G_{n,m} e^{2i\pi \left(\frac{(n-l)x}{d_x} + \frac{(m-q)y}{d_y} \right)} \quad (3.25)$$

$$f_1 \int_0^{d_x} dx \cdot \int_0^{d_y} dy \cdot \sum_{n \in \mathbb{Z}} \sum_{m \in \mathbb{Z}} \delta(x - nd_x) \delta(y - md_y) e^{-2i\pi \left(\frac{lx}{d_x} + \frac{qy}{d_y} \right)} = d_x d_y G_{n,m} \quad (3.26)$$

Integrating a Dirac delta multiplied by a function returns that function's value at the location of the Dirac delta, therefore since the only Dirac delta which is within the integration area occurs at $x = 0, y = 0$ then the integral returns 1 and the left hand side is simply f_1 :

$$f_1 = d_x d_y G_{n,m} \quad (3.27)$$

$$G_{n,m} = \frac{f_1}{d_x d_y} \quad (3.28)$$

Therefore, the coefficients of the Fourier expansion of $p_{rod1,tot}$ are all identical and can be taken outside the summations as a single coefficient W_1 :

$$p_{rod1,tot} = W_1 \sum_{n \in \mathbb{Z}} \sum_{m \in \mathbb{Z}} \psi_{n,m}(x, y), \quad W_1 = \frac{f_1}{d_x d_y} \quad (3.29)$$

Similarly, the upwards force distribution on the second plate due to all the rods $p_{rod2,tot}$ is expressed as:

$$p_{rod2,tot} = W_2 \sum_{n \in \mathbb{Z}} \sum_{m \in \mathbb{Z}} \psi_{n,m}(x, y), \quad W_2 = \frac{f_2}{d_x d_y} \quad (3.30)$$

3.3 Behaviour of plates

The inhomogeneous wave equation for the displacement $w(x, y)$ of a thin plate permitting bending motion only, with force distributions p_{top} and p_{bottom} on the top and bottom sides respectively can be expressed as:

$$D(\nabla^4 - k_B^4)w(x, y) = p_{top} - p_{bottom} \quad (3.31)$$

Here, D is the bending stiffness, w is the displacement and $k_B^4 = M_{plate}\omega^2/D$ is the bending wavenumber of the plate, and M_{plate} is the mass per unit area.

Substituting the velocity $u(x, y) = -i\omega w(x, y)$ gives the equivalent expression for plate velocity:

$$\frac{iD}{\omega}(\nabla^4 - k_B^4)u(x, y) = p_{top} - p_{bottom} \quad (3.32)$$

4. Behaviour of the air regions

The expansions for expressing the pressure in the air regions are presented here following the form derived in Section 2.6, and the implications of using these expansions related to the propagating and evanescent modes are examined. The existence of a low frequency region where only one reflected and one transmitted plane wave mode is generated is demonstrated, in the far field within this low frequency region the structure is indistinguishable from a layer of fluid with certain effective properties.

4.1 Reflected pressure field and the effective fluid layer region

The pressure in the domain above the top plate is expressed as the summation of the incident field and the scattered (reflected) field, as described in Section 1.2, so that the scattered field which gives the correct total field in combination with the incident field is determined by applying the matching conditions at the plate surface:

$$p_1(x, y, z) = p_{inc} + p_{scat} \quad (4.1)$$

The form of the incident field is defined in (1.2), and the scattered field is expressed in the form of a 3D expansion with 2D quasi-periodicity as illustrated in (2.33):

$$\sum_{n \in \mathbb{Z}} \sum_{m \in \mathbb{Z}} R_{n,m} \zeta_{n,m}(z) \psi_{n,m}(x, y) \quad (4.2)$$

As explained in [Section 2.6](#), in this case only real positive or positive imaginary z components of the wavenumber $k_z^{n,m}$ are permitted: real negative components are prohibited as they represent waves incident from $z = +\infty$, and negative imaginary components are prohibited as they cause exponential growth towards $z = +\infty$. Hence, only the part of the summation with $\zeta_{n,m}(z)$ terms is used and the part with $1/\zeta_{n,m}(z)$ terms is discarded.

In this case, the terms in the summation which feature imaginary $k_z^{n,m}$ are evanescent waves which exist only near the surface of the panel and decay exponentially with distance, propagating only along the plate surface. There is a certain frequency below which there is only one term in the summation corresponding to $n = 0, m = 0$ which results in a propagating wave with real $k_z^{0,0}$, and the rest of the terms are evanescent. In this case, at a sufficient distance from the panel where the evanescent waves can be neglected, the whole construction can be seen to act as a layer of effective fluid, generating just one propagating reflected wave with reflection coefficient $R_{0,0}$. This frequency limit is determined as follows: first the form of $k_z^{n,m}$ defined in [\(2.31\)](#) is examined, substituting the explicit forms of k_x^n and k_y^m :

$$k_z^{n,m} = + \sqrt{k^2 - \left(k_x^0 + \frac{2\pi n}{d_x}\right)^2 - \left(k_y^0 + \frac{2\pi m}{d_y}\right)^2} \quad (4.3)$$

The requirement is for $k_z^{n,m}$ to be imaginary for all n and m except for $n = 0, m = 0$. This actually results in two conditions:

$$\left(k_x^0 \pm \frac{2\pi}{d_x}\right)^2 > k^2, \quad \left(k_y^0 \pm \frac{2\pi}{d_y}\right)^2 > k^2 \quad (4.4)$$

Expressing k_x^0 and k_y^0 in terms of angles θ_x and θ_y in the xz and xy planes as defined in [\(1.3\)](#) results in:

$$k < \left|k \sin(\theta_x) \pm \frac{2\pi}{d_x}\right|, \quad k < \left|k \sin(\theta_y) \pm \frac{2\pi}{d_y}\right| \quad (4.5)$$

$$kd_x < \frac{2\pi}{1 + |\sin(\theta_x)|}, \quad kd_y < \frac{2\pi}{1 + |\sin(\theta_x)|} \quad (4.6)$$

$$k < \min\left(\frac{2\pi}{d_x(1 + |\sin(\theta_x)|)}, \frac{2\pi}{d_y(1 + |\sin(\theta_y)|)}\right) \quad (4.7)$$

Equivalently, in terms of the incident and ‘‘polarisation’’ φ_I and φ_R , also defined in [\(1.3\)](#):

$$k < \min\left(\frac{2\pi}{d_x(1 + |\sin(\varphi_I) \cos(\varphi_P)|)}, \frac{2\pi}{d_y(1 + |\sin(\varphi_I) \sin(\varphi_P)|)}\right) \quad (4.8)$$

When this condition is satisfied, assessing the panel's reflection property is very simple as only the $R_{0,0}$ coefficient is relevant, which has a magnitude related to the entire reflected energy (the evanescent waves do not carry any energy outwards from the structure) and a phase offset – when the frequency increases, more and more of the $R_{n,m}\zeta_{n,m}(z)\psi_{n,m}(x,y)$ components will start to propagate, at different angles, which means there will be no such straightforward far-field value as the different propagating reflected waves will always interfere with each other. The most straightforward option to assess amount of reflection at higher frequencies is the sum the energies of all propagating modes, i.e. add together $|R_{n,m}|^2$ corresponding to all n, m which yield real $k_z^{n,m}$.

4.2 Incident field expansion

Whereas the incident field is just one plane wave, to simplify the process of matching of the pressure at the boundaries it is convenient to also express it as an expansion as follows:

$$p_{inc}(x, y, z) = \sum_{n \in \mathbb{Z}} \sum_{m \in \mathbb{Z}} \frac{I_{n,m}}{\zeta_{n,m}(z)} \psi_{n,m}(x, y) \quad (4.9)$$

Here, the coefficients $I_{n,m}$ are all 0 except for $I_{0,0}$ which is equal to 1 (meaning $I_{n,m}$ is a 2D Kronecker delta). This may seem unnecessary, however this way when matching at the boundaries is performed, only one set of expressions is generated, whereas otherwise twice the amount of matching expressions would need to be manipulated in [Section \(5.3\)](#) as the $n = 0, m = 0$ would have to be dealt with separately to all other cases.

4.3 Transmitted pressure field

In a similar way to the scattered field, the transmitted field $p_3(x, y, z)$ on the opposing side of the second panel is expressed as just one half of the expansion [\(2.33\)](#), this time with the $1/\zeta_{n,m}(z)$ terms leading to real negative or negative imaginary $k_z^{n,m}$ only as the waves must either decay or propagate towards $z = -\infty$:

$$p_3(x, y, z) = \sum_{n \in \mathbb{Z}} \sum_{m \in \mathbb{Z}} \frac{T_{n,m}}{\zeta_{n,m}(z)} \psi_{n,m}(x, y) \quad (4.10)$$

The low frequency region given by [\(4.7\)](#) or [\(4.8\)](#) was shown to exhibit only one propagating reflected wave with reflection coefficient $R_{0,0}$ in [Section 4.3](#), if the same limit is adhered to then only one propagating transmitted wave with transmission coefficient $T_{0,0}$. Above this frequency, multiple transmitted modes will start to propagate and interfere with each other, so the far-field limit can no longer be taken and the structure no longer acts as a fluid layer.

4.4 Pressure inside the cavity

The pressure $p_2(x, y, z)$ inside the cavity has no restrictions on $k_z^{n,m}$ – waves can propagate in both directions, and evanescent waves from both inner plate surfaces can exist as the region is finite in z – therefore both sides of the expansion [\(2.33\)](#) are used, with coefficients $F_{n,m}$ and $B_{n,m}$

representing the waves travelling forwards and backwards (in relation to the incident wave direction) in the cavity respectively:

$$p_2 = \sum_{n \in \mathbb{Z}} \sum_{m \in \mathbb{Z}} \left(\frac{F_{n,m}}{\zeta_{n,m}(z)} + B_{n,m} \zeta_{n,m}(z) \right) \psi_{n,m}(x, y) \quad (4.11)$$

5. Solution

The full solution of the problem is derived in this section, referring to the prerequisites covered in [Section 2](#), [Section 3](#) and [Section 4](#).

5.1 Summary of system equations

The pressures p_1 above the top plate, p_2 in the cavity and p_3 below the bottom plate are represented as (see [Section 4](#) for more detail):

$$p_1(x, y, z) = \sum_{n \in \mathbb{Z}} \sum_{m \in \mathbb{Z}} \left(\frac{I_{n,m}}{\zeta_{n,m}(z)} + R_{n,m} \zeta_{n,m}(z) \right) \psi_{n,m}(x, y) \quad (5.1)$$

$$p_2(x, y, z) = \sum_{n \in \mathbb{Z}} \sum_{m \in \mathbb{Z}} \left(\frac{F_{n,m}}{\zeta_{n,m}(z)} + B_{n,m} \zeta_{n,m}(z) \right) \psi_{n,m}(x, y) \quad (5.2)$$

$$p_3(x, y, z) = \sum_{n \in \mathbb{Z}} \sum_{m \in \mathbb{Z}} \frac{T_{n,m}}{\zeta_{n,m}(z)} \psi_{n,m}(x, y) \quad (5.3)$$

For matching purposes, only the z component of the particle velocity is required. The corresponding velocities v_{1z} , v_{2z} and v_{3z} are:

$$v_{1z} = \frac{1}{\rho_0 \omega} \sum_{n \in \mathbb{Z}} \sum_{m \in \mathbb{Z}} k_z^{n,m} \left(R_{n,m} \zeta_{n,m}(z) - \frac{I_{n,m}}{\zeta_{n,m}(z)} \right) \psi_{n,m}(x, y) \quad (5.4)$$

$$v_{2z} = \frac{1}{\rho_0 \omega} \sum_{n \in \mathbb{Z}} \sum_{m \in \mathbb{Z}} k_z^{n,m} \left(B_{n,m} \zeta_{n,m}(z) - \frac{F_{n,m}}{\zeta_{n,m}(z)} \right) \psi_{n,m}(x, y) \quad (5.5)$$

$$v_{3z} = \frac{-1}{\rho_0 \omega} \sum_{n \in \mathbb{Z}} \sum_{m \in \mathbb{Z}} k_z^{n,m} \frac{T_{n,m}}{\zeta_{n,m}(z)} \psi_{n,m}(x, y) \quad (5.6)$$

The velocities u_1 and u_2 of the top and bottom plate respectively are represented as 2D quasi-periodic functions in the form of [\(2.19\)](#) as:

$$u_1 = \sum_{n \in \mathbb{Z}} \sum_{m \in \mathbb{Z}} U_{n,m} \psi_{n,m}(x, y) \quad (5.7)$$

$$u_2 = \sum_{n \in \mathbb{Z}} \sum_{m \in \mathbb{Z}} V_{n,m} \psi_{n,m}(x, y) \quad (5.8)$$

The upwards force distributions on the top and bottom plate respectively due to the interconnecting rods, as determined in [Section 3.2](#):

$$p_{rod1,tot} = W_1 \sum_{n \in \mathbb{Z}} \sum_{m \in \mathbb{Z}} \psi_{n,m}(x, y) \quad (5.9)$$

$$p_{rod2,tot} = W_2 \sum_{n \in \mathbb{Z}} \sum_{m \in \mathbb{Z}} \psi_{n,m}(x, y) \quad (5.10)$$

Where, following the results from [Section 3.1](#):

$$W_1 = \frac{f_1}{d_x d_y}, W_2 = \frac{f_2}{d_x d_y} \quad (5.11)$$

$$W_2 = i\omega M_{rod} \frac{u_{rod}}{d_x d_y} - W_1 \quad (5.12)$$

5.2 Boundary conditions

The plate wave equation (3.32) is used to match the forces seen by the plate to the pressures in regions 1 and 2 and the force distribution due to the rods acting on the plate:

$$\frac{iD}{\omega} (\nabla^4 - k_B^4) u_1 = p_1|_{z=0} - p_2|_{z=0} - p_{rod1,tot} \quad (5.13)$$

Similarly, the forces seen by the bottom plate are matched to pressures in regions 2 and 3 and the force distribution due to the rods acting on the plate:

$$\frac{iD}{\omega} (\nabla^4 - k_B^4) u_1 = p_2|_{z=-d_z} - p_3|_{z=-d_z} - p_{rod2,tot} \quad (5.14)$$

Note that the polarities of $p_{rod1,tot}$ and $p_{rod2,tot}$ in the two equations are the same despite the rod being on opposite sides of the two plates as it was already specified in [Section 3.1](#) and [Section 3.2](#) that these forces represent the upwards force distribution on each plate.

The velocity of the top plate must equal the particle velocities in the air in the regions either side to it: this is actually equivalent to two boundary conditions:

$$u_1 = v_1|_{z=0} = v_2|_{z=0} \quad (5.15)$$

Similarly, the velocity of the top plate must equal the particle velocities in the air in its adjacent regions:

$$u_2 = v_2|_{z=-d_z} = v_3|_{z=-d_z} \quad (5.16)$$

Finally, the rod velocity u_{rod} must be matched to the plate velocities at the interconnecting points – due to quasi-periodicity, doing this for one rod at $x = 0, y = 0$ is enough to enforce the condition in all unit cells. This introduces two constraints – noting that $\psi_{n,m}(0,0) = 1$, the resulting expressions are:

$$u_{rod} = \sum_{n \in \mathbb{Z}} \sum_{m \in \mathbb{Z}} U_{n,m} = \sum_{n \in \mathbb{Z}} \sum_{m \in \mathbb{Z}} V_{n,m} \quad (5.17)$$

Since the wavefunctions $\psi_{n,m}(x, y)$ are no longer present in the summations – these summations represent u_1 and u_2 at a single point rather than throughout space – these terms cannot be manipulated using orthogonality and must be evaluated once the form of $U_{n,m}$ and $V_{n,m}$ becomes known.

Orthogonal wavefunction coefficients occurring in summations such as these, which cannot be separated using orthogonality cause conversion between the different wavefunction modes: there is no longer a one-to-one relationship between all occurrences of mode m, n across different domains in the system – rather, mode m, n in one domain is equated to some superposition of multiple modes – or typically, all of the modes – in the other domain. In this specific problem, it is the rods that introduce mode conversion – it can be shown that if the rods are omitted from the system leaving just the two plates with an air cavity, mode conversion is no longer present.

5.3 Matching between plates, rods and air regions using orthogonality

Orthogonality is easily used to form one-to-one relationships between the terms within the Fourier expansions representing the quantities dealt with in the matching conditions (5.13), (5.14), (5.15) and (5.16). This is done explicitly once for the first condition for illustration, following which the result is given for the remaining conditions.

Observing that $\zeta_{n,m}(0) = 1$ and substituting the expansions (5.1), (5.2), (5.7) and (5.9) into the pressure boundary condition at the top plate (5.13) results in:

$$\begin{aligned} \frac{iD}{\omega} (\nabla^4 - k_B^4) \sum_{n \in \mathbb{Z}} \sum_{m \in \mathbb{Z}} U_{n,m} \psi_{n,m}(x, y) \\ = \sum_{n \in \mathbb{Z}} \sum_{m \in \mathbb{Z}} (I_{n,m} + R_{n,m}) \psi_{n,m}(x, y) - \sum_{n \in \mathbb{Z}} \sum_{m \in \mathbb{Z}} (F_{n,m} + B_{n,m}) \psi_{n,m}(x, y) \\ - W_1 \sum_{n \in \mathbb{Z}} \sum_{m \in \mathbb{Z}} \psi_{n,m}(x, y) \end{aligned} \quad (5.18)$$

Due to linearity, the operator $(\nabla^4 - k_B^4)$ can be applied to each term in the first summation independently:

$$\begin{aligned}
& \frac{iD}{\omega} \sum_{n \in \mathbb{Z}} \sum_{m \in \mathbb{Z}} \left(\left((k_x^n)^2 + (k_y^m)^2 \right)^2 - k_B^4 \right) U_{n,m} \psi_{n,m}(x, y) \\
&= \sum_{n \in \mathbb{Z}} \sum_{m \in \mathbb{Z}} (I_{n,m} + R_{n,m}) \psi_{n,m}(x, y) - \sum_{n \in \mathbb{Z}} \sum_{m \in \mathbb{Z}} (F_{n,m} + B_{n,m}) \psi_{n,m}(x, y) \\
&- W_1 \sum_{n \in \mathbb{Z}} \sum_{m \in \mathbb{Z}} \psi_{n,m}(x, y)
\end{aligned} \tag{5.19}$$

Now, orthogonality of the wavefunctions $\psi_{n,m}(x, y)$ is used as described in [Section 2.4](#) to obtain the 1-to-1 relationship between the coefficients in the summation corresponding to each $\psi_{n,m}(x, y)$ mode:

$$\frac{iD}{\omega} \left(\left((k_x^n)^2 + (k_y^m)^2 \right)^2 - k_B^4 \right) U_{n,m} = I_{n,m} + R_{n,m} - F_{n,m} - B_{n,m} - W_1 \tag{5.20}$$

This expression actually describes an infinite set of equations indexed by n, m . Now that the use of orthogonality has been illustrated, the expressions resulting from substituting the expansions into the boundary conditions and then applying orthogonality are presented directly. For use in the matching expressions at the second plate, the cavity phase factor $\phi_{n,m}$ is defined as:

$$\phi_{n,m} = \zeta_{n,m}(-d_z) \tag{5.21}$$

Substituting expansions [\(5.2\)](#), [\(5.3\)](#), [\(5.8\)](#) and [\(5.10\)](#) into the pressure boundary condition at the second plate [\(5.14\)](#) results in:

$$\frac{iD}{\omega} \left(\left((k_x^n)^2 + (k_y^m)^2 \right)^2 - k_B^4 \right) V_{n,m} = \frac{F_{n,m}}{\phi_{n,m}} + B_{n,m} \phi_{n,m} - \frac{T_{n,m}}{\phi_{n,m}} - W_2 \tag{5.22}$$

Substituting expansions [\(5.1\)](#), [\(5.2\)](#) and [\(5.7\)](#) into the velocity matching condition at the first plate [\(5.15\)](#); then similarly substituting expansions [\(5.2\)](#), [\(5.3\)](#) and [\(5.8\)](#) into the velocity boundary condition at the second plate [\(5.16\)](#) results in:

$$U_{n,m} = \frac{k_z^{n,m}}{\rho_0 \omega} (R_{n,m} - I_{n,m}) = \frac{k_z^{n,m}}{\rho_0 \omega} (B_{n,m} - F_{n,m}) \tag{5.23}$$

$$V_{n,m} = \frac{k_z^{n,m}}{\rho_0 \omega} \left(B_{n,m} \phi_{n,m} - \frac{F_{n,m}}{\phi_{n,m}} \right) = -\frac{k_z^{n,m}}{\rho_0 \omega} \left(\frac{T_{n,m}}{\phi_{n,m}} \right) \tag{5.24}$$

Now, all that remains is algebraic manipulation of the resulting equations to determine the unknowns.

[\(5.20\)](#) and [\(5.23\)](#) are combined to eliminate $U_{n,m}$:

$$\frac{iD}{\omega} \left(\left((k_x^n)^2 + (k_y^m)^2 \right)^2 - k_B^4 \right) \frac{k_z^{n,m}}{\rho_0 \omega} (R_{n,m} - I_{n,m}) = I_{n,m} + R_{n,m} - F_{n,m} - B_{n,m} - W_1 \tag{5.25}$$

[\(5.22\)](#) and [\(5.24\)](#) are combined to eliminate $V_{n,m}$:

$$\frac{iD}{\omega} \left((k_x^n)^2 + (k_y^m)^2 \right)^2 - k_B^4 \frac{k_z^{n,m}}{\rho_0 \omega} \left(B_{n,m} \phi_{n,m} - \frac{F_{n,m}}{\phi_{n,m}} \right) = \frac{F_{n,m}}{\phi_{n,m}} + B_{n,m} \phi_{n,m} - \frac{T_{n,m}}{\phi_{n,m}} - W_2 \quad (5.26)$$

A new term $Q_{n,m}$ is introduced for brevity:

$$Q_{n,m} = \frac{iD k_z^{n,m}}{\rho_0 \omega^2} \left((k_x^n)^2 + (k_y^m)^2 \right)^2 - k_B^4 \quad (5.27)$$

Therefore (5.25) and (5.26) become:

$$Q_{n,m}(R_{n,m} - I_{n,m}) = I_{n,m} + R_{n,m} - F_{n,m} - B_{n,m} - W_1 \quad (5.28)$$

$$Q_{n,m} \left(B_{n,m} \phi_{n,m} - \frac{F_{n,m}}{\phi_{n,m}} \right) = \frac{F_{n,m}}{\phi_{n,m}} + B_{n,m} \phi_{n,m} - \frac{T_{n,m}}{\phi_{n,m}} - W_2 \quad (5.29)$$

5.4 Reflection and transmission in terms of incident field and rod forces

The expressions (5.12) and (5.17) relating the rod forces and interconnected point velocities are used to determine the unknown terms W_1 and W_2 , however they need to be evaluated at the end – due to the mode conversion produced by the rods as explained at the end of Section 5.2, expression (5.17) features summations of the as of yet unknown coefficients $R_{n,m}$ and $T_{n,m}$, which cannot be split using orthogonality and hence are not usable until $R_{n,m}$ and $T_{n,m}$ are derived in terms of W_1 and W_2 (as well as the incident field). Only once these relations are derived can they finally be combined with the relations in (5.12) and (5.17) in order to determine all unknowns. Therefore, for now W_1 and W_2 are treated as if they were known, and the following 4 equations with are solved for the 4 unknowns $R_{n,m}$, $T_{n,m}$, $F_{n,m}$ and $B_{n,m}$ (the first two equations are rearranged versions of (5.28) and (5.29), and other two originate from (5.23) and (5.24)):

$$R_{n,m}(Q_{n,m} + 1) - F_{n,m} - B_{n,m} = W_1 + I_{n,m}(Q_{n,m} - 1) \quad (5.30)$$

$$\frac{F_{n,m}}{\phi_{n,m}}(1 - Q_{n,m}) + B_{n,m} \phi_{n,m}(Q_{n,m} + 1) - \frac{T_{n,m}}{\phi_{n,m}} = W_2 \quad (5.31)$$

$$R_{n,m} + F_{n,m} - B_{n,m} = I_{n,m} \quad (5.32)$$

$$B_{n,m} \phi_{n,m} - \frac{F_{n,m}}{\phi_{n,m}} + \frac{T_{n,m}}{\phi_{n,m}} = 0 \quad (5.33)$$

To eliminate $F_{n,m}$ and $B_{n,m}$, (5.32) and (5.33) are first combined:

$$F_{n,m} = \frac{T_{n,m} + \phi_{n,m}^2 R_{n,m} - \phi_{n,m}^2 I_{n,m}}{1 - \phi_{n,m}^2} \quad (5.34)$$

$$B_{n,m} = \frac{T_{n,m} + R_{n,m} - I_{n,m}}{1 - \phi_{n,m}^2} \quad (5.35)$$

These forms of $F_{n,m}$ and $B_{n,m}$ are now substituted into (5.30) and (5.31), and the resulting expressions are combined to determine $R_{n,m}$ and $T_{n,m}$:

$$T_{n,m} = \phi_{n,m} \frac{(Q_{n,m}(\phi_{n,m}^2 - 1) - 2\phi_{n,m}^2)W_2 - 2\phi_{n,m}W_1 + 4\phi_{n,m}I_{n,m}}{(Q_{n,m} - 2)^2 \phi_{n,m}^2 - Q_{n,m}^2} \quad (5.36)$$

$$R_{n,m} = \frac{2\phi_{n,m}W_2 + W_1(Q_{n,m}^2(1 - \phi_{n,m}^2) + 2\phi_{n,m}^2) + I_{n,m}(Q_{n,m}^2(\phi_{n,m}^2 - 1) - 2(\phi_{n,m}^2 + 1)Q_{n,m}^2)}{(Q_{n,m} - 2)^2 \phi_{n,m}^2 - Q_{n,m}^2} \quad (5.37)$$

5.5 Determining the rod forces

The final stage of the derivation is determining W_1 and W_2 . The relationship between W_1 and W_2 given by (5.17) involves the rod velocity u_{rod} , so the first step is to represent u_{rod} as the first variant of (5.17), with the now known form of $U_{n,m}$ from (5.23) – this step is equivalent to matching the rod velocity to the velocities of the interconnecting points on the top plate:

$$u_{rod} = \sum_{n \in \mathbb{Z}} \sum_{m \in \mathbb{Z}} U_{n,m} = \frac{1}{\rho_0 \omega} \sum_{n \in \mathbb{Z}} \sum_{m \in \mathbb{Z}} k_z^{n,m} (R_{n,m} - I_{n,m}) \quad (5.38)$$

Substituting the form of $R_{n,m}$ from (5.37) and splitting the summation by terms involving W_1 , W_2 and $I_{n,m}$ and results in:

$$\begin{aligned} &= \frac{W_1}{\rho_0 \omega} \sum_{n \in \mathbb{Z}} \sum_{m \in \mathbb{Z}} k_z^{n,m} \left(\frac{Q_{n,m}^2(1 - \phi_{n,m}^2) + 2\phi_{n,m}^2}{(Q_{n,m} - 2)^2 \phi_{n,m}^2 - Q_{n,m}^2} \right) + \frac{W_2}{\rho_0 \omega} \sum_{n \in \mathbb{Z}} \sum_{m \in \mathbb{Z}} k_z^{n,m} \left(\frac{2\phi_{n,m}}{(Q_{n,m} - 2)^2 \phi_{n,m}^2 - Q_{n,m}^2} \right) \\ &\quad - \frac{1}{\rho_0 \omega} \sum_{n \in \mathbb{Z}} \sum_{m \in \mathbb{Z}} k_z^{n,m} I_{n,m} \left(\frac{Q_{n,m}^2(1 - \phi_{n,m}^2) + 2\phi_{n,m}^2}{(Q_{n,m} - 2)^2 \phi_{n,m}^2 - Q_{n,m}^2} \right) \end{aligned} \quad (5.39)$$

The three summations no longer contain any unknowns, and can be assigned names for brevity, additionally the final sum to the right only requires the $n = 0, m = 0$ term as $I_{n,m}$ is a 2D Kronecker delta. The following 3 terms are hence introduced:

$$\gamma_1 = \frac{1}{\rho_0 \omega} \sum_{n \in \mathbb{Z}} \sum_{m \in \mathbb{Z}} k_z^{n,m} \left(\frac{Q_{n,m}^2(1 - \phi_{n,m}^2) + 2\phi_{n,m}^2}{(Q_{n,m} - 2)^2 \phi_{n,m}^2 - Q_{n,m}^2} \right) \quad (5.40)$$

$$\gamma_2 = \frac{1}{\rho_0 \omega} \sum_{n \in \mathbb{Z}} \sum_{m \in \mathbb{Z}} k_z^{n,m} \left(\frac{2\phi_{n,m}}{(Q_{n,m} - 2)^2 \phi_{n,m}^2 - Q_{n,m}^2} \right) \quad (5.41)$$

$$\alpha_1 = \frac{k_z^{0,0}}{\rho_0 \omega} \left(\frac{Q_{0,0}^2(1 - \phi_{0,0}^2) + 2\phi_{0,0}^2}{(Q_{0,0} - 2)^2 \phi_{0,0}^2 - Q_{0,0}^2} \right) \quad (5.42)$$

Expression (5.39) now takes on a far simpler form:

$$u_{rod} = W_1\gamma_1 + W_2\gamma_2 - \alpha_1 \quad (5.43)$$

Now, u_{rod} is expressed again in a similar way using the second variant of (5.17), with $V_{n,m}$ in the summation as given by (5.24) and therefore matching the rod velocity to the velocities of the interconnecting points on the bottom plate:

$$u_{rod} = \sum_{n \in \mathbb{Z}} \sum_{m \in \mathbb{Z}} V_{n,m} = \frac{-1}{\rho_0 \omega} \sum_{n \in \mathbb{Z}} \sum_{m \in \mathbb{Z}} k_z^{n,m} \frac{T_{n,m}}{\phi_{n,m}} \quad (5.44)$$

As before, the result of substituting $T_{n,m}$ from (5.36) can be split into three summations:

$$\begin{aligned} &= \frac{W_2}{\rho_0 \omega} \sum_{n \in \mathbb{Z}} \sum_{m \in \mathbb{Z}} k_z^{n,m} \frac{(Q_{n,m}(1 - \phi_{n,m}^2) + 2\phi_{n,m}^2)}{(Q_{n,m} - 2)^2 \phi_{n,m}^2 - Q_{n,m}^2} + \frac{W_1}{\rho_0 \omega} \sum_{n \in \mathbb{Z}} \sum_{m \in \mathbb{Z}} k_z^{n,m} \frac{2\phi_{n,m}}{(Q_{n,m} - 2)^2 \phi_{n,m}^2 - Q_{n,m}^2} \\ &\quad - \frac{1}{\rho_0 \omega} \sum_{n \in \mathbb{Z}} \sum_{m \in \mathbb{Z}} k_z^{n,m} \frac{4\phi_{n,m} I_{n,m}}{(Q_{n,m} - 2)^2 \phi_{n,m}^2 - Q_{n,m}^2} \end{aligned} \quad (5.45)$$

This expression contains the same terms already defined as γ_1 and γ_2 , plus an additional term:

$$\alpha_2 = \frac{k_z^{0,0}}{\rho_0 \omega} \left(\frac{4\phi_{0,0}}{(Q_{0,0} - 2)^2 \phi_{0,0}^2 - Q_{0,0}^2} \right) \quad (5.46)$$

Therefore, the result of matching velocity between the rods and the bottom plate is the following relation:

$$u_{rod} = W_1\gamma_2 + W_2\gamma_1 - \alpha_2 \quad (5.47)$$

Now, (5.43) and (5.47) are combined to determine W_1 and W_2 :

$$W_1 = \frac{\alpha_2 - \alpha_1 + i\omega \frac{M_{rod}}{d_x d_y} (\gamma_1 \alpha_1 - \gamma_2 \alpha_2)}{2(\gamma_2 - \gamma_1) + i\omega \frac{M_{rod}}{d_x d_y} (\gamma_1^2 - \gamma_2^2)} \quad (5.48)$$

$$W_2 = \frac{\alpha_1 - \alpha_2 + i\omega \frac{M_{rod}}{d_x d_y} (\gamma_1 \alpha_2 - \gamma_2 \alpha_1)}{2(\gamma_2 - \gamma_1) + i\omega \frac{M_{rod}}{d_x d_y} (\gamma_1^2 - \gamma_2^2)} \quad (5.49)$$

This concludes the derivation. These values of W_1 and W_2 can now be used in expressions (5.36) and (5.37) to calculate the reflected and transmitted waves. The infinite summations contained within W_1 and W_2 as terms γ_1 and γ_2 can be evaluated numerically given a certain truncation number which limits the absolute values of n and m . Truncating the summations has an effect akin to defining a spatial resolution limit, as it removes high spatial frequency content from the Fourier

expansions – providing the expanded functions are sufficiently smooth, the numerical converges to the exact solution as the truncation number increases.

If the problem is restricted to the low frequency region where there is only one propagating and only one reflected mode, only the terms $T_{0,0}$ and $R_{0,0}$ need to be evaluated in order to determine the far-field reflected and transmitted pressure:

$$T_{0,0} = \phi_{0,0} \frac{(Q_{0,0}(\phi_{0,0}^2 - 1) - 2\phi_{0,0}^2)W_2 - 2\phi_{0,0}W_1 + 4\phi_{0,0}}{(Q_{0,0} - 2)^2 \phi_{0,0}^2 - Q_{0,0}^2} \quad (5.50)$$

$$R_{0,0} = \frac{2\phi_{0,0}W_2 + W_1(Q_{0,0}^2(1 - \phi_{0,0}^2) + 2\phi_{0,0}^2) + Q_{0,0}^2(\phi_{0,0}^2 - 1) - 2(\phi_{0,0}^2 + 1)Q_{0,0}^2}{(Q_{0,0} - 2)^2 \phi_{0,0}^2 - Q_{0,0}^2} \quad (5.51)$$

6. Discussion and sample results

In this section, some consequences of the expressions derived in Section 5 are discussed, and sample results generated using the expressions are presented.

6.1 Relation to double-panel structure with air cavity

The total reflection and transmission can be seen as the sum of the reflection and transmission due to the double-panel structure with an air cavity, and the reflection and transmission due to the influences of the rods on the two panels. For instance, for the $n = 0, m = 0$ mode, the numerators of $T_{0,0}$ and $R_{0,0}$ from (5.50) and (5.51) can be split as:

$$T_{0,0} = \frac{4\phi_{0,0}^2}{(Q_{0,0} - 2)^2 \phi_{0,0}^2 - Q_{0,0}^2} - W_1 \frac{2\phi_{0,0}^2}{(Q_{0,0} - 2)^2 \phi_{0,0}^2 - Q_{0,0}^2} + W_2 \frac{(Q_{0,0}(\phi_{0,0}^2 - 1) - 2\phi_{0,0}^2)\phi_{0,0}}{(Q_{0,0} - 2)^2 \phi_{0,0}^2 - Q_{0,0}^2} \quad (6.1)$$

$$R_{0,0} = -\frac{2(\phi_{0,0}^2 + 1)Q_{0,0}^2}{(Q_{0,0} - 2)^2 \phi_{0,0}^2 - Q_{0,0}^2} + W_1 \frac{(Q_{0,0}^2(1 - \phi_{0,0}^2) + 2\phi_{0,0}^2)}{(Q_{0,0} - 2)^2 \phi_{0,0}^2 - Q_{0,0}^2} + W_2 \frac{2\phi_{0,0}}{(Q_{0,0} - 2)^2 \phi_{0,0}^2 - Q_{0,0}^2} \quad (6.2)$$

The response of the structure without the rods is recovered by setting W_1 and W_2 to 0 – it can be shown that this yields a result identical to following the derivation through without including the rods.

When either n or m (or both) are non-zero, only the terms related to the rod forces remain – this is because the incident field contains no modes outside of $n = 0, m = 0$ and the interconnecting rods are the only part of the system which exhibits mode conversion as described in Section 5.2:

$$T_{n,m} = W_2 \frac{(Q_{n,m}(\phi_{n,m}^2 - 1) - 2\phi_{n,m}^2)\phi_{n,m}}{(Q_{n,m} - 2)^2 \phi_{n,m}^2 - Q_{n,m}^2} - W_1 \frac{2\phi_{n,m}^2}{(Q_{n,m} - 2)^2 \phi_{n,m}^2 - Q_{n,m}^2} \quad (6.3)$$

$$R_{n,m} = W_2 \frac{2\phi_{n,m}}{(Q_{n,m} - 2)^2 \phi_{n,m}^2 - Q_{n,m}^2} + W_1 \frac{(Q_{n,m}^2(1 - \phi_{n,m}^2) + 2\phi_{n,m}^2)}{(Q_{n,m} - 2)^2 \phi_{n,m}^2 - Q_{n,m}^2} \quad (6.4)$$

6.2 Panel coincidence and cavity resonances

Several points about the nature of the reflected and transmitted modes in the low-frequency region given by (4.7) or (4.8) can be deduced by examining the expressions for reflection and transmission coefficients of order (0,0) given by (5.50) and (5.51). The denominators of the expressions reveal conditions under which the system response takes a simpler form. Firstly examining the definition of $Q_{n,m}$ in (5.27) and substituting $n = 0, m = 0$ results in:

$$Q_{0,0} = \frac{iDk_z^{0,0}}{\rho_0\omega^2} \left((k_x^0)^2 + (k_y^0)^2 \right)^2 - k_B^4 \quad (6.5)$$

Hence the term $Q_{0,0}$ becomes 0 when $\left((k_x^0)^2 + (k_y^0)^2 \right)^2 = k_B^4$, meaning when the length of the projection of the incident wave vector on the xy plane matches the plate bending wavenumber k_B . When this is the case, (6.1) and (6.2) simplify to:

$$T_{0,0} = 1 - \frac{W_2\phi_{0,0} + W_1}{2} \quad (6.6)$$

$$R_{0,0} = \frac{W_2 + W_1\phi_{0,0}}{2\phi_{0,0}} \quad (6.7)$$

The panel resonance occurs when:

$$\sin(\varphi_l) = \pm \frac{k_B}{k} \quad (6.8)$$

Therefore, when the xy projection of \vec{k}_0 matches k_B , panel coincidence leads in perfect transmission superimposed by interference caused by the rod interconnections.

The second scenario under which the expressions simplify is the cavity resonance: when $k_z = \{q\pi/d_z; q \in \mathbb{Z}\}$, meaning $\phi_{0,0} = (-1)^q$:

$$T_{0,0} = \frac{2}{2 - Q_{0,0}} - \frac{W_2(-1)^q + W_1}{2 - Q_{0,0}} \quad (6.9)$$

$$R_{0,0} = -\frac{2Q_{0,0}^2}{2 - Q_{0,0}} + \frac{W_1(-1)^q + W_2}{2 - Q_{0,0}} \quad (6.10)$$

Hence, the cavity resonances do not yield transmission peaks as high as the panel coincidence. The cavity resonances occur when:

$$\cos(\varphi_I) = \left\{ \frac{q\pi}{kd_z} : q \in \mathbb{Z} \right\} \quad (6.11)$$

The rod force terms W_1 and W_2 exhibit their own resonances – the terms are maximised when the denominator of expressions (5.48) and (5.49) is minimised – however, due to the presence of the γ_1 and γ_2 terms which contain summations over n and m , the conditions for this are not as straightforward to determine as the panel coincidence and cavity resonances.

6.3 Sample results

For illustrative purposes, results obtained for a structure with sample parameters – not necessarily representative of a practical structure, but selected to demonstrate key features of the system – are presented over the next few pages.

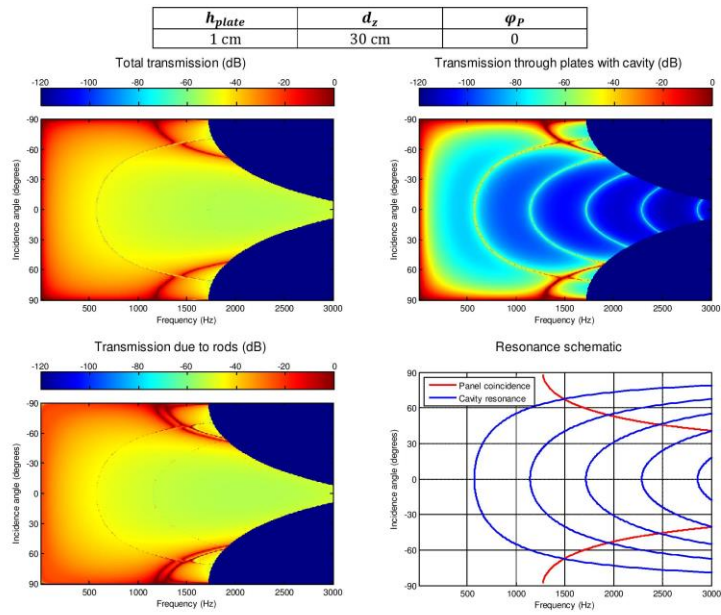
There are two sets of results, for two different structure. The first set is for thick panels spaced relatively far apart where there is little transmission without the introduction of rods, therefore the rods dominate the transmission – these results also demonstrate cavity resonances and panel coincidence. The second set of results is for thin panels spaced closer together, where there is notable transmission already without the rods – this set of results shows the interaction between cavity transmission and rod transmission, however due to the panel thickness the panel coincidence is not present and due to the small cavity only one cavity resonance appears.

Three subsets of results are shown within each set, with the “polarisation” angle φ_P (see (1.3) and the associated diagram) stepped between 0 , $\pi/8$ and $\pi/4$. Since a square grid ($d_x = d_y$) is used for both sets of results, $\varphi_P = 0$ and $\varphi_P = \pi/4$ correspond to incidence planes parallel to directions of strong periodicity: $\varphi_P = 0$ is parallel to the x axis whereas $\varphi_P = \pi/4$ is parallel to the unit cell diagonal line.

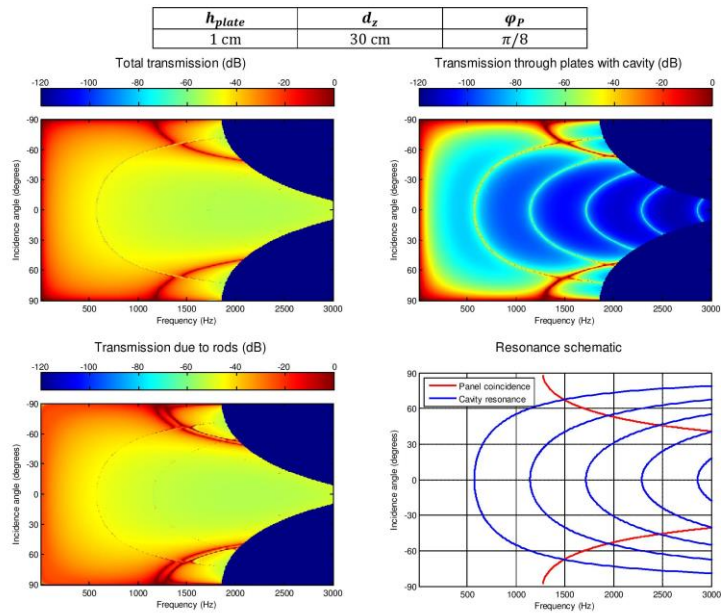
The graphs shown are 2D colour-maps, with frequency on the x axis and incidence angle φ_I (within the incidence plane – refer to (1.3)) on the y axis. The total transmission $T_{0,0}$ is shown within the low frequency region given by (4.7) or (4.8), the regions of the graph outside this area are removed (this results in the dark blue curved regions towards higher frequencies and higher incidence angles in the graphs), because whereas the data for $T_{0,0}$ would be correct, $T_{0,0}$ is no longer the only propagating mode and therefore no longer representative of all the transmitted energy. Alongside the total transmission, the transmission due to the two plates with a cavity alone, and due to the influence of the rods on the plates alone is shown separately. Finally, alongside the graphs is a schematic showing the locations of the panel coincidence lines and cavity resonances calculated using (6.11) and (6.8) in order to make these features recognisable in the colour maps.

The parameters used to generate the data which are constant throughout the results sets are shown below, parameters which vary are shown in the tables heading each set:

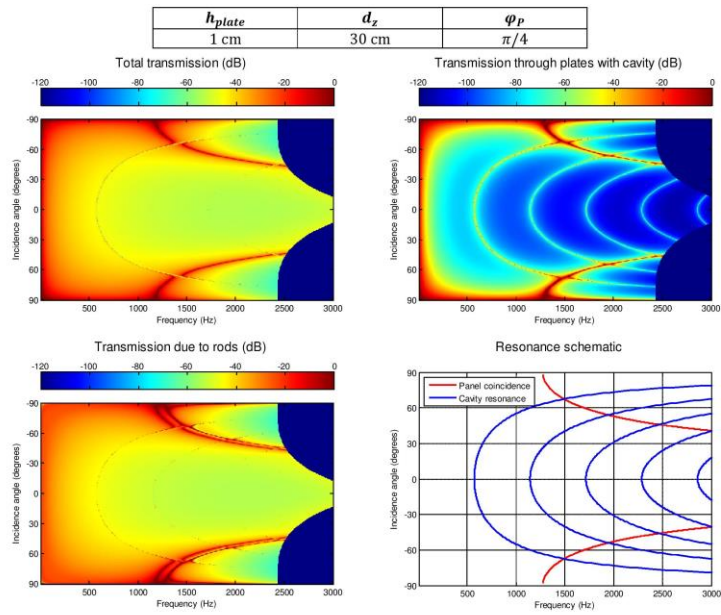
d_x	d_y	M_{plate}	D	ρ_{rod}	S_{rod}	ρ_0	c_0
10 cm	10 cm	27 kg/m ²	5.8 kPa · m ³	2.7 kg/m ³	1 cm ²	1.21 kg/m ³	343 m/s



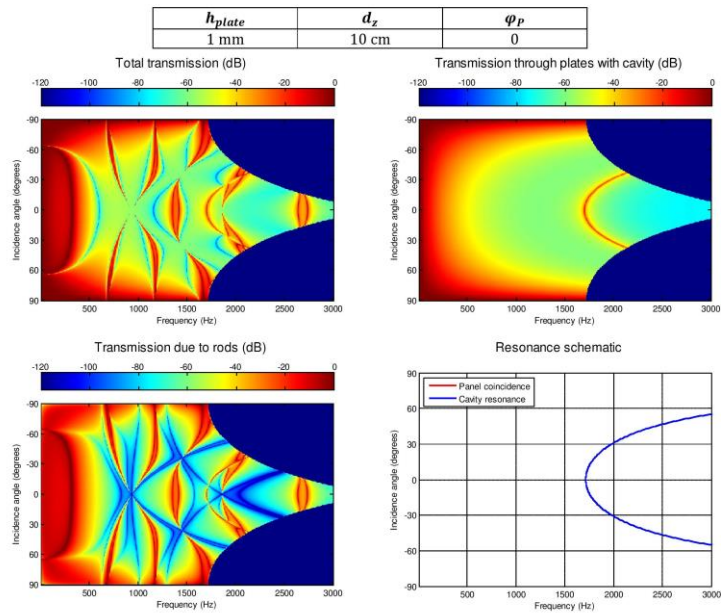
26



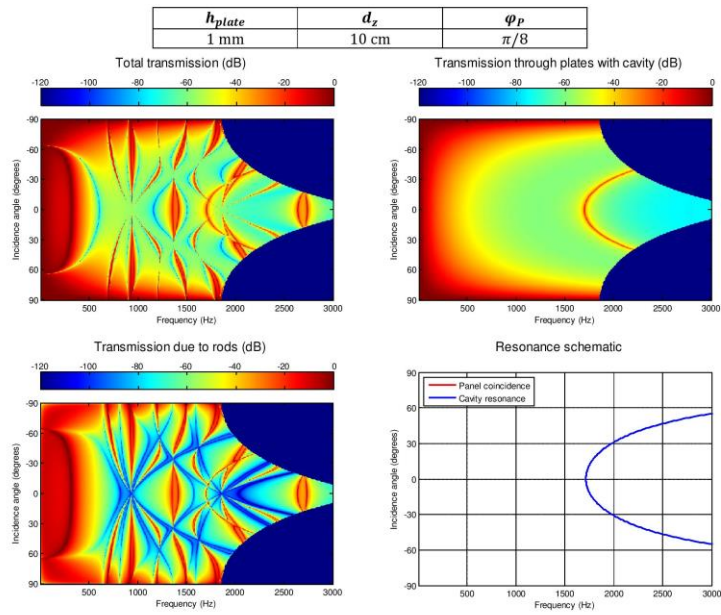
27



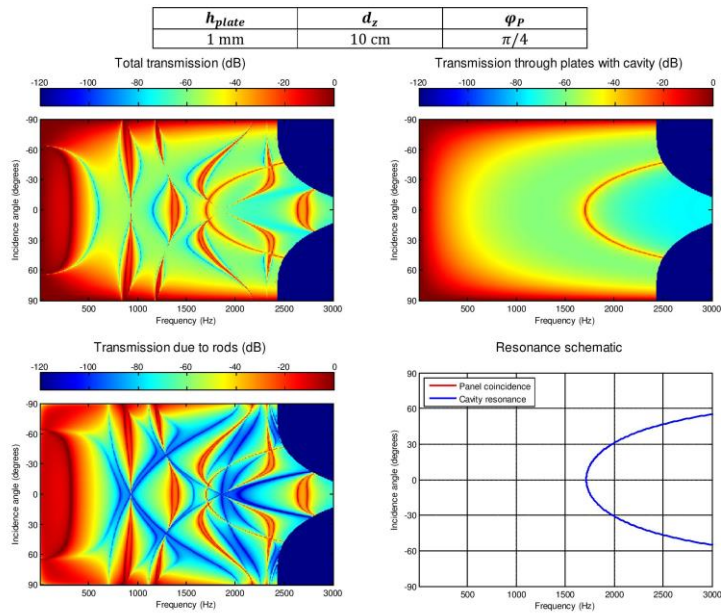
28



29



30



31